UNIVERSITÉ DE STRASBOURG

ÉCOLE DOCTORALE DE PHYSIQUE ET CHIMIE PHYSIQUE
INSTITUT PLURIDISCIPLINAIRE HUBERT CURIEN (IPHC), UMR 7178

THÈSE

PRÉSENTÉE PAR :

LUIS FELIPE PIÑERES RICO
soutenue le : **13/12/2022**

pour obtenir le grade de : **Docteur de l' Université de Strasbourg**
Discipline/Spécialité : Physique des particules

TRACK RECONSTRUCTION FOR THE TOP TRACKER OF THE JUNO NEUTRINO EXPERIMENT

THÈSE DIRIGÉE PAR :

DR. MARCOS DRACOS	Institut Pluridisciplinaire Hubert Curien

RAPPORTEURS :

DR. LUIS ALBERTO NUÑEZ DE VILLAVICENCIO MARTÍNEZ	Universidad Industrial de Santander (UIS)
DR. CLAUDIO GIGANTI	LPNHE

PRÉSIDENT :

DR ISABELLE RIPP BAUDOT	Institut Pluridisciplinaire Hubert Curien

Emmy Noether, the woman whose theorem revolutionized physics.
Called "an absolute mathematical genius" by Einstein in 1935.

Dedication

This thesis is dedicated to my daughter Emily[1], whose name honors Emmi Noether.

---

[1] Emmy in German

Acknowledgements

Although I believe that there should be no borders between the different languages that exist in the world, there is a part of my people who only speak Spanish. This is the main reason why I have taken the liberty of first writing part of the acknowledgements in my mother language.

Aunque creo que no debería existir fronteras entre los diferentes idiomas que existen en el mundo, lastimosamente hay una parte de los míos que solo hablan español. Esta es la razón principal por la que me he tomado la libertad de escribir la primera parte de los agradecimientos en mi lengua materna.

En primer lugar, quiero dedicar esta tesis a la vida, la cual me ha permitido compartir hermosos momentos pese a la adversidad. Mi hija, Emily, llegó en el momento justo y necesario para iluminar mis días. Sin su sonrisa, carcajada, mirada y sus palabritas, esta tesis no hubiese llegado a su final. También agradecerle a mi esposa, Katia, por su sacrificio, amor y disponibilidad en cada momento. También me gustaría agradecerle a mis padres Luis y Zenaida, a mis hermanos José y Duban. También a la familia de mi esposa. A Santiago, mi hermanito menor que me ve como ejemplo.

A mis amigos alrededor de este mundo también les debo un reconocimiento:

En Colombia, a los muchachos de la universidad del Atlántico (Amell, Camargo, Martin, Gomelo, Bebo, entre muchos otros), a algunos de la promoción del IEA (Ditta, Taty).

En Brazil, a Adelir , Paulinha, Rodrigo, Carlos y sobre todo a Pietro Chimenti.

En Francia, a mis estimados que han compartido conmigo: Amadeus, Venus, Diana, Cristian, Erick, José, Alex, Maria, Ligia, Pablo. En Alsacia, a Nini, Fernando y a sus hijos por permitirme entrar a su hogar, y brindarme esa admiración que he recibido de su parte. A Clemencia por darnos algunos consejos en los momentos más necesarios, por regalarnos un espacio en su hogar. A Luis y su familia por su gentileza y amor hacia nosotros. Y sobretodo, por mostrarnos el amor inmenso que debemos sentir hacia nuestro país, Colombia.

En estos momentos, llegan a mí unas palabras de Gabriel García Márquez "Colombia va a estar siempre conmigo, donde me encuentre, siempre escribiré una novela Colombiana, a pesar de que me encuentre en el exilio en México". Por eso, apesar de encontrarme en otro continente, sé que los pensamientos y deseos de cada uno de ustedes están siempre conmigo. Gracias a todos ustedes por haber creído en mí desde el primer día.

I am pleased to thank the University of Strasbourg, the IPHC and the QMat for supporting my research over the years. I would like to thank all the members of the examining committee of my PhD thesis : Luis Alberto Nuñez de Villavicencio Martínez, who is a pioneer of science in Colombia, for his acceptance to participate in the committee. I am thankful to Claudio Giganti for his comments. And above all I would like to thank Isabelle Ripp Baudot with her kind questions, despite not belonging to the field of neutrino physics, she decided to participate in the committee to learn more about neutrino physics. I consider this curiosity an honor for me.

I would like to thank Marcos Dracos for his patience, time, collaboration and dedication. Even though I did not work in experimental physics, he gave me an opportunity in the neutrino group. I am also indebted to João Pedro Athayde Marcondes de André. I want to thank him for his help in all aspects. Thank you for having clarified thousands of doubts during my PhD, even though most of the conversations were in Portuguese. I owe this thesis to both of them. To the other members of the neutrino group who are still here and to those who are no longer here, I want to thank immensely : Michal, Andrea, Marie Laure, Leonidas, Loris, Julie, Pascal, Elian, Erick, Rebin and Jacques.

I would also like to dedicate a word to the members of the JUNO experiment that I met during my doctoral work. To each of you, thank you for your questions, comments or suggestions during the collaboration meetings. Honestly, I never imagined in my life to be able to set foot on such a distant land (China) to present the results of my work. I can't deny the nerves that ran over my body. But the excitement of learning more about this collaboration gave me the strength to take this project forward and learn more from you.

I would like to thank the current PhD students (Mariam, Hassan, Deshan, Mohd), I must say I am proud of you. I met you when you were master students in the neutrino group and today you are in great research groups. I thank you for every word of encouragement at all times. And I am very happy to have helped you as much as possible.

CONTENTS

Part I

Introduction

Introduction

The natural radioactivity studied by Becquerel with phosphorescent materials (uranium salts) in 1896 provided the basis for understanding the phenomenon of atomic decays [1]. The formulation of new forms of radiation originated with the contributions of Curie, Rutherford and Villard in the search for new radioactive substances such as polonium, radium, actinium and others [1, 2, 3]. Thus, it is established that unstable atoms can be transformed into other atoms through three types of disintegration: α, β and γ [4]. The theory formulated in the β decay required the emitted electron to have a fixed energy, as this was a two-body decay. However, in 1914 Chadwick discovered a continuous electron energy spectrum [5]. In the absence of a convincing explanation for the beta decay anomaly, Bohr suggested abandoning the principle of conservation of energy. In 1930, Pauli postulated the existence of a neutral particle with spin 1/2 to guarantee the conservation of energy and angular momentum in this process [6, 7]. After the discovery of the neutron by Chadwick in 1932 [8], Fermi develops the theory of β decay in 1934 [9], incorporating the particle proposed by Pauli, baptizing it neutrino.

The first measurement of the neutrino was performed by Reines and Cowan in the Savannah River experiment in 1956 [10]. The 1995 Nobel Prize was awarded to Reines for the discovery of the neutrino. This type of neutrino is now known as the electron neutrino (ν_e). Lederman, Schwartz and Steinberger received the 1988 Nobel Prize for the discovery of the second type of neutrino, the muon neutrino (ν_μ), at the brand-new Alternating Gradient Synchrotron in 1962 [11]. While, the first direct evidence for the third neutrino, tau neutrino (ν_τ) was obtained at Fermilab, by the Direct Observation of the NeUtrino Tau (DONUT) experiment in 2000 [12]. Six years later, the Large Electron Positron Collider (LEP) experiments determine the constraint on the number of neutrino families: $N_\nu = 2.992 \pm 0.020$, that is only 3 types of neutrinos are produced in the decay of a neutral Z-boson [13]. These three types of neutrinos in the Standard Model of Particles Physics are called flavour neutrinos and are : $(\nu_e, \nu_\mu, \nu_\tau)$. In the 1960s, the Homestake experiment measured a deficit in the flux of neutrinos emitted by the Sun in comparison with the flux predicted by the Standard Solar Model [14]. This discrepancy between the theory and the experimental results was catalogued as the "Solar neutrino problem". In 1962, Z. Maki et al. proposed the oscillation between neutrino flavours [15, 16]. The oscillation phenomenon depends on three mixing angles (θ_{12}, θ_{13}, θ_{23}), two squared mass differences (Δm^2_{32}, Δm^2_{21}) and the CP violating phase δ_{cp} [17, 18]. This phenomenon cannot occur if the neutrino masses are zero. The evidence of neutrino oscillations was obtained in the atmospheric neutrino Super Kamiokande experiment [19, 20, 21] in 1998, and the solar SNO experiment in 2001 [22, 23]. Chapter 1 presents the theoretical framework used in neutrino physics and neutrino oscillations, the current experimental status of oscillation parameter measurements is also detailed.

After the discovery of the value of the non-zero parameter θ_{13} in the latest neutrino oscillation experiments [24, 25, 26], the neutrino mass hierarchy and the observation of CP symmetry violation of leptons are within reach of future neutrino projects. The Jiangmen Underground Neutrino Observatory (JUNO) [27, 28] is a multi-purpose underground liquid scintillator detector with a target mass of 20 kt, and an energy resolution of 3% at 1 MeV. The main goal of JUNO is to determine the neutrino mass hierarchy to 3σ over 6 years of operation, as well as to provide accurate measurements of the neutrino oscillation parameters, from the study of reactor antineutrino oscillation with a baseline of 53 km. The excellent energy resolution and large fiducial volume anticipated for the JUNO detector offer exciting opportunities for addressing many important topics in neutrinos and astro-physics. The JUNO detector consists of a Central Detector for neutrino detection, a Water Cherenkov Detector used as a cosmic muon veto, and a muon tracker called Top Tracker. A detailed description of the JUNO experiment and its physics program is found in Chapter 2.

The Top Tracker (TT) re-used the plastic scintillator modules of OPERA, a neutrino experiment which took place in Gran Sasso (Italy) between 2008 and 2012 [29, 30]. The role of the TT is to detect atmospheric muons and to reconstruct their trajectory in JUNO in order to study the cosmogenic background production and thus reduce the systematic errors on the mass hierarchy determination. My thesis is focused on the TT of JUNO. One goal of this thesis was perform some calibration tests, allowing to validate the new TT electronics, which will replace the OPERA electronics, not sufficiently performant for this new application. In Chapter 3, it is discussed the calibration tests developed for the TT prototype in Strasbourg. The TT prototype also provides us the possibility to prepare and test the reconstruction algorithms to be used in the whole TT detector after. The final objective of this thesis is focused on developing a reconstruction algorithm to filter out the background and the application on the muon analysis on the TT prototype data.

The reconstruction algorithm used in the JUNO official software has a limitation due to the numbers of reconstructed hits inside the detector, if there are too many hits the algorithm spends a huge time running. Therefore, a new faster and if possible more efficient method of reconstruction is required. For this purpose, an algorithm based on the Hough transform [31, 32, 33] will be used. The official JUNO software was adapted to simulate muons crossing the TT prototype. This allows us to optimize the Hough accumulator matrix, to calculate the detection efficiency, angular distributions, and above all to compare the JUNO and Hough reconstruction methods. In Chapter 4, it is detailed the key elements of this algorithm, how it is used for better muon track detection, and provides a performance evaluation of this algorithm.

It is found that the Hough method is more efficient and requires less execution time compared to the JUNO software. Thus offering the possibility of integrating Hough's method for the JUNO Top Tracker in the future.

Introduction

Dans les années 1960, l'expérience Homestake a mesuré un déficit dans le flux de neutrinos émis par le Soleil par rapport au flux prédit par le modèle solaire standard. Cette divergence entre la théorie et les résultats expérimentaux a été cataloguée comme le "problème des neutrinos solaires". En 1962, Z. Maki et al. ont proposé l'oscillation entre les saveurs de neutrinos. Le phénomène d'oscillation dépend de trois angles de mélange (θ_{12}, θ_{13}, θ_{23}), de deux différences de masse au carré (Δm^2_{32}, Δm^2_{21}) et de la phase de violation de CP δ_{cp}. Ce phénomène ne peut pas se produire si les masses des neutrinos sont nulles. La preuve de l'existence d'oscillations de neutrinos a été obtenue dans l'expérience Super Kamiokande sur les neutrinos atmosphériques en 1998, et dans l'expérience SNO sur les neutrinos solaires en 2001. Le chapitre 1 présente la physique des neutrinos.

L'Observatoire souterrain de neutrinos de Jiangmen (JUNO) est un détecteur souterrain polyvalent à scintillateur liquide dont la masse cible est de 20 kt et dont la résolution en énergie est de 3% à 1 MeV. L'objectif principal de JUNO est de déterminer la hiérarchie des masses de neutrinos à 3σ après 6 ans de fonctionnement, ainsi que de fournir des mesures précises des paramètres d'oscillation des neutrinos, à partir de l'étude de l'oscillation des antineutrino des réacteurs situés à $\sim$ 53 km du détecteur. JUNO offrent des possibilités intéressantes pour aborder de nombreux sujets importants dans le domaine des neutrinos et de l'astrophysique. Une description détaillée de l'expérience JUNO et de son programme de physique se trouve dans le chapitre 2.

Le détecteur JUNO se compose d'un détecteur central pour la détection des neutrinos, d'un détecteur Cherenkov à eau utilisé comme veto des muons cosmiques, et d'un trajectographe de muons appelé Top Tracker (TT). Le rôle du TT est de détecter les muons atmosphériques et de reconstruire leur trajectoire dans JUNO afin d'étudier la production du bruit de fond cosmogénique et ainsi réduire les erreurs systématiques sur la détermination de la hiérarchie des masses. Ma thèse est centrée sur le TT de JUNO. Un des objectifs de cette thèse était de réaliser des tests de calibration, permettant de valider la électronique du TT. Dans le chapitre 3 seront présentés les tests de calibration développés pour le prototype TT à Strasbourg.

Le prototype TT nous donne également la possibilité de préparer et de tester les algorithmes de reconstruction qui seront utilisés dans l'ensemble du détecteur TT. L'objectif final de cette thèse se concentre sur le développement d'un algorithme de reconstruction pour filtrer le bruit de fond et l'application de l'analyse des muons sur les données du prototype TT. Le chapitre 4 détaille les éléments clés de cet algorithme basé sur la transformée de Hough.Il s'avère que la méthode de Hough est plus efficace et nécessite moins de temps d'exécution par rapport au logiciel officiel de JUNO. Cela offre donc la possibilité d'intégrer la méthode de Hough dans le logiciel officiel du Top Tracker de JUNO dans le futur.

Chapter 1

Neutrino Physics

"I have done a terrible thing, I have postulated a particle that cannot be detected"
W. Pauli.

Contents

Since the hypothesis in 1930 by Pauli [6, 7] to safeguard the principle of conservation of energy and angular momentum in the spectrum of continuous β decay [5], neutrinos have been considered one of the most intriguing and fascinating particles of the Standard Model. The Standard Model[1] is a Quantum Field theory that combines special relativity and quantum mechanics based on the concepts of symmetries and gauge invariance [35, 36, 37]. The Standard Model is one of the most elegant, simple and well-structured theories developed in the late 1960s. In this theory, elementary particles are understood as excitations of quantum fields filling space-time.

---

[1] In 1975, the term "Standard" Model was first mentioned by Abraham Pais and Sam Treiman [34].

After photons, neutrinos are the second most abundant particle in the universe. Neutrinos are everywhere. However, their detection is a challenge due to their weak interaction with matter. The role played by neutrinos in particle physics in recent decades has been key to further understanding nuclear physics, astronomy , and to opening a window to theories beyond the Standard Model with the phenomenon of the neutrino flavour oscillation.

The aim of this chapter is to present an introduction about neutrino physics. The Standard Model of particle physics is discussed in Section 1.1. The neutrino hypothesis is postulated in Section 1.2, where the basic properties of neutrinos are presented. The formalism of the quantum phenomenon of neutrino oscillations is reviewed in Section 1.3. The current knowledge of neutrino oscillations parameters and the status of neutrino physics experiments is shown in Section 1.4. The chapter ends by addressing several questions that remain open in neutrino physics in Section 1.5.

1.1 The Standard Model of Particle Physics

The Standard Model describes three of the four fundamental interactions of nature : the electromagnetic, weak and strong forces. The model does not explain the quantum effects of the gravitational interaction.

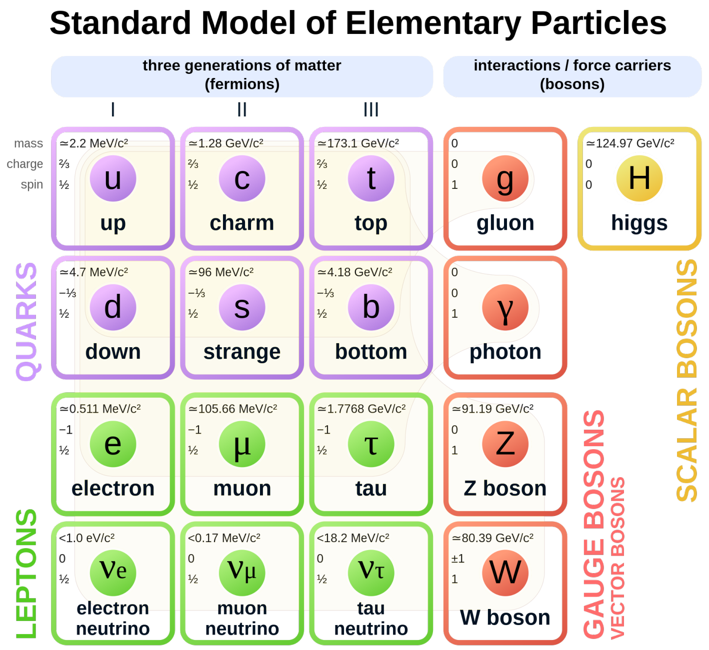

Figure 1.1: Standard Model of Elementary Particles [38] .

Fig. 1.1 illustrates the elementary particle content of the Standard Model. It shows some of their properties such as mass, charge and spin. In the Standard Model, the elementary particles are classified into 12 fermions and 13 bosons. Fermions have spin 1/2 and bosons have integer spin. Fermions describe the ordinary matter of the universe. The interactions between elementary particles are mediated by the gauge bosons of the Standard Model.

In the Standard Model, the bosons are divided into 12 gauge bosons and one scalar boson. The gauge bosons are classified by the kind of interaction in the model. The electromagnetic interaction is mediated by 1 gauge boson (γ), while 3 other gauge bosons are responsible for the weak interaction (W^+,W^-, Z^0). The strong interaction is mediated by 8 gauge bosons (gluons), while the scalar boson, called Higgs boson (H), plays a fundamental role in the mass generation mechanism of elementary particles.

The fermions are classified into 6 leptons and 6 quarks. The leptons are : electron (e), muon (μ), tau (τ), electron neutrino (ν_e) muon neutrino (ν_μ), and tau neutrino (ν_τ), while the quarks are : up (u), down (d), charm (c), strange (s), top (t), and bottom (b). The Standard Model organises the fermions into three families, where each family contains two quarks and two leptons. The only difference between the three fermion families is the mass scale. Second and third family are heavier replicas of the first family ($m_e \ll m_\mu \ll m_\tau$). This difference in mass is a manifestation of the coupling of the fermionic fields with the Higgs field. All neutrinos are considered massless particles [39].

The Standard Model is a theory invariant under internal symmetry groups : $SU(3)_C \otimes SU(2)_L \otimes U(1)_Y$ [35, 36, 37, 40, 41]. These groups of symmetries describe the interactions of nature. The first gauge theory, Quantum Electrodynamics describes the interactions of electrons with light. The model subsequently incorporates electroweak theory under $SU(2) \otimes U(1)$, which describes electromagnetic interactions and weak nuclear interactions. The Standard model also includes Quantum Chromodynamics, the theory of strong nuclear interactions under $SU(3)$ group. The interactions between elementary particles depend on their properties, such as electric charge, color charge and others. For example, all electrically charged particles interact with photons. On the other hand, only quarks and gluons experience the strong nuclear interaction. As for leptons, quarks, W^+, W^-, and Z^0 perceive the weak nuclear interaction.

Symmetries are very important for determining the physical laws that describe certain systems. An interesting connection between symmetries and constants of motion is explained in Noether's Theorem. The theorem establishes that for each continuous symmetry of the Lagrangian of a physical system there corresponds a quantity that is conserved during the dynamic evolution of the system [42]. We can cite as familiar examples of this relation, the conservations of energy, linear momentum and angular momentum, which are associated with invariance under temporal translations, spatial translations and rotations, respectively. In quantum mechanics, symmetries are associated with the degeneracy of energy levels. In the theory of Special Relativity, the connection between reference systems is made by the Lorentz transformations [43]. Therefore, Lorentz symmetry is a fundamental requirement for formulating a relativistic theory. The properties of quantum mechanics and the Lorentz group are the basis for the formulation of Quantum Field Theory. As already mentioned, symmetry has played an important role in the development of particle physics.

The Standard Model describes the fields (particles) using a Lagrangian language based on a quantum gauge field theory. Where the Lagrangian density $\mathcal{L}$ contains information about the kinetic energy, mass, and interactions of each field [44]. Some fields that will be used throughout this chapter are shown in the Table. 1.1. For example, the Higgs boson is described using the Klein Gordon's Lagrangian associated with a scalar field of spin 0. While the Dirac's Lagrangian is used for a spinorial field of spin 1/2 related to charged fermions. And the Maxwell's Lagrangian describes photons by a spin 1 vector field. In the Table. 1.1, m is a mass term, γ^{μ} are the Dirac matrices, ∂_{μ} are the covariant derivatives, and $F^{\mu\nu}$ the electromagnetic field strength tensor.

Table 1.1: Fields for some particles of the Standard Model and the Lagrangian.

Fields	Spin	Particle	Lagrangian
Scalar φ	0	Higgs boson	$\mathcal{L}_{KleinGordon} = \frac{1}{2}(\partial_{\mu}\Phi\partial^{\mu}\Phi - m^2\Phi^2)$
Spinorial ψ	$\frac{1}{2}$	Fermions charged	$\mathcal{L}_{Dirac} = \bar{\psi}\left(i\gamma^{\mu}\partial_{\mu} - m\right)\psi$
Vectorial A^{μ}	1	Photons	$\mathcal{L}_{Maxwell} = -\frac{1}{4}F_{\mu\nu}F^{\mu\nu}$

1.1.1 Electromagnetic Interaction

The race for the construction of a quantum model describing the electromagnetic interaction began with the formulation of relativistic quantum mechanics in 1928 by P. Dirac. Quantum Electrodynamics is the first well-established quantum field theory described in the 20th century. Precision comparison between measurement and theory of the electron anomalous magnetic moment was the starting point of stringent tests of Quantum Electrodynamics [45]. In this section is presented the construction of Quantum Electrodynamics based in the local abelian gauge symmetry U(1).

The Dirac's Lagrangian ($\mathcal{L}_{Dirac}$) shown in the Table. 1.1, describes a free fermion $\Psi(x)$ with charge q and mass m. Under a local gauge transformation $U(1)$, the spinorial field is transformed by the local phase $\theta(x)$.

$$\Psi(x) \to \Psi^{'}(x) = e^{iq\theta(x)}\Psi(x) \tag{1.1}$$

In this case the Dirac's Lagrangian is no longer gauge invariant.

$$\mathcal{L}_{Dirac} \to \mathcal{L}^{'}_{Dirac} = \bar{\Psi}(x)\left(i\gamma^{\mu}\partial_{\mu} - m\right)\Psi(x) - q\bar{\Psi}(x)\gamma^{\mu}\Psi(x)\partial_{\mu}\theta \tag{1.2}$$

In the language of quantum field theory, imposing the gauge principle allows to introduce vector fields to guarantee gauge invariance. Therefore, introducing a new field A_{μ} , the covariant derivative ∂_{μ} must be modified :

$$D_{\mu} = \partial_{\mu} + iqA_{\mu} \tag{1.3}$$

$$A_{\mu} \to A^{'}_{\mu} = A_{\mu} - \partial_{\mu}\theta \tag{1.4}$$

where the vector field A_{μ} is associated with the gauge boson called photon.

The Quantum Electrodynamics Lagrangian is given by :

$$\mathcal{L}_{QED} = \bar{\Psi}(x)\left(i\gamma^{\mu}\partial_{\mu} - m\right)\Psi(x) - \frac{1}{4}F_{\mu\nu}F^{\mu\nu} - A_{\mu}J^{\mu} \tag{1.5}$$

In the Lagrangian $\mathcal{L}_{QED}$, the first term describes a free fermion with the Dirac's Lagrangian. The second term is associated to the Maxwell's Lagrangian, where the electromagnetic field strength tensor $F_{\mu\nu} = \partial_{\mu}A_{\nu} - \partial_{\nu}A_{\mu}$. The coupling between charged particles and the electromagnetic field A_{μ} is given by the charged current J^{μ}. According to Noether's theorem the electric charge q is the quantity conserved due to the Abelian group $U(1)$. The current is given by $J^{\mu} = q\bar{\Psi}(x)\gamma^{\mu}\Psi(x)$. The gauge principle could be extended to other interactions not only in Quantum Electrodynamics. This principle is one of the fundamental pillars in the development of the Standard Model.

1.1.2 Strong Interaction

Quantum Chromodynamics is a non-Abelian gauge field theory. It describes the strong interactions based on the $SU(3)$ group [46]. Strong interaction is responsible for the stabililty of the atomic nuclei. In Quantum Chromodynamics the bosons mediating the interaction are the gluons. The Lagrangian of Quantum Chromodynamics [39] is given by :

$$\mathcal{L}_{QCD} = \sum_{q} \bar{\psi}_{q,a}\left(i\gamma^{\mu}\partial_{\mu}\delta_{ab} - g_s\gamma^{\mu}t^{C}_{ab}A^{C}_{\mu} - m_q\delta_{ab}\right)\psi_{q,b} - \frac{1}{4}G^{A}_{\mu\nu}G^{\mu\nu}_{A} \tag{1.6}$$

where the quark field is defined by $\psi_{q,a}$ with flavour q and mass m_q. The quantity associated to $SU(3)$ is the quantum number called colour. The A^{C}_{μ} correspond to the gluon fields, with C running from 1 to 8 (there are eight gluons). The color-index $a = 1, 2, 3$. The generator of the $SU(3)$ group is given by the $t^{C}_{ab} = \lambda^{C}_{ab}/2$, wherein the λ^{C}_{ab} are the Gell-Mann Matrices. The $G^{A}_{\mu\nu} = \partial_{\mu}A^{a}_{\nu} - \partial_{\nu}A^{a}_{\mu} - g_s f_{ABC}A^{B}_{\mu}A^{C}_{\nu}$, is the strength tensor for $SU(3)$, g_s the Quantum Chromodynamics coupling constant and f_{ABC} are the structure constants of the $SU(3)$ group [39].

The gluons couple to the quarks as well as to themselves. In nature, quarks and gluons have never been observed as free particles. Hadrons are color-singlets (i.e., color-neutral) combinations of quarks, anti-quarks and gluons. Particles with three different coloured quarks are called baryons (for example, proton (uud) , neutron (udd)), while, particles composed of quark-antiquark pair are called mesons, such as pion ($u\bar{d}$).

1.1.3 ElectroWeak Interaction

The contributions of Glashow, Salam and Weinberg allowed the formulation of the weak interaction in the framework of the electroweak theory of the Standard Model [35, 36, 37, 41, 47]. The symmetry group $SU(2)_L \otimes U(1)_Y$ describes the electroweak theory. The gauge fields corresponding to the group $SU(2)_L$ are three bosons $(W^{1}_{\mu}, W^{2}_{\mu}, W^{3}_{\mu})$, and one boson B_{μ} for the group $U(1)_Y$. The group $U(1)_Y$ is associated to the leptonic hypercharge (Y)

that is related to the weak isospin (T_3) and the electric charge via the Gell-Mann–Nishijima formula :

$$Q = T_3 + \frac{Y}{2} \tag{1.7}$$

The Table. 1.2 shows the three quantum numbers used in Glashow-Salam-Weinberg model for electroweak unification of quarks and leptons. In the Standard Model, the projection of the spin ($\hat{s}$) in the direction of momentum $\hat{p}$ is called helicity $\hat{h}$. For massless particles, helicity is the same as chirality. Chirality is an intrinsic property of a particle and is itself a Lorentz invariant.

$$\hat{h} = \frac{\hat{s} \cdot \hat{p}}{|\vec{p}|} \tag{1.8}$$

Chirality allows us to decompose Dirac fields, $\psi = \psi_L + \psi_R$, where the right-handed (ψ_R) or left-handed ψ_L components are defined by :

$$\psi_L = \frac{1}{2}(1 - \gamma_5)\psi, \quad \psi_R = \frac{1}{2}(1 + \gamma_5)\psi \tag{1.9}$$

For a spin 1/2 particle, the helicity of a particle is positive (right-handed, R) if the direction of the spin is the same as that of its motion. While, a helicity of a particle is negative (left-handed, L) occurs if the directions of spin and motion are opposite.

Table 1.2: The three quantum numbers used in Glashow-Salam-Weinberg model for electroweak unification of quarks and leptons in the Standard Model.

Particles	T_3	Y	Q
u_R, c_R, t_R	0	$+\frac{4}{3}$	$+\frac{2}{3}$
d_R, s_R, b_R	0	$-\frac{2}{3}$	$-\frac{1}{3}$
e_R, μ_R, τ_R	0	-2	-1
$\begin{pmatrix} u_L \\ d_L \end{pmatrix}, \begin{pmatrix} c_L \\ s_L \end{pmatrix}, \begin{pmatrix} t_L \\ b_L \end{pmatrix}$	$\begin{pmatrix} +\frac{1}{2} \\ -\frac{1}{2} \end{pmatrix}$	$+\frac{1}{3}$	$\begin{pmatrix} +\frac{2}{3} \\ -\frac{1}{3} \end{pmatrix}$
$\begin{pmatrix} \nu_{eL} \\ e_L \end{pmatrix}, \begin{pmatrix} \nu_{\mu L} \\ \mu_L \end{pmatrix}, \begin{pmatrix} \nu_{\tau L} \\ \tau_L \end{pmatrix}$	$\begin{pmatrix} +\frac{1}{2} \\ -\frac{1}{2} \end{pmatrix}$	-1	$\begin{pmatrix} 0 \\ -1 \end{pmatrix}$

As shown in the Table. 1.2, fermions are organized in left-handed and right-handed fields. The left-handed fermion fields transform as doublets under $SU(2)_L$ and the right-handed fields are singlets of $SU(2)_L$. Neutrinos have only left-handed chirality. In the electroweak theory formulated in 1962 by Glashow and Salam, there was a paradox about the mass of the particles W and Z. First, weak interactions required that such particles had large masses. Furthermore, the gauge symmetry imposes that they are massless. This contradiction vanishes if the masses of the bosons were apparent, that is, if their masses were acquired through an external mechanism, called the Higgs mechanism. The Higgs boson is a particle proposed in 1964 by Higgs, Brout, Englert in order to solve this paradox [48, 49]. A complex scalar Higgs doublet, ϕ, is added to the electroweak model for mass generation through spontaneous symmetry breaking with potential given by :

$$V(\Phi^{\dagger}\Phi) = \mu^2\Phi^{\dagger}\Phi + \frac{\lambda^2}{2}(\Phi^{\dagger}\Phi)^2, \qquad \phi \equiv \begin{pmatrix} \phi^+ \\ \phi^0 \end{pmatrix} \tag{1.10}$$

For $\mu^2 < 0$, ϕ develops a vacuum expectation value $v/\sqrt{2} = \left|\mu\right|/\lambda$, where $v = 246.22$GeV, breaking part of the electroweak gauge symmetry, after which only one neutral Higgs scalar, remains in the physical particle spectrum. The potential associated with the Higgs field is shown in the Fig. 1.2.

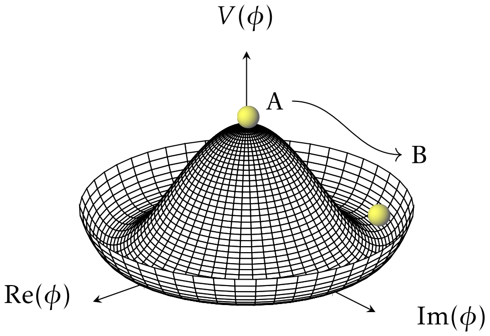

Figure 1.2: Higgs Potential.

After symmetry breaking the Lagrangian for the Dirac fermion fields becomes :

$$\begin{aligned}\mathcal{L}_F = \sum_i \bar{\psi}_i(i\gamma^{\mu}\partial_{\mu} - m_i - \frac{m_i H}{v})\psi_i - \frac{g}{2\sqrt{2}}\sum_i \bar{\psi}_i\gamma^{\mu}(1-\gamma^5)(T^+W_{\mu}^+ + T^-W_{\mu}^-)\psi_i \\ -e\sum_i Q_i\bar{\psi}_i\gamma^{\mu}\psi_i A_{\mu} - \frac{g}{2\cos\theta_w}\sum_i \bar{\psi}_i\gamma^{\mu}(g_V^i - g_A^i\gamma^5)\psi_i Z_{\mu}\end{aligned} \tag{1.11}$$

where θ_w is the weak mixing angle. Eq. 1.12 describes the relation of the weak mixing angle to the coupling constants of the group SU(2) and U(1) (g and $g^{'}$ respectively) and also to electromagnetic coupling constant (the electric charge e).

$$\tan\theta_w = \frac{g^{'}}{g} \qquad e = g\sin\theta_w \tag{1.12}$$

The physical particles responsible for the weak interaction ($W_{\mu}^{\pm}$, Z_{μ}) and electromagnetic interaction (A_{μ}) are produced by the spontanenous symmetry breaking caused by the Higgs mechanism :

$$A_{\mu} = \cos\theta_w B_{\mu} + \sin\theta_w W_{\mu}^3 \tag{1.13}$$

$$W_\mu^\pm = \frac{1}{\sqrt{2}}\left(W_\mu^1 \mp W_\mu^2\right) \tag{1.14}$$

$$Z_\mu = -\sin\theta_w B_\mu - \cos\theta_w A_\mu \tag{1.15}$$

At lowest order perturbation theory (tree level), the boson masses in the Electroweak sector are given by :

$$M_W = \frac{gv}{2} \tag{1.16}$$

$$M_Z = \frac{v}{2}\sqrt{g^2 + (g')^2} \tag{1.17}$$

$$M_H = \lambda v \tag{1.18}$$

$$M_\gamma = 0 \tag{1.19}$$

The first term in Eq. 1.11 gives rise to charged fermion masses through g_f Yukawa coupling as :

$$M_f = \frac{v g_f}{\sqrt{2}} \tag{1.20}$$

As shown in the Table. 1.2, since the neutrinos described by the Standard Model have only left-handed chirality. It is not possible to express the mass Lagrangian for neutrinos as is commonly used for other leptons. For this reason neutrinos are considered massless particles in the Standard Model. Therefore, some model is required to complete the Standard Model with massive neutrinos, the simplest extention to include a neutrino mass involves adding a right-handed neutrino.

The search for the Higgs boson, the particle responsible for the mechanism of mass generation in the Standard Model, has been one of the fundamental efforts of particle physics for several decades. The discovery of Higgs boson in 2012 by the LHC experiments in ATLAS [50] and CMS [51] completed a fundamental missing piece of the Standard Model of particle physics. In 2013, the Nobel Prize in Physics was awarded to Higgs and Englert for the "theoretical discovery that contributes to our understanding of the origin of the mass of subatomic particles". The Standard Model explains most of the known phenomena in elementary particle physics. However, there are some issues that the model fails to explain: dark energy, dark matter, matter-antimatter asymmetry in the universe, gravitational interaction and neutrino mass, more details can be found in [44]. New models have been developed to solve these problems, such as string theory [52], loop quantum gravity [53], supersymmetry [54] and extensions of the Standard Model [55].

1.1.4 Standard Neutrino interactions

In the Standard Model, neutrinos are neutral fermions. They interact with other fermions by the weak interaction through the exchange of W or Z bosons [39]. The interaction between the W boson and the neutrinos (or antineutrinos) is given by the charged current in Eq. 1.21. While the coupling of the Z boson and the neutrinos (or antineutrinos) is originated by the neutral current described in and Eq. 1.22. The standard neutrino interactions are illustrated in the Feynman diagrams in Fig. 1.3.

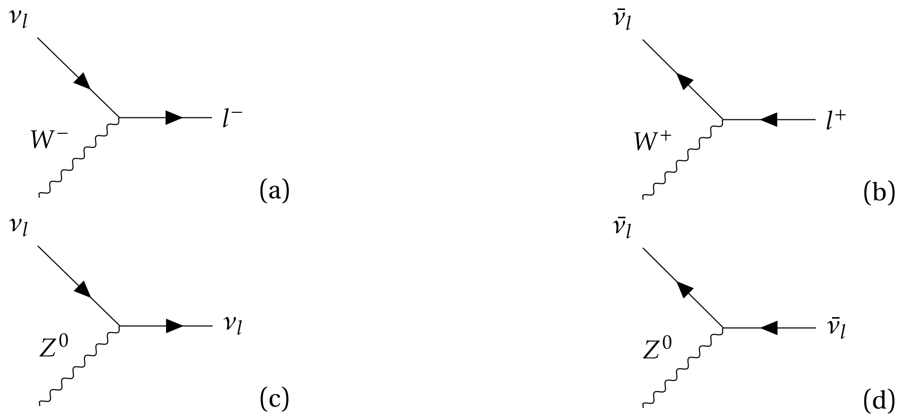

Figure 1.3: Standard Neutrino interactions : Charged current interaction between W-boson and (a) neutrino and (b) anti-neutrino. Neutral current interaction between Z-boson and (c) neutrino and (d) anti-neutrino.

$$\mathcal{L}_{CC} = -\frac{g}{\sqrt{2}} \sum_{l=e,\mu,\tau} \bar{l}\gamma^{\mu}\left(\frac{1-\gamma_5}{2}\right)\nu_l W^{-}_{\mu} + h.c \tag{1.21}$$

$$\mathcal{L}_{NC} = -\frac{g}{\sqrt{cos\theta_w}} \sum_{l=e,\mu,\tau} \bar{\nu}_l\gamma^{\mu}\left(\frac{1-\gamma_5}{2}\right)\nu_l Z_{\mu} + h.c \tag{1.22}$$

Both interactions only affect the left-handed chirality of the neutrinos. The measurement of the Z boson decay width performed by the LEP experiments concluded the existence of three types of "light" neutrinos in the Standard Model [13]. The decay width of the Z boson in light states of left-handed neutrinos is shown in Fig. 1.4.

However, some theories propose scenarios with more than three types of neutrinos. This gives way to the so-called sterile neutrinos, which are considered candidates for dark matter in some of these models. In this thesis we do not cover the sterile neutrino scenario. More details about the sterile neutrinos can be found in [56].

In 1934, Bethe and Peierls estimated the cross section of the interaction of neutrinos with nuclei. They showed that the cross section for neutrinos with an energy of about 1 MeV was extremely small ($\sigma < 10^{-44}$ cm^2) [57]. For many years, the neutrino was considered an "undetectable particle". Lee and Yang in 1956 postulated the existence of the violation of parity in the weak interaction [58, 59] and proved experimentally by Wu [60]. In 1958 the left-handed helicity of neutrinos is demonstrated by Goldhaber [61].

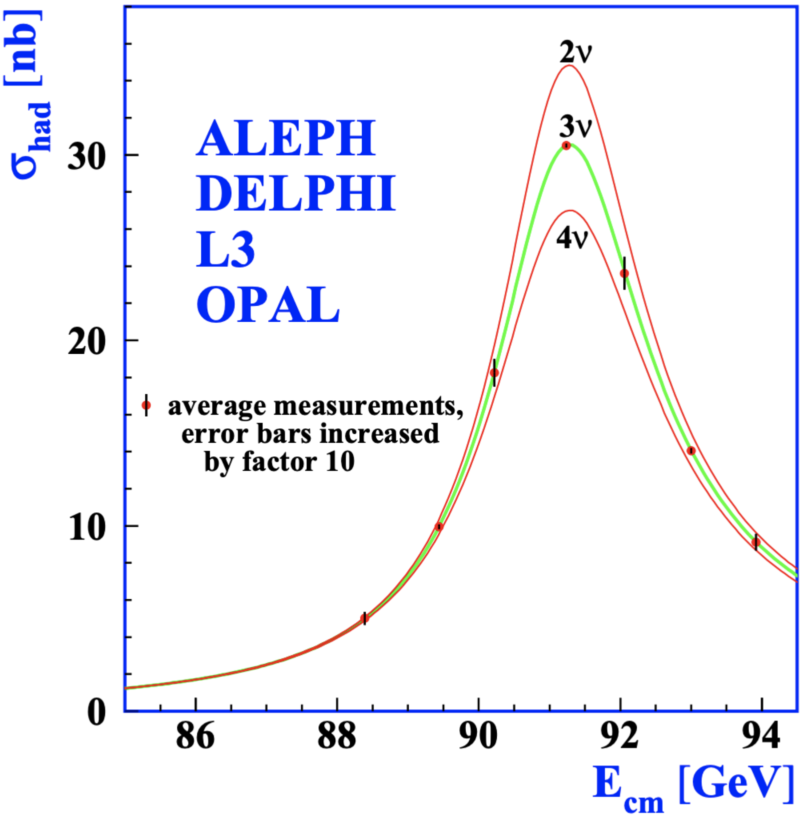

Figure 1.4: Combined result from the ALEPH, DELPHI, L3 and OPAL experiments at CERN, showing the hadron production cross section around the Z resonance and comparing the result to the prediction for 2, 3 and 4 neutrino families [13].

1.1.5 The neutrino Mass problem

As previously discussed, neutrinos are massless particles because they do not have a right-handed component. However, recent experiments have proven that neutrinos are massive particles. As will be discussed in the following sections, the phenomenon of neutrino oscillations imposes that these particles have masses. Extensions of the Standard Model try to explain the mass of neutrinos [62, 63]. One simple way would be to introduce a right-hand component for neutrinos, so that the mass of neutrinos can be generated by the Higgs mechanism. Eq. 1.23 shows the Dirac mass term :

$$\bar{\psi}\psi = (\bar{\psi}_L\psi_R + \bar{\psi}_R\psi_L) \tag{1.23}$$

Another alternative approach is to introduce Majorana neutrinos (their own anti-particles), ψ^M under the charge transformation,C. The Majorana mass term is expressed in Eq. 1.24.

$$\bar{\psi}^M\psi^M = \bar{\psi}_L^C + \bar{\psi}_L\psi_L^C \tag{1.24}$$

Nowadays, the nature of neutrinos is still unresolved: are neutrinos Dirac or Majorana particles? If a massive neutrino is a Dirac particle, this would dictate that an antiparticle with opposite lepton number exists. Whereas if the neutrino is a Majorana particle, it would be its own antiparticle giving rise to lepton number violation. Experimentally it is possible to probe the nature of Majorana neutrinos by observing the neutrinoless double beta decays ($0\nu\beta\beta$) [64]. The Feynman diagram for the $0\nu\beta\beta$ is illustrated in Fig. 1.5.

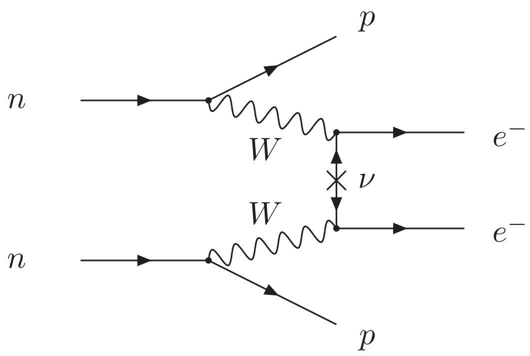

Figure 1.5: Feynman diagram for a neutrinoless double beta decay mediated by a Majorana neutrino.

Several experiments have focused on the search for this process, which is of vital importance for resolving the nature of neutrinos [65, 66, 67]. For more details, a review of neutrinoless double beta decay is presented in [68].

1.2 Introduction to Solar Neutrino Problem

A large number of physical processes generate neutrinos at different energy scales, with extremely intense fluxes for some of them. Neutrinos can come from natural sources in the universe. At the same time, our technological development has allowed us to create artificial sources of neutrinos. Solar neutrinos are created in the sun due to nuclear fusion process in the core of the sun. The cosmic rays interacting with the gas molecules of the atmosphere give rise to the so-called atmospheric neutrinos. Geoneutrinos are associated with natural radioactivity in the earth's crust and mantle. And there are also others kind of neutrinos such as supernovae neutrinos , astrophysical neutrinos and cosmological neutrinos. Nuclear fission reactors produce a large flux of electron antineutrinos due to beta decays of certain isotopes. These neutrinos are known as reactor neutrinos. Accelerator neutrinos are obtained through high-energy collisions in particle accelerators.

1.2.1 Solar Neutrino Problem

The Sun is a powerful source of neutrinos generated by nuclear fusion processes in its core (pp chain , CNO cycle and others). The summary reaction is the conversion of four protons and two electrons into a helium nucleus and two electron neutrinos :

$$4p + 2e^{-} \rightarrow^{4} \mathrm{He} + 2\nu_e \tag{1.25}$$

In the pp chain the first process is the proton-proton fusion in a deuterium nucleus :

$$p + p \rightarrow {}^2\,\mathrm{H} + e^+ + \nu_e \tag{1.26}$$

In the CNO cycle, there are some fusion processes (^{15}O,^{13}N,^{17}F) that produce neutrinos through β decay. The processes occurring in the sun were represented by Bahcall in the Standard Solar Model [69]. The energy spectrum of solar neutrinos produced by the pp chain, CNO cycle and other decays in the Standard Solar Model is shown in Fig. 1.6.

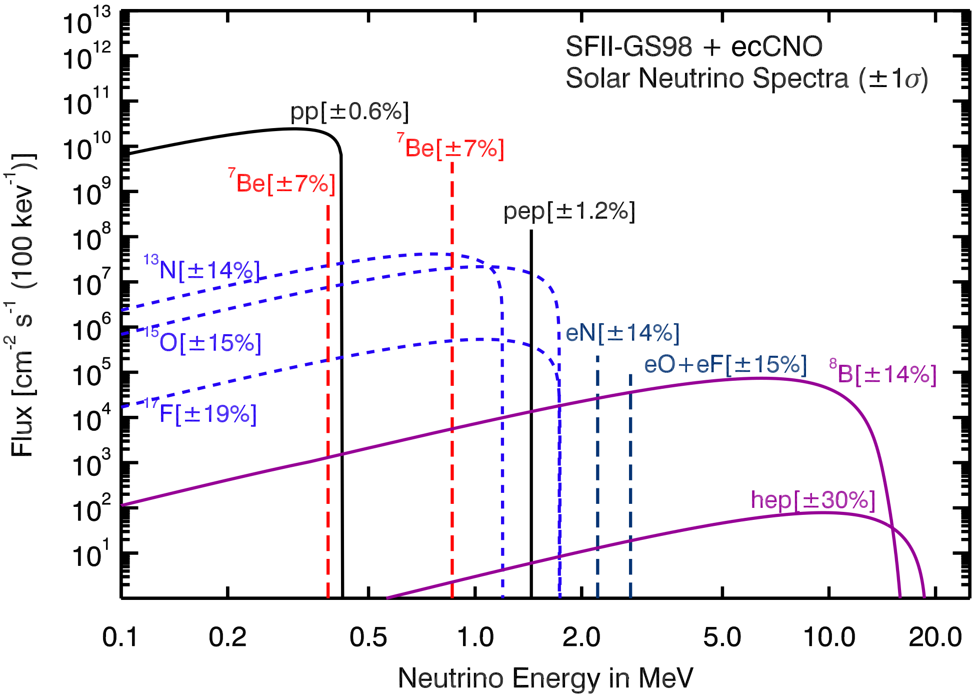

Figure 1.6: The predicted solar neutrino energy spectrum. The neutrino flux is given in cm^{-2}s^{-1}MeV^{-1} [70].

The Homestake experiment [71] was designed to detect solar neutrinos and test the Standard Solar Model. In this experiment the radiochemical technique proposed by Pontecorvo in the Cl-Ar [72] method (Eq. 1.27) was used with an energy threshold of 814 keV.

$${}^{37}\mathrm{Cl} + \nu_e \rightarrow {}^{37}\,\mathrm{Ar} + e^- \tag{1.27}$$

Others experiments such as GALLEX [73], GNO [74] and SAGE [75] were based on the observation of the gallium reaction described in Eq. 1.28 to detect solar neutrinos, which has a lower threshold of 233 keV.

$${}^{71}\mathrm{Ga} + \nu_e \rightarrow {}^{71}\,\mathrm{Ge} + e^- \tag{1.28}$$

The Kamiokande, SuperKamiokande and Sudbury Neutrino Observatory (SNO) observed solar neutrinos using the Cherenkov effect. Solar neutrinos were detected in the Kamiokande and Super-Kamiokande by their elastic scattering on electrons :

$$\nu_\alpha + e^- \rightarrow \nu_\alpha + e^- \tag{1.29}$$

In the SNO experiment, solar neutrinos were measured via : the elastic scattering on electrons (see Eq. 1.29) , charged current processes (see Eq. 1.30) and neutral current scattering processes (see Eq. 1.31) in deuterium (^{2}H).

$$\nu_e + ^2\mathrm{H} \rightarrow 2p + e^- \tag{1.30}$$

$$\nu_\alpha + ^2\mathrm{H} \rightarrow p + n + \nu_e \tag{1.31}$$

With the birth of the Standard Solar Model, it was possible to define the flux of neutrinos emitted by the Sun and compare it with those observed on Earth. This model predicts that most of the flux comes from neutrinos in the pp fusion chain with energies below 0.4 MeV. Due to their low threshold, Gallium experiments are sensitive to the pp component. The opposite case is SuperKamiokande, where the threshold is too high and only neutrinos from the ^{8}B reaction can be seen. Chlorine experiments can observe a part of the ^{7}Be line, and can also detect the other high components. Fig. 1.6 shows the predicted solar energy spectrum produced by the pp chain, the CNO cycle and others.

The Homestake measured an average solar neutrino rate of 2.56±0.23 SNU (Solar Neutrino Units). Whereas the Standard Solar Model for the Homestake predicted a rate of 8.1±1.2 SNU. This measured deficit gave rise to the "Solar Neutrino Problem". On the other hand, experiments such as SAGE and GALLEX confirmed this deficit.

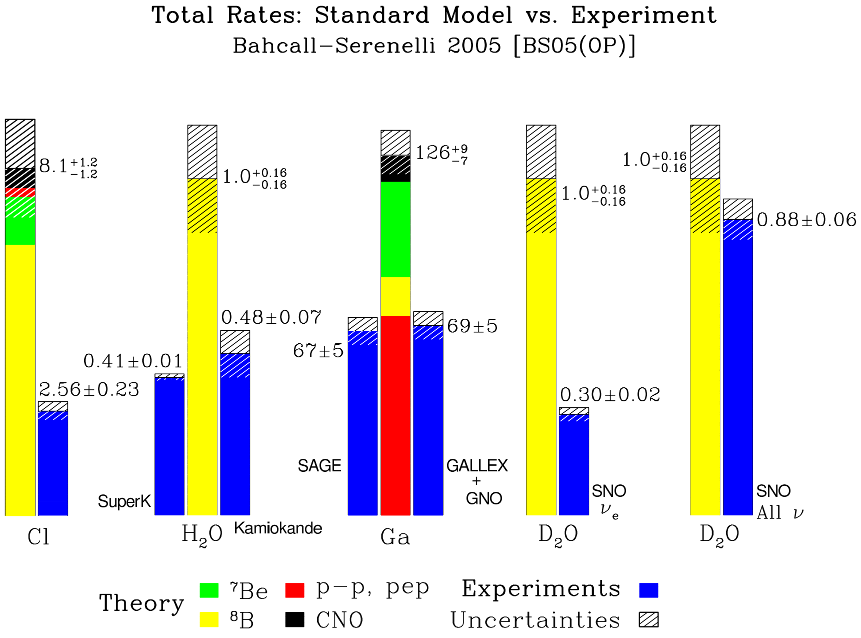

Figure 1.7: Neutrino solar flux measured by several experiments (blue) in comparison with the expected flux from the Standard Solar Model [76].

SAGE reported a neutrino capture rate of 67±5 SNU. GALLEX+GNO observed a rate of 69±5 SNU. For the Gallium experiments the Standard Solar Model predicted a solar neutrino flux of 126^{+9}_{-7}SNU. Fig. 1.7 illustrates the solar neutrino flux measured by various experiments(blue) compared to the flux expected by the Standard Solar Model[77].

The solar neutrino problem raised a series of questions: Is it necessary to reformulate the Standard Solar Model? Is there a problem in the experiments that does not allow to properly measure the neutrino flux? As a solution to the solar neutrino problem, neutrino oscillations appear as an alternative to these questions.

One part of the Neutrino experiments basically concentrate on the study of neutrino properties to determine more precisely the parameters of the oscillations. The following section gives an overview of neutrinos in the theory of neutrino oscillations in vacuum and matter. And in turn, in the following sections we will describe the current status of measurements of the different neutrino oscillation parameters.

1.3 Neutrino Oscillations and Mixing

The first idea of neutrino oscillations was proposed in 1957 by Pontecorvo. According to Pontecorvo, neutrinos could oscillate via $\nu_e \rightleftharpoons \bar{\nu}_e$ in analogy to $K^0 \rightleftharpoons \bar{K}^0$ oscillations [78]. Later, with the discovery of the muon neutrino (ν_μ), Pontecorvo proposes to extend the neutrino oscillation idea to $\nu_e \rightleftharpoons \nu_\mu$ [15]. In 1962, the theory of neutrino flavour oscillations is formulated in the works developed by Ziro Maki, Masami Nakagawa and S. Sakata [17].

1.3.1 Neutrino oscillations in vacuum

Neutrinos can be described by flavour eigenstates ν_α, $\alpha \in \{e, \mu, \tau\}$. The flavour eigenstates neutrinos are coherent superpositions of three mass eigenstates neutrinos $\nu_k, k \in \{1,2,3\}$. The neutrino mass states are the eigenstates of the Hamiltonian in vacuum. The superposition between flavour and mass eigenstates is carried out through an unitary mixing matrix U_{PMNS}[2].

$$|\nu_\alpha\rangle = \sum_k U^*_{\alpha k}|\nu_k\rangle \tag{1.32}$$

The massive states are orthonormal as are the flavour states $\langle\nu_\alpha|\nu_\beta\rangle = \delta_{\alpha\beta}$, $\langle\nu_k|\nu_j\rangle = \delta_{kj}$. The time evolution for a neutrino with a flavour α and energy E_k at time $t = 0$ is given by :

$$|\nu_\alpha(t)\rangle = \sum_k U^*_{\alpha k} e^{-iE_k t}|\nu_k\rangle \tag{1.33}$$

---

[2] Mixing matrix U in 3-neutrino scenario is called Pontecorvo-Maki-Nakagawa-Sakata matrix

The probability of neutrino change from a state with flavour α to another state with flavour β is written as :

$$P_{\nu_\alpha \to \nu_\beta}(t) = \left|\langle \nu_\beta | \nu_\alpha(t)\rangle\right|^2 = \sum_{k=1}^{3}\sum_{j=1}^{3} U^*_{\alpha k} U_{\beta k} U_{\alpha j} U^*_{\beta j} e^{-i(E_k - E_j)t} \tag{1.34}$$

Neutrinos are considered ultrarelativistic particles in Standard Model due to their extremely small mass m_k (i.e $E \sim p \gg m_k$). In a first order Taylor expansion, the energy is approximated by :

$$E_k = \sqrt{p^2 + m_k^2} \approx p + \frac{m_k^2}{2p} \approx E + \frac{m_k^2}{2E}, \qquad E_k - E_j = \frac{\Delta m^2_{kj}}{2E}, \;\; \Delta m^2_{kj} = m_k^2 - m_j^2 \tag{1.35}$$

Since neutrinos propagate almost at the speed of light, the approximation $t \cong L$ can be applied, where L is the distance between the neutrino source and the detector (baseline). The transition probability can be simplified as :

$$P_{\nu_\alpha \to \nu_\beta}(L,E) = \delta_{\alpha\beta} - 4\sum_{k>j} \mathfrak{Re}\left[M_{\alpha kj\beta}\right] \sin^2\left(\frac{\Delta m^2_{kj} L}{4E}\right) + 2\sum_{k>j} \mathfrak{Im}\left[M_{\alpha kj\beta}\right] \sin\left(\frac{\Delta m^2_{kj} L}{2E}\right) \tag{1.36}$$

where $M_{\alpha kj\beta} = U^*_{\alpha k} U_{\beta k} U_{\alpha j} U^*_{\beta j}$. The oscillation probability in Eq. 1.36 depends of the neutrino energy (E), baseline (L) and the differences of the square of their masses ($\Delta m^2_{kj} = m_k^2 - m_j^2$) rather than the absolute value of the masses. In a 3 neutrino flavours scenario, the standard parametrization of the unitary matrix U depends of the three mixing angles θ_{ij} and one phase of CP violation δ_{cp}. The probability of oscillation for the antineutrinos can be extracted exchanging U for U^*.

$$P_{\bar\nu_\alpha \to \bar\nu_\beta}(L,E) = \delta_{\alpha\beta} - 4\sum_{k>j} \mathfrak{Re}\left[M_{\alpha kj\beta}\right] \sin^2\left(\frac{\Delta m^2_{kj} L}{4E}\right) - 2\sum_{k>j} \mathfrak{Im}\left[M_{\alpha kj\beta}\right] \sin\left(\frac{\Delta m^2_{kj} L}{2E}\right) \tag{1.37}$$

In the framework of 3ν, from Eq. 1.36 and Eq. 1.37 the only difference between neutrino and antineutrino oscillation probability is the sign of the last term. The phase δ_{cp} gives rise to an asymmetry between neutrino and antineutrino oscillations in vacuum, the CP violation is manifested in the appearance channels ($\alpha \neq \beta$), where the oscillation probability for neutrinos and antineutrinos are different. The CP violation is quantified in terms of the leptonic Jarlskog invariant [79] defined by :

$$\mathfrak{Im}\left[U_{\alpha i} U^*_{\alpha j} U^*_{\beta i} U_{\beta j}\right] \equiv \sum_{\gamma = e,\mu,\tau}\sum_{k=1,2,3} J_{CP} \epsilon_{\alpha\beta\gamma} \epsilon_{ijk} = J^{max}_{CP} \sin\delta_{CP} \tag{1.38}$$

where J_{CP}^{max} is a function of the mixing angles θ_{ij}.

$$J_{CP}^{max} = \cos\theta_{12}\sin\theta_{12}\cos\theta_{23}\sin\theta_{23}\cos^2\theta_{13}\sin\theta_{13} \tag{1.39}$$

In the case where the flavours $\alpha = \beta$, the survival probability is the same for neutrinos and antineutrinos because the matrix $M_{\alpha k j \beta}$ becomes real.

2- flavour case

In a simple scenario, considering two neutrino flavours ν_α and ν_β. The Unitary mixing matrix U can be parametrized as a rotation matrix :

$$U = \begin{pmatrix} \cos\theta & \sin\theta \\ -\sin\theta & \cos\theta \end{pmatrix} \tag{1.40}$$

with the free parameter, θ, known as the mixing angle between two flavours. The appearance probability is defined by :

$$P_{\nu_\alpha \to \nu_\beta}(L, E) = \sin^2 2\theta \sin^2\left(\frac{1.27\Delta m^2}{E} L\right) \tag{1.41}$$

While the survival probability :

$$P_{\nu_\alpha \to \nu_\alpha}(L, E) = 1 - \sin^2 2\theta \sin^2\left(\frac{1.27\Delta m^2}{E} L\right) \tag{1.42}$$

The neutrino oscillation probability is expressed taking into account the units and magnitudes of the quantities involved such as energy, baseline and the difference of the mass squares. The factor 1.27 comes from the reintroduction of the values of c and $\hbar$ so that L is expressed in km, E in GeV and Δm^2 in eV^2/c^4. In the case of two neutrino flavours, the oscillations do not violate CP symmetry.

In Fig. 1.8 the transition probability (red line) and the survival probability (dashed blue line) are shown for a neutrino with an initial flavour ν_α with 1 GeV of energy in function of the baseline L. The amplitude of this transition probability is determined by $\sin^2 2\theta$. In this example, we have taken $\sin^2 2\theta = 0.8$, $\Delta m^2 = 0.003\text{eV}^2$. It is clear to note that the probability is conserved.

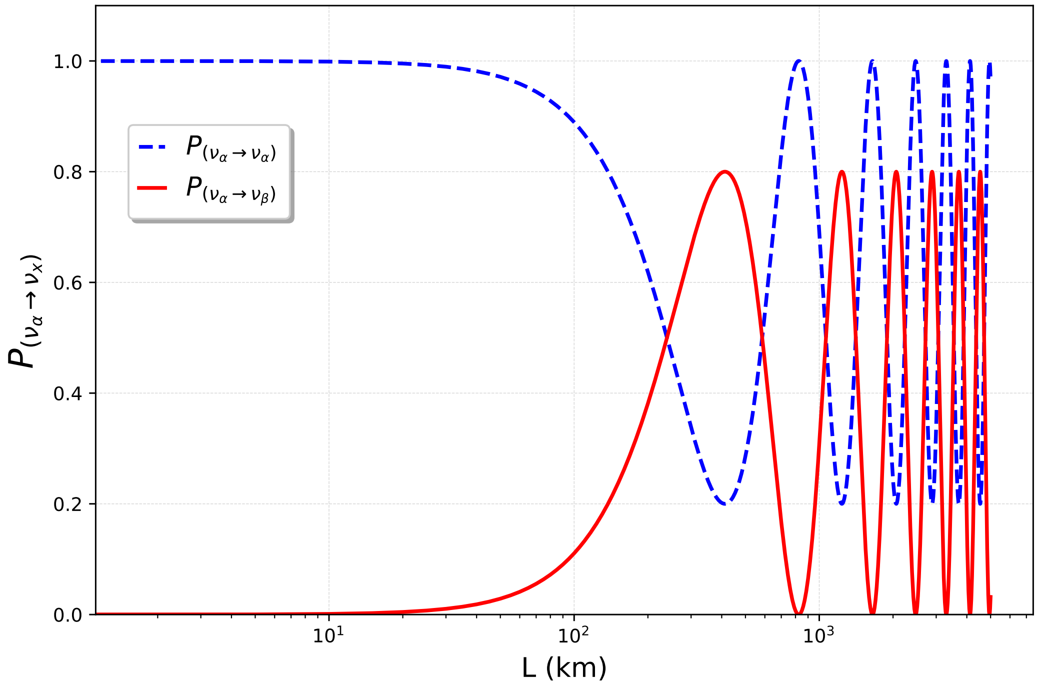

Figure 1.8: Neutrino Oscillation in two-flavour framework. Oscillation probability in function of the baseline L in (km) for a neutrino with energy of 1 GeV and $\sin^2 2\theta = 0.8$, Δm^2=0.003eV^2.

3- flavour case

The lepton mixing matrix U can be parametrized in terms of three angles θ_{12}, θ_{13}, θ_{23} and CP phase $\delta cp \in [0, 2\pi]$ as shown below.

$$U = \begin{pmatrix} 1 & 0 & 0 \\ 0 & c_{23} & s_{23} \\ 0 & -s_{23} & c_{23} \end{pmatrix} \begin{pmatrix} c_{13} & 0 & s_{13}e^{-i\delta_{cp}} \\ 0 & 1 & 0 \\ -s_{13}e^{i\delta_{cp}} & 0 & c_{13} \end{pmatrix} \begin{pmatrix} c_{12} & s_{12} & 0 \\ -s_{12} & c_{12} & 0 \\ 0 & 0 & 1 \end{pmatrix} \begin{pmatrix} e^{i\eta_1} & 0 & 0 \\ 0 & e^{i\eta_2} & 0 \\ 0 & 0 & 1 \end{pmatrix} \tag{1.43}$$

where $\theta_{ij} \in \left[0, \frac{\pi}{2}\right]$, $c_{ij} = \cos\theta_{ij}$ and $s_{ij} = \sin\theta_{ij}$. Here, η_1 and η_2 (both unknown at the present) are so-called Majorana phases that are decoupled from the phenomenon of neutrino oscillation.

Fig. 1.9 shows the muon neutrino oscillation in 3-flavour case. The oscillation probability $P_{\nu_\mu \to \nu_\tau}$ (green line) , $P_{\nu_\mu \to \nu_\mu}$(red line) , $P_{\nu_\mu \to \nu_e}$(blue line) are functions of L/E. The neutrino parameters used for generating these plots are, $\sin 2\theta_{12}$= 0.861, $\sin 2\theta_{13}$= 0.092, $\sin 2\theta_{23}$= 1, $\Delta m^2_{21} = 7.59 \times 10^{-5}$ eV^2 and $\Delta m^2_{31} = 2.43 \times 10^{-3}$ eV^2. CP violation phase δ_{cp} is taken to 0. Fig. 1.9 also shows to which amplitudes each θ_{ij} corresponds.

The survival probability of $\bar{\nu}_e$ in vacuum is given by :

$$P_{\bar{\nu}_e\rightarrow\bar{\nu}_e} = 1 - \sin^2 2\theta_{13}(\cos^2\theta_{12}\sin^2\Delta_{31} + \sin^2\theta_{12}\sin^2\Delta_{32}) - \cos^4\theta_{13}\sin^2 2\theta_{12}\sin^2\Delta_{21} \tag{1.44}$$

The survival probability is defined in function of θ_{ij} and $\Delta_{ij} = \Delta m^2_{ij}L/4E$ which in turn depends on baseline L , neutrino energy E and squared mass difference Δm^2_{ij}.

The main source of electron antineutrino signals in JUNO comes from nuclear reactors. JUNO uses the disappearance of the reactor electron antineutrino ($\bar{\nu}_e$) in vacuum for the analysis of the neutrino mass hierarchy problem. An introduction to the neutrino mass hierarchy is presented in the Section 1.5.1 and is the main objective in the JUNO experiment as discussed in Chapter 2.

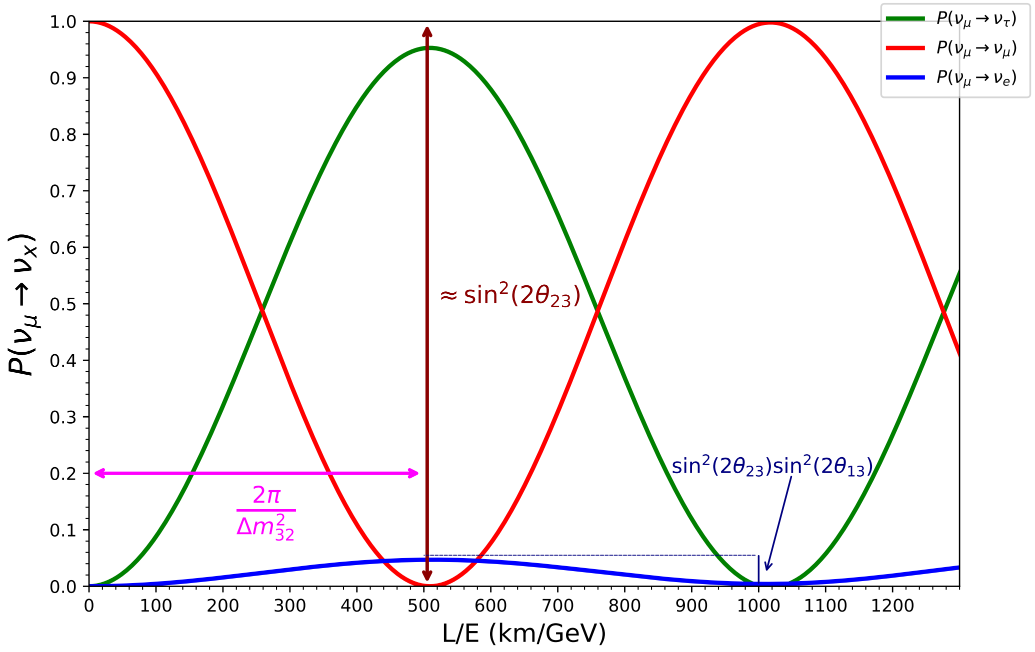

Figure 1.9: Muon neutrino oscillation in 3-flavours case.

1.3.2 Neutrino oscillations in matter

The neutrino oscillations in vacuum have been presented in the Section 1.3.1. But neutrinos interact through the weak force with matter. The interactions of neutrinos with electrons, protons and neutrons affect their propagation in matter. As a result, the parameters of the oscillations in matter are modified with respect to the parameters of the oscillations in vacuum. Matter effect is a quantum mechanics perturbation theory problem as shown in Eq. 1.45. This phenomenon is known as the Mikheev-Smirnov-Wolfenstein effect [80, 81].

The Hamiltonian H_m describes the neutrino matter effect [80]. This Hamiltonian can be decomposed into a free Hamiltonian, H_0 (in Eq. 1.46) and potential V (in Eq. 1.47). The neutrino propagation in vacuum is given by the kinetic energy H_0 and the potential term V induced by neutrino interactions in the medium :

$$H_m = H_0 + V \tag{1.45}$$

In the flavour basis, the vacuum Hamiltonian is given by :

$$H_0 = U\ Diag(E_1, E_2, E_3)\ U^{\dagger}, \qquad E_i = \sqrt{p^2 + m_i^2}, \tag{1.46}$$

where U is the lepton mixing matrix, p is the neutrino momentum and m_i is the mass of the i^{th} neutrino (i=1,2,3). The matter potential V receives a contribution due to the charged current and neutral current. The charged current is due to the exchange of W bosons, this current is present only for electron neutrinos, since ordinary matter does not contain muons and taus, while the neutral current is mediated by the exchange of the Z boson (neutral current), this current is identical for all neutrino flavours. In Fig. 1.10 illustrated these neutrinos interactions with the matter.

Figure 1.10: Tree-level Feynman diagrams of neutrino interactions due to charged current interaction (left) and neutral current interaction (right).

The matter potential V is diagonal at the base of the flavour [82]:

$$V_{\alpha\beta} = V_{\alpha}\delta_{\alpha\beta} = (V_{CC,\alpha} + V_{NC,\alpha})\delta_{\alpha\beta}, \tag{1.47}$$

the potential for the neutral current $V_{NC,\alpha}$ is universal for all neutrinos flavour and the potential for the charged current $V_{CC,\alpha}$ depends on a specific neutrino flavour α.

$$V_{CC,\alpha} = \begin{cases} \sqrt{2}G_F n_e(x) & \alpha = e \\ 0 & \alpha = \mu, \tau \end{cases} \qquad V_{NC,\alpha} = -\frac{G_F}{\sqrt{2}} n_n(x) \tag{1.48}$$

where G_F is the Fermi constant. For the potential of the neutral current, $n_n(x)$ is the neutron density of the medium. The number density of electrons and protons cancel each other out, so the V_{NC} depends only on the number density of neutrons. The potential due to the charged current (V_{CC}) is expressed as a function of the electron density $n_e(x)$ [82]. The density in the medium $n_n(x)$, $n_e(x)$ depend on the spatial position x. The matter potential for antineutrinos is defined by :

$$V_\alpha(\bar{\nu}) = -V_\alpha(\nu) \tag{1.49}$$

Neutral current interactions do not affect the oscillation probability, since they do not discriminate according to the neutrino flavour. Matter effect shows that the mixing angles, the difference of the squares of the masses will depend on the density of the matter with which the neutrinos interact in this effect due to the charged current potential [82].

For simplicity, in a 2 neutrino flavour scenario and constant electron density, the mixing angle in matter is defined as [82]:

$$\sin^2 2\theta_{matter} = \frac{\sin^2 2\theta}{\left(\cos 2\theta - 2\frac{EV_{CC}}{\Delta m^2}\right)^2 + \sin^2 2\theta} \tag{1.50}$$

and the squared mass difference in matter :

$$\Delta m^2_{matter} = \Delta m^2 \cdot \sqrt{\left(\cos 2\theta - 2\frac{EV_{CC}}{\Delta m^2}\right)^2 + \sin^2 2\theta} \tag{1.51}$$

with the factor ω :

$$\omega = \sqrt{\left(\cos 2\theta - 2\frac{EV_{CC}}{\Delta m^2}\right)^2 + \sin^2 2\theta} \tag{1.52}$$

when $\omega = 1$ the matter effect turned to vaccuum effect.

1.4 Current knowledge of neutrino oscillations

As mentioned in the previous sections, the framework of neutrino oscillations for three flavours depends on six free parameters: three mixing angles (θ_{12}, θ_{13} , θ_{23}), one CP-violation phase (δ_{cp}) and two differences of the squares of the neutrino masses (Δm^2_{21}, Δm^2_{32}). These parameters must be measured experimentally, since they are not predicted theoretically.

Historically the values of θ_{12} and Δm^2_{21} were measured through the solar neutrinos, so the part of the U_{PMNS} matrix that depends on the parameter θ_{12} was called the "solar sector" (the third matrix in Eq. 1.43). Similarly, the values of θ_{23} and Δm^2_{32} were measured by the neutrinos produced in the Earth's atmosphere. The first matrix in Eq. 1.43 was called the "atmospheric sector". Finally, since the first experiments that measured and set limits for the θ_{13} parameter were reactor-based experiments, this sector was termed the "reactor sector" (the second matrix in Eq. 1.43).

In this section we present a brief review of these experimental measurements. We catalog the results obtained in different experiments using solar neutrinos, atmospheric neutrinos and reactor neutrinos.

1.4.1 Measurement of θ_{12} and Δm^2_{21}

The results obtained by the SNO collaboration using solar neutrinos, knowing that the sun only produces electron neutrinos, indicated that the electron neutrinos were transformed into other types of neutrinos. Thus showing that the total neutrino flux is consistent with the Standard Solar Model prediction, see Fig. 1.11. It is noteworthy that the SNO provided the answer to the solar neutrino enigma in 2001 by proving the existence of neutrino oscillations in the solar sector [83].

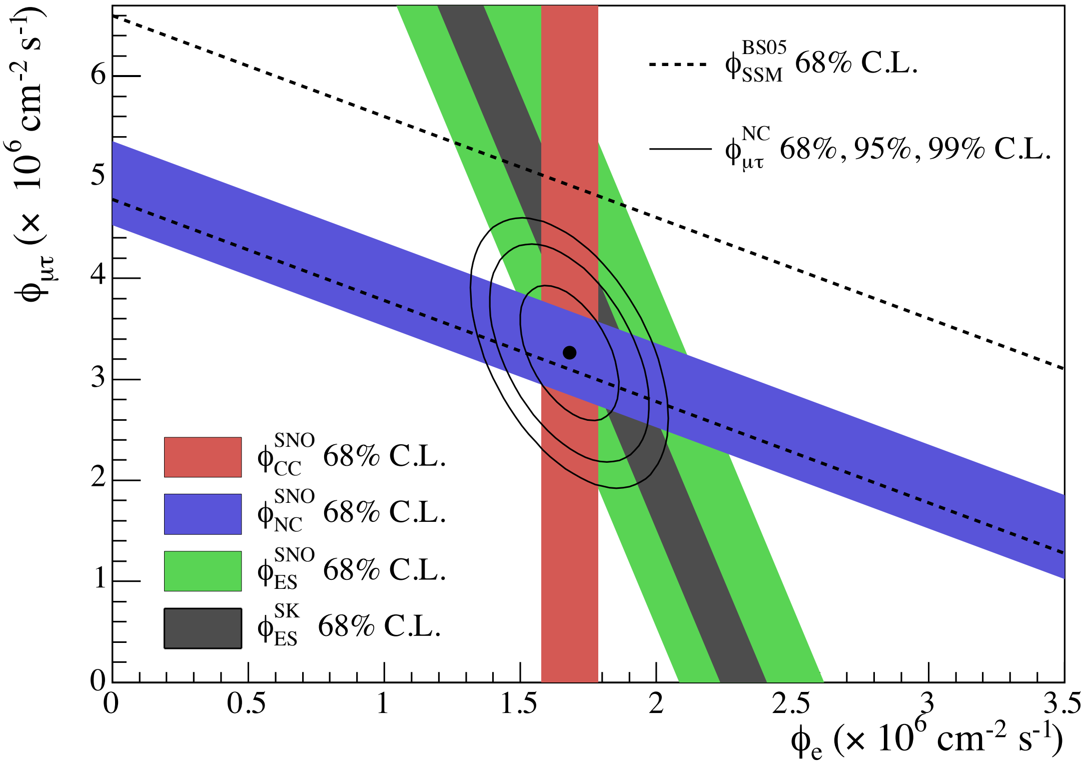

Figure 1.11: Solar neutrino flux vs flux of electron neutrinos in the three detection channels used in SNO (charged current neutrino-nucleus interactions, neutral current interactions and elastic scatters). The dotted lines show the prediction of the Standard Solar Model [83] .

In addition to solar neutrino measurements, these parameters were also measured by reactor neutrinos. The KamLAND experiment [84] observed at first the reactor neutrino oscillation, and measured the dependence of the survival probability on L/E as shown in Fig. 1.12.

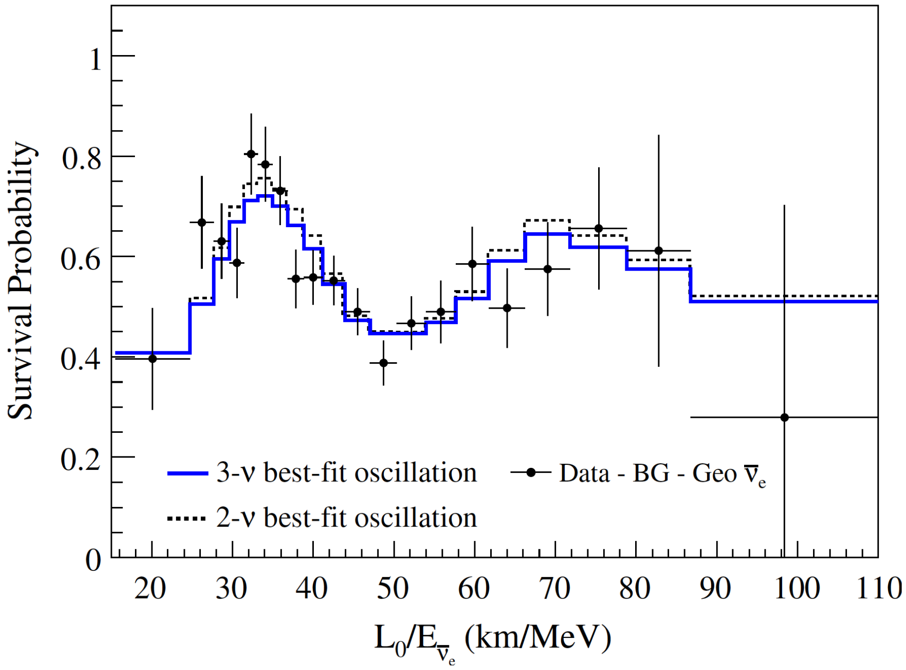

Figure 1.12: Ratio of the background and geoneutrino-subtracted $\bar{\nu}_e$ spectrum to the expectation for no-oscillation as a function of $L_0/E_{\bar{\nu}_e}$. The effective baseline is L_0= 180 km [84].

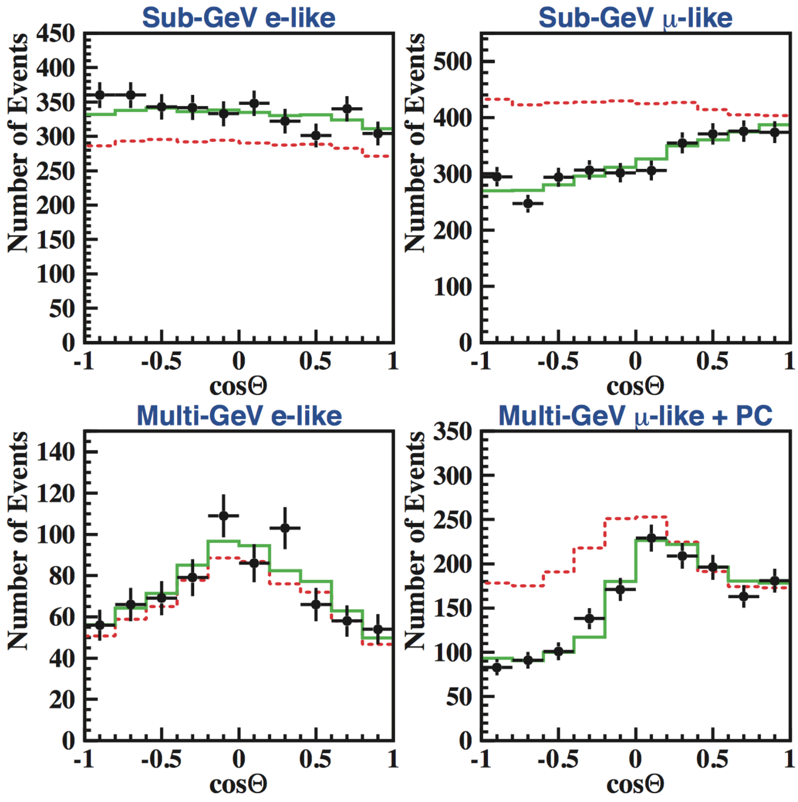

Figure 1.13: Measurement by the Super-Kamiokande experiment of muon and electron neutrino fluxes as a function of the arrival direction of the neutrinos [85].

1.4.2 Measurement of θ_{23} and Δm^2_{32}

The first evidence of neutrino oscillations came from atmospheric neutrinos measured by Super-Kamiokande in 1998 [85]. Fig. 1.13 shows the measurement of muon or electron neutrino flux as a function of the arrival direction of the neutrinos (with $\cos\theta = -1$ meaning upward going), showing that muon neutrinos "disappear" (change flavour) during their travel through the Earth. The red-dotted line shows the expectations in case of no-oscillation.

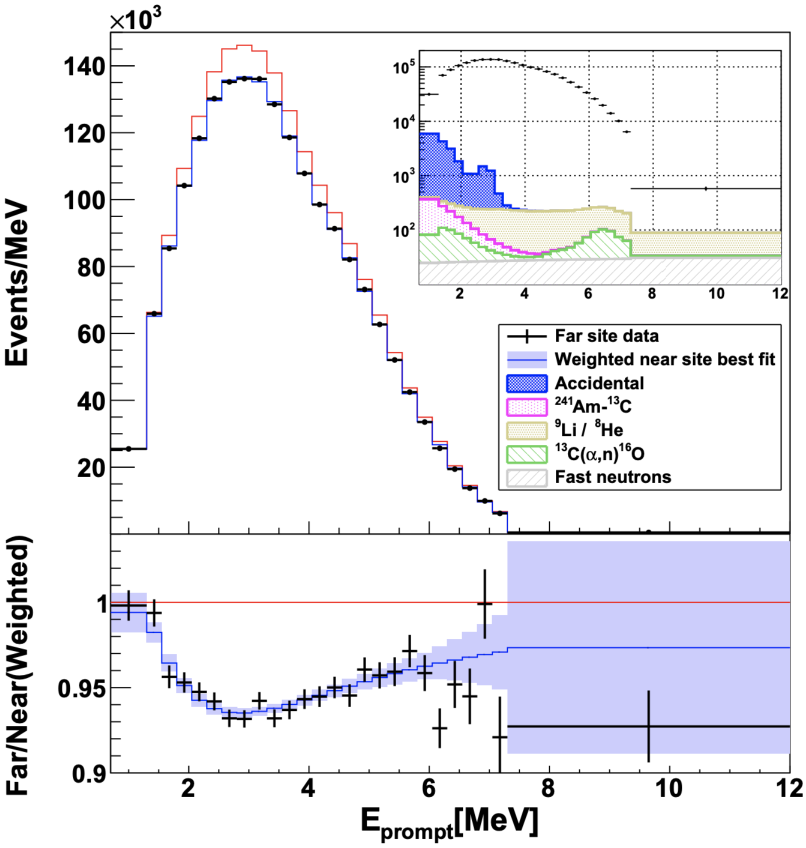

Figure 1.14: The measurement of prompt-energy spectra in Daya Bay : The top panel shows the background-subtracted spectrum at the far site (black points) and the expectation derived from near-site measurements excluding (red line) or including (blue line) the best-fit oscillation. The bottom panel shows the ratios of data over predictions with no oscillation [86].

.

1.4.3 Measurement of θ_{13}

More recent reactor experiments, Double CHOOZ[24], Daya Bay[26] and RENO [25] have focused on precisely measuring the value of θ_{13}. The non-zero θ_{13} was established in 2011. Fig. 1.14 shows the reconstructed prompt energy spectrum observed in the far site, as well as the best-fit predictions in the measurement of electron antineutrino oscillation with 1958 days of operation at Daya Bay [86]. They observed respectively a deficit in the energy spectrum at their far detectors compared to the non-oscillation expectation. Their near to far ratios all have a clear distortion revealing the θ_{13} driven neutrino oscillation.

1.5 Open questions in Neutrinos

The discovery of neutrino oscillations proves that neutrinos have mass. Takaaki Kajita (at SuperKamiokande) and Arthur B. McDonald (at SNO) were awarded the 2015 Nobel Prize in Physics [87]. Today, we are certain that neutrino oscillations are a proven fact in many experiments around the world. As has been shown throughout this chapter, the phenomenon of oscillations for a scenario with three types of neutrinos has been well established.

However, some questions remain open in the field of neutrino physics, despite the enormous progress made in the last decades with solar, atmospheric, reactor and accelerator neutrinos experiments have determined, with remarkable accuracy, most of the necessary parameters describing the three-flavour oscillation framework. In this section we explore some aspects of neutrino physics that remain open and are currently being studied in future experiments.

1.5.1 Neutrino Mass Hierarchy

With solar neutrino observations it has been established the mass ordering of m_1 and m_2, however, the position of m_3 remains unknown. It is not clear whether m_3 is the heaviest or the lightest among the three neutrino mass states. This puzzle is called the neutrino mass hierarchy problem. In Fig. 1.15 the two possibilities of ordering the neutrino masses are presented. In the first case, where m_3 is the heaviest neutrino, it is known as the normal mass hierarchy ($m_1 < m_2 < m_3$). In the inverted mass hierarchy, m_3 is the lightest neutrino: ($m_3 < m_1 < m_2$). One way to determine the neutrino mass hierarchy is to use reactor antineutrino disappearance experiments. Using the constraint $\Delta m^2_{31} = \Delta m^2_{21} + \Delta m^2_{32}$, the electron antineutrino survival probability described in Eq. 1.44 is reformulated as :

$$\begin{aligned} P_{\bar{\nu}_e\to\bar{\nu}_e} = 1 - \cos^4\theta_{13}\sin^2 2\theta_{12}\sin^2\Delta_{21} - \sin^2 2\theta_{13}\sin^2(|\Delta_{32}|) \\ -\cos^2\theta_{12}\sin^2 2\theta_{13}\sin^2\Delta_{21}\cos(|2\Delta_{32}|) \\ -\left[\pm\frac{1}{2}\cos^2\theta_{12}\sin^2 2\theta_{13}\sin(2\Delta_{21})\sin(|2\Delta_{32}|)\right] \end{aligned} \tag{1.53}$$

The sign ± in the last term of Eq. 1.53 provides information about the two scenario of the neutrino mass hierarchy. Here normal mass hierarchy (NMH) is present when the sign is "+" and inverted mass hierarchy (IMH) when it is "-". Fig. 1.16 illustrates the electron antineutrino survival probabilities of electrons for both neutrino mass hierarchies as a function of the neutrino energy, with a baseline of 52.5 km. The neutrino energy is considered from 1.8 MeV which is the inverse beta decay (IBD)interaction threshold. The patterns of the oscillations for the two neutrino mass hierarchy cases are different. A "slow" oscillation is dominated by ($\Delta m^2_{21}, \theta_{12}$) and a "fast" oscillation is dominated by (Δm^2_{32}, θ_{13}).

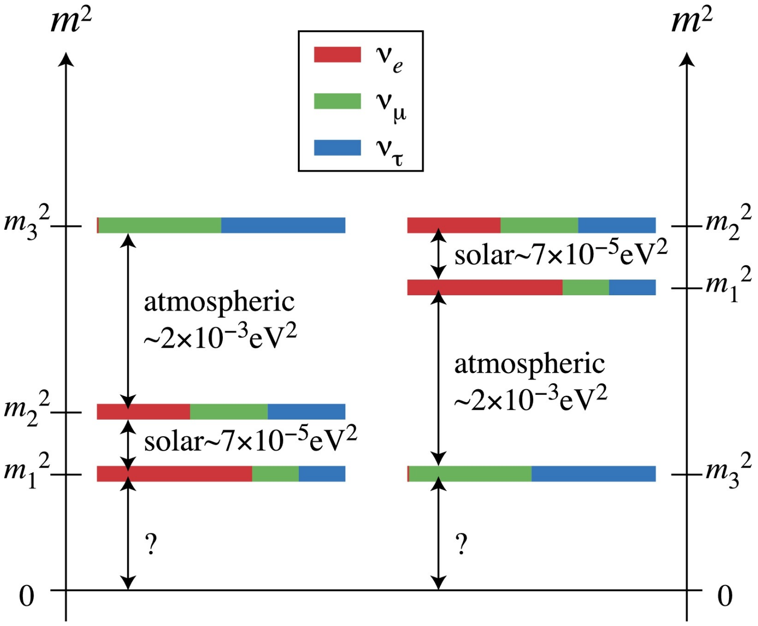

Figure 1.15: The neutrino Mass Hierarchies. The neutrino mass states are illustrated in terms of flavour states. The left and right panels of the figure are referred to as normal or inverted mass hierarchy, respectively [88].

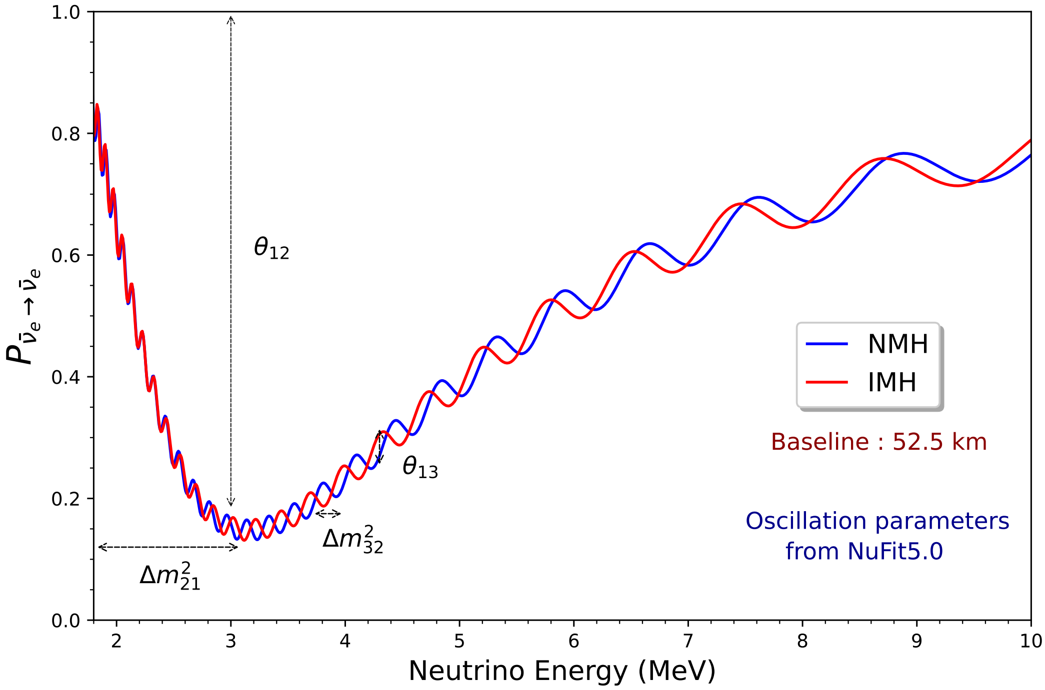

Figure 1.16: The reactor electron antineutrino survival probability as a function of the neutrino energy.

Neutrino oscillations based on the three-neutrino framework have been well established. In conclusion we present in the Table. 1.3 the result of the global analysis of existing neutrino oscillation data [89].

Table 1.3: Values of neutrino oscillation parameters obtained from the global fit of existing data [89].

Parameter	Normal Hierarchy	Inverted Hierarchy
$\sin^2\theta_{12}$	$0.304^{+0.013}_{-0.012}$	$0.304^{+0.013}_{-0.012}$
$\sin^2\theta_{23}$	$0.570^{+0.018}_{-0.024}$	$0.575^{+0.017}_{-0.021}$
$\sin^2\theta_{13}$	$0.02221^{+0.00068}_{-0.00062}$	$0.02240^{+0.00062}_{-0.00062}$
$\delta_{cp}(^\circ)$	195^{+51}_{-25}	286^{+27}_{-32}
Δm^2_{21}	$7.42^{+0.21}_{-0.20}\times 10^{-5}\mathrm{e\,V}^2$	$7.42^{+0.21}_{-0.20}\times 10^{-5}\mathrm{e\,V}^2$
Δm^2_{32}	$2.514^{+0.028}_{-0.027}\times 10^{-3}\mathrm{e\,V}^2$	$2.497^{+0.028}_{-0.028}\times 10^{-3}\mathrm{e\,V}^2$

The neutrino mass hierarchy has an impact on the absolute neutrino mass scale [90], neutrinoless double beta decay [91] and CP violation [92]. Some references on the importance of the neutrino mass hierarchy can be found in [93, 82, 94, 95]. In Chapter 2 we present the Jiangmen Underground Neutrino Observatory (JUNO), whose main objective is to address this question.

Résumé du premier chapitre : La physique des neutrinos

> *"J'ai fait une chose terrible, j'ai postulé une particule qui ne peut être détectée. "*
> **W. Pauli**.

Le Modèle Standard de la Physique des Particules est une théorie quantique des champs qui combine la théorie spéciale de la relativité et la mécanique quantique sur la base des concepts de symétrie et d'invariance de jauge. Dans le modèle, les particules élémentaires sont classées en 12 fermions et 13 bosons. Les fermions décrivent la matière ordinaire de l'univers. Les interactions entre les particules élémentaires sont médiées par les bosons de jauge. Le modèle est une théorie invariante sous des groupes de symétrie internes : $SU(3)_C \otimes SU(2)_L \otimes U(1)_Y$.

Le modèle intègre la théorie électrofaible sous $SU(2) \otimes U(1)$, qui décrit les interactions électromagnétiques et les interactions nucléaires faibles. Les bosons de jauge responsables de l'interaction faible sont : W^+, W^-, Z^0. Et le boson de jauge responsable de l'interaction électromagnétique est le photon. Le modèle inclut également la chromodynamique quantique, la théorie des interactions nucléaires fortes sous le groupe $SU(3)$. L'interaction forte est médiée par 8 bosons de jauge (gluons), tandis que le boson scalaire, appelé boson de Higgs, joue un rôle fondamental dans le mécanisme de génération de la masse des particules élémentaires. Le modèle n'explique pas les effets quantiques de l'interaction gravitationnelle.

Dans le Modèle Standard, les fermions sont classés en 6 leptons et 6 quarks. Les leptons sont : électron, muon, tau, neutrino de l'électron (ν_e), neutrino du muon (ν_μ), et neutrino du tau (ν_τ), tandis que les quarks sont : up, down, charm, strange, top, et bottom. Les fermions sont organisés en trois familles, où chaque famille contient deux quarks et deux leptons. La seule différence entre les trois familles de fermions est l'échelle de masse. Cette différence de masse est une manifestation du couplage des champs fermioniques avec le champ de Higgs. Dans le Modèle Standard les neutrinos n'ont pas de masse.

En 1930, Pauli a postulé les neutrinos pour préserver le principe de conservation de l'énergie et du moment angulaire dans le spectre continu de la désintégration bêta. Dans le Modèle Standard de la physique des particules, les neutrinos sont considérés comme des fermions neutres sans masse, qui n'interagissent que par le biais de l'interaction faible.

La première mesure du neutrino a été effectuée par Reines et Cowan dans l'expérience de Savannah River en 1956. Le prix Nobel 1995 a été attribué à Reines pour la découverte du neutrino. Ce type de neutrino est maintenant connu sous le nom de neutrino de l'électron (ν_e). Lederman, Schwartz et Steinberger ont reçu le prix Nobel de 1988 pour la découverte du deuxième type de neutrino, le neutrino du muon (ν_μ), au tout nouveau synchrotron à gradient alternatif en 1962. Alors que, la première preuve directe pour le troisième neutrino, le neutrino du tau (ν_τ), a été obtenue au Fermilab, par l'expérience "observation directe du neutrino tau" (DONUT) en 2000. Six ans plus tard, le grand collisionneur d'électrons positron (LEP) déterminent la contrainte sur le nombre de familles de neutrinos, c'est-à-dire que seuls 3 types de neutrinos sont produits lors de la désintégration d'un boson Z neutre.

Aujourd'hui, on sait que le phénomène des oscillations des neutrinos établit que les neutrinos doivent être massifs. Ce fait ouvre la voie à une nouvelle physique au-delà du Modèle Standard. Les oscillations de neutrinos sont apparues comme une solution au problème des neutrinos solaires. Ce problème concernait la divergence entre les flux de neutrinos solaires donnés par le modèle standard solaire et les flux mesurés dans diverses expériences telles que Homestake, SuperKamiokande, Gallex, GNO, SAGE.

L'oscillation des neutrinos est un phénomène quantique, il se produit lorsqu'un neutrino est produit avec une saveur leptonique spécifique et que, lorsqu'il se propage dans l'espace, il change de saveur. Cela résulte du mélange des états propres de saveur (ν_e, ν_μ, ν_τ) et des états propres de masse des neutrinos (ν_1, ν_2, ν_3 de masse m_1, m_2, m_3 respectivement). Cette combinaison est basée sur la matrice unitaire de Pontecorvo-Maki-Nakagawa-Sakata. Les éléments de cette matrice sont construits à partir des angles de mélange θ_{ij} et d'une phase δ_{cp}. Le phénomène d'oscillation dépend de trois angles de mélange (θ_{12}, θ_{13}, θ_{23}), de deux différences de masse au carré (Δm^2_{32}, Δm^2_{21}) et de la phase δ_{cp}. Ce phénomène ne peut pas se produire si les masses des neutrinos sont nulles. La preuve des oscillations de neutrinos a été démontrée par l'expérience de neutrinos atmosphériques Super Kamiokande et par l'expérience de neutrinos solaires SNO. On peut donc conclure que, contrairement à la description du Modèle Standard, les neutrinos ont une masse non nulle.

La découverte des oscillations des neutrinos prouve que les neutrinos ont une masse. Takaaki Kajita (au SuperKamiokande) et Arthur B. McDonald (au SNO) ont reçu le prix Nobel de 2015 en physique. Aujourd'hui, nous sommes certains que les oscillations de neutrinos sont un fait avéré dans de nombreuses expériences à travers le monde. Comme cela a été montré tout au long de Chapitre 1, le phénomène d'oscillations pour un scénario avec trois types de neutrinos a été bien établi. Le résultat de l'analyse globale des données existantes sur l'oscillation des neutrinos est résumé dans le tableau 1.3.

Cependant, certaines questions restent ouvertes dans le domaine de la physique des neutrinos, malgré les énormes progrès réalisés au cours des dernières décennies avec des expériences sur le soleil, l'atmosphère, les réacteurs et les accélérateurs. Les expériences sur les neutrinos ont permis de déterminer, avec une précision remarquable, la plupart des paramètres nécessaires décrivant le cadre de l'oscillation à trois saveurs.

De nombreuses expériences ont été réalisées pour étudier les paramètres des oscillations des neutrinos. Cependant, de nombreuses questions restent ouvertes. La probabilité d'oscillation est sensible au carré des différences de masse des trois neutrinos, mais la hiérarchie de ces dernières est encore inconnu. Deux schémas pour solutionner la hiérarchie des masses des neutrinos sont considérés : la hiérarchie normale avec $m_1 < m_2 < m_3$, ou la hiérarchie inversée dans laquelle $m_3 < m_1 < m_2$. La phase δ_{cp}, dont la valeur est inconnue pour le moment, a une implication dans la violation de la symétrie CP dans le secteur leptonique. Les réponses à ces questions sont essentielles à une compréhension plus profonde de notre univers. Après la découverte de la valeur du paramètre non nul θ_{13} dans les dernières expériences d'oscillations de neutrinos, la hiérarchie de masse des neutrinos et l'observation de la violation de la symétrie CP des leptons sont à la portée des projets neutrino à venir.

En résumé, le Chapitre 1 présente brièvement les secteurs du Modèle Standard de la Physique des Particules. Il aborde également le cadre théorique utilisé dans la physique des neutrinos et détaille les oscillations des neutrinos. Le chapitre se termine par le statut expérimental actuel des mesures des paramètres d'oscillation des neutrinos.

CHAPTER

2

The JUNO Neutrino Experiment

> *"Neutrino physics is largely an art of learning a great deal by observing nothing."*
> **Haim Harari.**

Contents

The Jiangmen Underground Neutrino Observatory is a multi-purpose underground liquid scintillator detector with a target mass of 20 kt, and an energy resolution of 3% at 1MeV.

JUNO will be able to determine the Neutrino Mass Hierarchy to $\sim 3\sigma$ over 6 years of operation, as well as to provide accurate measurements of the neutrino oscillation parameters $\theta_{12}, \Delta m^2_{21}, \Delta m^2_{31}$, using the reactor electron antineutrino flux.

JUNO will also cover a rich physics program for measurements on geoneutrinos, solar neutrinos, atmospheric neutrinos, supernovae neutrinos and searching for new physics beyond the Standard Model. The vast program in neutrino physics makes JUNO one of the most important neutrino experiments in future generations.

This chapter focuses on the description of the JUNO Neutrino experiment. The JUNO experimental site is described in Section 2.1. The expected energy spectrum of the reactor electron antineutrinos in JUNO without considering oscillatory effects is presented in Section 2.2. The JUNO detector is described in Section 2.3. The objective of this work is focused on the JUNO Top Tracker (TT), a detailed review of the TT is given in Section 2.4. The JUNO official software is described in Section 2.5. The physics program of JUNO is presented in Section 2.6.

2.1 JUNO Experimental Site

The JUNO experiment is located in southern China, near the Jiangmen city, Guangdong province. The geographic location of JUNO is 112°31′05″ E and 22°07′05″ N [96]. Some megacities such as Hong Kong, Guangzhou or Shen Zhen can be found in this region. The location of the JUNO experiment is shown in Fig. 2.1. To optimize the analysis of the neutrino mass hierarchy, JUNO site is located $\sim$ 53 km from two nuclear power plants (NPP) : Yangjiang NPP and Taishan NPP.

Figure 2.1: Location of the JUNO site [96].

The construction of the JUNO detector began in 2015[28]. The experiment expected the construction of ten nuclear reactors : four for Taishan NPP and six for Yangjang NPP. However, only eight nuclear reactors were realized at present. Two reactor cores at Taishan NPP with 4.6 GW$_{th}$ and six for Yangjiang NPP of 2.9 GW$_{th}$ [97].

The total thermal power of all cores between Taishan and Yangjiang NPPs is 26.6 GW$_{th}$. Table. 2.1 shows the distances between the cores to the JUNO detector (baseline) and the thermal power of each core.

Table 2.1: Summary of the thermal power and baseline to the JUNO detector for the Yangjiang (YJ) and Taishan (TS) reactor cores, as well as the remote nuclear power plants of Daya Bay (DYB) and Huizhou (HZ) [96].

Cores	YJ-1	YJ-2	YJ-3	YJ-4	YJ-5	YJ-6	TS-1	TS-2	DYB	HZ
Power (GW)	2.9	2.9	2.9	2.9	2.9	2.9	4.6	4.6	17.4	17.4
Baseline (km)	52.74	52.82	52.41	52.49	52.11	52.19	52.77	52.64	215	265

In 2018, Taishan Antineutrino Observatory (TAO) was proposed as a satellite experiment of JUNO. TAO has an energy resolution of less than 2% at 1 MeV. TAO is expected to collect about 2 million IBD events in three years, which is 20 times the statistics of JUNO [98]. Due to the high statistics and good energy resolution TAO provides a reference of the reactor electron antineutrino spectrum with high precision. This energy spectrum will be used as input to the JUNO analysis to eliminate the model dependence of the unknown fine structure in the spectrum. Another task of the TAO experiment is to provide a benchmark to test nuclear databases [98].

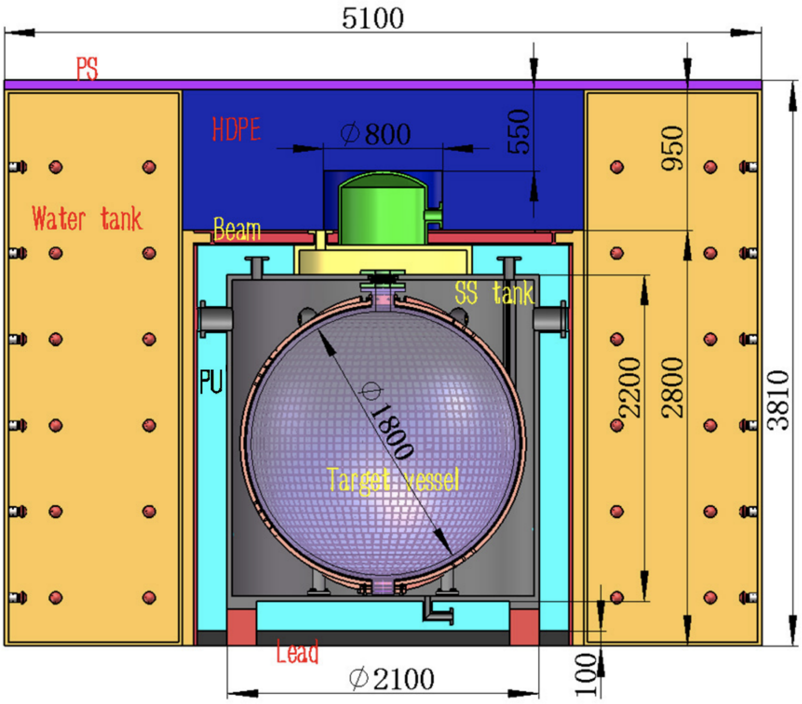

Figure 2.2: The JUNO-TAO detector [98].

TAO is located ∼ 30 m from one of the cores of the Taishan nuclear power plant. A schematic drawing of the TAO detector is shown in Fig. 2.2. TAO detector consists of 2.8 tons (1-ton fiducial volume) of Gadolinium-doped liquid scintillator contained in a spherical acrylic vessel of 1.8 m in inner diameter [98]. TAO has a surface of 10 m^2 of silicon photomultipliers panels operated at -50 °C [98].

JUNO is expected to be operational in 2023. TAO is expected to start data taking at a similar time as JUNO. The description of the JUNO experiment can be found in Section 2.3.

2.2 Reactor Neutrino Signal

The main source of electron antineutrino signals in JUNO comes from nuclear reactors. This section describes how $\bar{\nu}_e$ are produced in the reactor, and how the expected energy spectrum is calculated.

2.2.1 Reactor Neutrino Flux

In nuclear reactors, electron antineutrinos are emitted through inverse beta decay, mainly from the fissions of four isotopes : ^{235}U, ^{238}U, ^{239}Pu and ^{241}Pu, generate more than 99.7% of the reactor antineutrinos. The expected electron antineutrino spectrum at a reactor $\Phi(E_{\bar{\nu}_e})$ can be predicted as :

$$\Phi(E_{\bar{\nu}_e}) = \frac{W_{th}}{\sum_i f_i e_i} \cdot \sum_i f_i \cdot S_i(E_{\bar{\nu}_e}) \tag{2.1}$$

where W_{th} is the thermal power of the reactor, f_i is the fission fraction, e_i is the thermal energy in each fission and $S_i(E_{\bar{\nu}_e})$ is the neutrino spectrum per fission for the i-th isotope. Table. 2.2 shows the parameters e_i, f_i, S_i for each of the relevant isotopes.

Table 2.2: Parameters used in the reactor neutrino flux for different isotopes [99, 100].

Isotopes	e_i(MeV)	f_i	S_i
^{235}U	201.92	0.58	$\exp(0.870 - 0.160E_\nu - 0.091E_\nu^2)$
^{238}U	205.52	0.07	$\exp(0.976 - 0.162E_\nu - 0.0790E_\nu^2)$
^{239}Pu	209.99	0.30	$\exp(0.896 - 0.239E_\nu - 0.0981E_\nu^2)$
^{241}Pu	213.60	0.05	$\exp(0.793 - 0.080E_\nu - 0.108E_\nu^2)$

The study of reactor neutrino oscillation is performed via the $\bar{\nu}_e$ disappearance channel. The liquid scintillator is commonly used for the reactor $\bar{\nu}_e$ detection via the IBD reaction [101, 102]. The IBD, described in Eq. 2.2, is the interaction between an electron antineutrino and a proton from the liquid scintillator. The reaction produces a neutron and a positron in the final state.

$$\bar{\nu}_e + p \rightarrow n + e^+ \tag{2.2}$$

The cross section of IBD process σ is a function of the energy E_{e^+} and the momentum of the positron p_{e^+} [103] :

$$\sigma = 9.52 \times \left[E_{e^+} p_{e^+} \times \frac{10^{-44}\mathrm{cm}^2}{\mathrm{MeV}^2} \right] \tag{2.3}$$

The neutrino energy $E_{\bar{\nu}_e}$(MeV) is deduced from the prompt signal :

$$E_{\bar{\nu}_e} = E_{e^+} + 1.293\mathrm{MeV} \tag{2.4}$$

where 1.293 MeV is the difference of the proton and neutron mass. A key point to take into account in reactor neutrino experiments is the creation of a prompt-delayed signature in IBD events as shown in Fig. 2.3. This technique based on time and space coincidence is useful for background suppression. Due to the large mass difference of positron and neutron, most of the neutrino energy is carried by the positron.

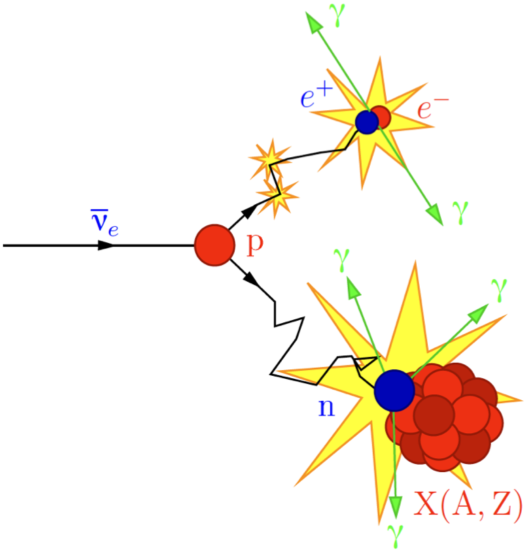

Figure 2.3: Creation of prompt and delayed signals in an inverse beta decay event [95].

This positron deposits its kinetic energy in the liquid scintillator. And the positron annihilates with an electron, emitting two 0.511 MeV photons. This process in the liquid scintillator is called prompt signal. Meanwhile, the neutron scatters in the liquid scintillator and is thermalized, the neutron is captured by a hydrogen in the detector, this recoil neutron produces a signal called a delayed signal about 200 μs after the IBD reaction.

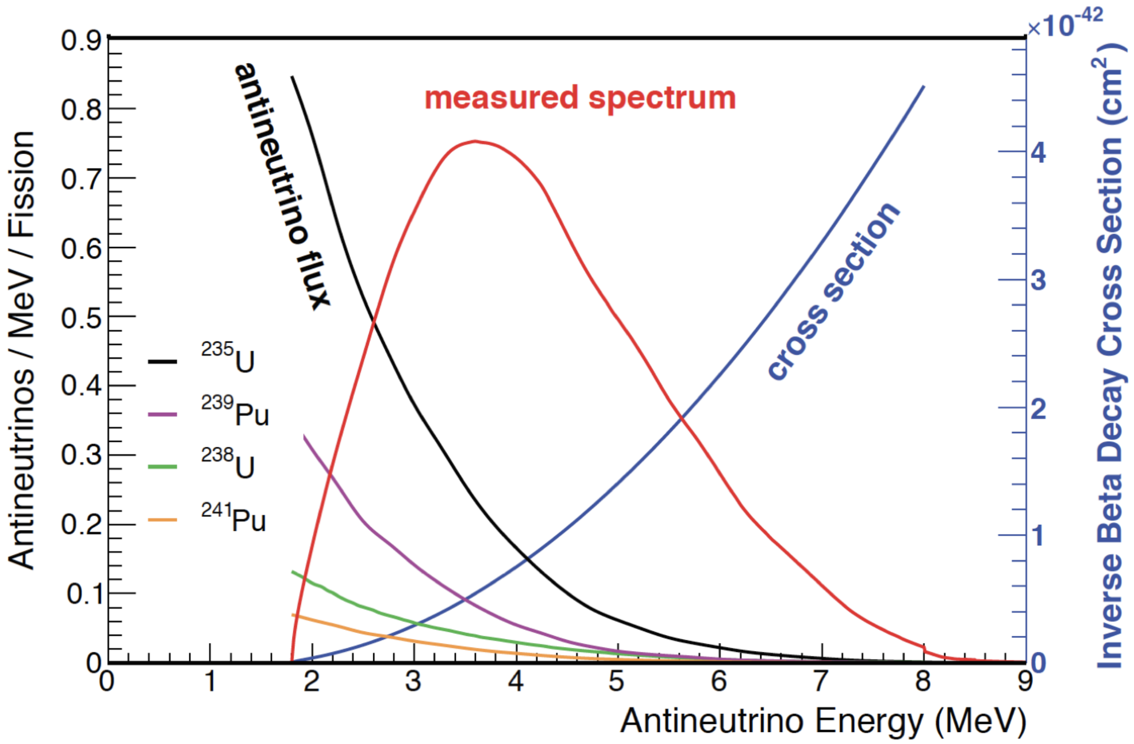

Figure 2.4: The observable electron antineutrino spectrum (red line) is a product of the antineutrino flux from reactor and the cross section of inverse beta decay (blue line). The contributions of four fission isotopes to the antineutrino flux are shown [104].

Fig. 2.4 shows the inverse beta decay cross section (in blue) from Eq. 2.3, the electron antineutrino flux yields per fission of four major fissile isotopes weighted by their corresponding fission fractions. In the axis on right side shows the interaction cross section of the IBD. In the x-axis represents the antineutrino energy. The antineutrino flux is dominated by ^{235}U (in black). The figure also shows the expected unoscillated IBD spectrum (in red). The observable IBD spectrum is arbitrarily normalised. The measured spectrum is obtained by convoluting the reactor antineutrino flux and the cross section.

2.2.2 Reactor Neutrino Energy Spectrum at JUNO

Given the reactor neutrino disappearance probability, the reactor neutrino flux and the inverse beta decay cross section, the reactor neutrino energy spectrum at JUNO is illustrated in Fig. 2.5, where the non-oscillation, normal mass hierarchy oscillation and the inverted mass hierarchy oscillation cases are shown. The normal mass hierarchy and inverted mass hierarchy manifest as different oscillation patterns in the energy spectrum. Experimentally, the Neutrino Mass Hierarchy and oscillation parameters information can be extracted through a precise measurement of the oscillated energy spectrum in which the energy resolution and energy scale control are critical. It needs to be mentioned that Fig. 2.5 is only used to illustrate the oscillation information embedded in the spectrum, and it does not take into account the energy resolution of the detector.

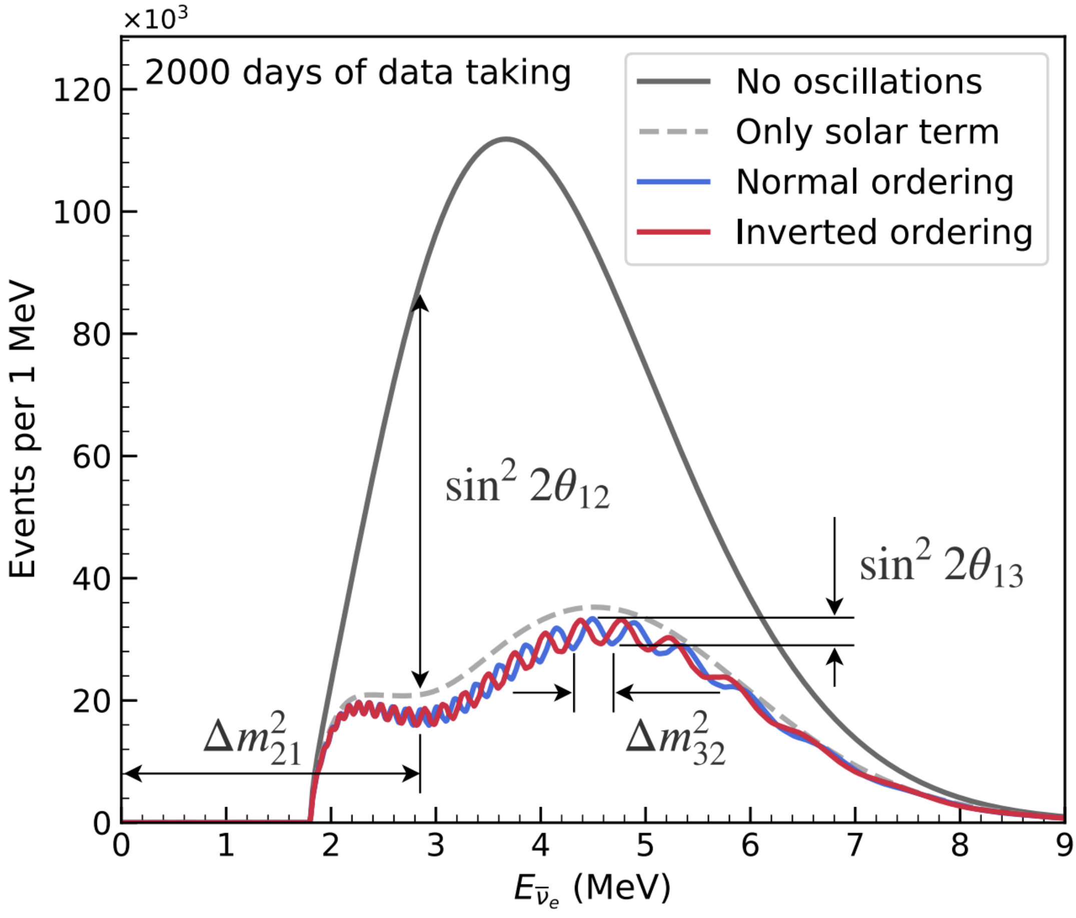

Figure 2.5: The expected antineutrino energy spectrum weighted by IBD cross section with and without oscillation at the JUNO experiment for normal hierarchy (normal ordering) and inverted hierarchy (inverted ordering) assuming 2000 days of data-taking. Dependence on the four oscillation parameters is shown [96].

2.2.3 Inverse beta decay backgrounds

The expected IBD rate in JUNO is about 60 counts per day (after all IBD event selection cuts applied [96]), therefore a careful control of the background sources is critical. The sources of background in JUNO comes from : the decay of natural radioactivite isotopes, the cosmogenic isotopes (^{8}He/^{9}Li) induced by cosmic muons, the spallation fast neutron created by cosmic muons, the $^{13}\text{C}(\alpha,n)^{16}\text{O}$ derives from the alpha particles interacting with ^{13}C and the geo-neutrinos [96] from radioactive decays of Th and U inside the earth.

In order to reduce the background due to cosmic muons, the detector will be placed underground with about 700 m of rock on top of the experimental hall. The JUNO detector is composed of three main parts: the Central Detector, the Water Cherenkov Detector and the Top Tracker (TT). The central detector contains a 20 kton liquid scintillation target , which is responsible for the measurement of the antineutrino energy spectrum. The water Cherenkov detector is a pool filled with purified water and instrumented with photomultipliers surrounding the central detector to be used as a veto for external events, protecting the central detector from external radioactivity. The TT is used to accurately track some of the cosmic muons entering the detector. A description of the central detector and water Cherenkov detector can be found in Section 2.3. Since the study of the TT is the main objective of this thesis, a description of this part of the detector is presented in Section 2.4.

The following is a description of the main backgrounds in JUNO. The criteria considered in order to reduce background and optimise the selection of reactor antineutrinos are presented in Section 2.2.4.

Accidental background

Random single energy depositions that mimic prompt-delayed coincidence of the IBD are called accidental background. These signals are originated by natural radioactivity, cosmogenic isotopes, spallation neutrons and electronic noise. The total rate of accidental backgrounds is estimated to be 0.9/day, after the JUNO selection criteria.

^{8}He/^{9}Li background

Cosmic muons create cosmogenic isotopes. Cosmogenic isotopes are rare nuclides created when cosmic rays interact with the Central Detector. The cosmogenic isotopes such as ^{8}He/^{9}Li produce the $\beta - n$ decays which mimic the IBD signature. The total rate of ^{8}He/^{9}Li is estimated to be 1.6/day, after applying the JUNO rejection criteria. Others isotopes, such as ^{11}Li, ^{12}Be, ^{14}B, ^{16}C, ^{17}N and ^{18}N, produce fake IBD signals but with a much lower rate.

Fast Neutron background

Energetic neutrons are produced by cosmic muons that only pass through the surrounding rock of the water pool. These fast neutrons can mimic IBD signals by scattering into a proton and being captured in the Central Detector. Based on a full simulation without optical processes, the rate of fast neutrons is estimated to be 0.1/day.

^{13}C$(\alpha, n)^{16}$O background

The α particles emitted by the U or Th decay chains, can react with the ^{13}C of the liquid scintillator. This interaction creates neutrons and ^{16}O nucleus. The delayed signal is originated by the capture of the neutron after its thermalization, while the prompt signal is created by the processes that the neutron undergoes (by the elastic scattering of the neutron on the proton). If ^{16}O is in the excited state, it emits a γ or a conversion electron by de-excitation, which also contributes to the prompt signal. Based on the estimated natural radioactivity concentrations, the (α, n) background rate is estimated to be 0.05/day.

Geo-neutrino background

Inside the Earth crust and mantle, atoms such Th and U emmit geo-neutrinos ($\bar{\nu}_e$) via beta decay with an energy below 3 MeV. They are not distinguishable from the reactor neutrinos. JUNO is expected to have 1.1 geo-neutrino IBD events per day.

With 3% of energy resolution and six year running statistics, the estimated spectra for the antineutrino signal (black line) and the background in JUNO in function of the neutrino energy are shown in Fig. 2.6. The five kinds of main backgrounds include the accidental (blue line), fast neutron (green line), ^{8}He/^{9}Li (red line),^{13}C$(\alpha,n)^{16}$O (cyan line) and geo-neutrinos (purple line).

In the top right corner of the Fig. 2.6 shows the same plot but the ordinate axis is in logarithmic scale. From the plot, the geo-neutrinos and accidental backgrounds are dominant when the neutrino energy E < 3.5 MeV. In the case, where the neutrino energy E > 3.5 MeV, the dominant background is given by ^{8}He/^{9}Li, one of the most important background in JUNO, and requires to be addressed with more carefully.

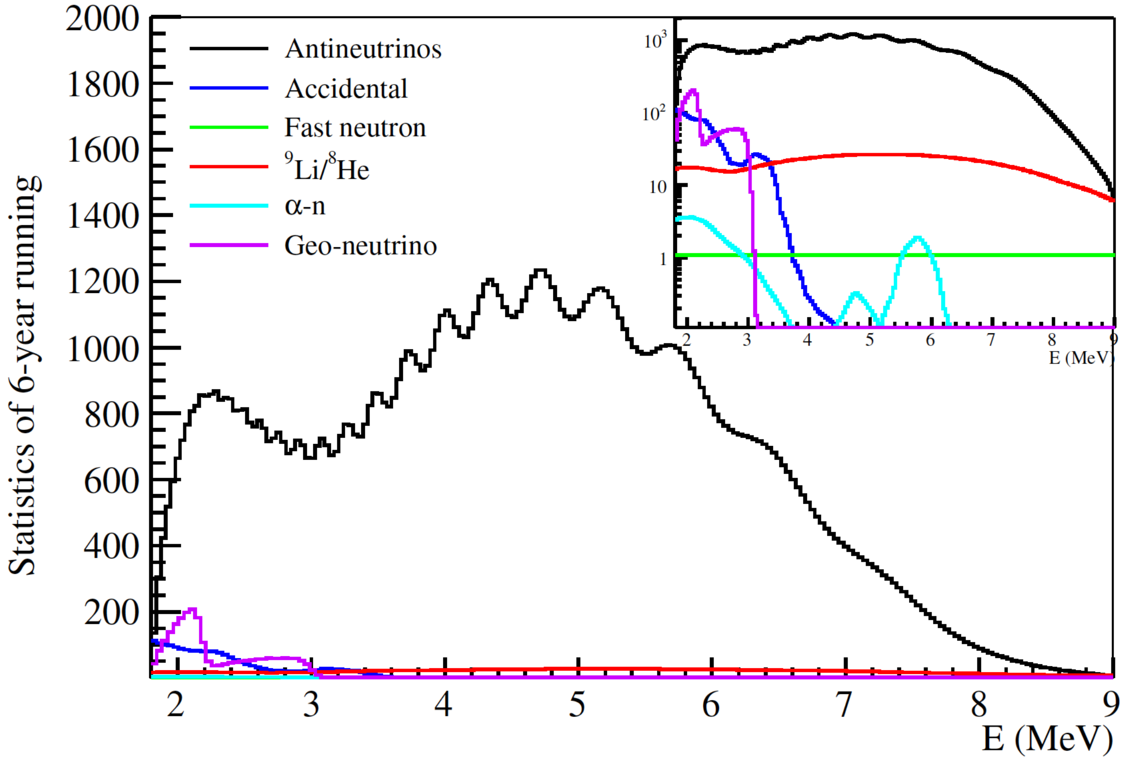

Figure 2.6: Spectra for the reactor antineutrino signals and the backgrounds in JUNO [27].

2.2.4 Inverse beta decay signal selection

A series of criteria have been considered at JUNO in order to reduce the background and optimise the selection of reactor antineutrinos [96].

- Fiducial volume cut : radius < 17 m;
- Prompt energy cut : 0.7 MeV < E_{prompt} < 12 MeV;
- Delayed energy cut 1.9 MeV < $E_{delayed}$ < 2.5 MeV;
- Time interval cut between the prompt and delayed signal : ΔT <1.0 ms;
- Prompt-delayed distance cut : $R_{prompt-delayed}$ <1.5 m

- Muon veto criteria :
    - For muons tagged by the water Cherenkov detector or the Top Tracker, veto the whole liquid scintillator volume for 1.5 ms;
    - For well-tracked muons in the Central Detector, veto the detector volume within a cylinder of distance to the muon track $R_{d2\mu} < 3$ m and within time to the preceding muon $T_{d2\mu} < 1.2$ s;
    - For tagged, non-trackable muons in the Central Detector, veto the whole liquid scintillator volume for 1.2 s.

Table 2.3: The efficiencies of antineutrino selection cuts, signal and backgrounds rates [27].

Selection	IBD efficiency	IBD	Geo-νs	Accidental	^{8}He/^{9}Li	Fast neutron	(α, n)
-	-	83	1.5	-	84	-	-
Fiducial	91.8	76	1.4	410	77	0.1	0.05
Energy cut	97.8	73	1.3		71		
Time cut	99.1						
Vertex cut	98.7			1.1			
Muon Veto	83	60	1.1	0.9	1.6		
Combined	73	60	3.8				

The background rates and reduction with electron antineutrino selection cuts are summarised in Table. 2.3 considering the preliminary selection criteria reported [27]. These values have been calculated considering 10 nuclear reactors as planned at the beginning of the experiment. These values were recalculated considering 8 reactors and varoius improvements in the analysis and simulation of JUNO recently [97], however [97] does not provide a detailed breakdown of the background as in [27] to help understand the impact of each cut. For this reason, in this document we continue using the value from [27] rather than the latest ones from [97].

Table 2.4: Summary of detectable neutrino signals in the JUNO experiment and the expected signal rates and major background sources [27].

Research	Expected signal	Energy region	Major background
Reactor antineutrino	60 IBDs/day	0 - 12 MeV	Radioactivity cosmic muon
Solar neutrino	hundreds per year for ^{8}B	0 - 16 MeV	Radioactivity
Atmospheric neutrino	hundreds per year	0.1 - 100 GeV	Negligible
Geo-neutrino	$\sim$ 400 per year	0 - 3 MeV	Reactor ν
Supernova burst	5000 IBDs at 10 kpc 2300 elastic scattering	0 - 80 MeV	Negligible
DSNB	2-4 IBDs/years	10 - 40 MeV	Atmospheric ν

The Table. 2.3 summarises the efficiencies of antineutrino selection cuts. The antineutrino selection efficiency due to : the fiducial volume cut is 91.8% the energy cut is 97.8%, time cut is 99.1%, and vertex cut 98.7%. Assuming 99% muons have good reconstructed track, the efficiency of above muon veto cut is estimated to be 83%. JUNO will observe 60 IBDs/day, with about 6% background [27]. These criteria were optimized according to the MC simulation of JUNO. Based on the above selection criteria, in JUNO the reactor neutrino event rate is estimated to be 60 events per day, and the background rate is 3.8 events per day [27]. The expected neutrino signal rates and major background sources are summarized in Table. 2.4.

2.3 The JUNO Detector

The dimensions and design of the experimental setup selected for JUNO has been based on terms of the excellent energy resolution , the highly demanding performance in terms of high statistical precision and its low background level. The JUNO detector system is shown in Fig. 2.7. The aim of this section is to present a brief description of the conceptual design of the central detector and the water Cherenkov detector of the JUNO experiment. The TT will be discussed in the Section 2.4.

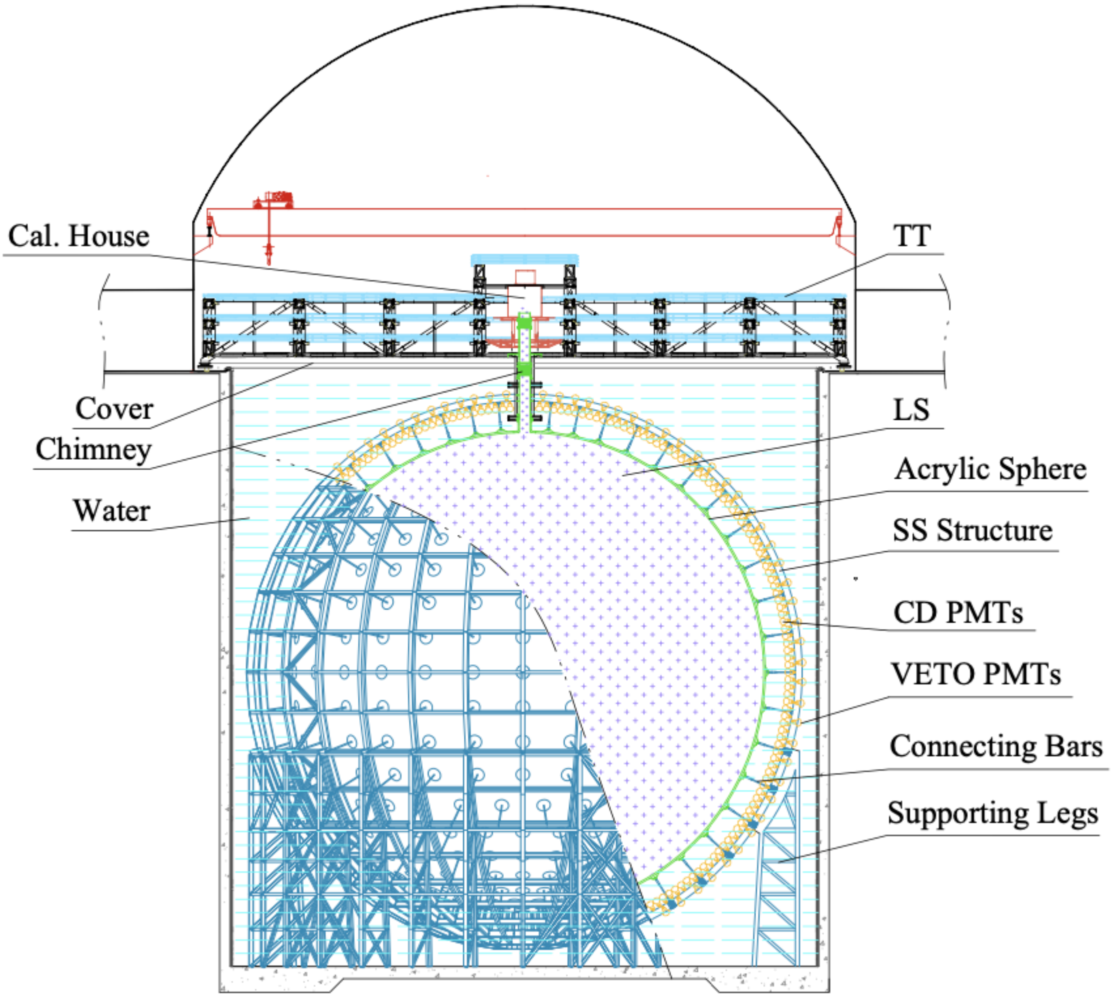

Figure 2.7: Schematic of the main JUNO detector [96].

2.3.1 Central Detector

The central detector is a spherical Acrylic Vessel with an inner diameter of 35.4 m and a thickness of 120 mm. The Acrylic Vessel will be supported by a spherical stainless steel shell structure with an inner diameter of 40.1 m via 590 connecting bars. The design of the Central Detector is presented in Fig. 2.8.

The Acrylic Vessel is filled with 20kton of liquid scintillator which is used as a target medium to measure antineutrinos from the reactors. In the liquid scintillator, neutrino detection occurs by transferring neutrino energy to visible energy in terms of photons. Details about the scintillation processes can be found in [105, 106]. In JUNO, the composition of liquid scintillator has been optimized in dedicated studies with a Daya Bay detector. Liquid scintillator uses linear alkylbenzene (LAB) as the solvent. LAB is a straight alkyl chain of carbons attached to a benzene ring. LAB is used as the detection medium due to its excellent transparency, high flash point, low chemical reactivity, and good light yield. The liquid scintillator will contain 2.5 g/L 2,5-diphenyloxazole (PPO) as the fluor. The photon wavelength shifter to the sensitive region of the photosensors is given by 3 mg/L p-bis-(o-methylstyryl)-benzene (bis-MSB) [96]. In order to detect the scintillation light via IBD : 17,612 20-inch PMTs[1] (referred to as "large PMT's system") and 25,600 3-inch PMTs (known as " small PMT's system") will be installed in the main structure.

The objective of the central detector is the detection of physical events to complete the study of the extensive JUNO program. To achieve this goal (e.g., to reach the sensitivity of the central detector design to detect solar reactors and neutrinos), JUNO also consists of an Online Scintillator Internal Radioactivity Investigation System (OSIRIS) [107], which allows to monitor the radiopurity of the liquid scintillator during the filling of the central detector over several months.

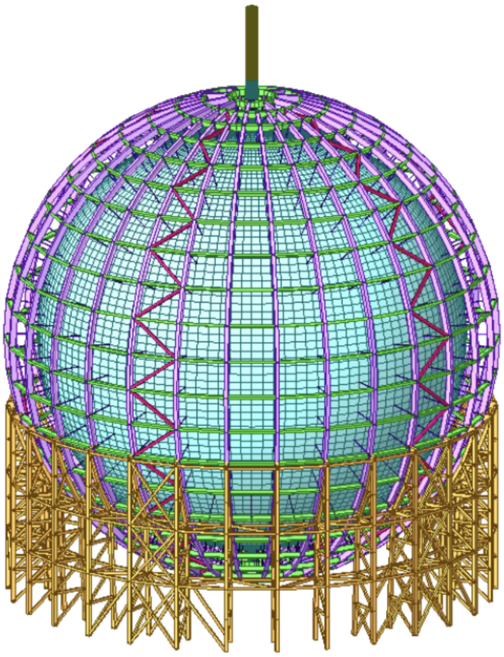

Figure 2.8: Scheme of the JUNO Central Detector [96].

Detector performance is affected due to the presence of the geomagnetic field. The earth's magnetic field significantly reduces the detection efficiency of PMTs by approximately 60% below the geomagnetic field strength ($\sim$ 0.5G). Therefore, a compensation system for shielding the geomagnetic field has been extended around the central detector [108]. The active shielding based on compensation coils will be included in the veto system.

---

[1] The description of the photomultiplier (PMT) is found in the Section 2.4.2

2.3.2 Water Cherenkov Detector

Although the detector is located at 700 m depth, the flux of cosmic muons that induce fake IBD signals in JUNO imposes the use of an efficient veto system for the characterization and reduction of this background. The veto system consists of two subsystems, the Water Cherenkov and the Top Tracker, which will ensure efficient background reduction.

The water Cherenkov detector is a cylinder filled with 35 ktons of ultrapure water. The central detector is immersed in the Water Cherenkov Detector. Water Cherenkov detector has a 43.5 m diameter and 44 m height. Cherenkov light produced by muons passing through the volume is detected by 2400 large photomultipliers installed on the outer surface of the water Cherenkov detector's stainless steel structure. The central detector and the water Cherenkov detector are optically separated [96]. Tyvek reflective sheeting provides a coating to the pool walls and stainless steel support structure to increase light collection efficiency. Passive shielding of the water significantly reduces the gamma background in the central detector due to rock radioactivity.

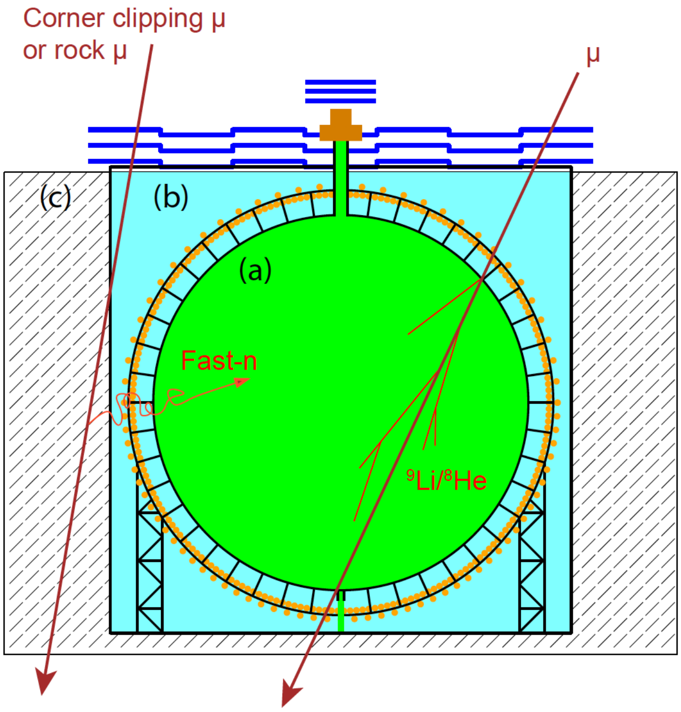

Figure 2.9: Configurations considered for the induced noise in (a) the central detector, (b) the water pool and (c) the surrounding rock.

The muon flux in the experimental hall is 0.004 Hz/m^2 [96]. The average muon energy is 207 GeV. According to the JUNO detector simulation, the average path length of muons traversing the pool is about 13 m. The efficiency of muon tagging can reach 99.5%. Most of the un-tagged muons have short tracks (< 0.5 m) and are far from the central detector, contributing to the fast neutron background. The dangerous background induced by cosmic muons come from the generation of unstable elements such as ^{9}Li and ^{8}He. The configurations considered for the induced noise in the central detector, the water pool and the surrounding rock are illustrated in Fig. 2.9.

2.4 Top Tracker

The role of the Top Tracker is to detect cosmic muons and to reconstruct their trajectory in order to study the cosmogenic background production and thus reduce the systematic errors on the neutrino mass hierarchy determination. The TT re-used the plastic scintillator modules of the OPERA Target Tracker [30]. In this section we describe the detection principle, the TT geometry, the readout electronics and the TT operation modes.

2.4.1 Plastic scintillator strip

The scintillators are a group of materials emitting light when exposed to ionising radiation, thus experiencing the phenomenon of luminescence. This phenomenon is produced when these materials absorb particles and subsequently create photons. This light can be collected by detectors to study the properties of the incident charged particle (e.g. muons). Scintillators have a wide range of applications in medicine, biology and particle physics experiments. The plastic scintillator has many advantages such as fast rise and decay times, high optical transmission and durability [109].

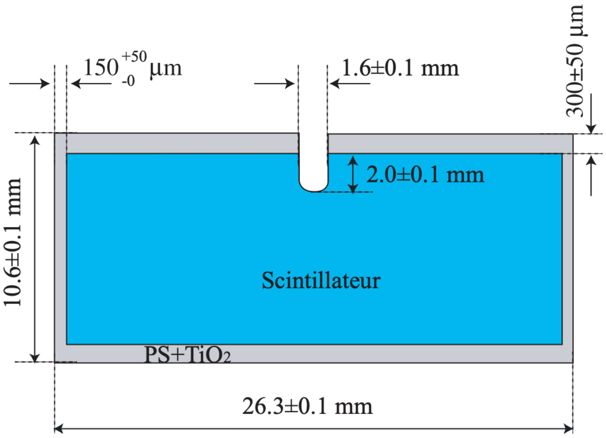

Figure 2.10: Scintillator strip geometry [30].

In the TT, the basic element is the plastic scintillator strip. The scintillator strips are made of polystyrene with 2% p-Terphenyl (primary fluor) and 0.02% POPOP (secondary fluor). The scintillator strips are coated with a thin diffusing white layer of TiO_2 [30]. The TiO_2 coating is applied for better light collection. The Scintillator strip geometry is described in Fig. 2.10.

Fig. 2.11 illustrates this charged particle detection. When a particle crosses the scintillator strip, it will deposit energy creating a "blue" scintillation photon. A wavelength shifting fiber is placed in the center of the strip. With this fiber, the "blue" photons will be re-emitted at a green wavelength. These "green" photons will propagate through the wavelength shifting fiber to the multi-anode photomultipliers (MA-PMT).

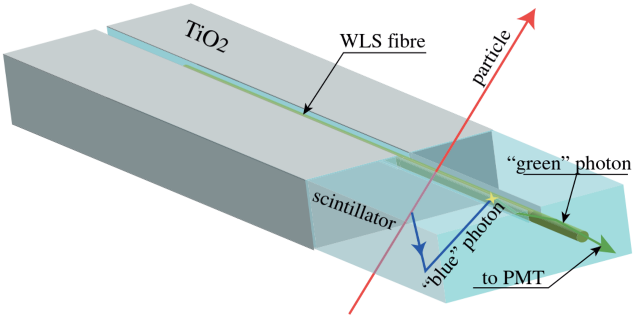

Figure 2.11: Schematic view of a scintillation strip [30].

2.4.2 Photomultiplier

A photomultiplier is a device that converts the light to an electrical signal. The PMT response is proportional to the intensity of the incident light. The significant advantage of the PMT over other light detectors lies in the ability to have a large detection area, a high gain and the ability to detect a single photon.

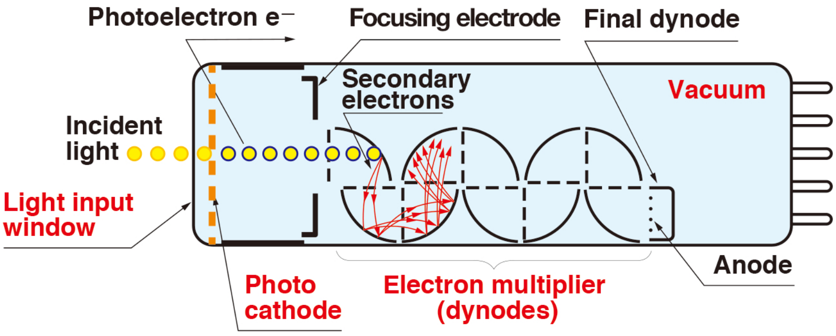

Figure 2.12: A schematic view of a photomultiplier [110].

A PMT relies primarily on the photoelectric effect and the secondary electron emission. In the PMT, the photocathode converts the flux of photons into a flux of electrons through the photoelectric effect. These electrons are called photoelectrons (p.e.). Only photoelectrons with energy above the work function will be able to escape from the photocathode and continue to the focusing electrode. In the focusing electrode, the p.e are accelerated and directed towards the electron multiplier, where an amplifier system is obtained from a chain of dynodes (secondary emitting electrodes). Finally in the anode, the flux of electrons from the amplifier is collected and subsequently the electrical output signal is produced. A schematic view of a PMT is shown in Fig. 2.12.

The sensitivity of the photocathode is measured in terms of quantum efficiency η, which determines how many photons N_λ with wavelength λ are converted into photoelectrons N_e.

$$\eta = \frac{N_e}{N_\lambda}. \tag{2.5}$$

The gain (G) of a PMT is the ratio between the number of electrons collected at the anode and those received at the first dynode with N stages.

$$G = \prod_{i=1}^{N} g_i = \prod_{i=1}^{N} \delta_i n_i \tag{2.6}$$

where the sub-index i indicates each dynode with a secondary emission coefficient δ_i and a collection efficiency of n_i for each individual gain g_i. The factors influencing the gain and response time of the multiplier are the materials and geometry. The usually set PMT gain is high, with values ranging from 10^3 to 10^8.

2.4.3 Geometry of the Top Tracker

A basic unit of the TT is the module. Each module is composed by 64 scintillator strips. The TT uses 6.86 m long, 10.6 mm thick, 26.4 mm wide scintillator strips. The light produced in the strips of the TT is collected by Hamamatsu MA-PMT H7546. The MA-PMT is equivalent to incorporating multiple PMT in a single housing. These MA-PMT are powered by a negative polarity high voltage. This MA-PMT has been extensively evaluated in several experiments such as OPERA[30] and others. Each channel contains two sets of 12 dynodes and covers a surface of 2.3×2.3 mm^2 as sketched in Fig. 2.13. A view of a MA-PMT H7546 is displayed in Fig. 2.14.

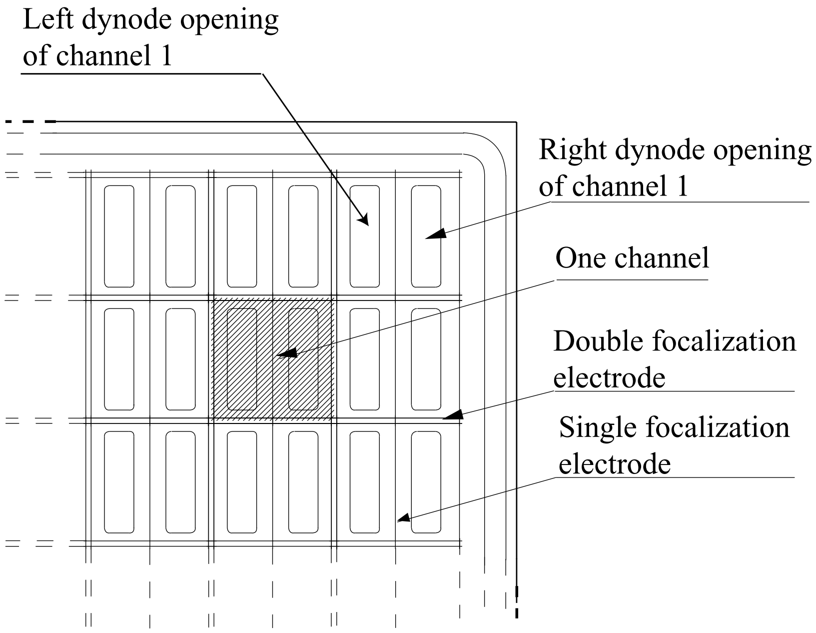

Figure 2.13: Hamamatsu MA-PMT H7546 [30].

The MA-PMT is operated from 800 to 950 V which corresponds to a gain of 10^6 [30]. In the module, the wavelength shifting fibers in the strips are read from both sides by 64-channel MA-PMT placed at each end of the TT modules. The schematic view of the end-cap of a scintillator strip module is shown in Fig. 2.15.

A TT plane is formed by 4 TT modules. Each plane has a sensitive area of $6.7\times6.7\,\mathrm{m}^2$, not including the end-caps. Each TT wall is made using a total of 512 strips of plastic scintillator distributed in 8 modules placed in two planes with perpendicular orientations along the x and y axis to have a 2D space information. All signals created in the TT wall can be read by 16 MA-PMTs (labeled 0 to 15). Fig. 2.16 illustrates the TT wall.

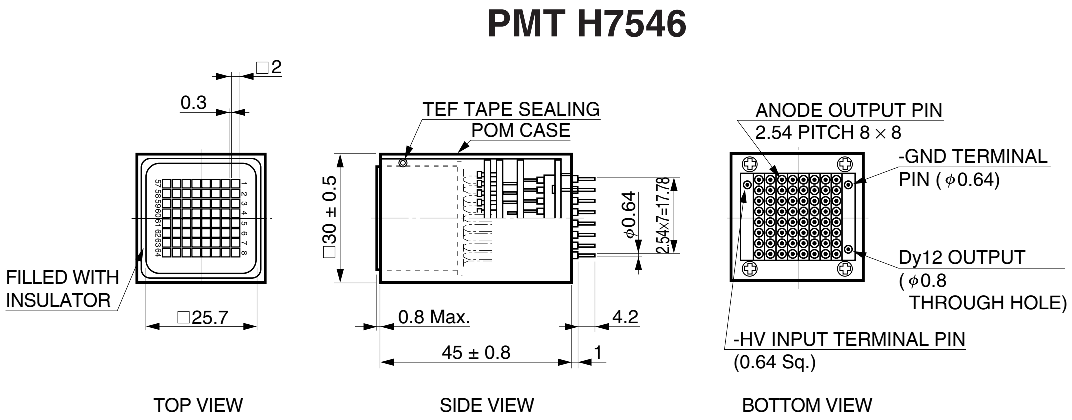

Figure 2.14: Schematic view of a part of a Multianode PMT showing the channel separation by focalization electrodes [30].

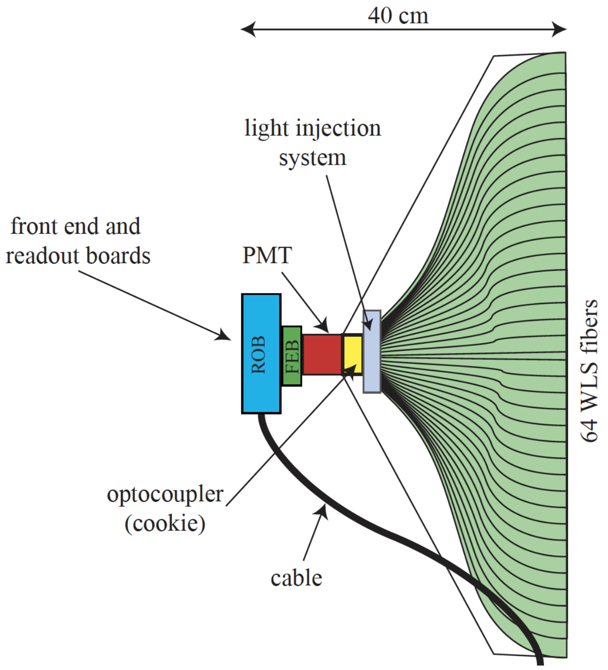

Figure 2.15: Schematic view of an end–cap of a scintillator strip module.

The TT has three horizontal layers, separated by 1.5 m. Each TT layer is a 3×7 horizontal grid with 21 TT walls horizontally placed. The schematic view of the JUNO Top Tracker on top of the central detector and water Cherenkov detector is shown in Fig. 2.17.

The TT covers about 2/3 of the surface above the central detector and water Cherenkov detector. The TT walls at the center are lifted because of the presence of the Chimney to access the central detector and the calibration house. These elevated TT walls are referred to as TT Chimney walls. The walls above the Chimney are 2.8 m above the top layer and have a vertical spacing of 20 cm between layers [96].

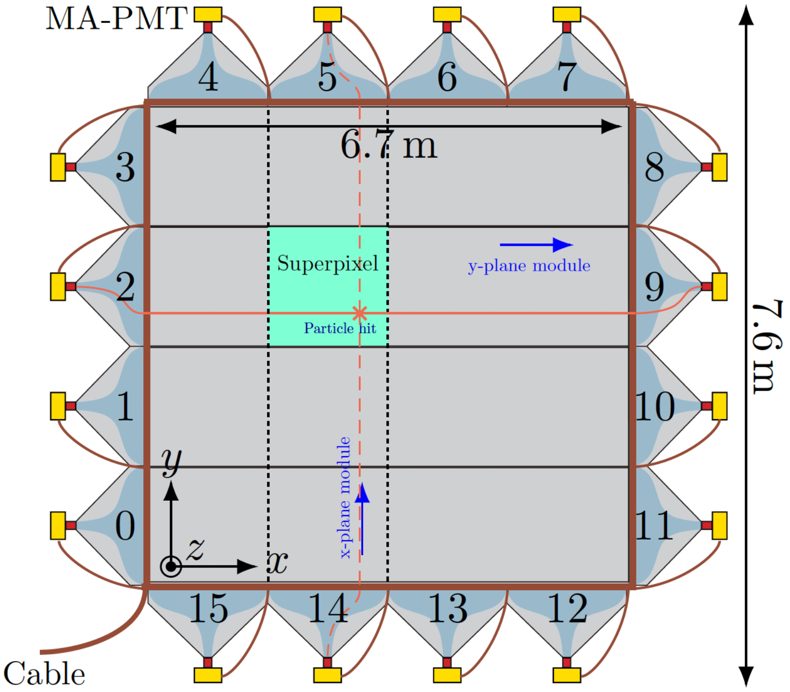

Figure 2.16: Schematic view of a plastic scintillator strip wall from the top [95]

.

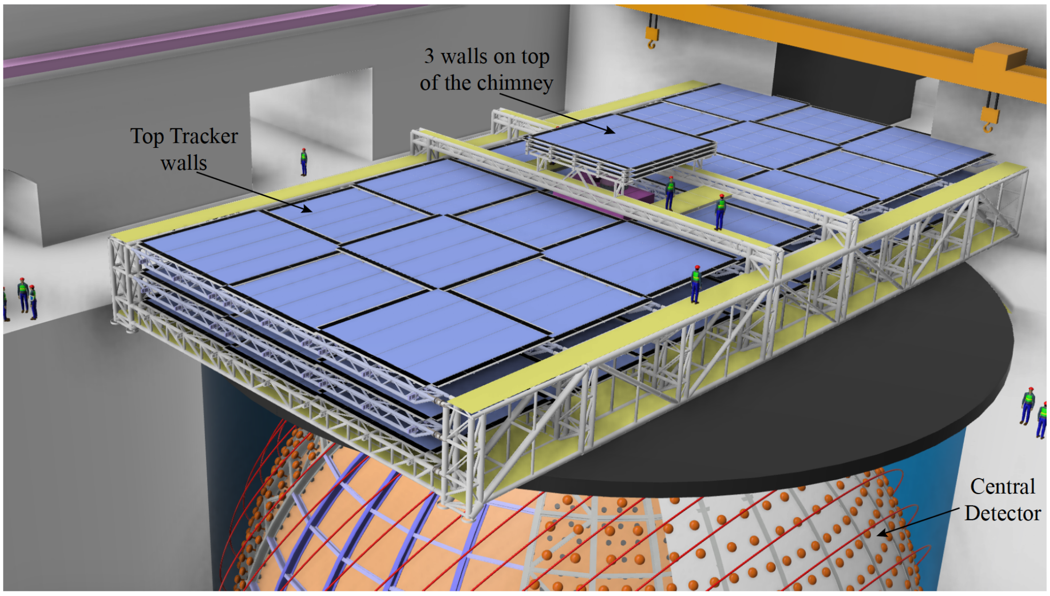

Figure 2.17: Schematic view of the Top Tracker on top of the Central Detector.

From the current aging monitoring in the TT using cosmic rays any extra deterioration of the plastic scintillator properties have not been observed. The expected overall efficiency of a TT module is 98.0 ± 0.5% for a 1 p.e threshold [96]. This number depends on the scintillator properties, the threshold, and the geometry of the TT modules.

2.4.4 Trigger rate

The OPERA experiment operated in the underground Laboratori Nazionali del Gran Sasso (LNGS). The Target Tracker modules of OPERA were protected by the emulsion/lead bricks, while in the case of the JUNO Top Tracker there is no such protection. The TT is directly exposed to the radioactivity of the rock in the JUNO cavern.

Table 2.5: Rock radioactivity in OPERA site (Laboratori Nazionali del Gran Sasso) and in the JUNO site.

Isotope	Activity (Bq/Kg)	
	OPERA site	JUNO site
^{40}K	26 ± 2	1340 ± 50
^{238}U	1.8 ± 1	110 ± 10
^{232}Th	1.5 ± 1	105 ± 10

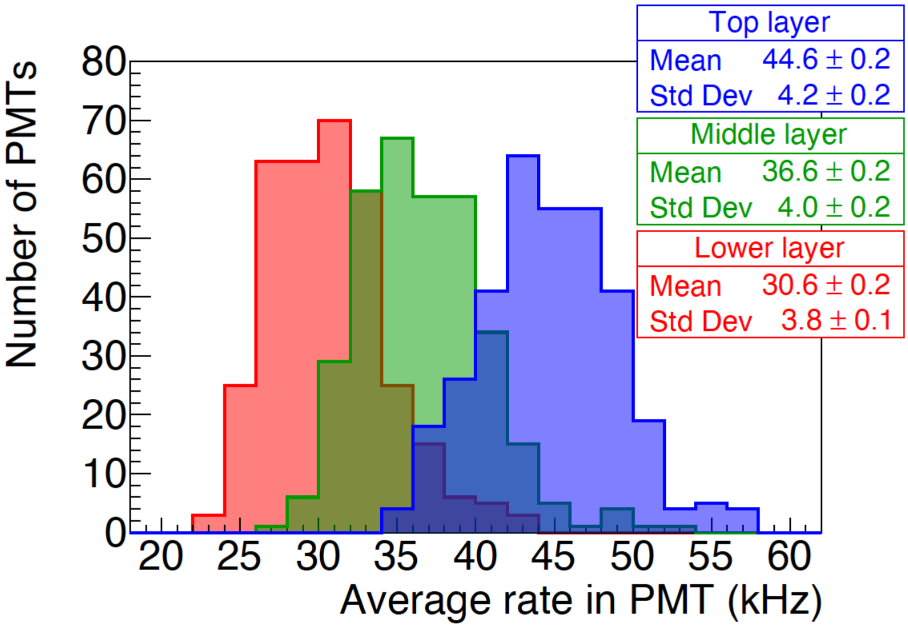

Figure 2.18: Trigger rate per MA-PMT for the three TT layers. A MA-PMT trigger threshold of 1/3 p.e. is assumed.

The natural radioactivity level in the JUNO cavern was measured by Centre d'Etudes Nucléaires de Bordeaux-Gradignan (CENBG) Bordeaux using a Ge detector. The measurements of the natural radioactivity in JUNO is about 100 times higher than in the LNGS, as shown in Table. 2.5. This higher radioactivity rate requires that the TT readout chain electronics has to be redesigned.

The MA-PMT trigger rate induced by this background is estimated using the JUNO simulation. A description about the JUNO official simulation[111] is found in the Section 2.5.

During the simulation, the decays produced in the rock are simulated individually and the particles originating from the decays are propagated. All the energy deposited in the plastic scintillator is then converted into the expected signal in the MA-PMT. The MA-PMT trigger rate induced by the rock radioactivity is shown in Fig. 2.18.

According to this simulation, the average trigger rate per MA-PMT varies between 20 kHz and 60 kHz. The observed rate at each MA-PMT will depend on its position since modules closer to the rock will be more exposed to radiation than more central modules.

Since the radioactivity produced by the decay of isotopes (^{40}K, ^{238}U, ^{232}Th) and their decay products normally do not pass through more than one layer of the TT, it is possible to reduce this noise using a trigger system as will be discussed in the next section.

2.4.5 Readout electronics of the Top Tracker

The global electronics readout chain is composed by 4 different electronics cards : the Front-End Board (FEB), the Read-Out Board (ROB), the Concentrator Board (CB), and the Global Trigger Board (GTB). A scheme of the TT electronics chain is illustrated in Fig. 2.19.

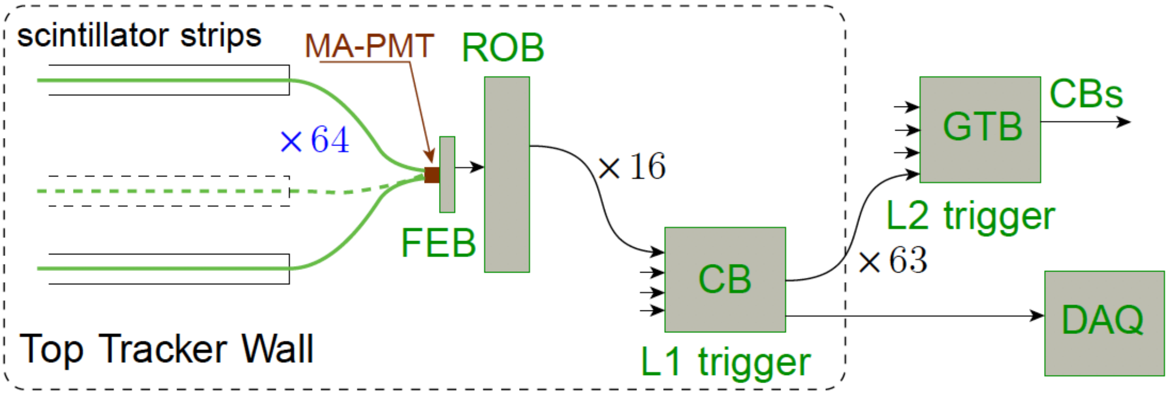

Figure 2.19: The schematic of the TT readout electronics of a wall (the dashed frame) is presented. In a module the 64 scintillation bars are connected to a MA-PMT which is connected to a FEB and ROB. Subsequently the 16 modules are connected to a CB to originate the L1 trigger. The CB's of the 63 walls are connected to the GTB which will originate the L2 trigger.

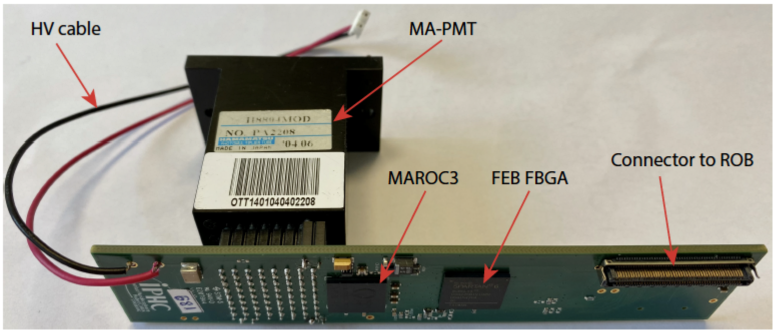

Figure 2.20: The FEB connected to a MA-PMT.

Front-End Board (FEB)

The FEB is responsible for the MA-PMT digitization. The FEB is a MA-PMT interface taking part in the MA-PMT readout. This board houses a MAROC3, which is responsible for most of the FEB functionality, as shown in Fig. 2.20. In total, 992 boards are required.

MAROC3

The readout of the MA-PMT channels is provided by an application specific integrated circuit (ASIC), the MAROC3 [112]. The charge and hit information are given by the MAROC3 chip. The individual trigger outputs are subsequently serialised by the FEB FPGA[2] and sent to the ROB. In addition to that, it exits a FAST-OR output, which is a global OR of the trigger outputs for all 64 channels. The MAROC3 starts the readout of the charge for all 64 channels when a signal is over-threshold and a HOLD signal is sent. During the processing, no new charge readout is possible, so the processing time can be considered as the dead time of the MAROC3[112]. In Fig. 2.21, the components of MAROC3 are presented.

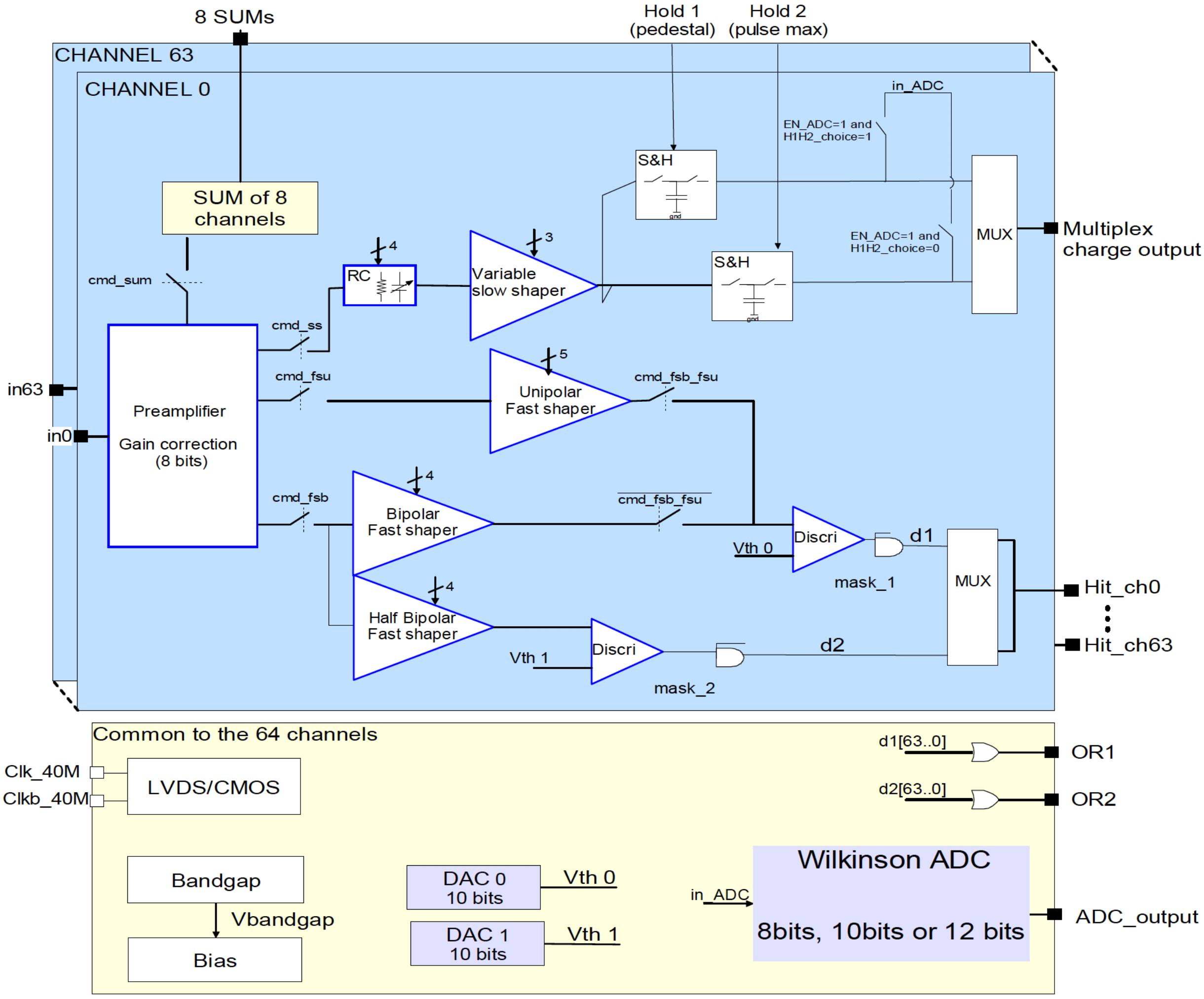

Figure 2.21: Architecture of MAROC3 [112].

---

[2] Field-Programmable Gate Array

At the chip entrance a variable amplification factor is provided per channel. This factor is used to equalise the gain of the 64 channels of the MA-PMT. It has to be mentioned here that a spread on the gain of a factor up to 3 is observed among the 64 channels, which cannot be recovered by adjusting the High Voltage since this is common to all the channels[112]. These gain pre-amplifiers (0-4) are codified in a scale varying between 0 and 255, with a value of 64 corresponding to an amplification factor of 1 (0 means that the channel is switched off)[112]. The trigger efficiency is expected to be higher than 99% for a threshold corresponding to $\sim$ 50fC for a MA-PMT operating at a gain of 10^6. The cross-talk between neighbouring channels inside the MAROC3 is negligible.

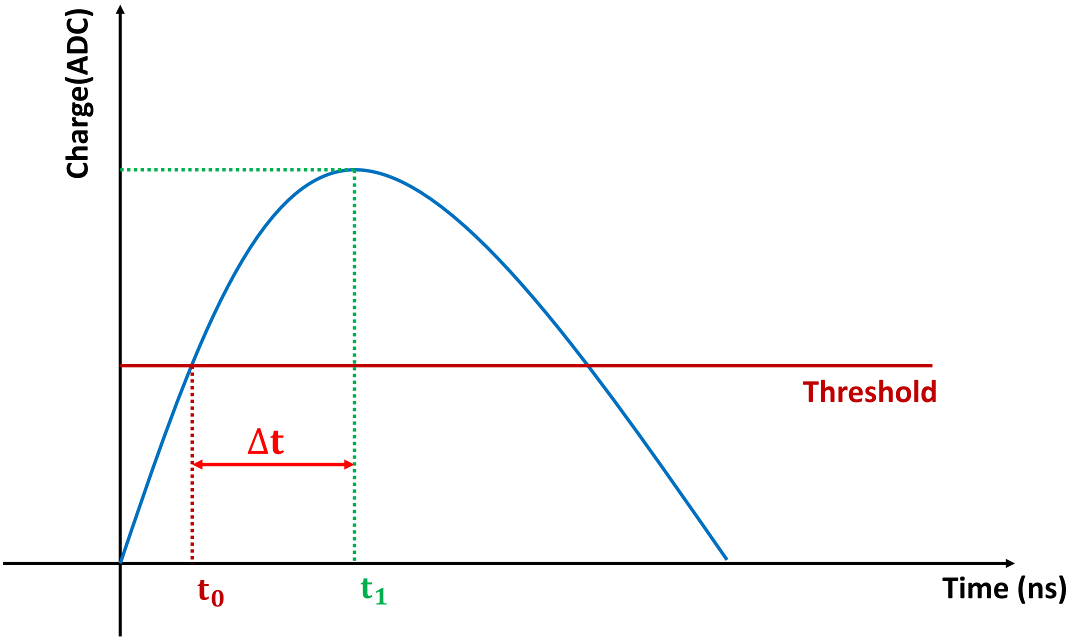

Figure 2.22: MAROC3 Hold delay determination. The charge as a function of time is illustrated. At time t_0, the charge will pass the threshold (red line) and then the maximum charge at time t_1 will be recorded. The hold delay time is defined as Δt.

In the MAROC3, all the charge measurements are performed using internal Wilkinson ADC. The hold delay time is the time required for the input signal after a trigger with time t_0 to reach its maximum charge in a time t_1, in few words, the time difference (Δt) between the trigger and the measurement as shown in Fig. 2.22.

The determination of the hold delay time (Δt) depends on the operation conditions of the MAROC3. In Chapter 3 will be discussed the study of the hold delay time.

Read-Out Board (ROB)

The ROB is responsible for finishing the MA-PMT readout and sending the data to the CB. The ROB provides the MA-PMT High Voltage and it is responsible for the slow control. In total, 992 boards are required. Fig. 2.23 shows the design of the ROB.

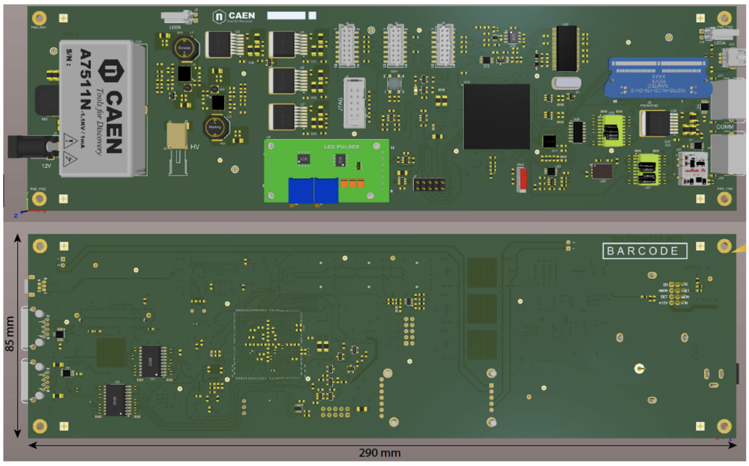

Figure 2.23: Top and bottom faces of the ROB.

Concentrator Board (CB)

The CB gathers hits detected by the 16 MA-PMT of a wall and seeks for x-y coincidences (L1 trigger). Fig. 2.24 shows a picture of the CB. The CB reduces significantly the electronic noise contribution and a large part of hits produced by natural radioactivity. The CB has also the responsibility to communicate with the JUNO acquisition system.

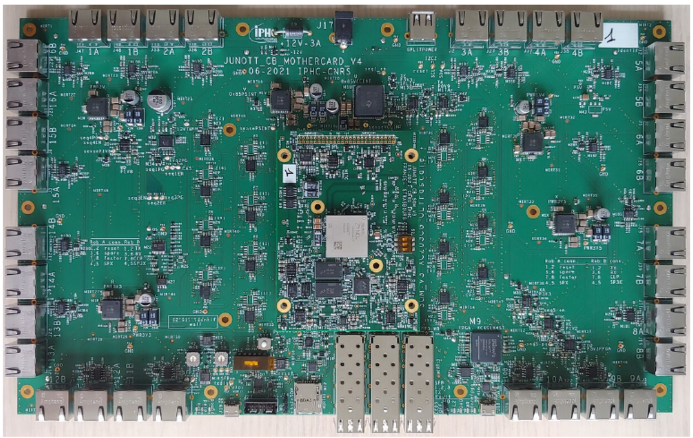

Figure 2.24: Photo of the most recent Concentrator Board.

Fig. 2.25 shows the CB connected to 16 FEB/ROB in one wall. In total, 63 boards are required.

Global Trigger Board (GTB)

In the readout system, the MAROC3 is located in the FEB, and the digitised signals from the MAROC3 are sent to the ROB. To suppress background, the signal must be validated by a trigger condition defined by CB and GTB. The GTB combines information of all L1 triggers from all 63 CB and produce a L2 trigger. To generate the L2 trigger coincidences over the 3 TT layers on modules that are aligned are required. Fig. 2.26 shows the schematic view of the TT trigger card location and connection.

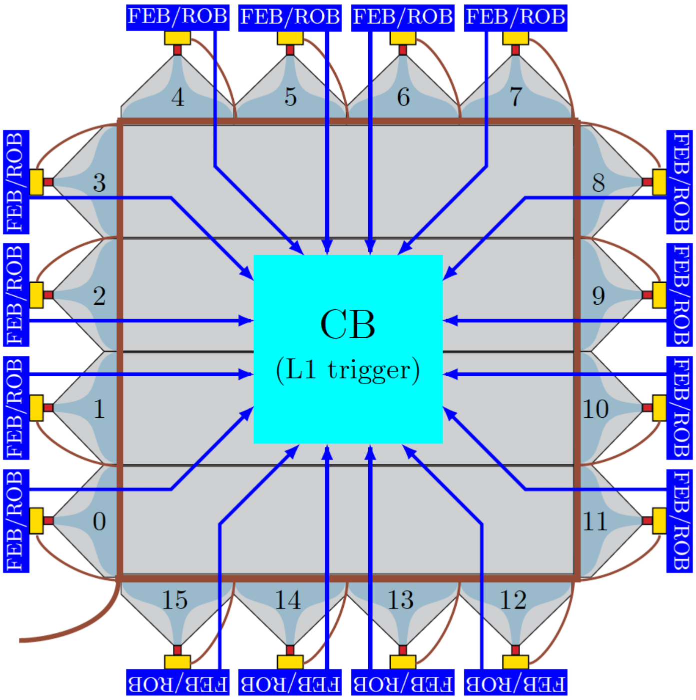

Figure 2.25: Schematic view of the TT wall electronics.

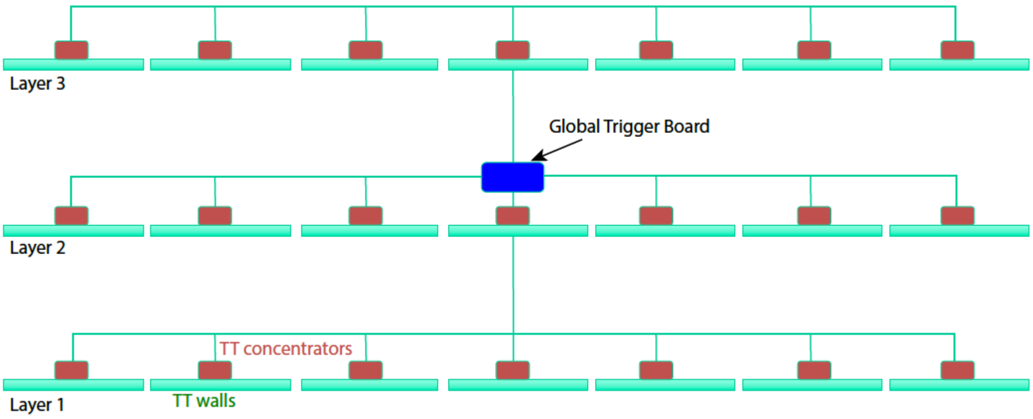

Figure 2.26: Schematic view of the TT global trigger card location and connection.

2.4.6 TT operation modes

In electronic systems, the interpretation of physical charge is obtained from digital converters (ADC) and digital-to-analogue converters (DAC). The process of sampling signals that measure them and convert the resulting samples into digital numeric values is called Digital data acquisition (DAQ). There are four different modes for the TT operation. With these modes it is possible to monitor the stability or calibrate the TT or take regular date to perform its function within JUNO.

The series of digital data acquisition in the TT are :

Trigger rate test mode (TRT) : The TRT mode is used to measure the trigger rate per channel, which corresponds to the number of triggers in a given time window (typically 1 s). This mode allows to define the trigger threshold and to search for light leaks in the modules. TRT mode can also be used to identify noisy channels in the modules.

Pedestal mode (PED) :

The PED mode is used to obtain the charge in the absence of signal. This charge corresponds to the electronic background in the detector. The pedestal charge is obtained using a periodic external trigger instead of using the signal given by the MA-PMT to trigger the detection.

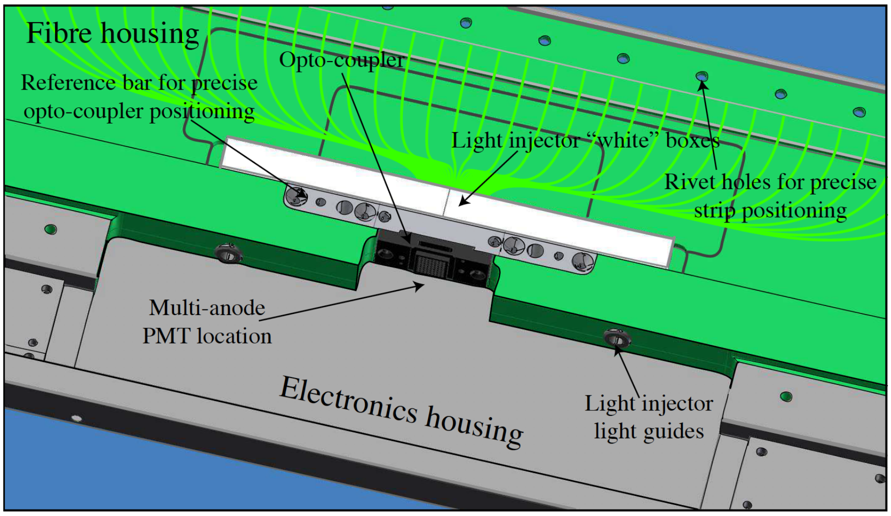

Figure 2.27: 3D view of the central part of an end–cap.

LED light injection mode (LED) : The LED mode refers to the signal emitted by a controlled light source (LED), which has a fixed frequency. The charge distributions are created for each channel of the MA-PMT where the light illuminates each optical fiber using the module is light injection system. Fig. 2.27 illustrates the electronics housing, the MA-PMT location and the light injection system. The light injection system is used to test and monitor all the electronic channels and the data acquisition system.

The light injection system consists of 2 LED (emitting with a wavelength of 475 nm) illuminating the 64 fibers. The LED intensity can be configured to produce a signal with intensity around the single p.e.

Normal run mode :

The Normal run mode is used for regular data acquisition. In this case, the MA-PMT signal passing the threshold will produce a trigger.

In the Chapter 3, we will present some results concerning the TT data acquisition modes using a prototype of the TT. In addition, using this TT prototype the electronics required for the Top Tracker can be optimized and validated.

2.5 JUNO Simulation

The JUNO offline simulation software is based on the SNiPER (Software for Noncollider Physics ExpeRiment)[113] framework and Geant4[114]. With SNiPER, all functional modules are implemented in C++ and the process flow is controlled with Python configuration scripts.

The simulation chain consists of four components: particle generators, detector simulation, electronics simulation and trigger simulation. The detector geometry is constructed by Geant4 based on inputs of the detailed mechanical designs of Central Detector, Water Cherenkov and Top Tracker. For the purpose of this thesis, only the particle generators and Top Tracker configurations are relevant and will be described below.

The natural radioactive decay are customized using data from the ENDF database [115]. With a digitized topographic map of the JUNO location and the MUSIC muon simulation code were used to simulate cosmic muons [116]. The average energy of cosmic muons is $\sim$ 200 GeV.

The TT geometry described in the Section 2.4.3 is used by Geant4 in order to create the TT detector. Each TT signal is simulated according to the energy deposit in the scintillation strips using Geant4. The number of photoelectrons from energy deposits in the TT is normalised to the strip calibration estimated in OPERA[30], which depends on the distance between of the position of the charge deposition and the MA-PMT along the optical fiber.

2.5.1 Top Tracker simulation

The JUNO Simulation software was introduced in the Section 2.5. As mentioned, the TT geometry is implemented based on the description in Section 2.4.3. In this section, we will describe how the TT signal simulation is implemented.

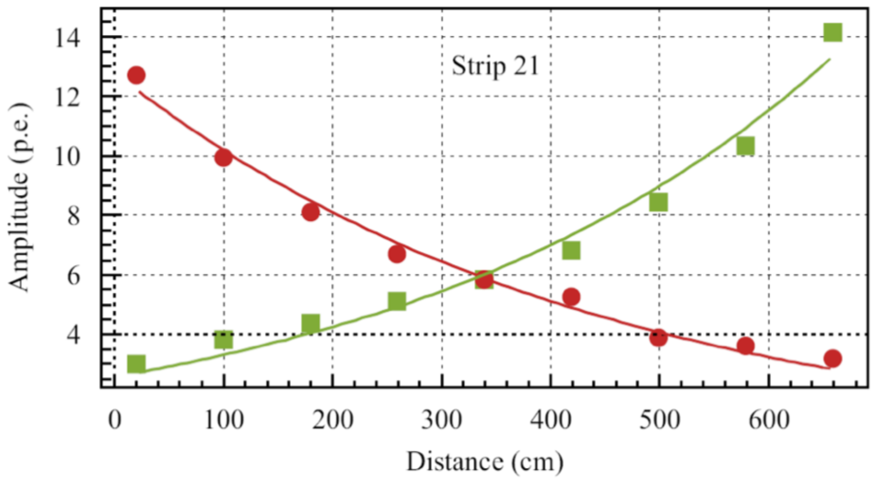

Figure 2.28: The strip calibration curve of the OPERA Tracker [30].

The cosmic muons are created in the JUNO cavern. During their trajectory, they will interact with matter (some processes such as scattering, production of other particles will be simulated). The cosmic muons that reach the Top Tracker will deposit energy in the scintillation bars producing photons that will later be recorded by the MA-PMTs.

In the TT simulation, the OPERA strip calibration curve [30] is used to convert the deposited energy into number of p.e. Eq. 2.7 describes this relation.

$$N_{pe}(x) = \frac{E_{dep}}{2.15} \times \left(\alpha_0 \exp^{-\beta_0 x} + \alpha_1 \exp^{-\beta_1 x}\right) \tag{2.7}$$

where x is the light propagation distance in the wavelength shifting fibers, N_{pe} is the number of p.e, the energy deposited in MeV in the scintillator strip is given by E_{dep}, $\alpha_0 = 4.9\text{MeV}^{-1}, \alpha_1 = 8.3\text{MeV}^{-1}$, $\beta_0 = 0.0107\text{cm}^{-1}, \beta_1 = 0.00163\text{cm}^{-1}$. Theses coefficients are calculated using the calibration curve of each strip. For example, Fig. 2.28 shows the number of detected p.e on each extremity of the TT strips as a function of the hit position with respect to the left (red) and right (green) MA-PMT. In the middle of the strip (most disfavoured position for detection) about 6 p.e. are detected that provides high detection efficiency (the zero probability is negligible).

The total number of p.e represents the mean of a Poisson distribution. The ADC charge on each channel of the MA-PMT is simulated with a Gaussian distribution. In the simulation, the signals in the Top Tracker are based on the calibration results obtained in the OPERA target tracker. The threshold is implemented at 1/3 p.e.

2.6 Physics with JUNO

JUNO not only covers the determination of the neutrino mass hierarchy , but also has a vast program in other subjects [27]. High precision measurements of neutrino oscillation parameters is one of JUNO's goals. Beyond the use of reactor neutrinos, we can also mention that as JUNO is a multipurpose neutrino observatory, it has the capability to measure and analyse neutrinos from different sources, such as neutrinos from the sun, the Earth's atmosphere, supernovae or geoneutrinos. This section aims to address to the physics program of JUNO.

2.6.1 Neutrino Mass Hierarchy determination

The basic configuration assumed by JUNO in [27] for the sensitivity of the Neutrino Mass Hierarchy is summarised in the following list :

- 20kt liquid scintillator target medium.
- Detector energy resolution of 3% $\sqrt{E(MeV)}$.

- Baseline of 52.5 km.
- Total thermal power of 36 GW_{th}.
- Nominal running time of six years of statistics (2000 effective days).
- 73% IBD detection efficiency.
- The reactor antineutrino flux model from ILL and Vogel is adopted [117, 118].

Nowadays, it is expected to use a thermal power is 26.6 GW_{th}.

The neutrino mass hierarchy sensitivity is quantified employing the least-squares minimisation method [27], constructing the χ^2 function as :

$$\chi^2 = \sum_{i=1}^{Nbin} \frac{\left[M_i - T_i\left(1 + \sum_k \alpha_{ik}\epsilon_k\right)\right]^2}{M_i} + \sum_k \frac{\epsilon_k^2}{\sigma_k^2} \tag{2.8}$$

In Eq. 2.8, the measured neutrino events and predicted neutrino events with oscillations in the i-th energy bin are M_i and T_i respectively, σ_k is the systematic uncertainty on each pull parameter, ϵ_k is the pull parameter, and α_{ik} is the contribution fraction of the IBD event of the k-th pull parameter to the i-th energy bin [27]. The considered systematic uncertainties include the correlated (absolute) reactor uncertainty (2%), the uncorrelated (relative) reactor uncertainty (0.8%), the background uncertainties, the spectral shape uncertainty (1%) and the non-linearity uncertainty[27].

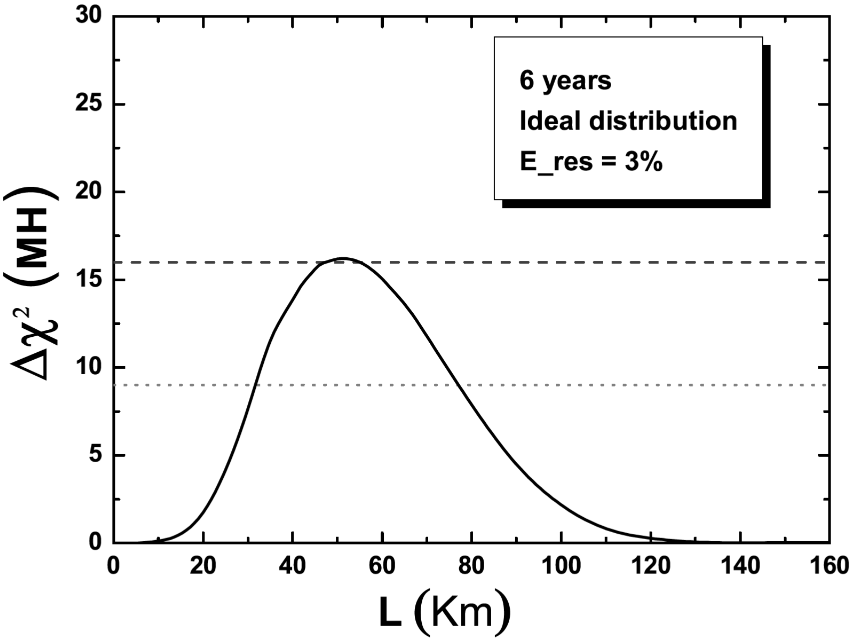

Figure 2.29: The neutrino mass hierarchy discriminator as the function of the baseline [27].

The best fit with χ^2 method for each neutrino mass hierarchy allows obtain the minimum of Eq. 2.8. Statistically, the neutrino mass hierarchy sensitivity at $n\sigma$ (with $n = \sqrt{\Delta\chi^2_{MH}}$)

can be interpreted in terms of the discriminator $\Delta\chi^2_{MH}$ [27]. The neutrino mass hierarchy discriminator can be defined as :

$$\Delta\chi^2_{MH} = \left|\chi^2_{min}(NH) - \chi^2_{min}(IH)\right| \tag{2.9}$$

The optimal baseline is calculated using the discriminator defined in Eq. 2.9, which are shown in Fig. 2.29. JUNO has chosen its site at ~ 53km baseline as this distance maximises the $\Delta\chi^2_{MH}$ discriminator.

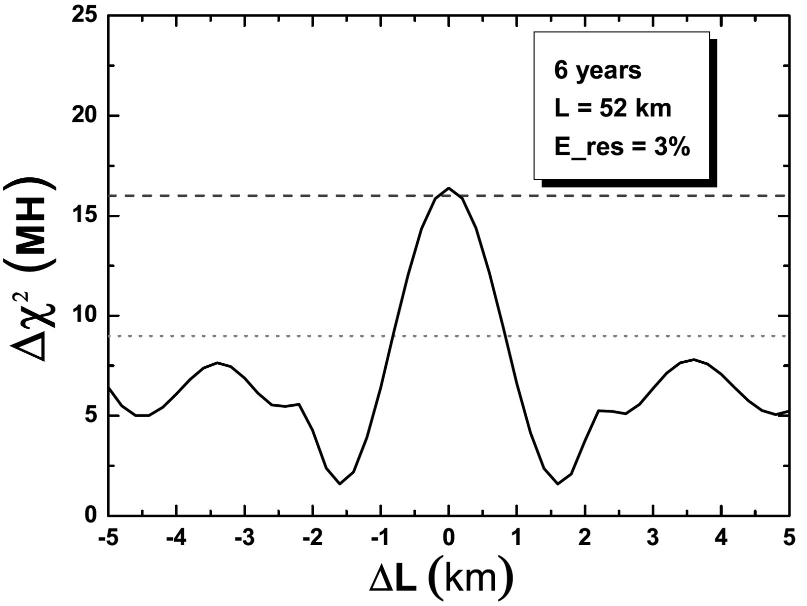

Figure 2.30: The neutrino Mass Hierarchy discriminator as the function of the baseline difference of two reactors [28].

The neutrino mass hierarchy discriminator as function of the baseline difference of two reactors is shown in Fig. 2.30. To ensure a sensitivity better than $3\sigma(\Delta\chi^2_{MH} > 9)$, the difference between any two cores must be less than 500 m.

The maximal neutrino mass hierarchy discriminator 4σ ($\Delta\chi^2_{MH} \sim 16$) occurs when JUNO has chosen the baselines for both Taishan and Yangjiang reactors at ~ 53km. JUNO can achieve a sensitivity for neutrino mass hierarchy of ~ 3σ with six years of statistics [27].

The detector energy resolution of 3% $\sqrt{\text{E(MeV)}}$ is defined from the photon-electron statistics (1200 p.e/MeV), the energy E defined as the visible energy of the positron [96]. For a real experimental environment, the energy resolution is affected by some important factors beyond the photon-electron statistics such as : dark noise from PMT and electronics, and others [96].

The detector energy resolution is parameterised as function of the visible energy using a Gaussian function with a standard deviation $\sigma_{E_{vis}}$ given by [27] :

$$\frac{\sigma_{E_{vis}}}{E_{vis}} = \sqrt{\left(\frac{a}{\sqrt{E_{vis}}}\right)^2 + b^2 + \left(\frac{c}{E_{vis}}\right)^2} \tag{2.10}$$

The parameters a, b, c must be determined experimentally. The term a is associated with the Poisson statistics of the total number of detected photoelectrons, c is dominated by the PMT dark noise, and b is dominated by the detector's spatial non-uniformity [27].

To achieve a 3σ sensitivity in 6 six years. The energy resolution is a critical parameter for JUNO [27].

2.6.2 Precision measurement of neutrino oscillation parameters

The JUNO electron antineutrino spectrum, as described in Section 2.2.2 provides access to the oscillation parameters $\theta_{12}, \theta_{13}, \Delta m^2_{21}, \Delta m^2_{31}$ [27, 96]. The high precision of the oscillation parameters is important to contribute to the unitary test of the U_{PMNS} matrix, the three neutrino model or the mass sum rule test $\Delta m^2_{31} + \Delta m^2_{21} + \Delta m^2_{32}$, and to probe new physics beyond the Standard Model.

Table 2.6: A summary of precision levels for the oscillation parameters. The current knowledge (PDG2020 [39]) is compared with 6 years of JUNO data taking [97].

	Central Value	PDG2020	6 years
Δm^2_{31} $\times 10^{-3}$ eV^2	2.5283	±0.034	±0.0047
Δm^2_{21} $\times 10^{-5}$ eV^2	7.53	±0.18	±0.024
$\sin^2\theta_{21}$	0.307	±0.013	±0.0016
$\sin^2\theta_{13}$	0.0218	±0.0007	±0.0026

The energy resolution and large statistics allows JUNO to measure with a sub-percent precision the three neutrino oscillation parameters : $\theta_{12}, m^2_{21}, \Delta m^2_{31}$ as shown in the Table. 2.6. Fig. 2.31 illustrates the $\Delta\chi^2$ profiles of JUNO compared to the current state of the oscillation parameters obtained by PDG2020 [39].

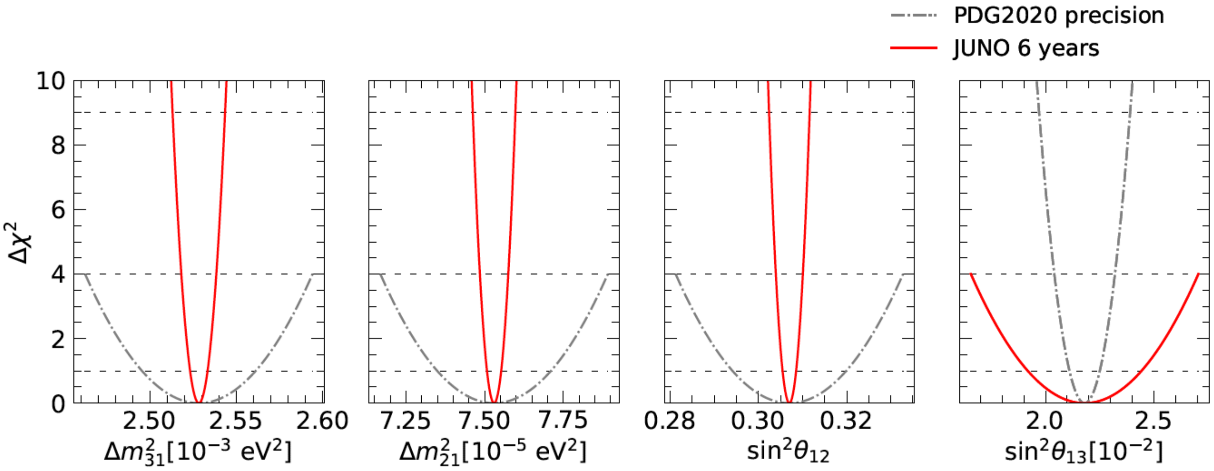

Figure 2.31: Comparison of $\Delta\chi^2$ distributions of oscillation parameters: PDG2020(dashed black curve)[39] v.s. projection with 6 years data taking of JUNO (solid red curve) [96].

2.6.3 Solar neutrinos

The significant impact of neutrino oscillations from the use of solar neutrinos has led to a better understanding of neutrino physics and in turn astrophysics. JUNO, to be competitive in this sector, must achieve a radioactivity level of 10^{-17} g/g. Table. 2.7 summarises the expected event numbers of electic scattering (ES), charged current (CC) and neutral current (NC) channels, for a 200 kt·year exposure and a 100% detection efficiency.

Table 2.7: Reactions via ES, CC and NNC channels for ^{8}B and *hep* solar neutrinos in JUNO [96].

	Type	Reaction	Threshold (MeV)	Final products	^{8}B	*hep*
1	ES	$\nu + e^- \rightarrow \nu + e^-$	0	e^-	3×10^5	640
2	CC	$\nu_e +^{12}\mathrm{C} \rightarrow e^- +^{12}\mathrm{N}$	16.8	e^-	0	0.41
3	CC	$\nu_e +^{13}\mathrm{C} \rightarrow e^- +^{13}\mathrm{N}$	2.2	e^- and ^{13}N decay	3768	14
4	NC	$\nu +^{12}\mathrm{C} \rightarrow \nu +^{12}\mathrm{C}(1^+)$	15.1	γ	0.2	5
5	NC	$\nu +^{13}\mathrm{C} \rightarrow \nu +^{13}\mathrm{C}(\frac{3}{2}^-)$	3.685	γ	3165	13.5

In the left side of the Fig. 2.32 the signal and background spectra above 2 MeV expected after the selection cuts is illustrated. In the right side of the Fig. 2.32 the expected precision of $\sin^2\theta_{12}$ and Δm^2_{21} using ^{8}B solar neutrinos and reactor antineutrinos at JUNO is presented [119].

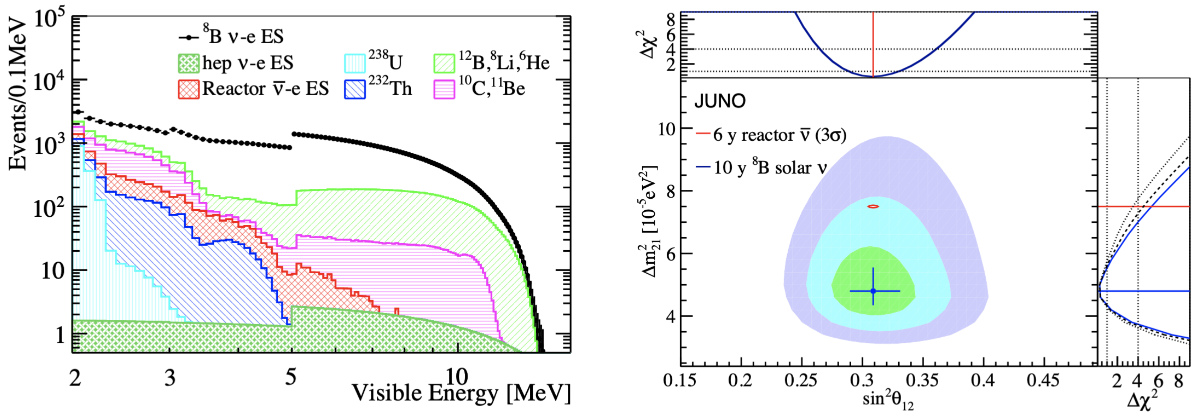

Figure 2.32: Left : The expected signal and background spectra. Right : The expected sensitivity of $\sin^2\theta_{12}$ and Δm^2_{21}. [119]

2.6.4 Geo-neutrinos

Geo-neutrinos are created from the decays of radioactive elements inside the Earth. Using Geo-neutrinos, we could study the formation and chemical composition of our planet from its radiogenic power, and bring insights into its formation and chemical composition. The IBD on protons with 1.8 MeV threshold makes it possible to measure geo-neutrinos from ^{238}U and ^{238}Th decay chains. JUNO has the potential to study geo-neutrinos with a large statistics ($\sim$ 400 events/year) [27, 96]. It is expected to record more geo-neutrino events than all other detectors accumulated. The main challenge for the JUNO geo-neutrino measurement is the large reactor antineutrino background. In addition, there are other non-antineutrino backgrounds relevant for geo-neutrino detection, like cosmic muons, cosmogenic backgrounds, fast neutrons. The expected energy spectrum of Geo-neutrinos (magenta line) after the selection cuts is shown in Fig. 2.6.

2.6.5 Atmospheric neutrinos

An important source of neutrinos is the decays of pions and kaons in extensive air showers initiated by the interaction of cosmic rays with the Earth's atmosphere. Atmospheric neutrinos have played an important role for studying the neutrino oscillation phenomenon. Super-Kamiokande[85] in 1998 showed the first evidence of neutrino oscillation based on a zenith-angle dependent deficit of atmospheric muon neutrinos (refer the Section 1.4.2).

Fig. 2.33 shows a comparison of the expected atmospheric neutrino spectrum between JUNO [96] and other experiments.

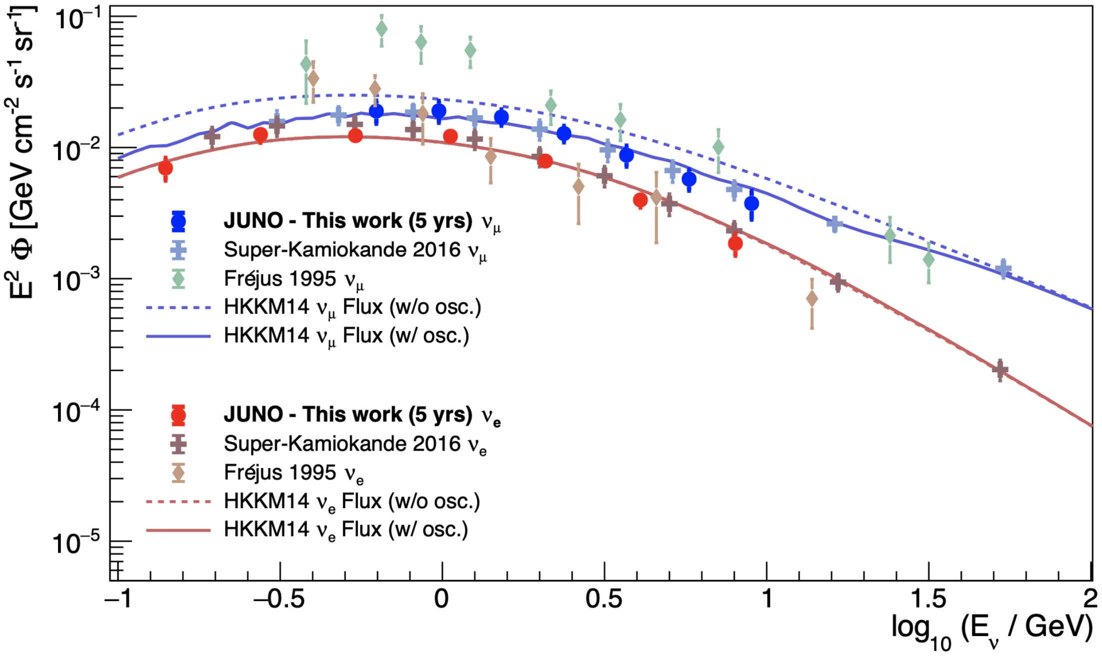

Figure 2.33: Atmospheric neutrino energy spectra reconstructed by the JUNO detector for ν_μ (blue color) and ν_e (red color), compared with present Super-Kamiokande and Fréjus measurements in the same energy region [96].

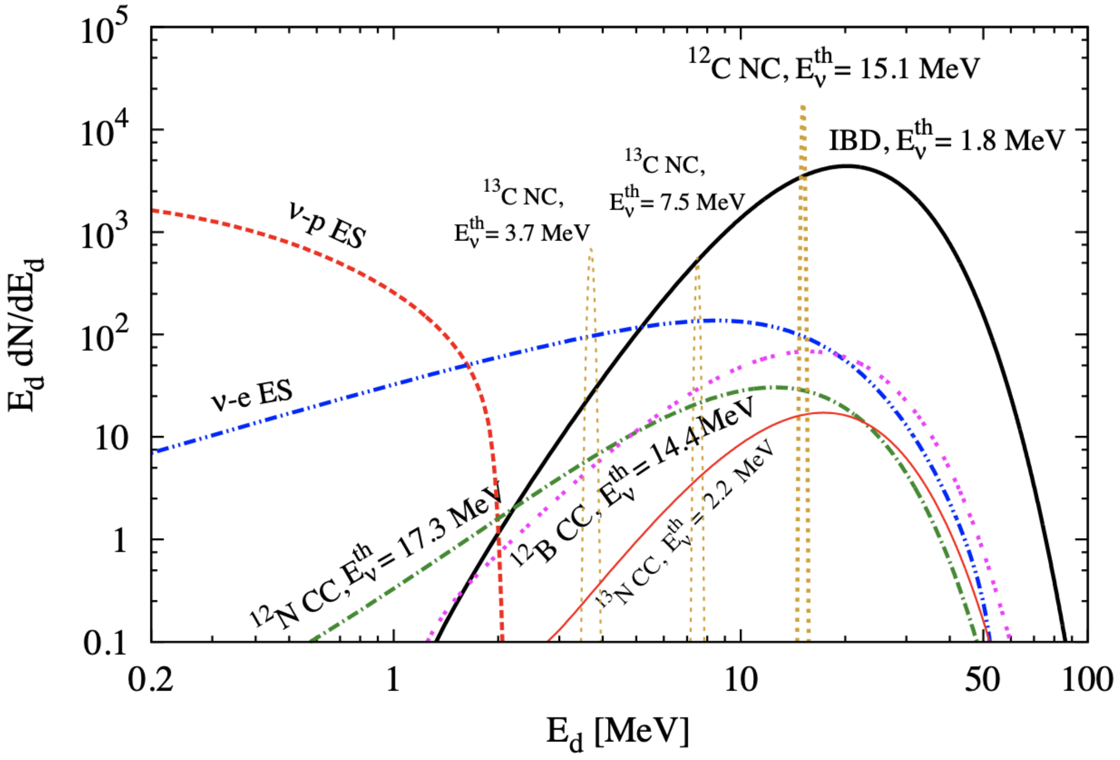

Figure 2.34: The neutrino spectra with respect to the visible energy Ed in the JUNO detector for a typical SN explosion at 10 kpc [96].

2.6.6 Supernova neutrinos

About ~ 99% of the energy originating from a Supernova (SN) outburst is released through neutrinos within a few seconds. During all stages of stellar collapse and stellar explosion, neutrinos are crucial players, providing valuable information about the mechanism of the SN explosion and the intrinsic properties of the neutrinos.

One of the points in the JUNO program is to detect SN neutrinos with high statistics through various detection channels [96]. The multichannel detection is mainly via :

- The inverse beta decay (IBD) : $\nu_e + p \rightarrow e^+ + n$,
- The elastic neutrino-electron scattering (eES) : $\nu + e^- \rightarrow \nu + e^-$
- The elastic neutrino-proton scattering (pES) : $\nu + p \rightarrow \nu + p$.

JUNO has excellent capability of detecting all neutrinos flavors from SN. For a typical galactic distance of 10 kpc and typical SN parameters, JUNO will register ~ 5000 IBD events, ~ 300 eES events and ~2000 pES events [96]. The neutrino spectra are shown in Fig. 2.34. For simplicity the neutrino oscillations are not considered. The main detection channels are represented by IBD (black) , eEs (blue), pES(red).

In addition to the topics mentioned as central to the JUNO program, JUNO is an ambitious project that aims to address a wide range of open questions in the fields of particle physics, nuclear physics, astrophysics and cosmology. JUNO also offers the opportunity to study new physics beyond the SM. The following list presents some of these other topics from the JUNO physics program:

- Sterile Neutrinos
- Nucleon Decays
- Neutrinos from Dark Matter
- Exotic Searches with Neutrinos
- Non-standard Interactions
- Lorentz Invariance Violation
- Unitarity violation in the lepton mixing matrix

A discussion of these topics is found in [27].

L'Observatoire souterrain de neutrinos de Jiangmen

> *"La physique des neutrinos est en grande partie un art d'apprendre beaucoup en n'observant rien."*
> **Haim Harari**.

L'Observatoire souterrain de neutrinos de Jiangmen (JUNO) est un détecteur souterrain polyvalent à scintillateur liquide. L'objectif principal de JUNO est de déterminer la hiérarchie des masses de neutrinos.

L'expérience JUNO est située dans le sud de la Chine, près de la ville de Jiangmen, dans la province de Guangdong. Afin d'optimiser l'analyse de la hiérarchie des masses des neutrinos, le site JUNO est situé à 53 km de deux centrales nucléaires (NPP) : Yangjiang NPP et Taishan NPP. La puissance thermique totale de tous les noyaux entre les coeurs des centrales nucléaires de Taishan et de Yangjiang est de 26,6 GWth.

JUNO est un scintillateur liquide dont la masse cible est de 20 kton et dont la résolution en énergie est de 3% à 1 MeV. L'objectif principal de JUNO est de déterminer la hiérarchie des masses de neutrinos à 3σ après 6 ans de fonctionnement, ainsi que de fournir des mesures précises des paramètres d'oscillation des neutrinos. Pour ce faire, JUNO utilise des antineutrinos des réacteurs se situant à une distance 53 km de son détecteur. L'excellente résolution en énergie et le grand volume prévus pour le détecteur JUNO offrent des possibilités intéressantes pour aborder de nombreux sujets importants dans le domaine des neutrinos et de l'astrophysique. JUNO couvrira également un riche programme de physique avec des mesures sur les géoneutrinos, les neutrinos solaires, les neutrinos atmosphériques, les neutrinos de supernovae et la recherche d'une nouvelle physique au-delà du Modèle Standard.

Le détecteur JUNO est composé de 3 parties différentes : le détecteur central, qui est responsable de la mesure du spectre d'énergie des antineutrinos ; le détecteur d'eau cherenkov, une piscine remplie d'eau purifiée et instrumentée de photomultiplicateurs entourant le détecteur central ; et le Top Tracker (TT), qui assure un suivi précis des muons cosmiques.

Le détecteur central est un récipient sphérique en acrylique d'un diamètre intérieur de 35,4 m et d'une épaisseur de 120 mm. Il est rempli de 20 kton de scintillateur liquide. Ce scintillateur est utilisé comme cible pour mesurer les antineutrinos électroniques provenant des réacteurs nucléaires. La détection des neutrinos se fait en transférant l'énergie de l'antineutrino en énergie visible sous forme de photons. Pour détecter la lumière de scintillation par désintégration bêta inverse, 17,612 photomultiplicateurs de 20 pouces et 25,600 photomultiplicateurs de 3 pouces sont utilisés. JUNO comprend également un système de recherche de la radioactivité interne (OSIRIS), qui permet de contrôler la radiopureté du scintillateur liquide pendant le remplissage du détecteur central.

Bien que le détecteur soit situé à une profondeur de 700 m, il reste encore un très faible flux de muons cosmiques qui induisent des erreurs de détection. Les faux signaux de désintégration bêta inverse apparaissant du au passage de ces muons dans JUNO nécessitent l'utilisation d'un système de veto efficace pour la caractérisation et la réduction de ce bruit de fond. Le système de veto se compose de deux sous-systèmes, le détecteur d'eau Cherenkov et le Top Tracker, qui assureront une réduction efficace du bruit de fond.

Le détecteur d'eau Cherenkov est une piscine cylindrique remplie de 35 ktons d'eau ultrapure. Cette piscine a un diamètre de 43,5m et une hauteur de 44m. Le Détecteur Central est immergé dans cette piscine. L'effet Cherenkov produit par les muons cosmiques traversant la piscine est détecté par 2400 photomultiplicateurs. installé sur la surface extérieure de la structure en acier inoxydable. Le rôle du Top Tracker est de détecter les muons cosmiques et de reconstruire leurs trajectoires pour étudier la production du bruit de fond cosmogénique (^{9}Li,^{8}He) qui est le principal bruit de fond induit par les muons atmosphériques dans le détecteur central. Le Top Tracker permet de contrôler les erreurs systématiques induites par le bruit de fond cosmogénique dans l'étude de la détermination de la hiérarchie des masses des neutrinos. Le Top Tracker réutilise les modules de scintillateur plastique du traqueur de cibles de l'expérience OPERA.

Le TT se compose de 3 couches de détecteurs bidimensionnels constitués de bandes de scintillateur plastique et couvrira environ 60% de la surface au-dessus du détecteur central. Les modules du TT sont montés dans des murs dont la surface sensible est de $6,7 \times 6,7$ m^2. Chaque mur est composé de 8 modules placés en deux couches avec des orientations perpendiculaires le long des axes x et y pour avoir une information spatiale en 2D. Un module est composé de 64 bandes scintillantes, qui sont lues des deux côtés par des photomultiplicateurs multi-anodes (MA-PMT) à 64 canaux. Lorsqu'une particule traverse une bande scintillante, elle dépose de l'énergie et des photons sont créés. Les photons se propagent dans les fibres à décalage de longueur d'onde et sont collectés et convertis en un signal électrique.

Le niveau de radioactivité naturelle mesuré dans la caverne de JUNO est environ 100 fois plus élevé que sur le site d'OPERA. Ce taux de radioactivité plus élevé nécessite une nouvelle conception de l'électronique de la chaîne de lecture Top Tracker. Cette chaîne est constituée de 4 cartes électroniques différentes : la carte frontale (FEB), la carte de lecture (ROB), la carte concentratrice (CB) et la carte de déclenchement globale (GTB).

Le logiciel de simulation JUNO est basé sur le cadre SNiPER et Geant4. La chaîne de simulation se compose de quatre éléments : générateurs de particules, simulation du détecteur, simulation de l'électronique et simulation du déclenchement. La géométrie du détecteur est construite par Geant4 sur la base des entrées des conceptions mécaniques détaillées du détecteur central, détecteur de l'eau Cherenkov et

Top Tracker. Dans le cadre de cette thèse, seules les configurations des générateurs de particules et du Top Tracker sont pertinentes.

La décroissance radioactive naturelle est personnalisée en utilisant les données de la base ENDF. Une carte topographique numérisée de l'emplacement de JUNO et le code de simulation de muons MUSIC ont été utilisés pour simuler les muons cosmiques. L'énergie moyenne des muons cosmiques est de 200 GeV. Chaque signal TT est simulé en fonction du dépôt d'énergie dans les bandes de scintillation à l'aide de Geant4. Le nombre de photoélectrons provenant des dépôts d'énergie dans le TT est normalisé à l'étalonnage des bandes estimé dans OPERA.

JUNO ne couvre pas seulement la détermination de la hiérarchie des masses des neutrinos, mais dispose également d'un vaste programme dans d'autres domaines. programme dans d'autres domaines. Les mesures de haute précision des paramètres d'oscillation des neutrinos sont l'un des objectifs de JUNO. Au-delà de l'utilisation des neutrinos du réacteur, nous pouvons également mentionner que que, comme JUNO est un observatoire de neutrinos polyvalent, il a la capacité de mesurer et d'analyser des neutrinos provenant de différentes sources, comme les neutrinos du soleil, de l'atmosphère terrestre, des supernovae ou des géoneutrinos.

Part II

Top Tracker Prototype

Chapter

3

Calibration of Top Tracker Prototype

> *"Neutrinos ... win the minimalist contest: zero charge, zero radius, and very possibly zero mass."*
> Leon M. Lederman.

Contents

At the IPHC, a prototype of the TT called Muon Telescope (MT) has been built to test the full readout/trigger chain of the TT. The MT can be used to optimise the reconstruction algorithms needed in the analysis of cosmic muons in JUNO. The main purpose of this chapter is to introduce the Muon Telescope.

The geometry of the MT is presented in Section 3.1. The MT operation modes are discussed in Section 3.2. The determination of some parameters from calibration tests are presented in the Section 3.3 and the Section 3.4. A test bench was designed to calibrate the electronic chain will be used in TT. The comparison of the results obtained in the MT and test bench are found in the Section 3.5. As we will see throughout this chapter a new calibration was required, these results are summarised in Section 3.6. And finally, the muon detection efficiency is presented in Section 3.7.

3.1 The Muon Telescope

The Muon Telescope was manufactured using the same scintillation strips as those of the Top Tracker. In the MT, these strips are 1.7 m long. TT has of 3 layers while the MT has 4. In the MT, each layer is made of two planes perpendicularly oriented, creating a granularity of $2.64 \times 2.64 \text{cm}^2$ due to the width of the strips. Each plane has 64 scintillation strips read on one side by a 64-channel MA-PMT. Due to differences in the length of scintillator strips, the MT has a detection surface of 1/16 of one TT wall.

In Fig. 3.1, the schematic view of the MT is presented. The MT is composed of 4 XY plastic scintillator layers (8 modules). The layers are numbered from the bottom (layer 0) to the top layer (layer 3). In Fig. 3.1, the MT is shown in horizontal position, but it is possible to change the position of the telescope using a motor installed in the rotation axis.

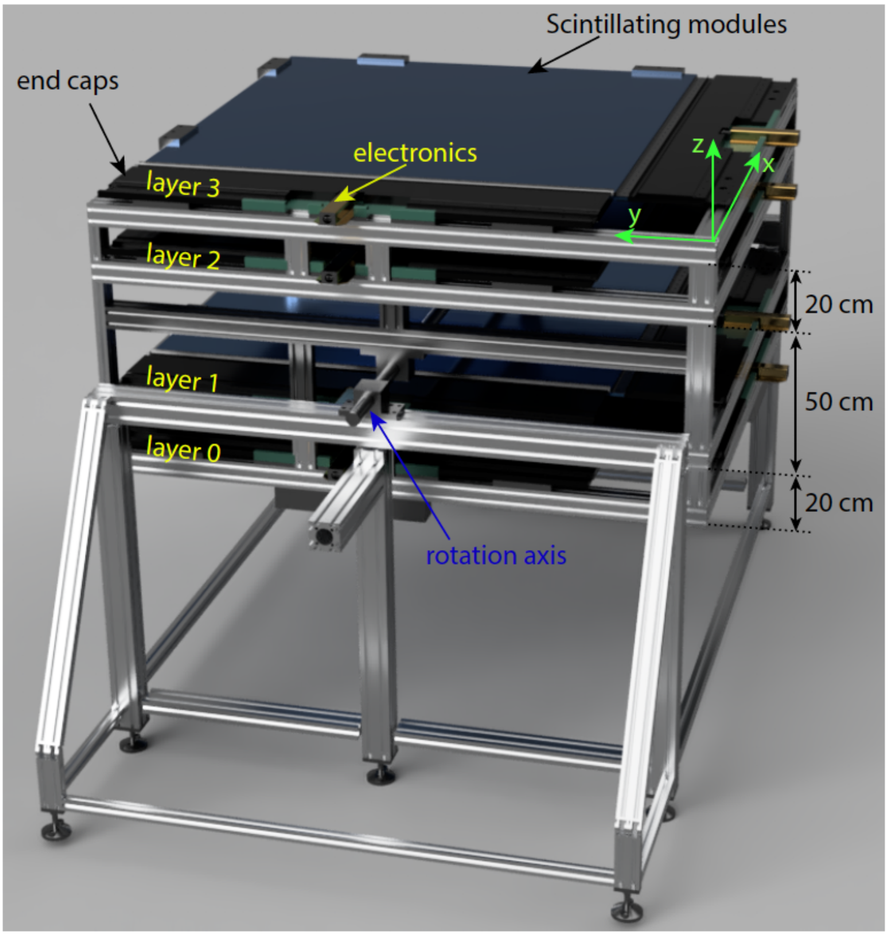

Figure 3.1: Schematic view of the Muon Telescope (MT).

The full telescope system of the MT is equipped with 8 FEB/ROB.The electronics chain was completed last year (2021) with a CB, however the CB has not been used during this work. As discussed in Section 2.4.5, the charge and hit information are given by the MAROC3, while the timing is provided by a modified version of the ROB that implemented some of the CB functionality (timestamping, communication with Data Acquisition system) for testing. In absence of the CB, xy correlations at the level of a wall where done offline.

A picture of the electronic cards is shown in Fig. 3.2. For simplicity, it was decided to name the boards in terms of their layer and their position (left or right, from the perspective of someone at the DAQ computer). For example, the board which is located in layer 3 and it is on the right side of the MT is named "C3R".

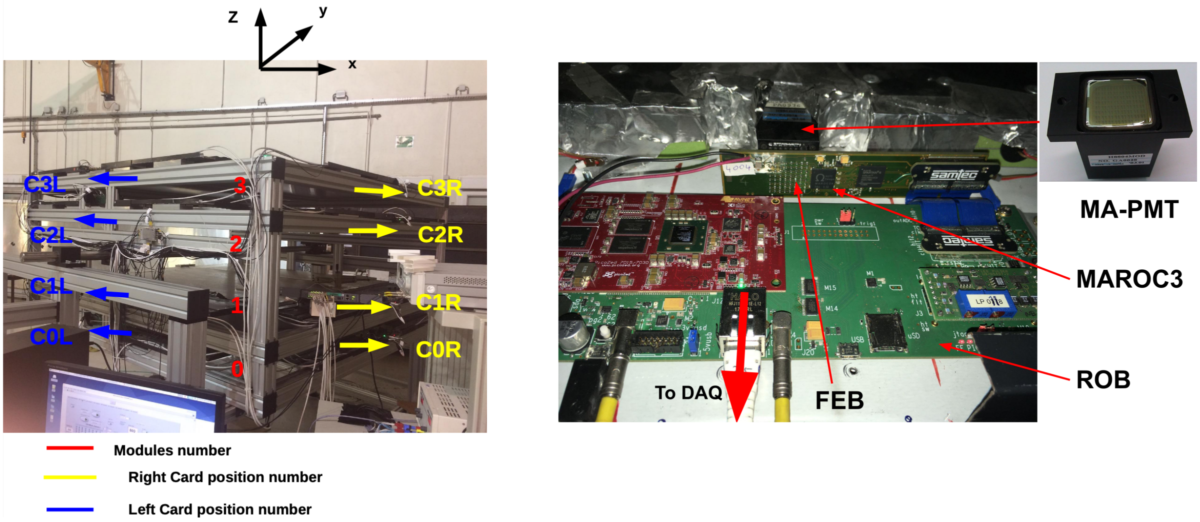

Figure 3.2: Left: Layout of the electronics boards on the MT. Right: One electronic card mounted on the MT.

3.2 TT operation modes

The series of TT operation modes was discussed in the Section 2.4.6. The MT consists of the same data acquisition modes. One of the tasks of this work was to develop the decoding codes of the operation modes in the MT.

Fig. 3.3 shows the operation of the TRT mode. In the TRT mode, an internal trigger is generated by the signals themselves. This trigger reaches the FEB and is transmitted to the ROB. The ROB counts these signals. Subsequently, the number of triggers in the last second per channel are sent to the DAQ.

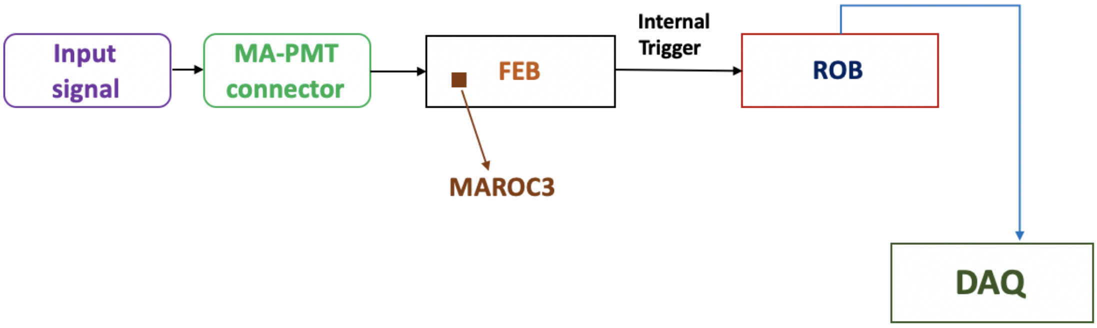

Figure 3.3: Operation of the TRT mode. The signals themselves generate an internal trigger. This trigger reaches the FEB and is transmitted to the ROB. The ROB counts these signals. Subsequently, the number of triggers per channel is sent to the DAQ.

The trigger rate versus channel number for the C2R (blue line) and the C3L (red line) are shown in Fig. 3.4. There is a difference in the trigger rate between the C3L and the other board. The channels 14 and 63 of the C3L have a low trigger. Theses channels are probably suffering from damaged fibers and/or aged scintillation strips. It has to be said that the OPERA modules used for this prototype are mainly those rejected during the production at that time.

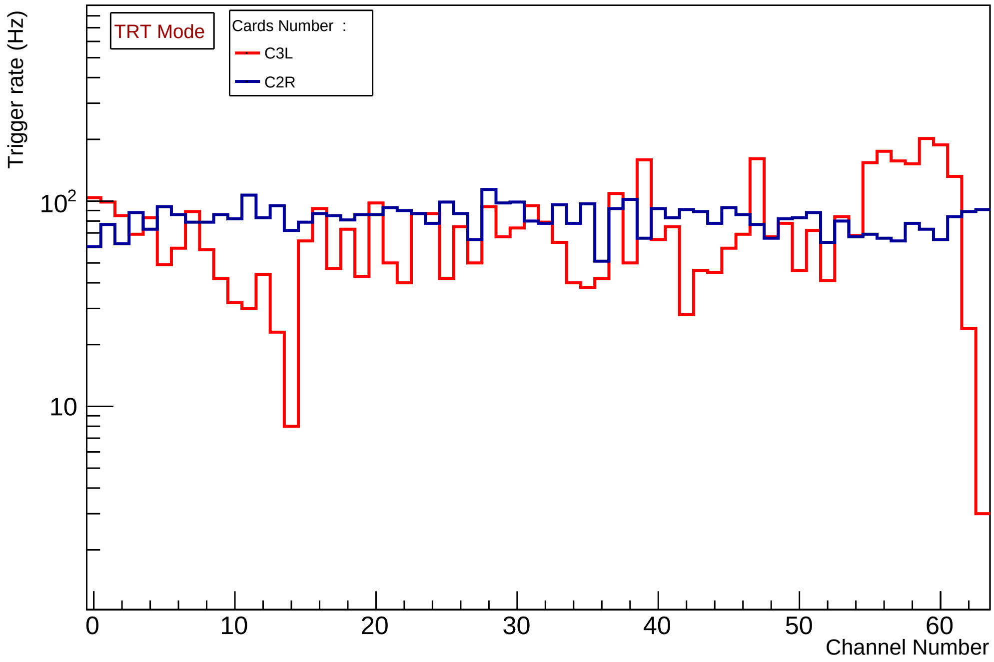

Figure 3.4: TRT Mode : The trigger rate versus channel number for the C2R (blue line) and the C3L (red line).

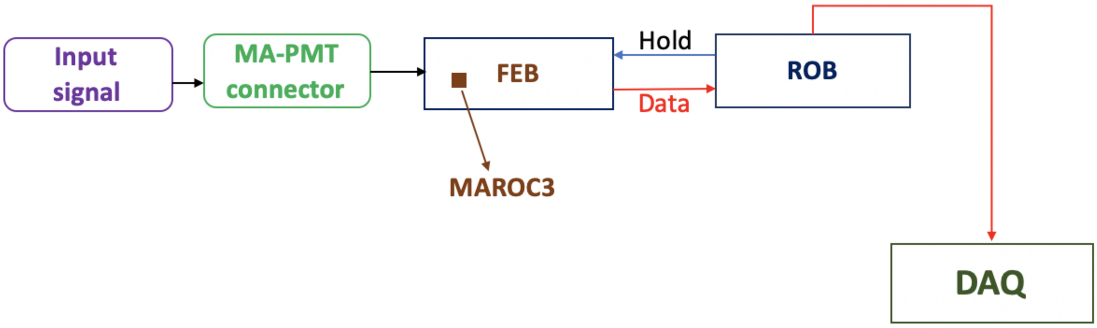

Figure 3.5: Operation of the pedestal mode. The ROB periodically sends a hold signal to the FEB. This signal reaches the FEB which reads the charge and transmits it to the ROB. The ROB will then send the data to the DAQ.

In the pedestal mode, the ROB sends a hold signal to the FEB periodically (with no correlation to PMT triggers). This signal arrives at the FEB which reads the charge and transmits it to the ROB. The ROB then sends the data to the DAQ. Fig. 3.5 illustrates the operation of the PED mode. Since this data is not taken in correlation to an input signal it corresponds to the electronics noise seen by the system in absence of any charge.

Fig. 3.6 shows the pedestal distribution for one channel of the C2R when the pedestal mode is selected. The standard deviation is of the order of 0.47 ADC counts which represents 0.06 p.e. (this conversion is explained in Section 3.3) for a MA-PMT gain of 10^6. The pedestal mean value is around 30 ADC counts for the 64 channels of one MA-PMT. The internal Wilkinson 8-bit MAROC3 ADC was used in this data taking.

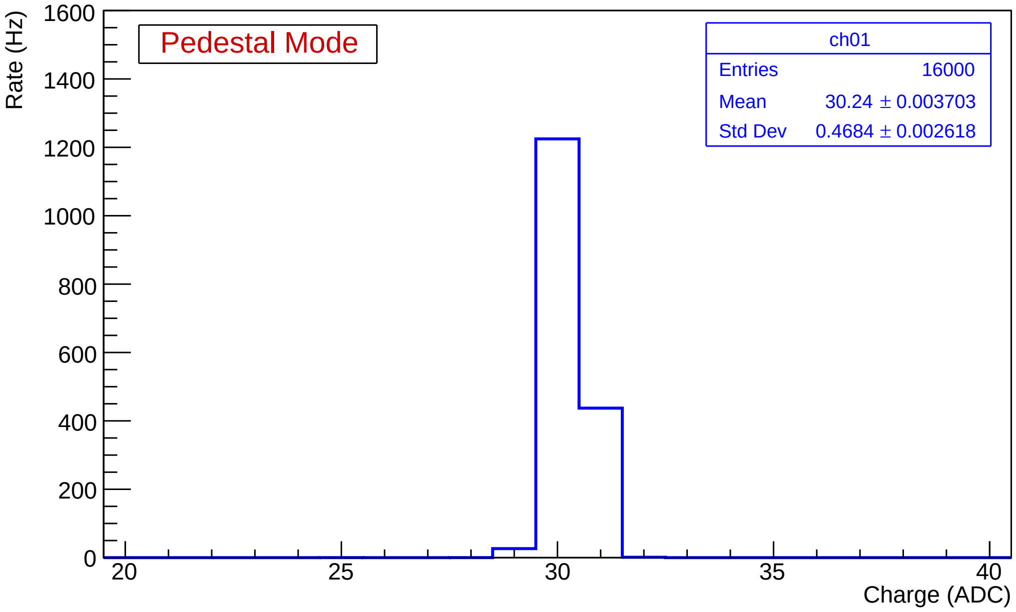

Figure 3.6: Pedestal distribution in one channel of the C2R.

The LED mode works in the same way as the pedestal mode described beforehand, however in this mode a pair of LEDs in the end-cap are flashed by the ROB with an adjustable time delay with respect to the hold signal. The ROB then sends the data directly to the DAQ. Fig. 3.7 illustrates the operation of the LED mode. The intensity of the light flash by the LED is adjusted by changing the amplitude of the pulse sent to the LED by the ROB.

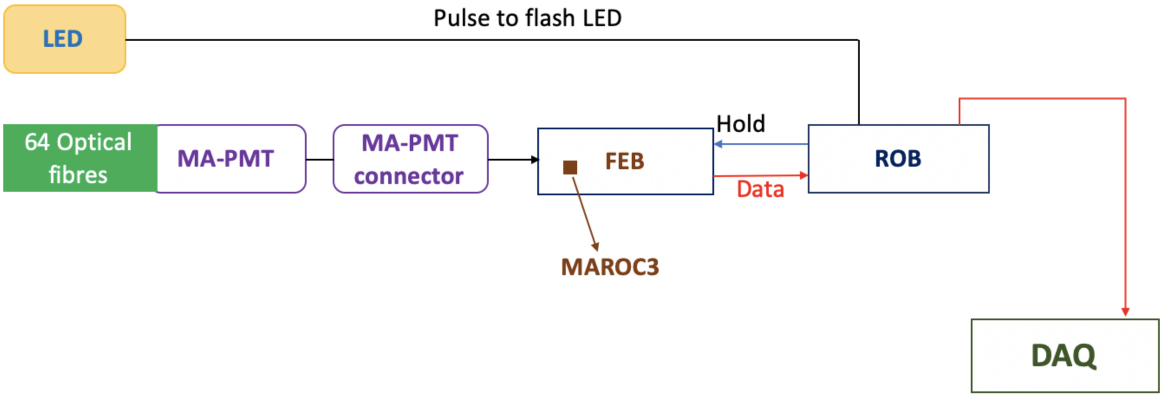

Figure 3.7: Operation of the LED mode. The LED mode behaves in the same way as the pedestal mode. In this mode, a pair of LEDs in the end-cap are flashed by the ROB (with an adjustable time delay with respect to the hold signal). The ROB then sends the data directly to the DAQ.

Fig. 3.8 illustrates the charge distribution for one channel. In this example the pedestal (Q_0) is of the order of 30.4 ADC counts with a width (σ_0) of 0.48 ADC counts, while the MA-PMT gain (Q_1) is 11.3 ADC counts with an R.M.S. (σ_1) of 0.91 ADC counts. The mean number of p.e. (μ) per trigger is 1.92. In this Fig. 3.8 it is also shown the fitted position of several number of p.e. (1 p.e. up to 5 p.e). The method developed for fitting the charge distribution is described in Section 3.3.3.

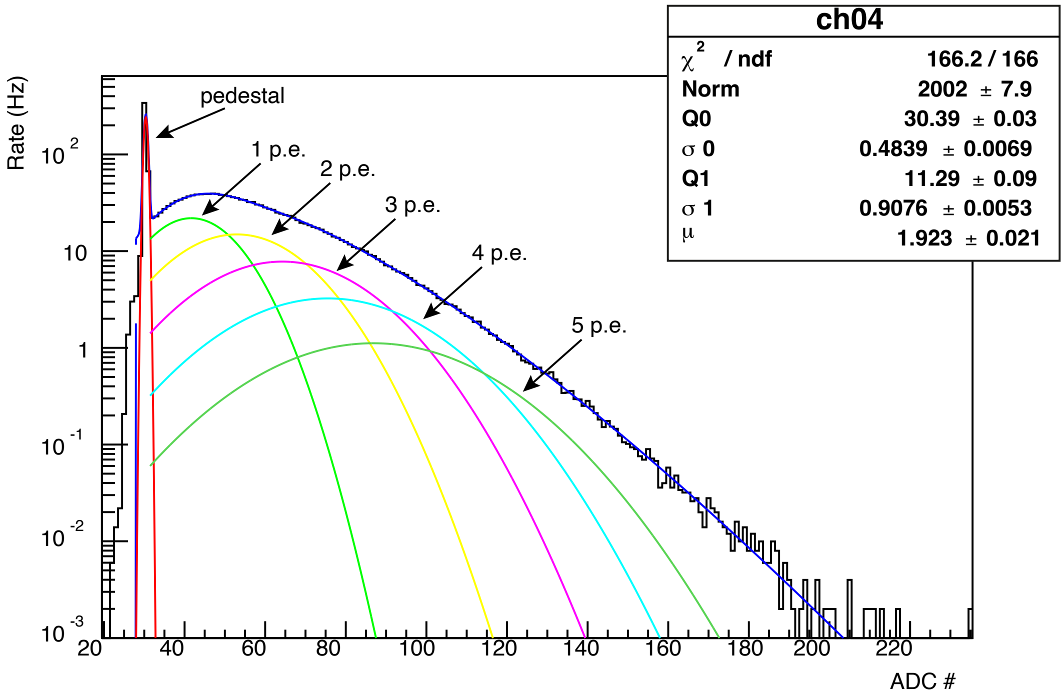

Figure 3.8: LED mode : Charge distribution using the light injection system for one channel of the C2R.

In the Normal mode an internal trigger is used. This trigger is created in the FEB and is transmitted to the ROB. In the ROB, a Hold is created and sent to the FEB, the FEB receives it and transmits after digitisation the data back to the ROB. The ROB sends the data to the DAQ. Fig 3.9 shows the operation of the Normal mode.

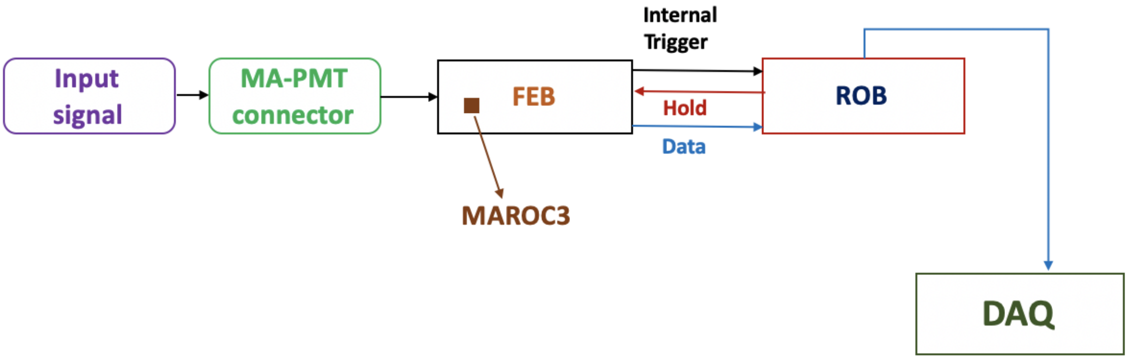

Figure 3.9: Operation of the Normal mode. In the Normal mode an internal trigger is used. This trigger is created in the FEB and is transmitted to the ROB. In the ROB, a Hold is created and sent to the FEB, the FEB receives it and transmits after digitisation the data back to the ROB. The ROB sends the data to the DAQ.

Fig. 3.10 shows the charge distribution in this mode. The pedestal is still present because all MA-PMT channels are read and not just those with a trigger. The saturation region is the regime in which the detector response is not linear anymore. In this operation mode, it is possible to measure experimentally the dead-time of the electronics (Δt_d). In particle detectors, the dead-time is the time after each event during which the system cannot record another event. The dead-time is defined as the time difference between two consecutive hits. Fig. 3.11 shows the time between two consecutive hits. The dead-time in this configuration is $\sim 10\mu$s, depending on the charge readout time of the 8-bit Wilkinson (maximum 14μs).

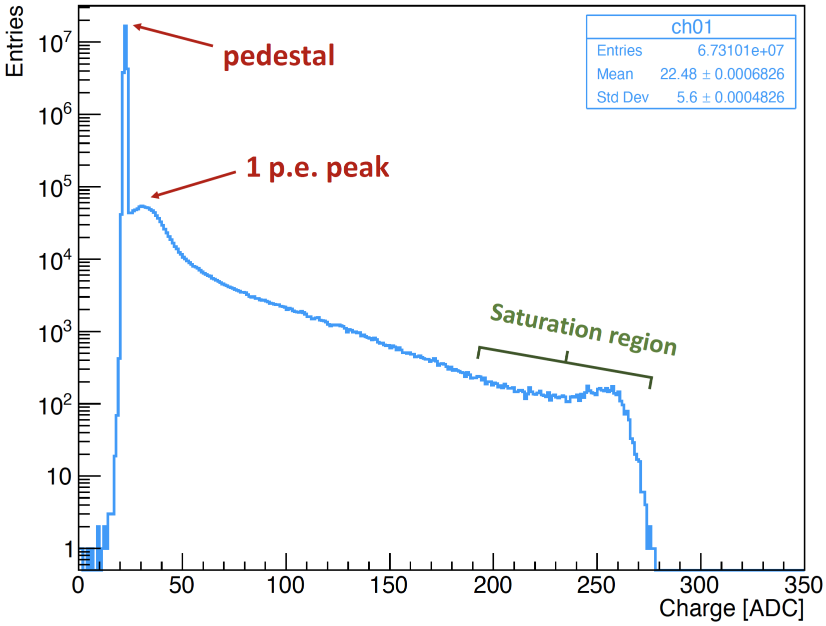

Figure 3.10: Normal mode : Charge distribution for a channel in one channel of the C2R.

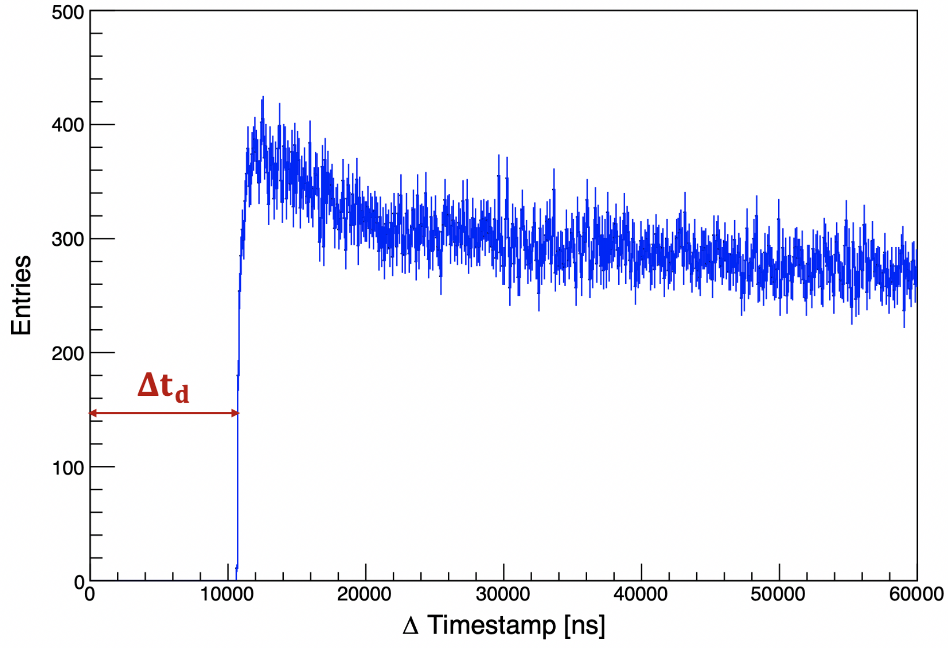

Figure 3.11: Determination of the electronics dead-time (Δt_d) of one channel in the C2R.

3.3 Charge Calibration

In order to define the running configuration of the MT, some calibration tests were required. The experimental threshold defined in the TT electronics and the conversion factor between physical charge and ADC counts were determined. A charge injection system was used for this purpose. Fig. 3.12 illustrates the setup for the charge injection system.

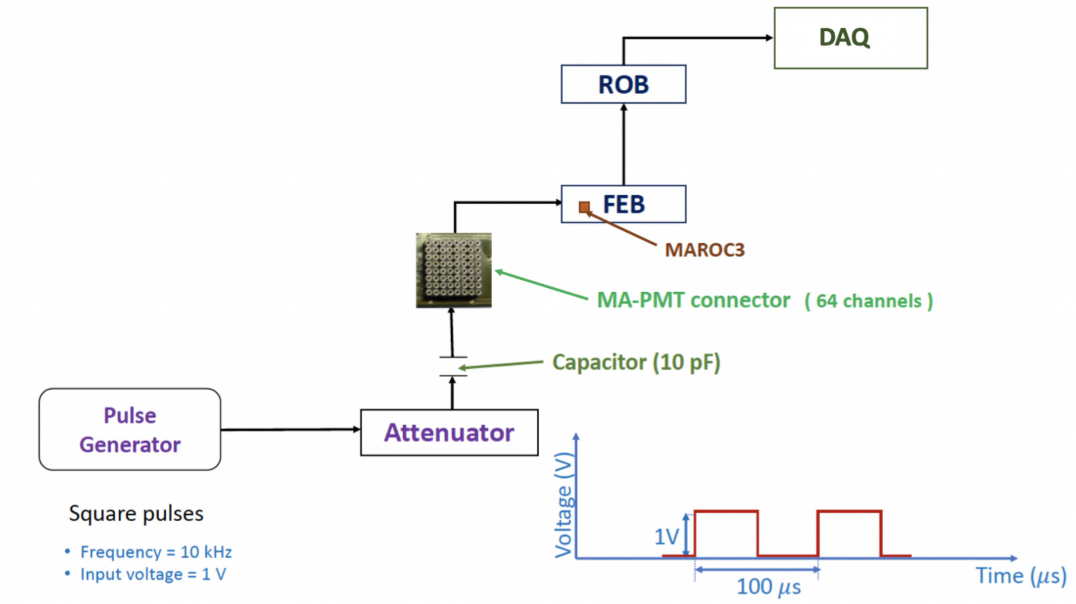

Figure 3.12: Setup of the charge injection system. Square wave pulses are sent to an attenuator. The attenuator is used to precisely control the amount of charge injected into a capacitor that is connected to a MAROC3 channel.

In this setup, the pulse generator sends square wave pulses to an attenuator. The attenuator is used to precisely control the amount of charge injected to the capacitor (10pF). The next step is to select a MAROC3 channel to inject the required charge. The charge injected Q_{inj} is expressed as a function of the attenuation A_v (in dB) :

$$Q_{inj}(\mathrm{pC}) = C * V = 10^{(\frac{-A_v}{20}+1)} \tag{3.1}$$

where the input voltage of the generator is 1V. The generator frequency used is 10kHz. For an attenuation of A_v= 46 dB , the charge injected is $\sim$ 50fC which is equivalent to $\sim 1/3$ p.e. at a MA-PMT gain of 10^6. This threshold will be applied during the experiment.

3.3.1 Threshold/Charge calibration

During the scintillation process, a muon is expected to deposit a charge of 3 to 6 p.e. on a TT strip [96]. Therefore, it is of crucial importance to reduce the background level as low as possible. This leads to adjusting the detection threshold just above the electronics noise to increase the detection efficiency to >99%. This detection threshold corresponds to 1/3 p.e.

The threshold is common to all 64 MA-PMT channels and it is set using the MAROC3 chip in the FEB. The threshold in the FEB is set using its own arbitrary units, called DAC units, and needs to be determined properly.

For the threshold determination, the charge injection system was used. One MA-PMT channel was selected, the MA-PMT gain factor was set to 64, and the attenuation was set to 46dBs corresponding to 1/3 p.e. The trigger efficiency (ε) describes the relation between the number of triggers per second (N_i) for each threshold value used and the total number of triggers N_{total}. The trigger efficiency is given by :

$$\varepsilon = \frac{N_i}{N_{total}} \tag{3.2}$$

The error on the efficiency ($\delta\varepsilon$) is calculated via propagation of errors as :

$$\delta\varepsilon = \sqrt{\frac{\varepsilon(1-\varepsilon)}{N_{total}}} \tag{3.3}$$

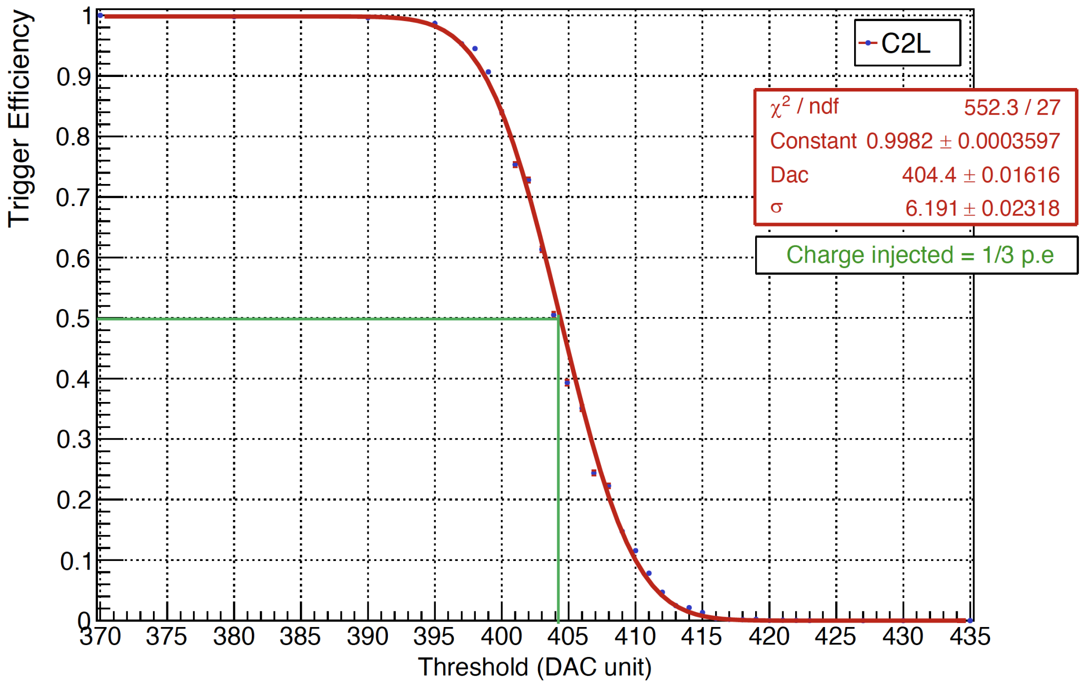

Figure 3.13: DAC threshold determination for one channel of C2L when injecting a charge corresponding to 1/3 p.e.

By definition, the threshold is set at 50% of the Trigger efficiency for a charge injected. The charge distribution expected from this charge injection follows a Gaussian distribution. Fitting to a Gaussian cumulative distribution described in Eq. 3.4.

$$S(x) = \frac{A}{2} * Erf(\frac{x-\mu}{\sigma}) \tag{3.4}$$

The amplitude (A), mean (μ) and standard deviation (σ) are measured. The mean is related to the threshold in DAC units while the standard deviation is related to the electronics noise during the measurement.

Fig. 3.13 shows the trigger efficiency versus the threshold in DAC units for one channel of C2L when injecting a charge corresponding to 1/3 p.e. In the statistics box of Fig. 3.13, the parameter Constant represents the parameter A, the parameter Dac is the mean (μ) described in Eq. 3.4. For this specific card and channel, the threshold would correspond to a DAC of 404, which is applied for all channels of this card as only one threshold can be set. The R.M.S. is 6.2 DAC units.

The threshold determination was done for one channel of each card. Injecting a charge of 1/3 p.e. Fig. 3.14 shows a dispersion of 28 DAC units ($\sim$ 20 fC) between the extremes : C0L (393 DAC units) and C0R (421 DAC units).

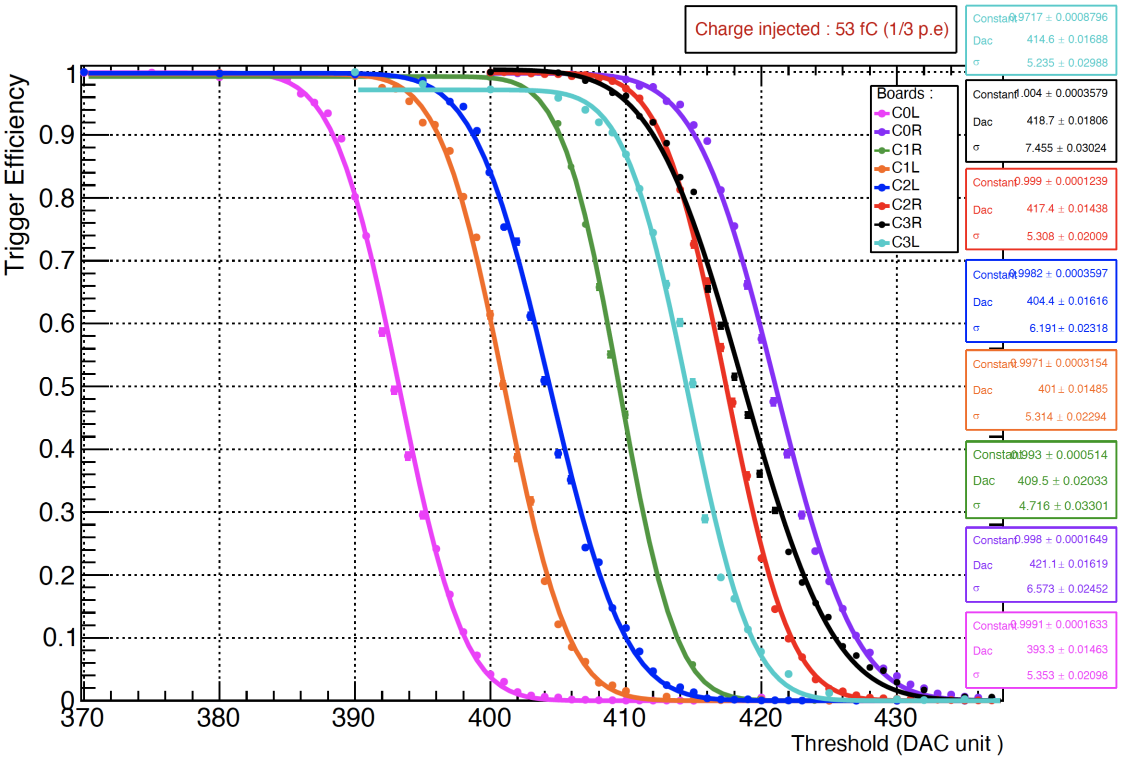

Figure 3.14: DAC/threshold determination for all 8 boards of the MT.

With the purpose of analyzing the relation between the threshold and the injected charge (i.e., number of p.e.) the threshold determination was applied for different charge injections in one channel of the C0L. The behavior of the threshold as a function of the number of p.e. injected is linear. The measurements obtained are in accordance with Eq. 3.5.

$$th = a * n_{pe} + b \tag{3.5}$$

where th is the threshold in Dac units, n_{pe} is the number of p.e. injected, the conversion factor between the threshold and the number of p.e injected could be extracted with the parameter a (slope).

Fig. 3.15 shows the value a = 251.4 DAC/p.e. i.e. to increase the threshold by 1 p.e. need to increase the threshold by 251 DAC units. To select charge higher than 1 p.e. a threshold of 540 DAC units must be applied.

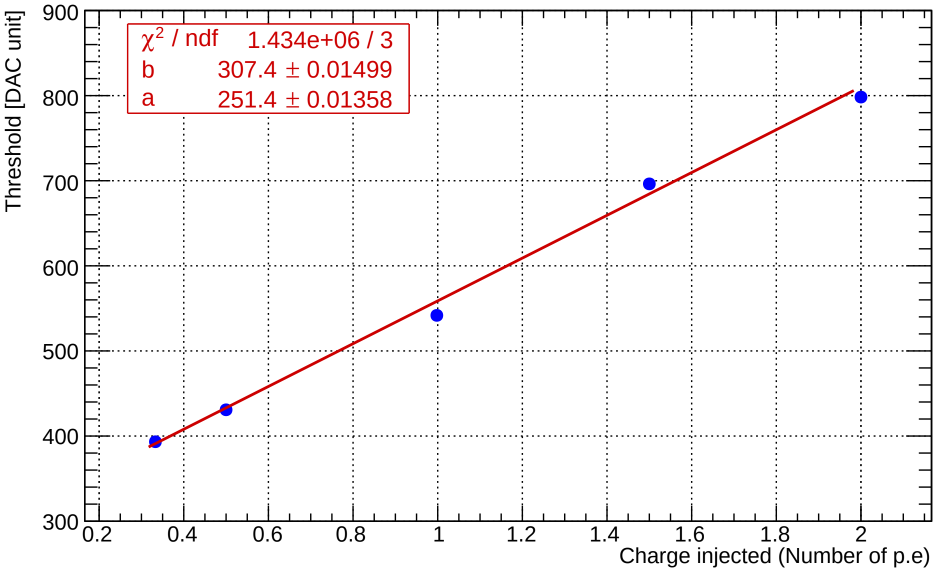

Figure 3.15: Threshold versus the number of p.e. for C0L.

3.3.2 Linearity Calibration

The interpretation of the output charge in ADC of the FEB corresponding to the MA-PMT signals and the physical charges (commonly in pC) is obtained from the conversion factor from ADC units to physical charge. This factor can be determined from the linearity calibration.

For this work, the same system of charge described in Fig. 3.12 is used. In contrast to the determination of the threshold for a specific charge, in the linearity calibration, different values of charge are injected by varying the attenuation. Thus, a wide range between 0pC and 10pC is reached. The linearity calibration test was done for one channel in one card of the MT. The charge measured in ADC counts is a function of the charge injected in pC.

Fig. 3.16 shows the distribution fitted using a polynome of 3 degrees, where the value of p_0 is the pedestal, the conversion factor (ADC/pC) is given by p_1 and p_2, p_3 describe a possible saturation. In MT, it is expected that physical charges originating from 1 p.e (0.16pC) or up to 10 p.e (1.6pC) will be recorded as discussed in Section 2.5.1.

As it can be seen in Fig. 3.16, in this range the detector response is still in linear regime. The electronics saturation (regime in which the detector response is not anymore linear) is experienced with higher charges (>3 pC), as shown in the charge distribution. The conversion factor was obtained considering the linear regime.

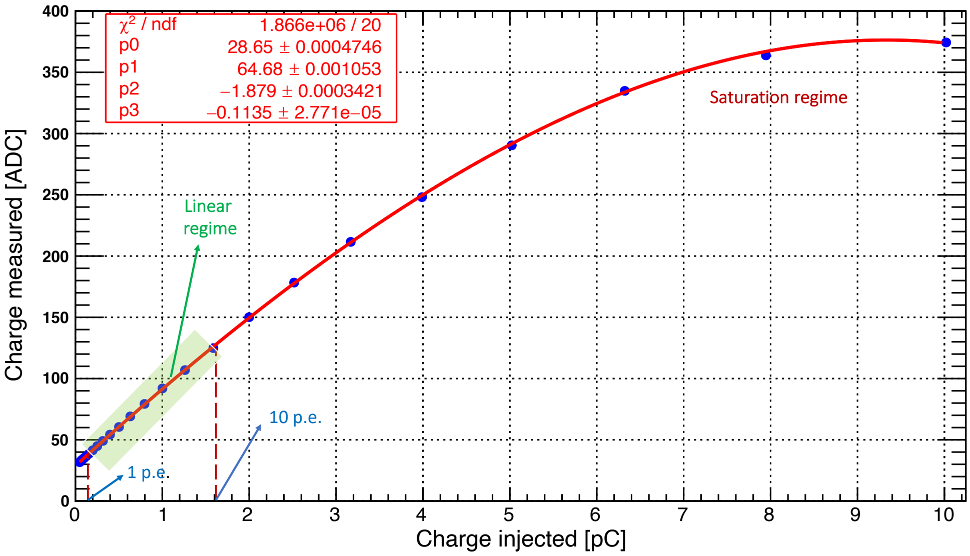

Figure 3.16: Charge injected at the entrance of MAROC3 versus the detected charge in ADC counts.

Fig. 3.17 is a zoom of Fig. 3.16 for low charge. It can be seen that the fit with a linear function depends on the parameters pedestal (p_0) and the conversion factor (p_1).

$$Q_m = p_1 * Q + p_0 \tag{3.6}$$

where Q_m is the charge measured in ADC counts, Q is the charge injected in pC, the pedestal is $p_0 = 28.81$ ADC counts and the conversion factor is $p_1 = 63.51$ ADC counts/pC.

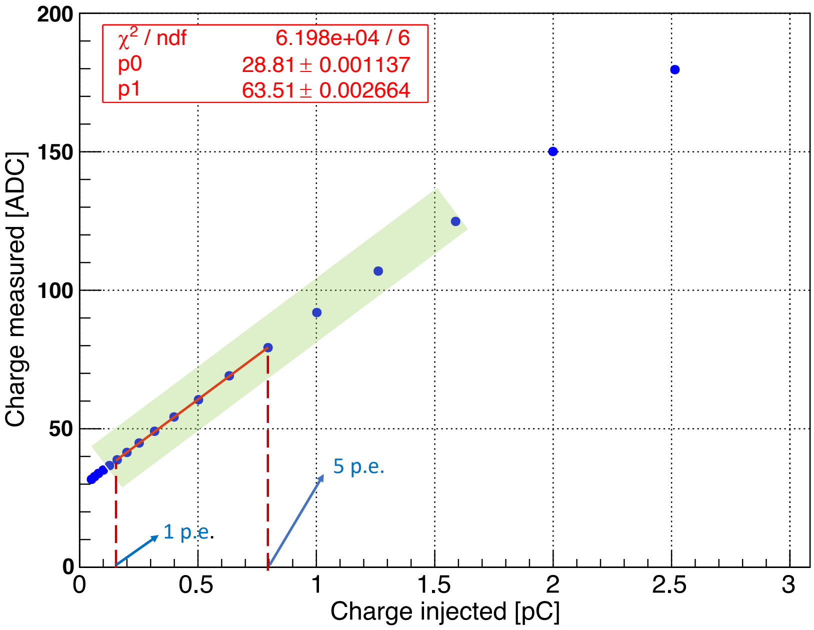

Figure 3.17: Fitting small charge of the linearity test for the C3L.

A relevant parameter to characterise the system is the MA-PMT gain (Q_1), which is the number of ADC counts for 1 p.e (0.16pC). The MA-PMT gain is given by :

$$Q_1 = p_1 * 0.16\text{pC} \tag{3.7}$$

In Fig. 3.17, the MA-PMT gain is 10.2 ADC counts. The MA-PMT gain makes it possible to determine the number of p.e. released by the photocathode, after measurement of the total number of electrons collected at the anode. The determination of this number is an important parameter for studies of the scintillator response. JUNO expects to have a MA-PMT gain of 10^6 for all the channels in the TT. For the charge calibration of the C3L this corresponds to $\sim$ 10.2 ADC as mentioned previously.

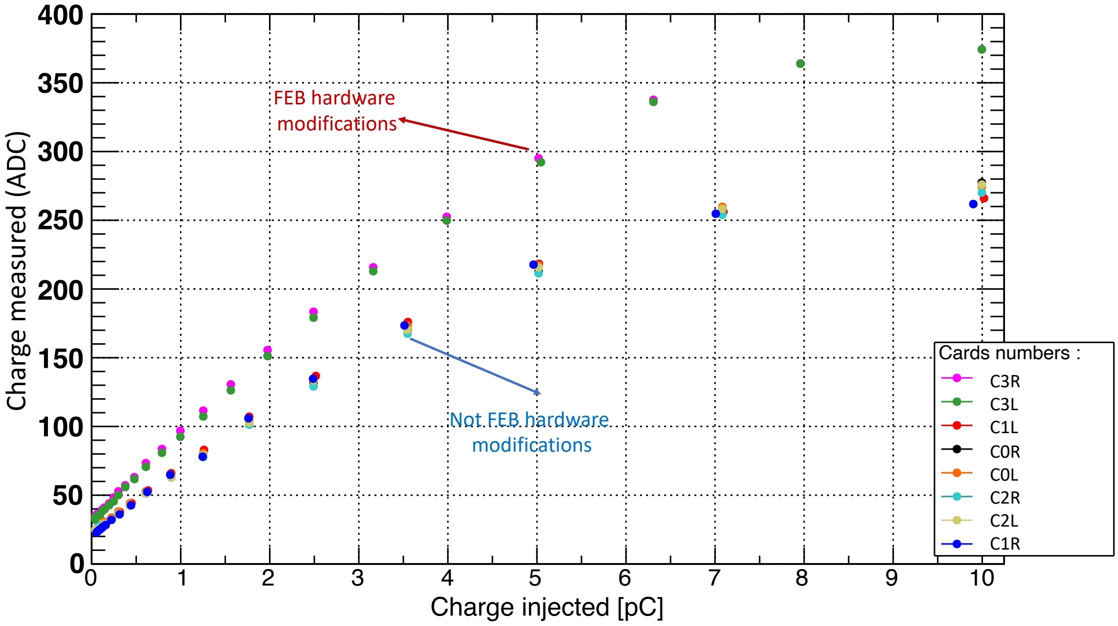

Figure 3.18: Linearity test for all the cards in the MT.

The first versions of the electronic boards developed were used to evaluate the performance of the prototype. However, when testing the final version of the FEB a problem was observed (not enough power was available for MAROC3), so some modifications were made to the FEB hardware to correct the problem. During the first electronics calibration, two of the prototype cards were fixed to test if the problem was solved (C3L, C3R), while six were not (C0L, C0R, C1L, C1R, C2L, C2R). Fig. 3.18 shows the linearity charge calibration for one channel on each board in the MT. This shows that the cards are grouped into two clusters. One group (C3L, C3R) shows higher amplification due to the modifications in the FEB . While the linearity curves of the others boards (C0L, C0R, C1L, C1R, C2L, C2R) are grouped under the first group. As expected cards with same hardware behaved similarly.

Fig. 3.19 summarises the MA-PMT gain values for all the electronic cards of the MT. The procedure is the same as described above for the C3L, we fit a linear function in the region of interest. We obtain the parameter p_1 and calculate the MA-PMT gain using Eq. 3.7. Of this analysis, two groups are presented as discussed above, the cards in the layer 3 have a MA-PMT gain around 10 - 11 ADC, while the other cards have a MA-PMT gain (7 - 8) ADC. This is corresponds to the two different slopes in Fig. 3.18 as discussed in the previous paragraph.

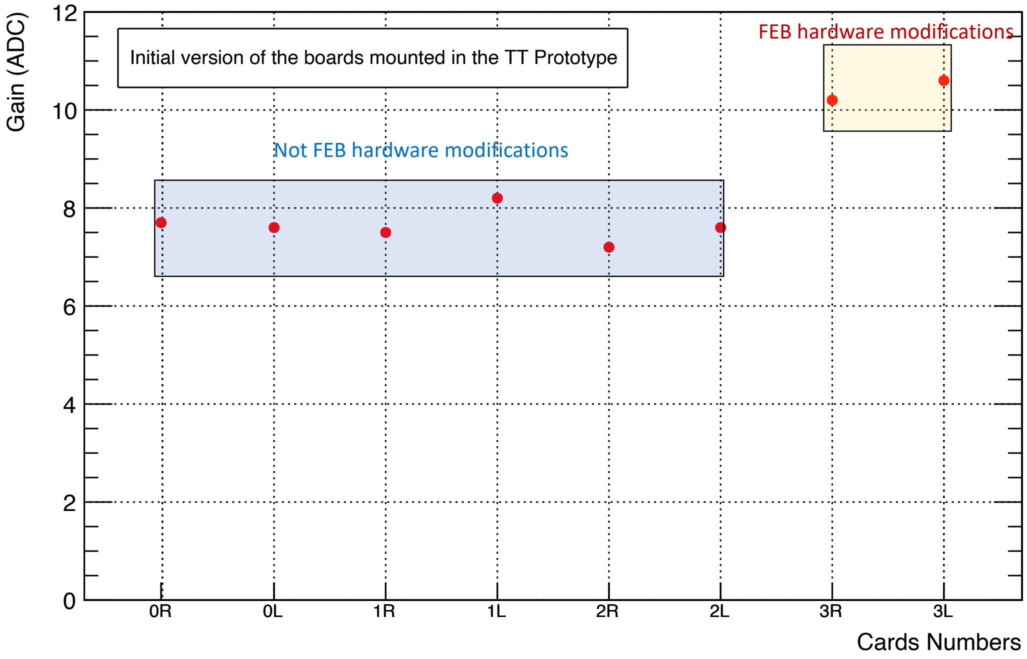

Figure 3.19: Determination of the MA-PMT gain in ADC counts for all the cards in the MT.

3.3.3 Bellamy's Method : A model of photomultiplier response.

A mathematical method for determining the gain of photomultipliers was first proposed by Bellamy et al in 1994 [105]. This model will be used to characterise the relevant parameters in the calibration of PMTs. This method treats the PMT as an instrument consisting of two independent processes: photoconversion and amplification. In the photodetector, the photon flux is converted into electrons, while the amplifier (dynode system) amplifies the initial charge emitted by the photocathode.

Photoconversion and electron collection

The flux of photons incident on the photocathode of the PMT produces p.e. through the photoelectric effect. The distribution of the number of p.e. collected by a PMT channel can be expressed by the Poisson distribution:

$$P(\mu, n) = \frac{\mu^n e^{-\mu}}{n!} \tag{3.8}$$

where n is the number of observed p.e. and μ is the mean number of p.e. collected by the first dynode. The probability for zero p.e. is given when $n = 0$ in Eq. 3.8, this probability is given by :

$$P(\mu, 0) = \frac{N_0}{N_{tot}} = e^{-\mu} \tag{3.9}$$

where N_0 is the number of entries in the pedestal peak, N_{tot} is the total number of entries in the output PMT signal. Using Eq. 3.9, the mean number of p.e. is expressed as :

$$\mu = -\ln\left(\frac{N_0}{N_{tot}}\right) \tag{3.10}$$

Amplification

The amplification for the dynode system is characterised by approximately a Gaussian distribution. The response for a single p.e. is described by :

$$\mathtt{G}_1(Q_1, \sigma_1, x) = \frac{1}{\sigma_1\sqrt{2\pi}} \exp\left(-\frac{(x-Q_1)^2}{2\sigma_1^2}\right) \tag{3.11}$$

where x is the charge, Q_1 is the average charge at the PMT output when one electron is collected by the first dynode, σ_1 is the corresponding standard deviation of the charge distribution.

The convolution of n Gaussians describes the signal for n p.e. as :

$$\mathtt{G}_n(Q_1, \sigma_1, x) = \frac{1}{\sigma_1\sqrt{2\pi n}} \exp\left(-\frac{(x-nQ_1)^2}{2n\sigma_1^2}\right) \tag{3.12}$$

In the limit $n \longrightarrow 0$, the Gaussian distribution described in Eq. 3.12 becomes a delta function $\delta(x)$. This condition ensures that amplification of a null input charge results in a zero charge as output.

The response of an ideal PMT defined by the convolution of the distributions described in Eq. 3.8 and Eq. 3.12 is given by:

$$S_{ideal}(x) = P(n,\mu) \otimes \mathtt{G}_n(x) = \sum_{n=0}^{\infty} \frac{\mu^n e^{-\mu}}{n!} \frac{1}{\sigma_1\sqrt{2\pi n}} \exp\left(-\frac{(x-nQ_1)^2}{2n\sigma_1^2}\right) \tag{3.13}$$

Background processes

In a real scenario, the output charge spectrum of the PMT is affected by several background sources. These backgrounds generate an additional charge which modifies the output of the charge spectrum. The possible background sources are: thermoelectron emission from the photocathode and/or the dynode system; leakage current in the PMT anode circuit; electron autoemission by electrodes; external and internal radioactivity, etc. The background charge distribution is described by two contributions :

- **The background type I :**

  The signal obtained when no p.e.. has been emitted from the photocathode is considered as the Pedestal. This background is produced due to the low charge processes originating from electronic noises (e.g. leakage current, etc.). This absence of an input is modelled with a Gaussian with mean Q_0 and standard deviation σ_0.

- **The background type II :** when photons are not converted on the PMT photo-cathode but converted to electrons at the first dynode, thus missing one amplification. This noise is created either by thermoemission , noise initiated by measured light, etc. This background is described by an exponential with decay α.

Both backgrounds described above are modelled by the distribution $B(x)$:

$$B(x) = \frac{(1-w)}{\sigma_0\sqrt{2\pi}}\exp\left(\frac{-x^2}{2\sigma_0^2}\right) + w\theta(x)\alpha\exp(-\alpha x) \tag{3.14}$$

where w is the probability that the background type II occurs, $\theta(x)$ is the Heaviside function, which is added to limit the exponential below the pedestal.

The realistic response function of the PMT

The realistic response is defined by the convolution between the signal (Eq. 3.13) and the background (Eq. 3.14) as :

$$S_{real}(x) = \int S_{ideal}(y)B(x-y)dy = \int (P(n,\mu)\otimes \mathrm{G}_n(y))B(x-y)dy \tag{3.15}$$

The PMT response function is approximately [105] :

$$S_{real}(x) \approx S_{real\,1}(x) + S_{real\,2}(x) \tag{3.16}$$

where :

$$S_{real\,1}(x) = \left[\frac{(1-w)}{\sigma_0\sqrt{2\pi}}\exp\left(\frac{-(x-Q_0)^2}{2\sigma_0^2}\right) + w\theta(x-Q_0)\alpha\exp(-\alpha(x-Q_0))\right]e^{-\mu} \tag{3.17}$$

$$S_{real\,2}(x) = \sum_{n=1}^{\infty}\frac{\mu^n e^{-\mu}}{n!}\frac{1}{\sigma_1\sqrt{2\pi n}}\exp\left(-\frac{(x-Q_0-Q_{sh}-nQ_1)^2}{2n\sigma_1^2}\right) \tag{3.18}$$

where $Q_{sh} = w/\alpha$ is the effective spectrum shift due to background.

The mean (Q) and the standard deviation (σ) charge of the real signal is given by :

$$Q = Q_0 + \mu Q_1 \tag{3.19}$$

$$\sigma = \sqrt{\sigma_0^2 + \mu(\sigma_1^2 + Q_1^2)} \tag{3.20}$$

Using Eq. 3.19, the MA-PMT gain (Q_1), can be expressed as function of the mean charge, the mean number of p.e. and the pedestal.

$$Q_1 = \frac{Q - Q_0}{\mu} \tag{3.21}$$

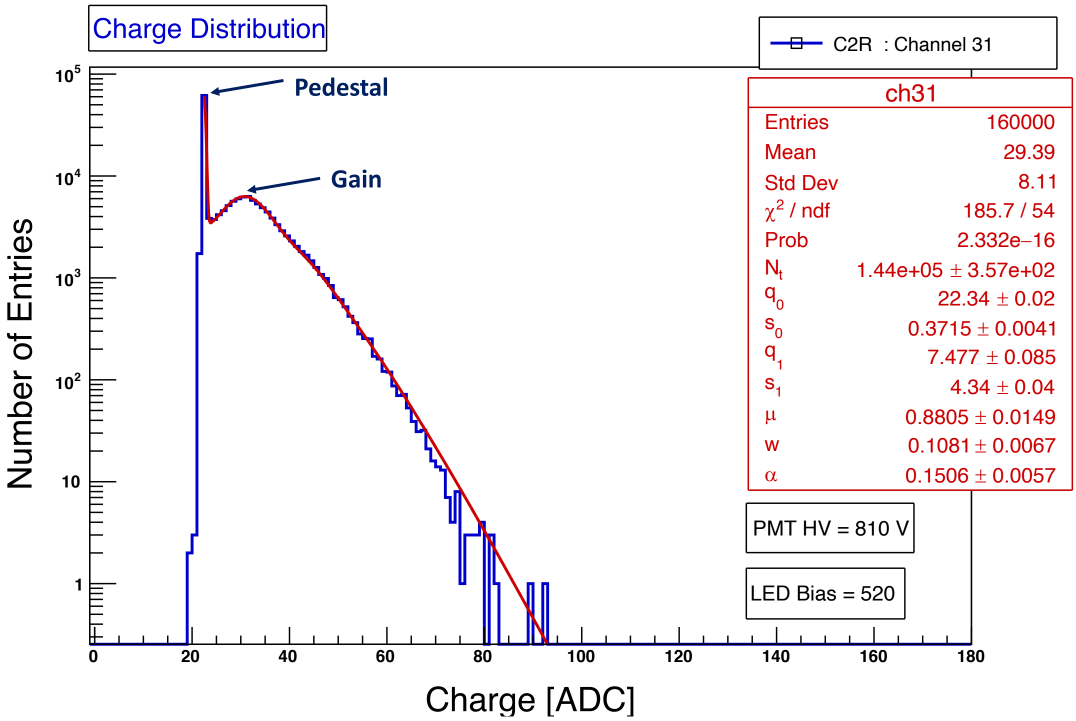

Figure 3.20: MA-PMT Charge Distribution fitted by Bellamy's Method.

In the MT, LED biases allow to control the intensity of the light emitted in the light injection system. The MA-PMT is biased by a single high voltage, common to all the channels. Fig. 3.20 shows the charge distribution obtained in one channel of C2R for a MA-PMT High voltage of 810 V and LED Bias of 520 mV. This charge distribution was fitted with the Bellamy's method. In the statistics box, the pedestal is Q_0=22.34± 0.02 ADC counts ; the MA-PMT gain is Q_1 = 7.48± 0.08 ADC counts and the mean number of p.e (μ) is 0.88± 0.01 ADC counts. This also shows that about 10.8% (parameter w) of the photons are converted on the first dynode.

3.3.4 Gain Calibration

To set the MA-PMT gain for all channels and all MA-PMT's at 10^6 the High Voltage is adjusted. As already said, there is also a gain discrepancy between the 64 channels of the same MA-PMT going up to a factor of 3, which, can be compensated using the MAROC3 amplification factors for each channel. To determine the MA-PMT gain for each MA-PMT channel the LED system has been used with the bias adjusted to detect 1-2 p.e. per channel in average. The procedure per card consists to fit the charge distribution for each channel using the Bellamy's method described in Section 3.3.3, to extract parameters such as pedestal, gain, mean number of p.e. Fig. 3.21 shows the gain per channel before the gain calibration procedure. The channel with the highest gain of the MA-PMT is used as a reference to define MAROC3 amplification factors, as will be seen in Section 3.3.6. In the C2R, the highest MA-PMT gain is found in the channel number 31 for a MA-PMT HV = 825 V and Led Bias = 520mV.

The mean number of p.e. (μ) per channel is presented in Fig. 3.22. The distribution is non uniform due to the position of the wavelength shifting fibers. The LED bias was adjusted so the mean number of p.e. in each channel was between 0.5 and 2.5 to guarantee the best results when doing this fit. Indeed, when $\mu \ll 1$ the noise dominates and when $\mu \gg 3$ the pedestal is not anymore visible. In the case when the average number of photons observed is in the 1–2 range, both the pedestal and the single p.e. peak are clearly visible.

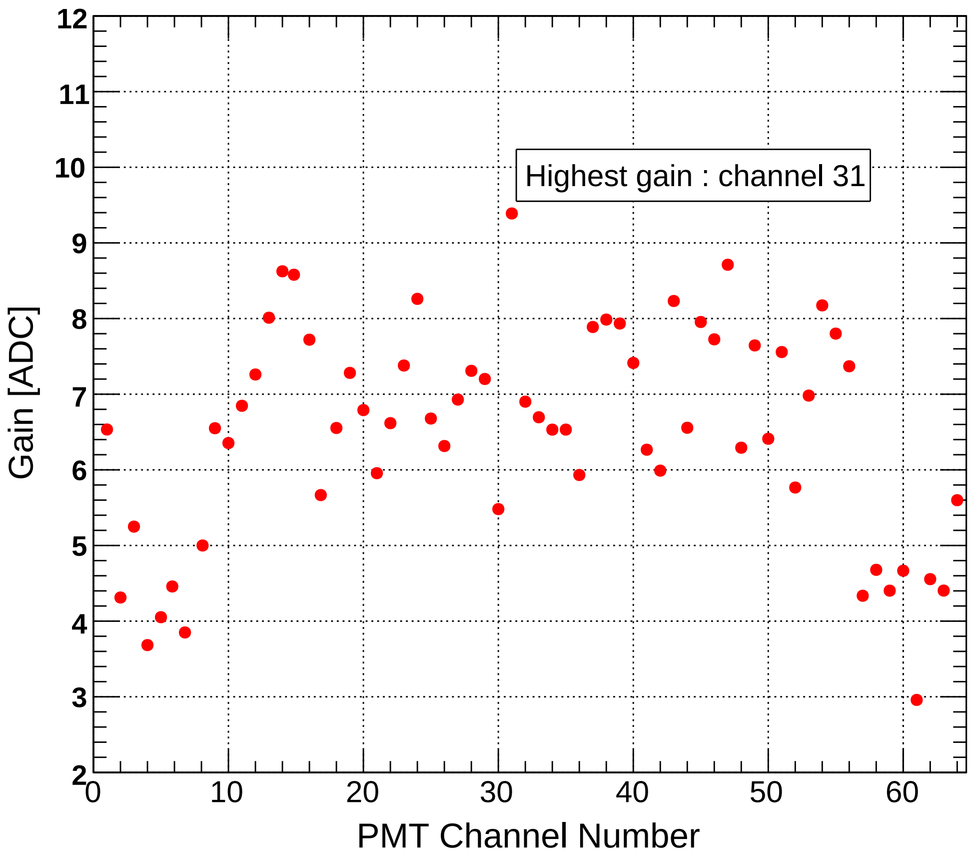

Figure 3.21: Gain versus PMT channel number, before gain equilisation for C2R.

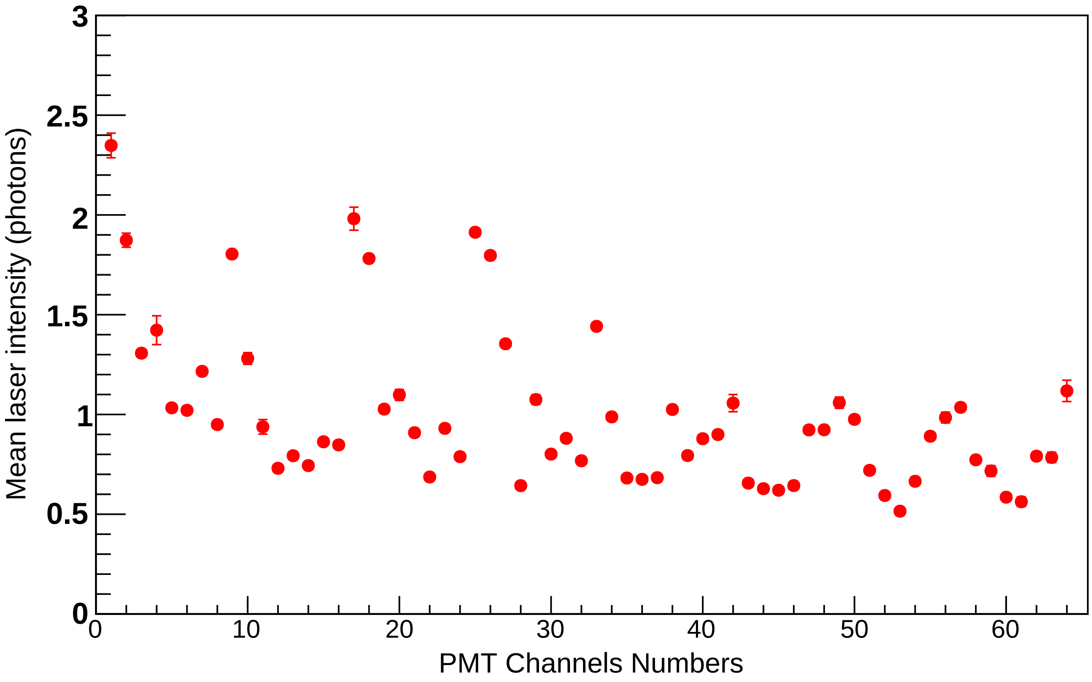

Figure 3.22: Mean number of p.e. before gain equalisation for C2R.

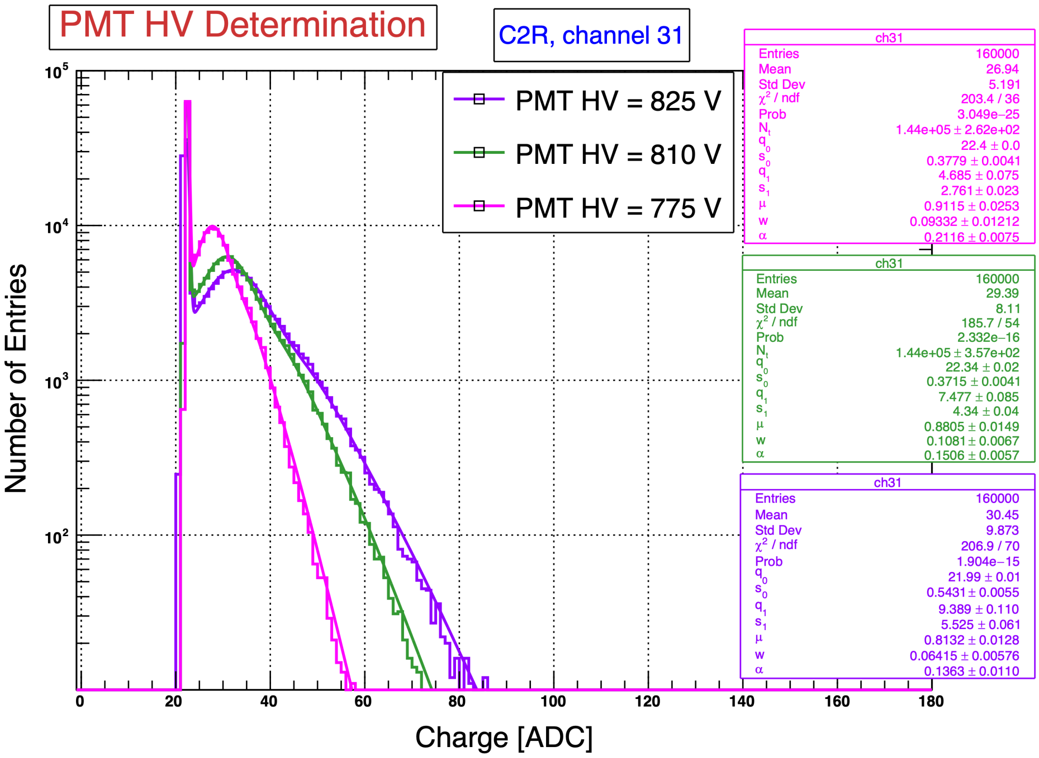

Figure 3.23: Charge distribution fitted as function of different MA-PMT High Voltage.

3.3.5 MA-PMT HV Determination

The MA-PMT operates with a single high voltage supply, common to all the 64 MA-PMT channels. The MA-PMT HV is determined using the channel with the highest gain for each MA-PMT and varying the nominal MA-PMT HV from 775 V to 825 V. The MA-PMT HV value giving a gain 10^6 (for example, 7.2 ADC counts) is selected as nominal value to operate the studied MA-PMT. Fig. 3.23 shows the charge distribution for different MA-PMT HV of the highest MA-PMT gain in the C2R.

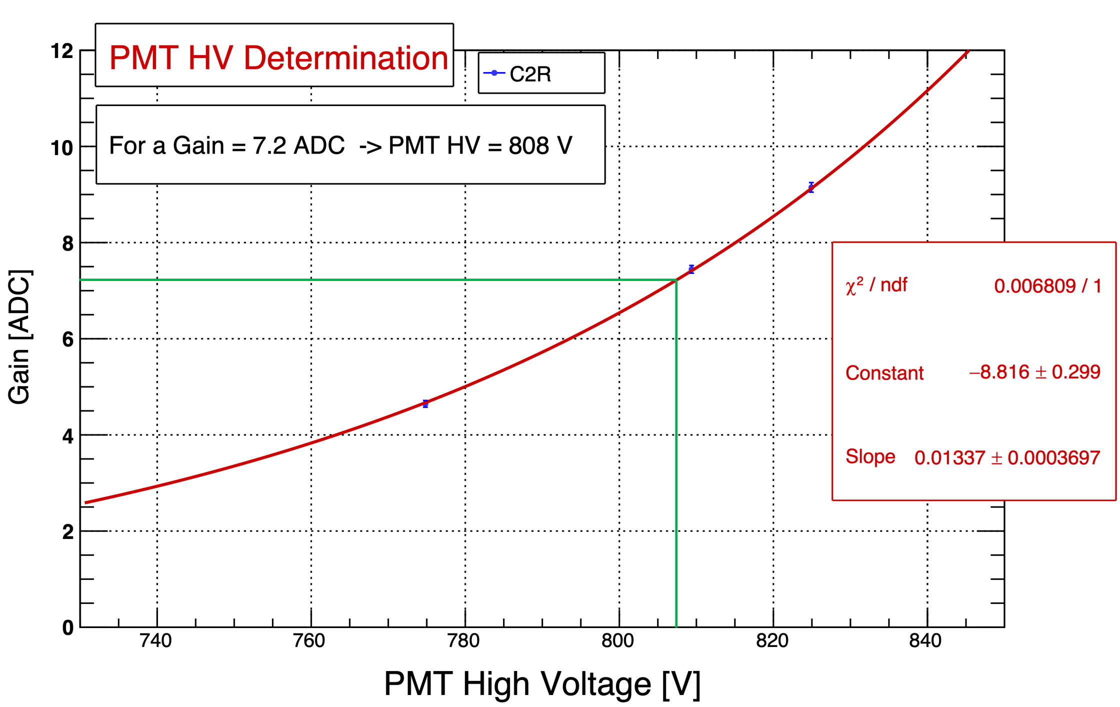

Figure 3.24: Measured MA-PMT gain on channel 31 of the C2R as a function of the MA-PMT High Voltage.

Fig. 3.24 shows the MA-PMT gain versus High Voltage of the channel 31 in C2R. The data are fitted with an exponential function. From this adjustment, we obtain the PMT HV corresponding to the expected gain of 10^6. For this card, we are looking for the value of the PMT HV when the gain is 7.2 ADC, which corresponds to PMT HV = 808 V. The MA-PMT HV for each board in the MT giving a MA-PMT gain of 10^6 is summarised in the Table. 3.1.

3.3.6 MAROC3 amplification factors

With the Bellamy's method, we extract the gain per channel ($Q_{1,i}$), determine the maximum gain channel ($Q_{1,max}$) set to a gain of 10^6 by varying the PMT High Voltage and amplify the other channels by using the MAROC3 amplification factors ($\mathrm{c_i}$) to equalize the gain for all 64 channels. The amplification factor formula is given by :

$$\mathrm{c_i} = \frac{Q_{1,max}}{Q_{1,i}} \tag{3.22}$$

Table 3.1: MA-PMT HV to obtain 10^6 MA-PMT gain and corresponding to ADC counts for each card in the MT.

Board	**MA-PMT Gain (ADC)**	**MA-PMT HV (V)**
C0L	7.6	771
C0R	7.7	824
C1L	8.2	848
C1R	7.5	808
C2L	7.6	818
C2R	7.2	808
C3L	10.2	884
C3R	10.6	808

The amplification factor of the channel with the highest MA-PMT gain is 1 by definition. To obtain the amplification factors and to equalise the MA-PMT gain for all channels, a new LED run is performed at the particular MA-PMT HV determined in the section above. In the MAROC3 the amplification factors are integer in the range (0,255). A factor of 64 corresponds to an amplification factor of 1. Thus, all values calculated in Eq. 3.22 must be multiplied by 64 and rounded off to the nearest integer.

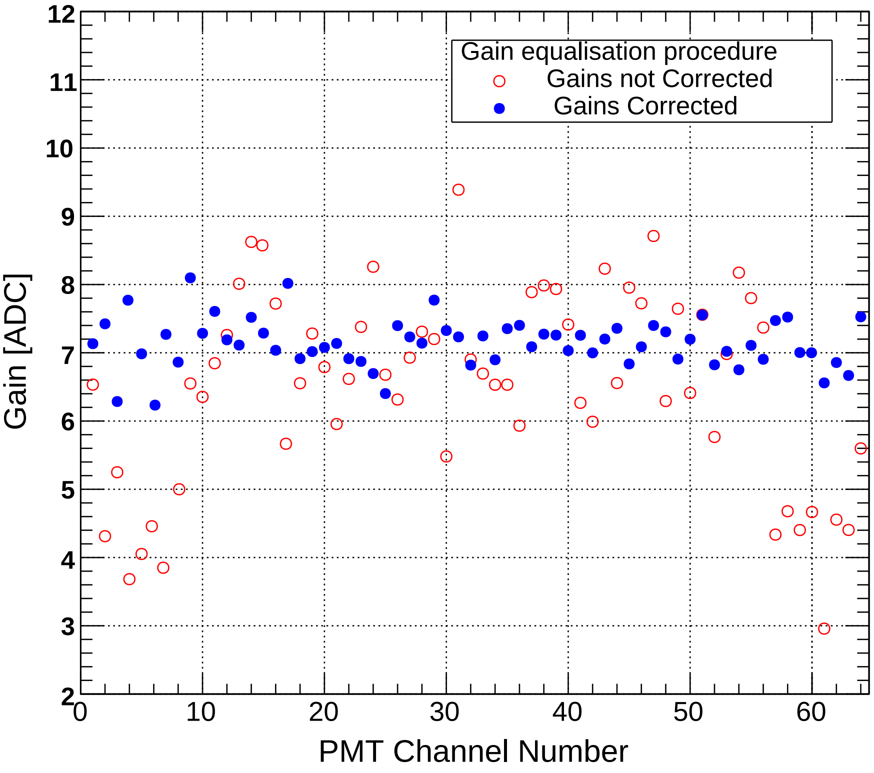

Figure 3.25: A comparison of MA-PMT gain distribution before (red) and after (blue) to insert the correction factor for C2R.

Fig. 3.25 illustrates the MA-PMT gain for each channel before and after applying these amplification factors. This figure shows a large dispersion between channels before using the amplification factors (red points). After applying these amplification factors, a relatively flat distribution (blue points) is obtained with a MA-PMT gain around a 7.2 ADC.

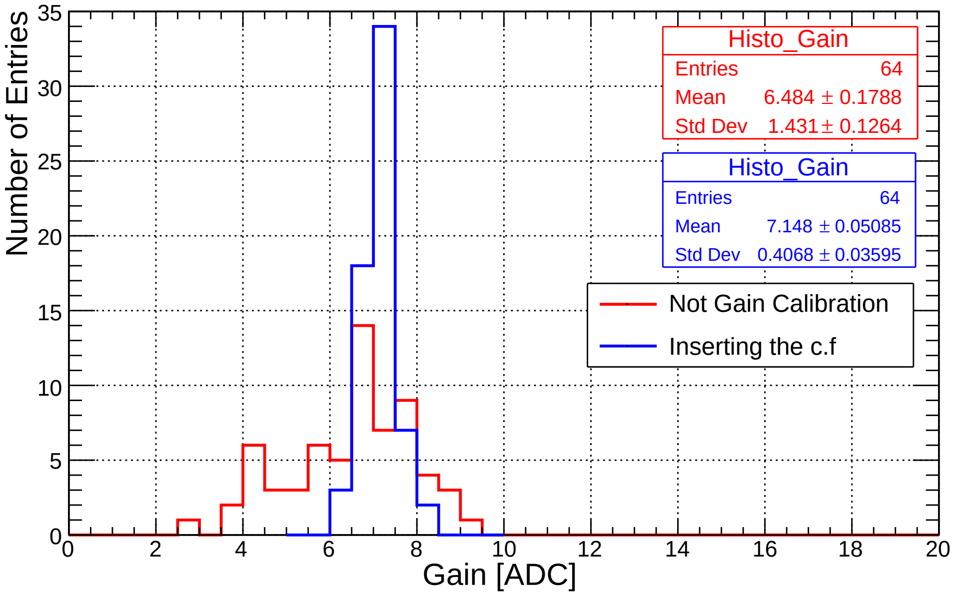

Figure 3.26: Gain distribution before and after inserting the amplification factors for the C2R.

The MA-PMT gain distributions before and after calibration are shown in Fig. 3.26. It can be seen that the distribution after the MA-PMT gain correction has a mean gain in the vicinity of 7.2 ADC as expected for the C2R.

3.4 Time Calibration

The calibration developed in the previous section was based on the charge response. However, this is not the only calibration that the Muon telescope requires. This section will describe the relevant results for the time calibration.

3.4.1 Hold delay time determination

The total input signal can be determined from its time response curve, this charge as a function of time is called the slow shaper signal of MAROC3. The amplitude of the curve is measured by finding the time position where the charge is maximum. Once the signal passes the threshold, i.e. detection is triggered, the electronics will wait for a certain time interval before the charge is sampled at the maximum amplitude. This time interval is known as the Hold delay (see Fig. 2.22).

In order to have a fast and accurate charge measurement, it is crucial that the value of the Hold delay is determined relatively accurately for the detection of triggered channels. Otherwise, the measurement will be an underestimate of the deposited charge. Therefore the Hold delay is a crucial parameter for the measure of the charge.

A Hold delay signal must be issued by the ROB to correspond to the peak time of the MAROC3 slow shaper output. Time jitters can affect this measurement as those induced by the trigger timing. The triggered channels are given by the readout register recorded by the FEB/FPGA.

The main purpose of this study is to estimate the value of the internal Hold delay that will be used in the TT in the future. At the same time, it could give the first indications of the possible parameters of the slow shaper that could be used in the TT electronics. To reconstruct the slow shaper signal of MAROC3 and to determine the Hold delay, the main part of the setup was based on the charge injection system.

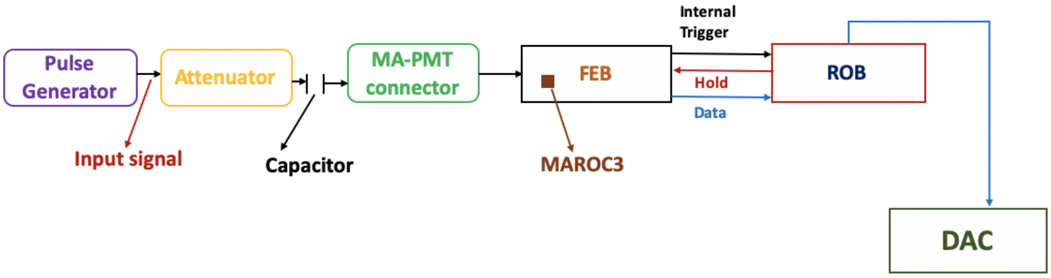

Figure 3.27: Setup used to determine the best value of the Hold delay. The input signal created by the pulse generator goes to the FEB and reaches the ROB, in the ROB a Hold is created and sent to the FEB.

Fig. 3.27 shows the setup for the internal Hold delay time. The input signal created by the pulse generator goes to the FEB and reaches the ROB, in the ROB a Hold is created and sent to the FEB. The Hold delay internal is the time in the ROB that needs to elapse before the Hold signal is sent in order to reach the maximum charge amplitude. The slow shaper curve was reconstructed by observing the output signal while varying the delay time. This time can be modified in the ROB.

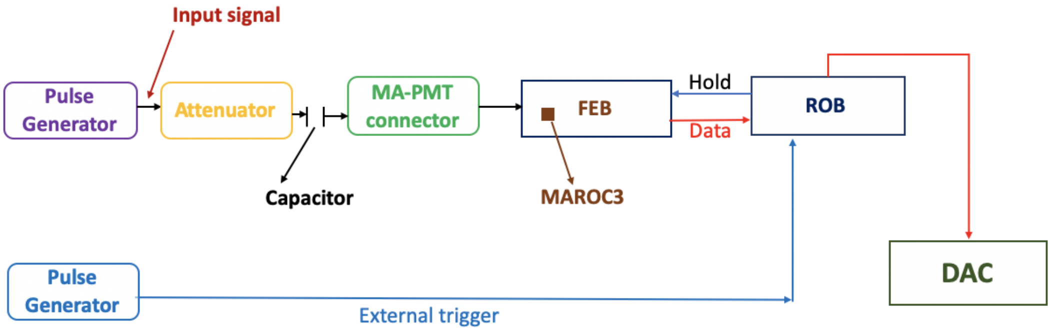

Figure 3.28: External Hold delay Setup. A generator creates an initial signal in one channel, while the other generator channel simulates an external trigger. The delay time between the trigger and the signal is known as external Hold delay.

In the case of the external Hold delay, a generator creates an initial signal in one channel, while the other generator channel simulates an external trigger. The delay time between the trigger and the signal is known as external Hold delay. The slow shaper curve was reconstructed by observing the output signal while varying the delay time between the trigger and the signal. Fig. 3.28 shows the configuration used.

Fig. 3.29 shows the charge measured as function of the external Hold delay when 1 p.e. is injected for two slow shaper settings. In the plot the magenta line represents a mesurement with a slow shaper of 0.6 pF, in this case the external Hold delay is ≈ 42ns for the charge maximum. While, for 0.3 pF shaper, the external Hold delay is ≈ 30ns. It should be noted that these curves show a large undershoot of the signal, characteristic of MAROC3.

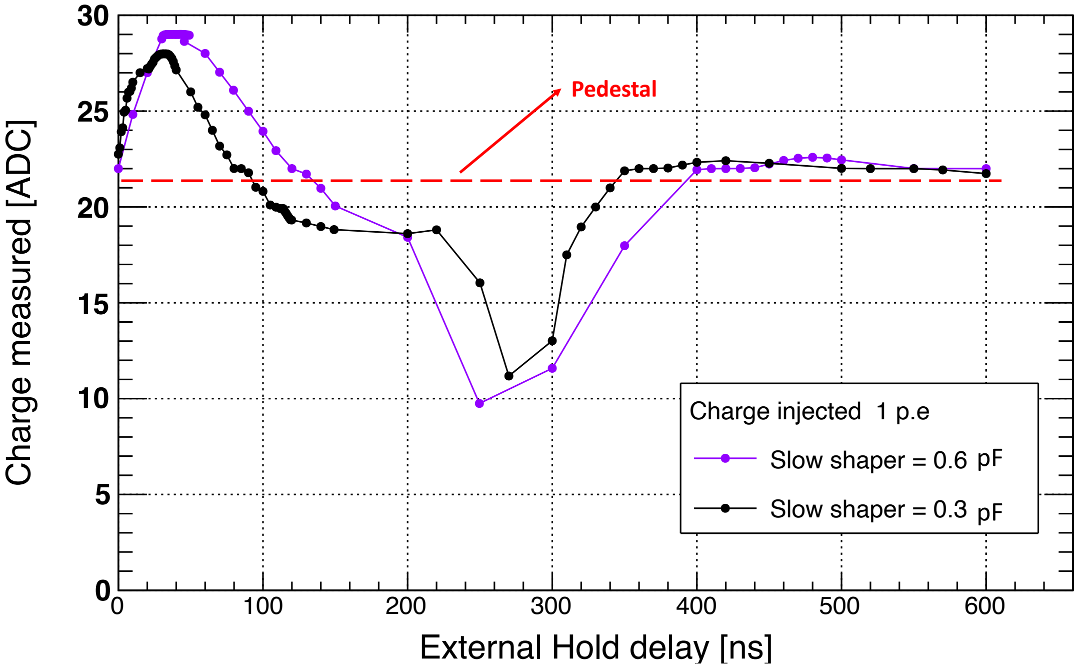

Figure 3.29: Measured charge as a function of the external Hold Delay for 1 p.e injected charge for two slow shaper settings.

In order to investigate a dependence between the charge and the hold delay value a high charge of 5pC has been injected. Fig. 3.30 shows the slow shaper curve for a charge injected of 5 pC. The red line represents a measurement for a slow shaper of 1.2pF, in this case the external Hold delay is ≈ 59ns. The magenta line represents a mesurement with a slow shaper of 0.6pF, in this case the external Hold delay is ≈ 41ns. While, the measurement for a slow shaper of 0.3pF (the black line), the external hold delay is ≈ 30ns. Fig. 3.29 and Fig. 3.30 show the dependence between the external hold delay when the injected charge increases considering the same slow shaper. Fig. 3.29 and Fig. 3.30 also show the dependece between the slow shaper and the external Hold delay. With the increase of the slow shaper, the external Hold delay time increases. However, the external Hold delay do not change for different injected charge with the same slow shaper. The slow shaper selected was 0.3pF, which corresponds to the fastest external Hold delay.

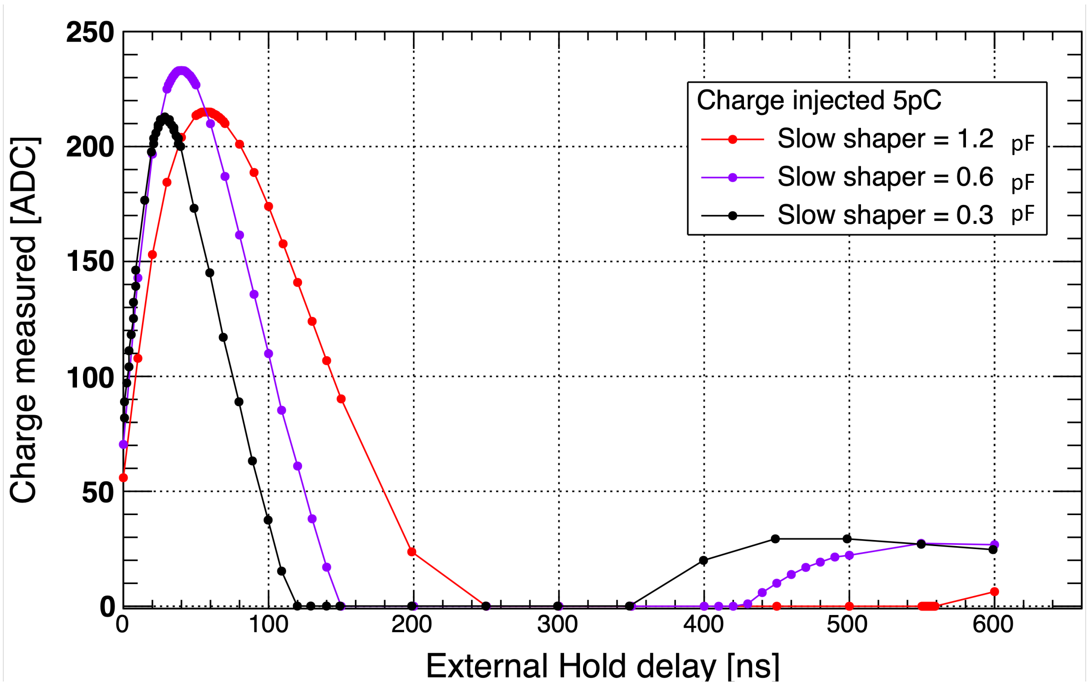

Figure 3.30: Measured charge as a function of the external Hold Delay for 5 pC injected charge for three slow shaper settings.

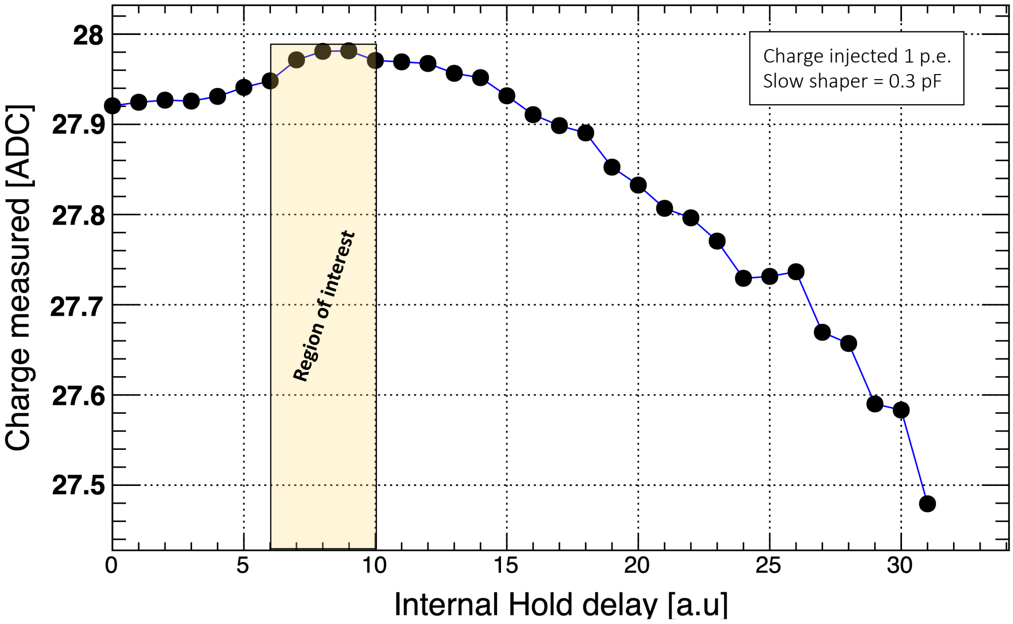

Figure 3.31: Measured charge as a function of the internal Hold Delay for 1 p.e injected charge for a slow shaper of 0.3 pF.

Fig. 3.31 shows the slow shaper curve using the internal Hold delay for a charge injected of 1 p.e and a slow shaper to 0.3 pF. The possible values of the internal Hold delay time are shown in the region of interest. The internal Hold delay time minimum required is 6 a.u and the maximum 10 a.u.

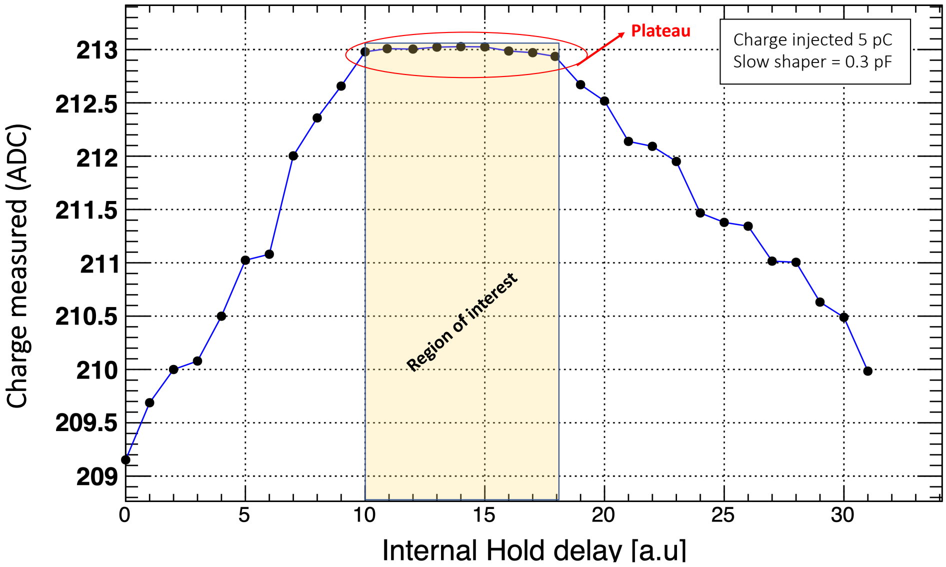

Figure 3.32: Measured charge as a function of the internal Hold Delay for 5pC injected charge for a slow shaper of 0.3pF.

Fig. 3.32 shows the measured charge as a function of the internal Hold delay for a charge injected of 5pC and a slow shaper of 0.3pF. Fig. 3.32 shows that the region of interest starts at 10 a.u. and ends at 14 a.u. In Fig. 3.31, the region of interest ends at 10 a.u. That means, there is a dependence of the injected charge and the internal Hold delay. The best compromise between low and high charges is a Hold delay of 10 a.u.

3.4.2 Time Walk determination

Time resolution and time walk are parameters associated with the response time of a detector. The time walk (t_{walk}) is due to the variation of the pulse amplitudes and the fixed threshold.

Fig. 3.33 illustrates the definition of time walk. The figure shows the charge as a function of time for two signals. The position of the threshold (red line) is also depicted. When the signal passes the threshold a time is recorded. The time walk is given by :

$$t_{walk} = t_0 - t_1 \tag{3.23}$$

where t_0 is the time when the high charge (blue line) passes the fixed threshold and for the low charge (orange line) a time (t_1) is associated. Fig. 3.34 shows the setup used for the determination of the time walk.

Fig. 3.35 shows the variation in the trigger time as a function of the injected charge, with an asymptote in 36ns (intrinsic MAROC3 delay), the time decreases for larger charges injected as expected. In a scenario with a threshold of 1/3 p.e and considering different charges, 1 p.e (160 fC) vs 2 p.e, using Eq. 3.23, we obtain from Fig. 3.35 a $t_{walk} \approx 2$ ns.

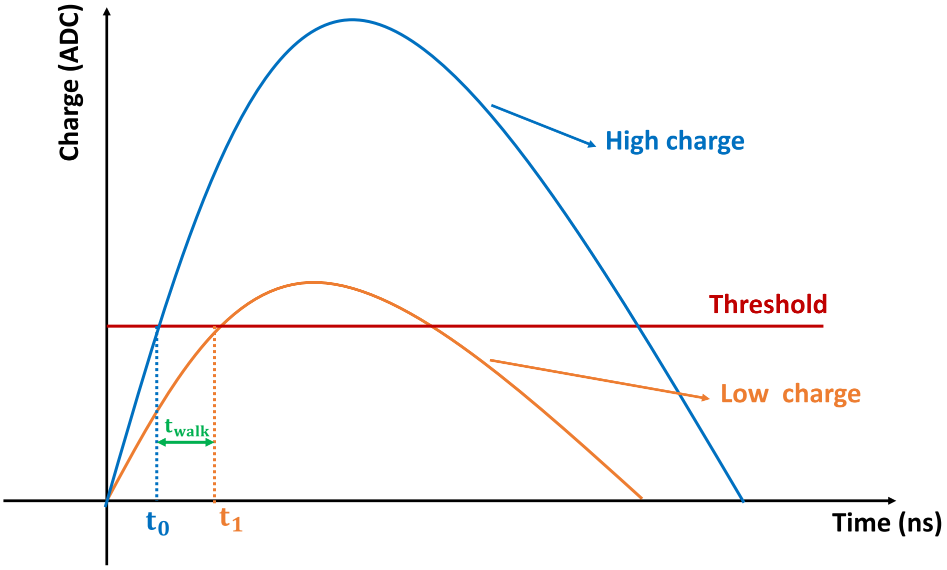

Figure 3.33: Time Walk determination. At time t_0, the high charge (blue line) will pass the threshold (red line), while at time t_1, the low charge (orange line) will pass the threshold. The time walk is defined as t_{walk} using Eq. 3.23.

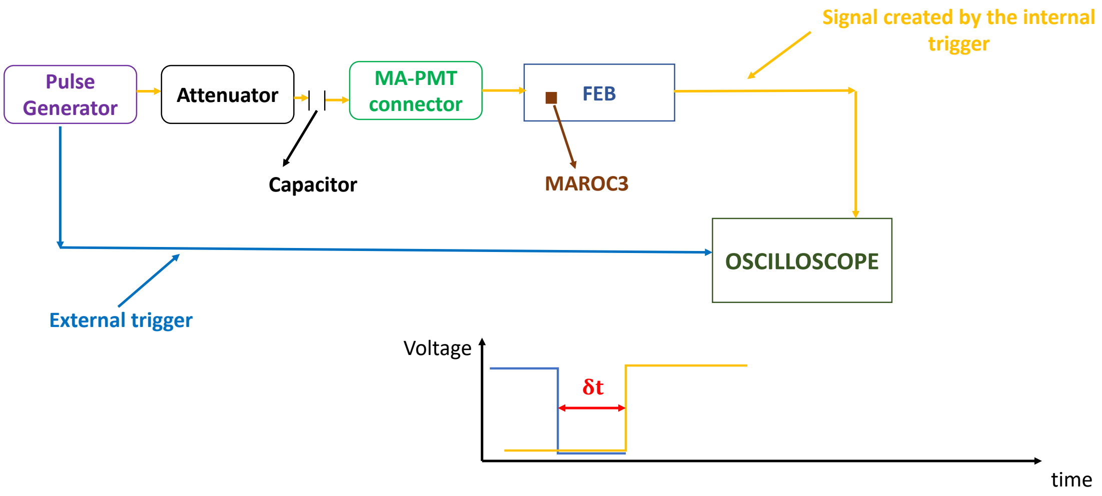

Figure 3.34: Time walk setup. An external trigger is created and recorded on an oscilloscope, in turn an internal trigger will also be displayed on the oscilloscope. At the bottom, a voltage versus time illustrates both signals, the time difference δt will originate from the time difference between the signal originated by the external trigger (blue line) and the internal trigger (orange line).

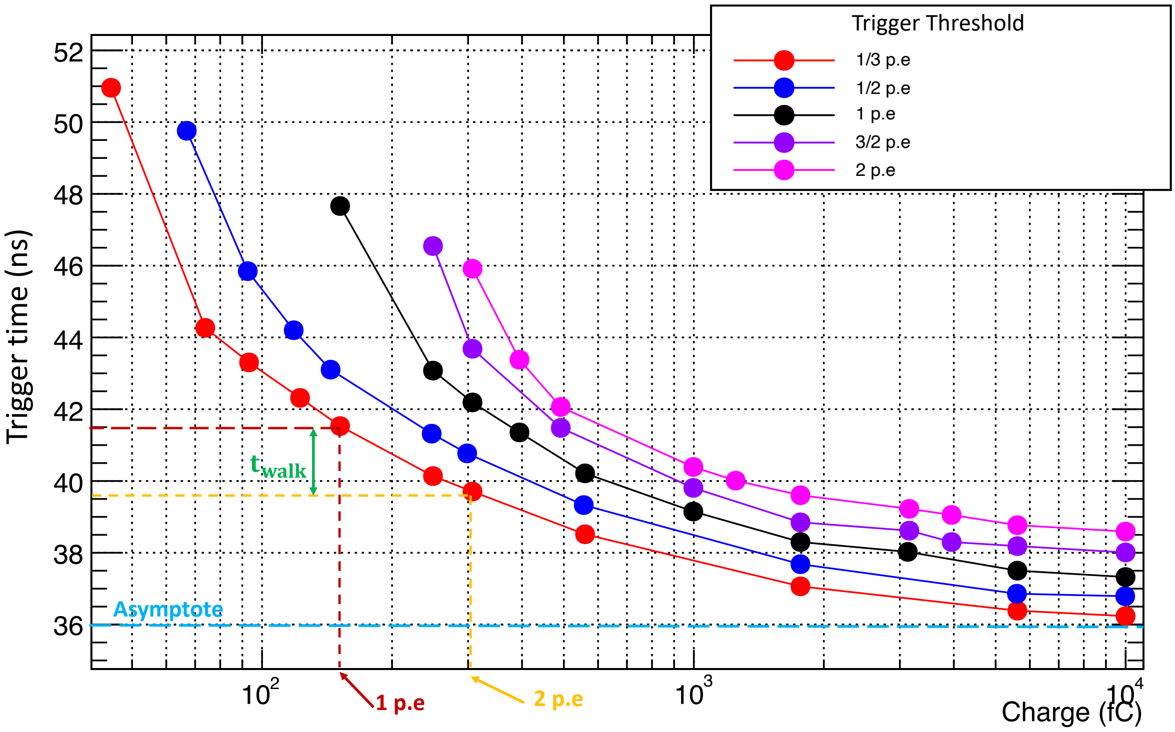

Figure 3.35: Trigger time as function of the injected charge.

3.5 FEB Test bench

The development of a test bench was necessary to test and characterise the full production of the final version of the FEB (1200 cards) to be used on Top Tracker. This test bench is automated and is equipped with a charge injection system. It is also possible to extract some calibration parameters coming from the linearity or the trigger efficiency tests, in addition to measure the pedestal and verify other functionalities of the FEB (like the ability to mask noisy channels). The setup used in the FEB test bench is shown in Fig. 3.36.

The FEB test bench software is programmed to validate different tests. In the test bench there are 64 capacitors that allow to have a charge injection system on each MA-PMT channel. Among the first tests, the HV line between the ROB/FEB is checked to ensure that HV reaches the PMT. The pedestal can also be verified, thus analyzing the electronic noise on each channel when no charge is injected. Threshold determination is calculated for zero charge injection and for 1/3 p.e. Also, using the charge injection system we can apply the linearity test on a limited set of points.

Of the 1200 FEB cards tested, 1160 have been accepted (almost 97%), which have already been sent to China for future installation on the TT. In the end, Top Tracker will use 992 of these cards, the rest will be used as spare cards. The 8 boards used in the MT have also been tested using the test bench.

Fig. 3.37 shows the results of the test bench (black line) and the measurements made on the MT (red line) for the linearity test. In the case of the test bench, 5 charge injection points are considered: (0.058 , 0.158 , 0.5 , 2 , 10) pC. These points were selected in order to optimise the calibration of the FEB to be tested.

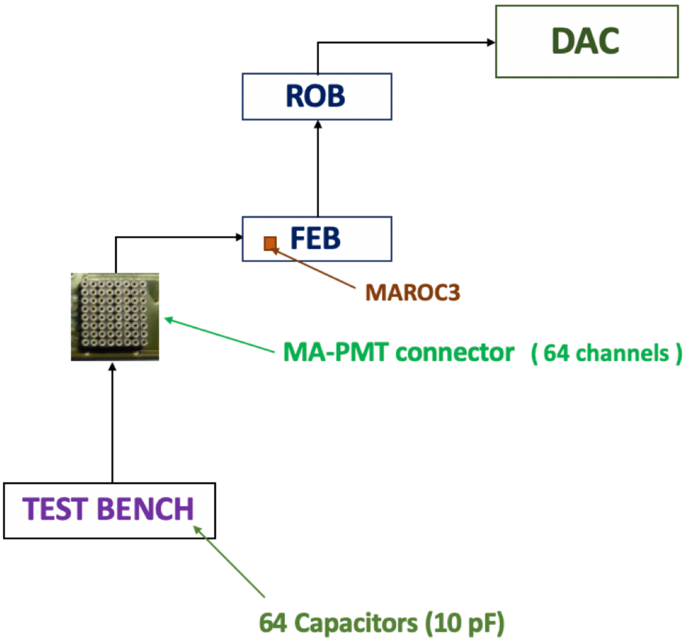

Figure 3.36: Configuration of the test bench based on an automated charge injection system with 64 capacitors.

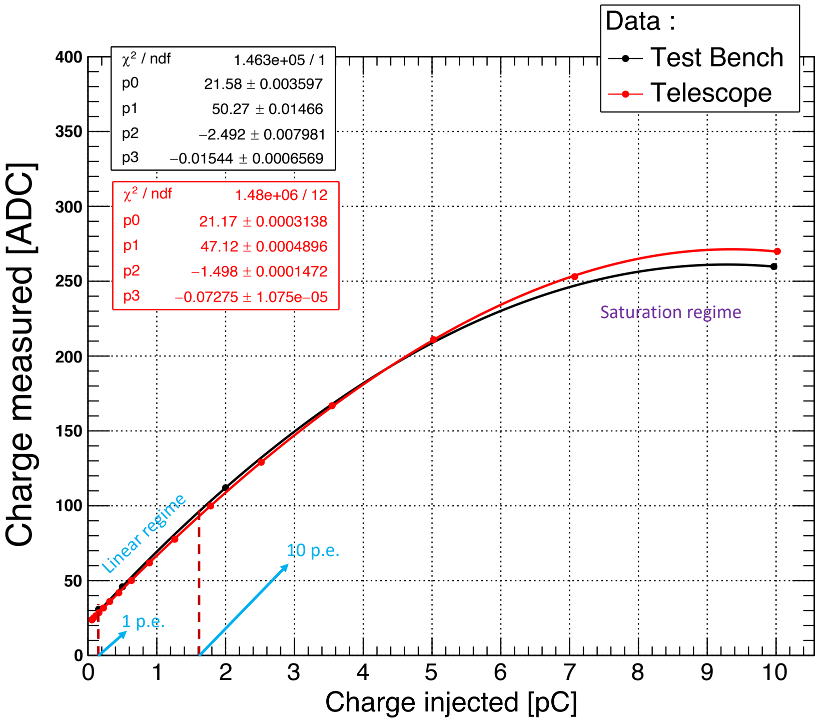

Figure 3.37: Linearity calibration for one channel of the C2R from test bench (black line) and my measurement (red line).

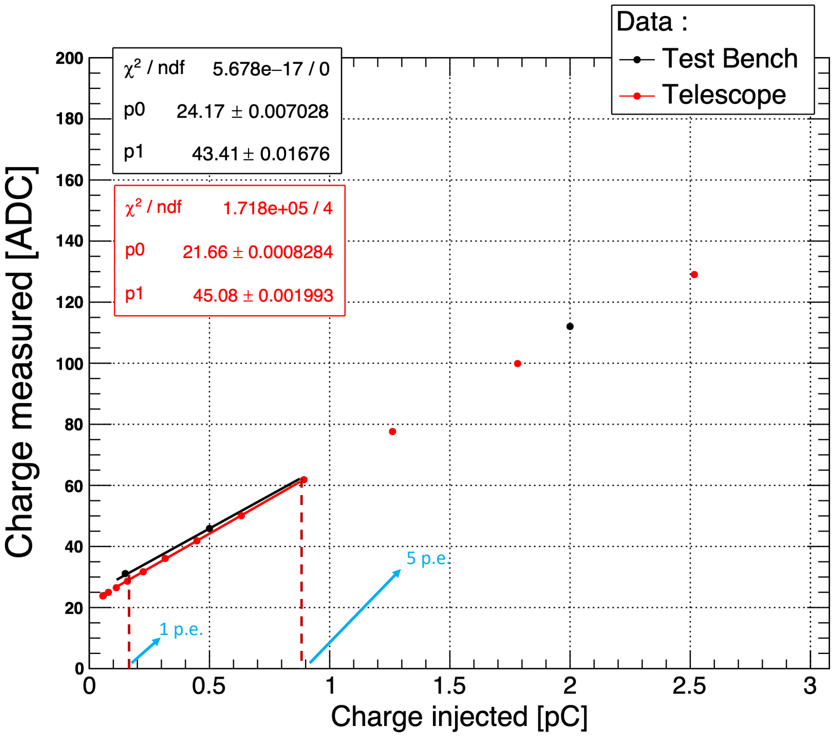

Figure 3.38: Fitting small charge of the linearity calibration for one channel of the C2R from test bench (black line) and my measurement (red line).

Fig. 3.38 shows a zoom of Fig. 3.37 in the linear regime. In the linear regime we obtain the information of values such as the pedestal (p0) and the conversion factor between the charge ADC and pC. The linearity test procedure has already been developed in the case of the MT measurements described in the previous sections. Using the same procedure, we compare both data sets to validate how to use the available information for TT.

Using the information in Fig. 3.38, the gains are calculated. The two data differ by less than 1 ADC as shown in Fig. 3.39. As mentioned in Section 3.3.2 some FEB hardware differences explain the different behavior of cards in layer 3. In the next section, we summarise the final calibration of the last version of the boards, where the previously mentioned hardware issue has been fixed for all 8 boards of the MT.

The test bench offers the possibility also to study the threshold. Fig. 3.40 represents the determination of the threshold for the 64 channels of the C3L in the test bench and my measurements in the MT. For the MT telescope (blue points), the threshold varies in the range (413 - 435) DAC units, for the the test bench data, the range of the threshold is (417 - 446) DAC units. Fig. 3.41 shows the projection of the y-axis of the Fig. 3.40. Considering the 64 channels, the mean threshold for the test bench is $\sim$ 431 DAC units and the standard deviation is $\sim$ 6 DAC units. The average threshold is $\sim$ 9 DAC units less than that recorded by the test bench, the standard deviation decreases by at least one DAC unit in comparison with that of the test bench. These differences are due to the different electronics environment (pedestal and electronic noise) and the electronic configuration.

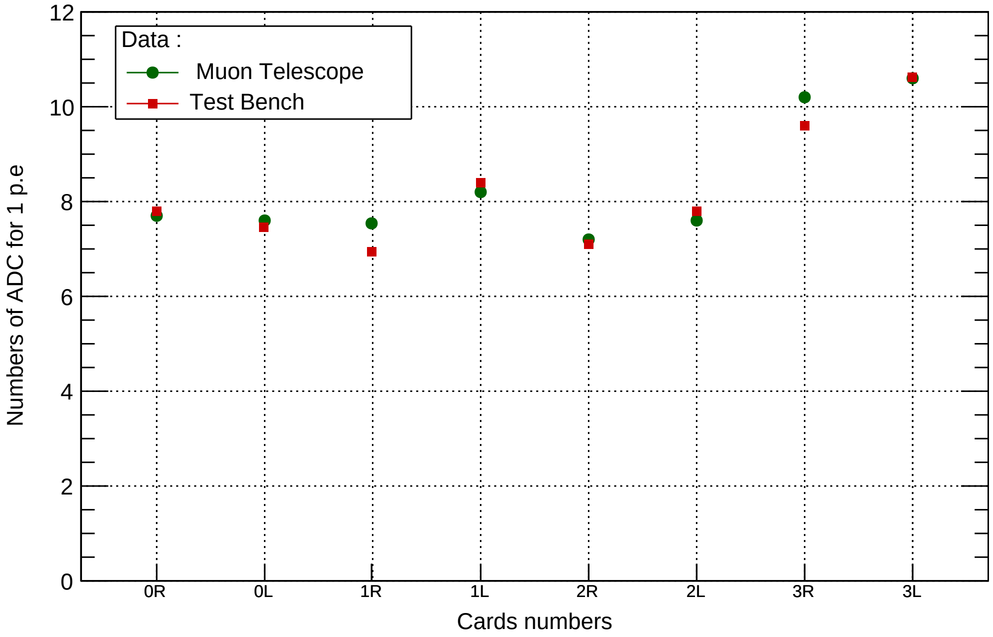

Figure 3.39: Gain for each MT card obtained from test bench (red points) and from my measurements (green points).

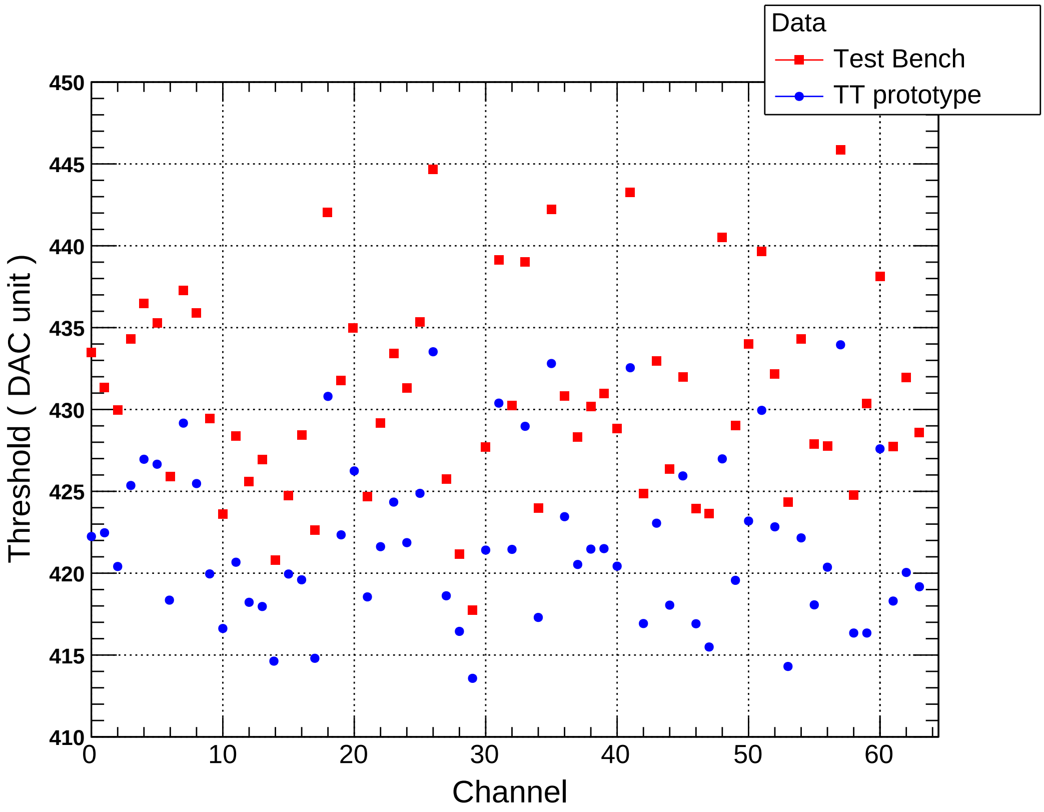

Figure 3.40: Threshold determination in DAC units corresponding to 1/3 p.e.

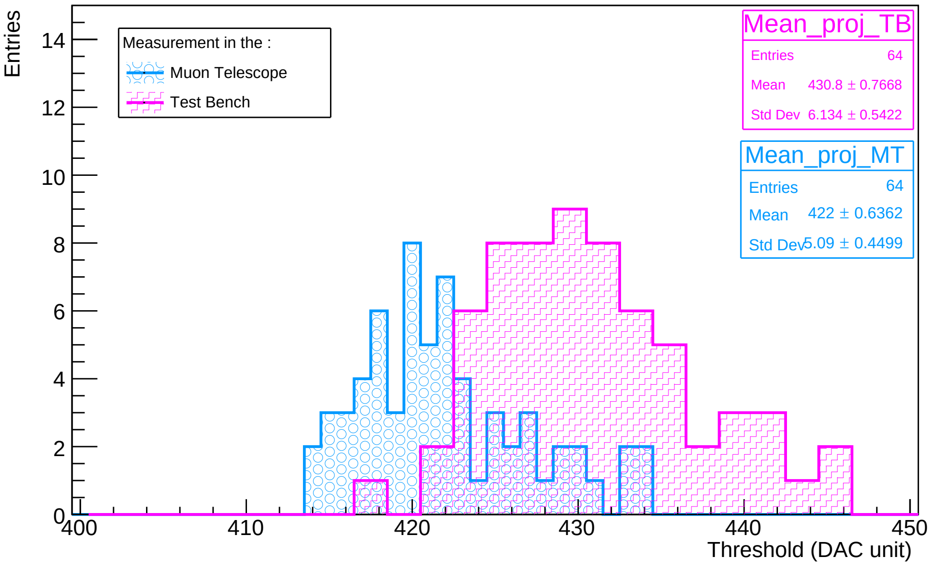

Figure 3.41: Threshold determination for 1/3 p.e injected.

3.6 Final Calibration of the MT

The initial electronic boards used in the MT were also "prototype boards". During the calibration of these boards as noted in the previous sections, some differences in distributions have arisen between C3L, C3R and the others boards. Now, all the cards have been fixed to match the ones that will be used in JUNO. Therefore, it was necessary to check which of the previous calibrations have changed. It is expected that the MT will be more uniform after these changes. We have also retested the 2 cards (C3L, C3R) that had already been fixed and check the stability of the calibration. This section will present the results obtained from the calibration of the final version of the electronics cards.

The determination of the threshold was redone for one channel of the 8 boards of the MT. A channel of the C2R was selected to inject charge of 1/3 p.e using the charge injection system, the procedure of this test was described in Section 3.3.1. In Fig. 3.42 is shown that the threshold varied by almost one DAC unit between the initial (blue line) and the final calibration (red line). The R.M.S. (σ) for the initial calibration (5.3 DAC) units decrease almost one DAC unit in the final calibration version.

Fig. 3.43 shows the threshold determination using 1/3 p.e injected charge for one channel of each card. The plot illustrates the good agreement between initial (red point) and final (blue point) calibration. From the final calibration, a dispersion of 33 a.u (21 fC) between the extremes is observed. The thresholds are uniform and stable.

The determination of the threshold as function of the injected charge was done for each card. Fig. 3.44 shows the results of a linear fit on the data. The parameter a describes the conversion factor between the threshold and the number of p.e injected. In the initial version, this test was applied just for two boards. The results of this test for C0L (see Fig. 3.15) shows the value a = 251.4 DAC/p.e. In the final version this test was extended for all 8 boards (just one channel with the highest gain) of the MT. In this case, for C0L, the value *a* for the final version is 261.5 DAC/p.e. To select charge higher than 1 p.e. a threshold of 575 DAC units must be applied.

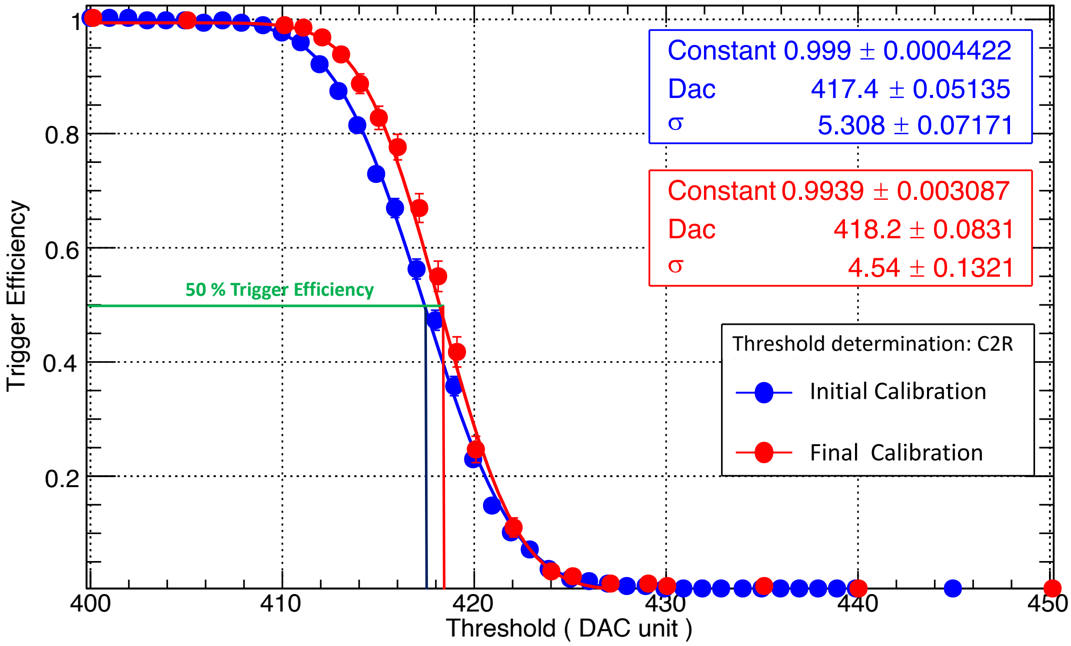

Figure 3.42: Threshold determination for 1/3 p.e injected for the C2R. Initial (blue line) and final (red line) calibrations are shown.

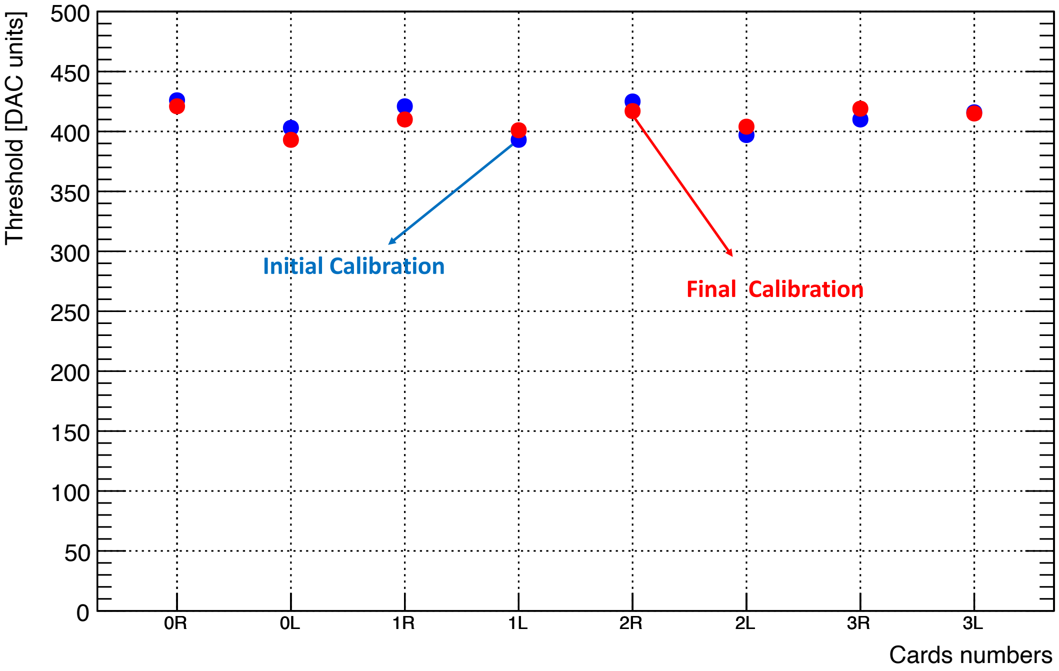

Figure 3.43: Threshold determination for 1/3 p.e injected for the 8 boards of the MT. Initial(blue line) and final(red line) calibrations are shown.

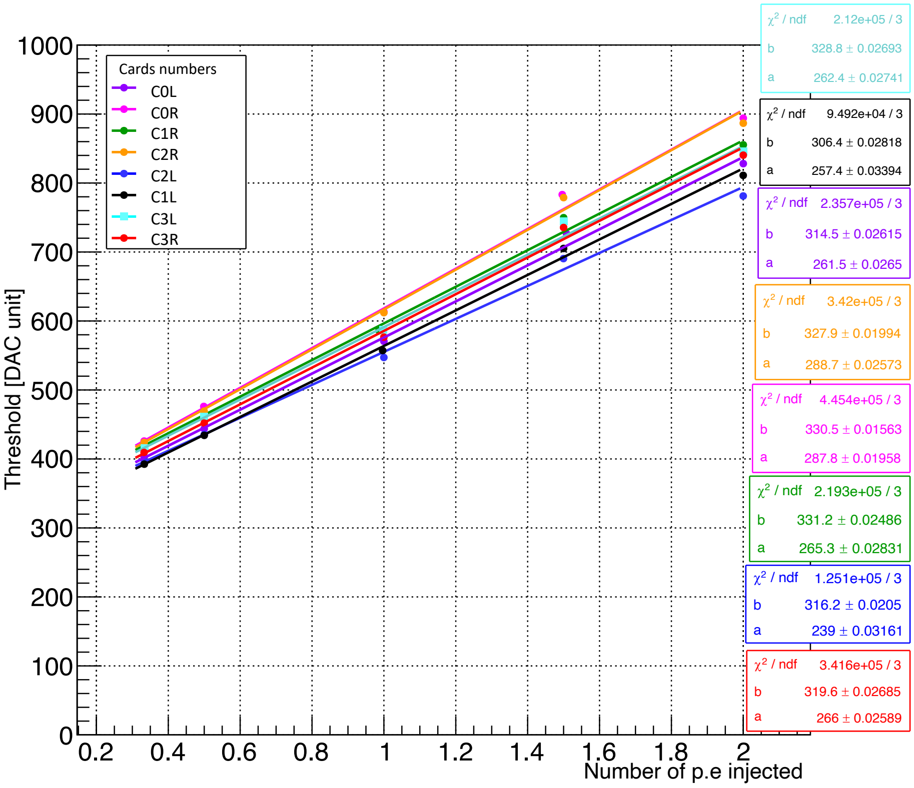

Figure 3.44: Threshold determination as function of the number of p.e injected in the final calibration for 8 boards of the MT.

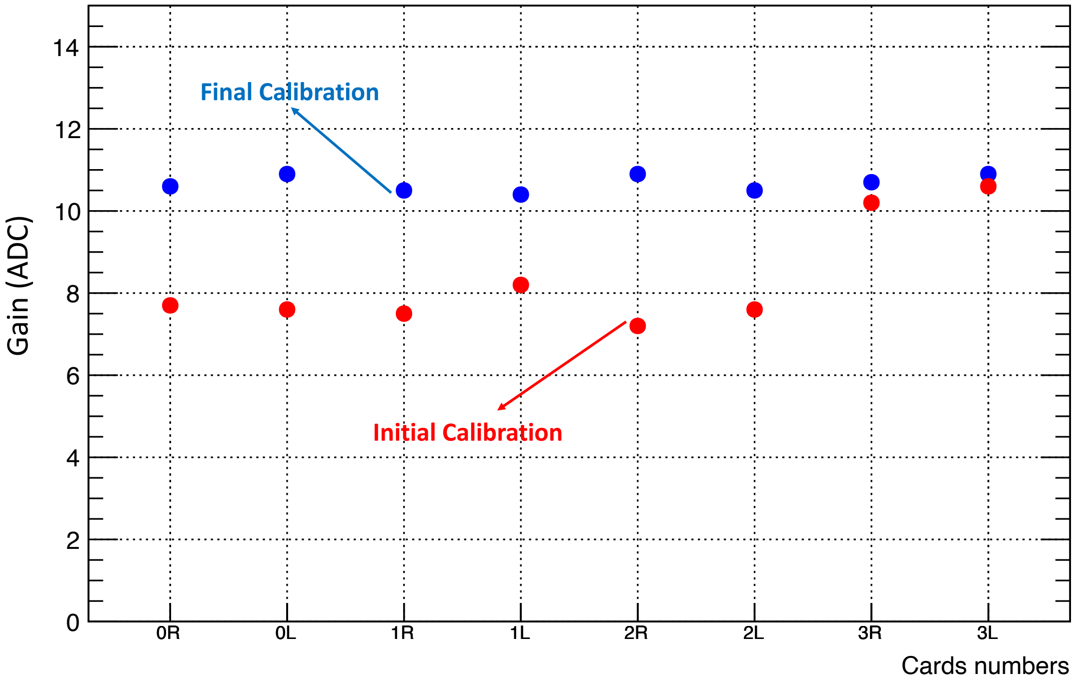

Figure 3.45: Comparison of gain measurement between initial(red line) and final(blue line) calibration for 8 boards of the MT.

The next test done was the linearity calibration. The procedure of this test was described in Section 3.3.2. Fig. 3.45 shows the gain (numbers of ADC counts/p.e.) in the linear region for one specific channel of each card, comparing the initial calibration (red points) and final calibration (blue points). As described in the initial calibration, six boards show a gain around 7.5 ADC counts/p.e, while the C3L, C3R show a higher amplification leading to a value of 10.5 ADC counts/p.e.

These changes are due to FEB hardware upgrade. After the change in hardware in six cards, we observe thier gains increased from 7.5 ADC counts/p.e. to 10.5 ADC counts/p.e., while for the two cards that were not changed the gain remained stable at 10.5 ADC counts/p.e. This demonstrates that the difference of the measured gain was due to the difference in the FEB hardware,as expected. It is also worth highlighting the stability of the measurement of the two unchanged cards (C3R, C3L).

3.7 Muon candidates

Most muons are produced high in the atmosphere, typically 15 km. Muons lose energy before reaching the ground by ionization. Muons lose energy also by severals radiative processes as : bremsstrahlung, direct production of pairs, and photonuclear interactions. At sea level, the muons are the charged particles most abundant, the integral intensity of vertical muons ≈ 1 GeV/c is $\approx 70\ \mathrm{m}^{-2}\mathrm{s}^{-1}\mathrm{sr}^{-1}$. The mean energy of muons is ≈ 4 GeV.

The technology equipped in the MT allows us to measure the muon flux arriving in Strasbourg. The main objective of this section is to describe how we will classify the most probable muon events.

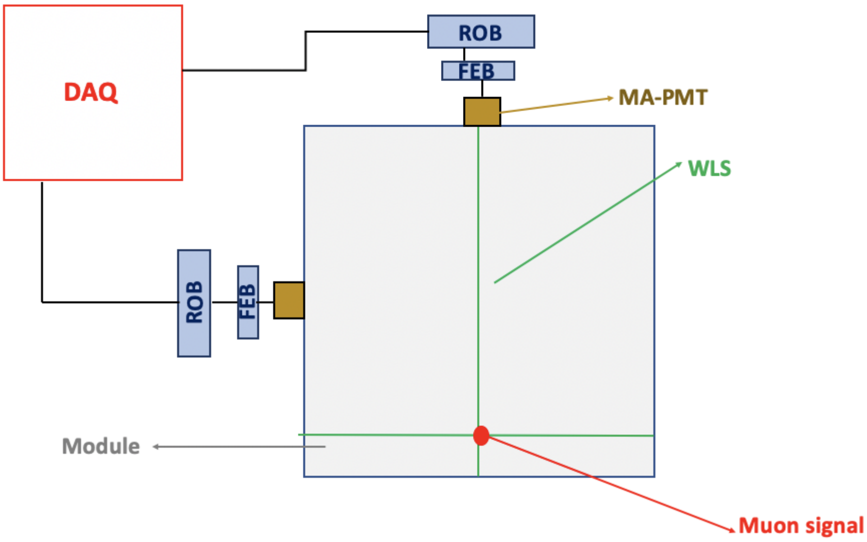

Figure 3.46: XY Coincidences projection in a layer. A signal is observed in a strip channel oriented in the Y direction (left card). This signal propagates in a wavelength shifting fiber and is read by the MA-PMT. The same procedure is identified for another signal in the X direction (right card). Each signal is identified by its charge, time and position.

In the absence of the CB in the MT, the L1 and L2 trigger strategy has been developed using the FEB/ROB information of each layer. To select the possible muon candidates, the procedure is based on an XY coincidence with a time window of 100 ns for each MT layer. Fig. 3.46 illustrates the XY projection in a layer. In this figure, a signal is placed on a strip channel oriented in the Y direction (left card). This signal propagates in a wavelength shifting fibers and is read by the MA-PMT. Each signal is identified by its charge, time and position. The same procedure is identified for another signal in the X direction (rigth card).

The time information of each hit is given by the timestamp defined by the ROB. The time distribution of coincidences on the same layer depends of the variable ΔTimeStamp. This variable is a function of the timestamp of each ROB, given by :

$$\Delta\text{TimeStamp} = \text{TimeStamp}_{\text{Right}} - \text{TimeStamp}_{\text{Left}} \tag{3.24}$$

The signal is considered as a muon candidate if $|\Delta\text{TimeStamp}| \leq \text{timewindow}$. The time window is set to 100 ns. Fig. 3.47 shows the time distribution of coincidences on the same layer.

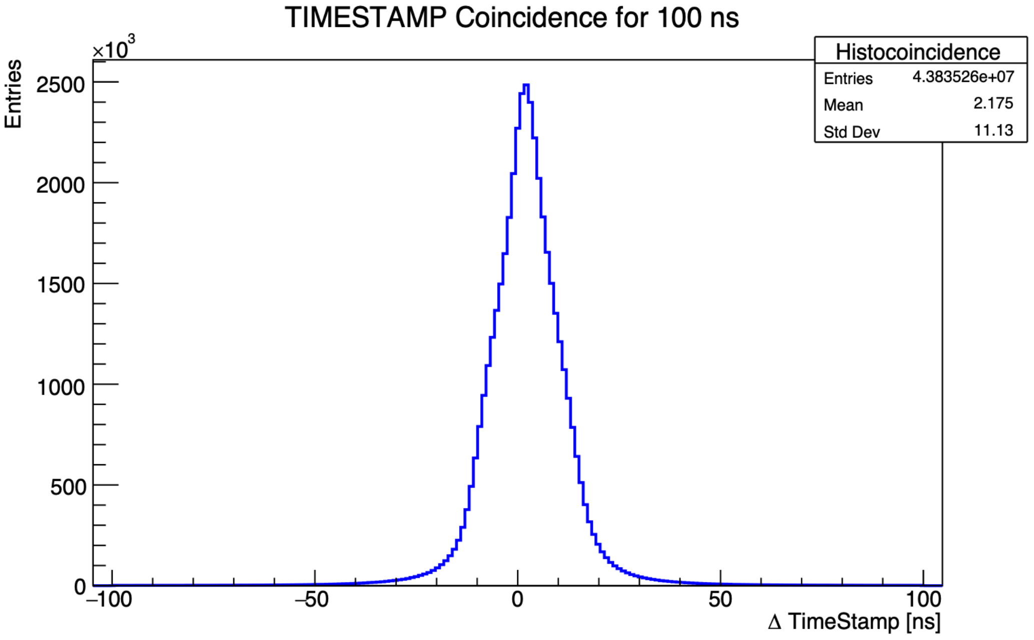

Figure 3.47: The time distribution of XY coincidences for layer 0.

In Fig. 3.47, the mean is the time needed whether the hit arrives first on one card than on the other. And the standard deviation is the time needed by the light to cross the length of the optical fiber within a strip. A very narrow distribution is obtained with the standard deviation of 11 ns proving well that XY coincidences are observed. The XY coincidence rate is measured to be around 500 Hz/layer. The time distribution of coincidences is affected by the decay fiber time, decay scintillation time, the distance of the strips and time walk.

The Coincidence Rate per layer is summarised in the Table. 3.2. Layer 3 shows a lower rate among all layers. This is due in large part to the quality of the scintillator strips. The calculation of the muon rate will be discussed in Chapter 4. Fig. 3.48 shows the distribution of the average time difference between left and right cards as a function of the strip which triggered the MA-PMT in each card was measured. The distribution is centered on zero (white color), when the signal in both cards arrives at the same time in each card. While, the blue or red region corresponds when the signal arrives earlier on one of the cards. This distribution is originated due to the different length wavelength shifting fibers in each strip.

Table 3.2: Coincidence Rate per layer.

Layer	**Rate (Hz)**
0	531
1	551
2	589
3	420

Fig. 3.49 describes the XY coincidences rate per strip crossing. Each point (x,y) has a surface of 2.64 cm × 2.64 cm due to the granularity of the MT. The maximum rate at an (x,y) point can reach about 0.7 Hz.

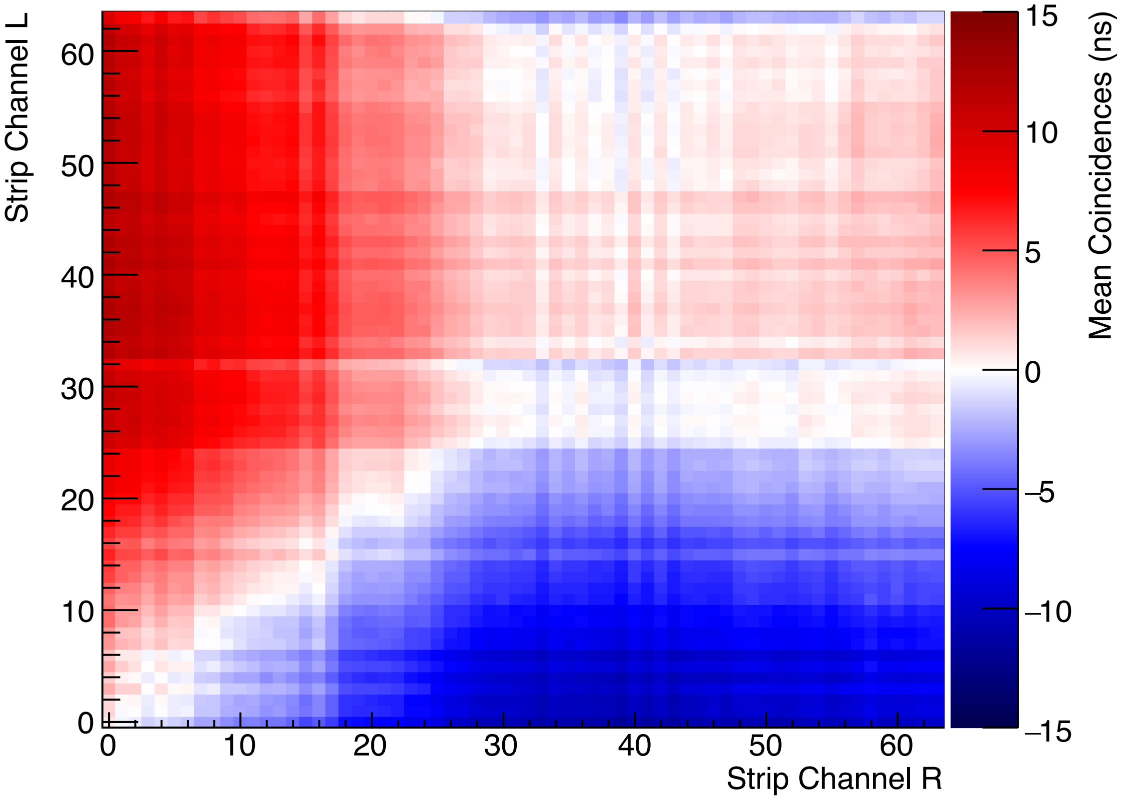

Figure 3.48: Distribution of the average time difference between left and right cards as a function of the strip triggered by the MA-PMT in each card. The distribution is centered on zero (white color), when the signal in both cards arrives at the same time in each card. While, the blue or red region corresponds when the signal arrives earlier on one of the cards.

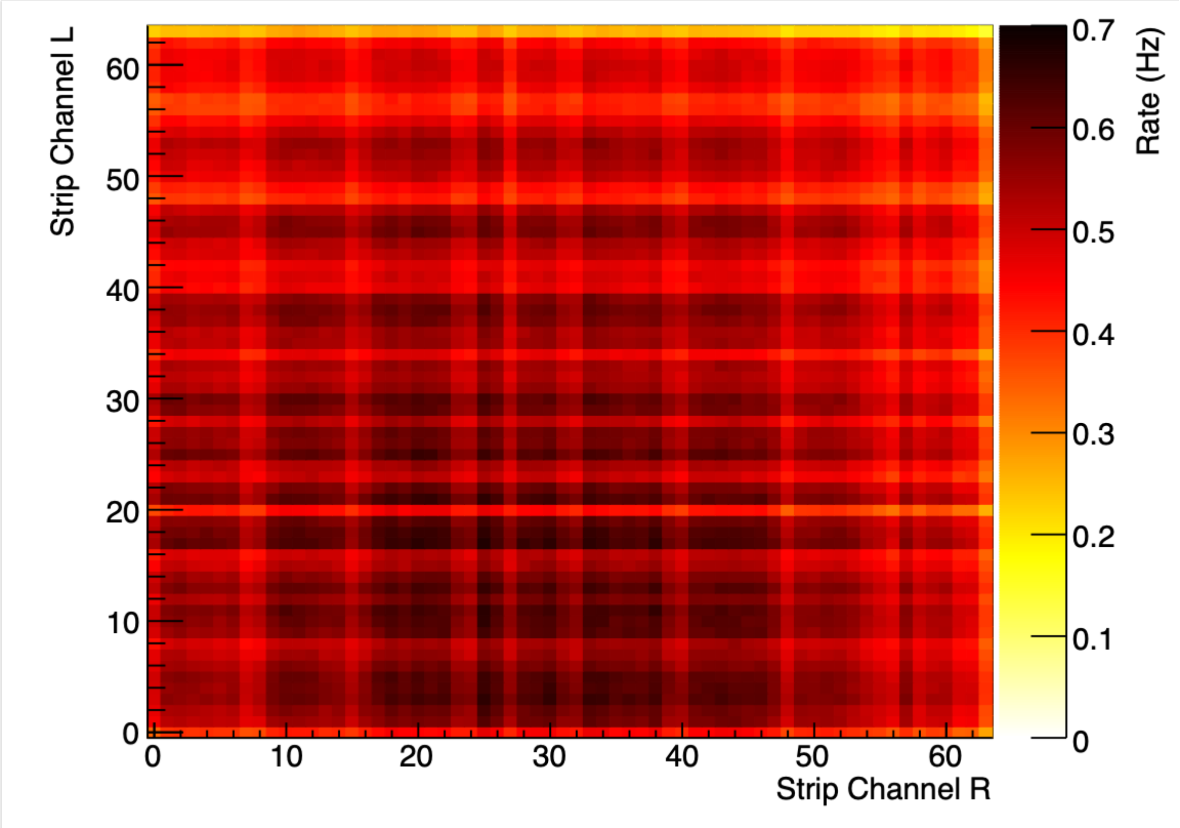

Figure 3.49: XY coincidences rate per strip crossing. Each point (x,y) has a surface of 2.64 cm × 2.64 cm due to the granularity of the MT.

The technology used in the MT allows us to measure the atmospheric muon flux arriving in Strasbourg based on the above mentioned selection criteria. The first step is to check the XY coincidences per layer in order to build 3D points from triggered MA-PMT channels. This flux will be used to study different reconstruction methods for the MT and TT in the next chapter.

L' Étalonnage du prototype de Top Tracker

"Les neutrinos ... remportent le concours du minimalisme : charge nulle, rayon nul, et très probablement masse nulle."
Leon M. Lederman.

À l'IPHC, un prototype du Top Tracker appelé Télescope à Muons (MT) a été construit pour tester la chaîne complète de lecture et déclenchement du Top Tracker. Le Télescope à Muons peut être utilisé pour optimiser les algorithmes de reconstruction nécessaires à l'analyse des muons cosmiques dans JUNO.

Le MT a été fabriqué en utilisant les mêmes bandes scintillantes que celles du Top Tracker. Dans le MT, ces bandes mesurent 1,7 m de long. Le TT comporte 3 couches alors que le MT en comporte 4. Dans le MT, chaque couche est constituée de deux plans orientés perpendiculairement, créant une granularité de $2,64 \times 2,64 \mathrm{cm}^2$ en raison de la largeur des bandes. Chaque plan comporte 64 bandes de scintillation lues sur un côté par un MA-PMT à 64 canaux. Le MT a une surface de détection de 1/16 d'un mur du TT de JUNO. Mon travail a porté sur la préparation et l'optimisation du TT en participant aux tests de la nouvelle électronique de lecture sur le prototype.

Le MT est constitué de 4 couches de scintillation plastique XY (8 modules). Les couches sont numérotées du bas (couche 0) au haut (couche 3). Les résultats présentés tout au long de cette thèse correspondent au moment où la position du MT était horizontale (cependant, il est aujourd'hui possible de changer la position du télescope à l'aide d'un moteur installé sur l'axe de rotation).

Le prototype est équipé de 8 FEB et 8 ROB. Le système d'injection de lumière est utilisé pour tester et contrôler tous les canaux électroniques. Le prototype dispose de plusieurs modes de prise de données : Piédestal (bruit électronique), TRT (nombre de coups par seconde pour identifier les canaux bruyants et les fuites de lumière), LED (déclenchement externe avec une impulsion de LED pour contrôler le gain de chaque canal des MaPMT) et Normal (déclenchement interne).

Comme mentionné précédemment, la chaîne électronique qui sera utilisée dans le TT de JUNO peut être testée à l'aide du prototype. Comme tous les FEB (1200) de JUNO doivent être vérifiés, un banc de test a été créé à cet effet, pour enregistrer de nombreux paramètres pertinents tels que les courbes de linéarité et les seuils, comme nous le verrons plus loin.

En utilisant les premières versions des cartes électroniques développées par notre groupe, j'ai pu comparer les performances du prototype et du banc de test. Cette comparaison a permis de déceler certains problèmes qui ont été corrigés par la suite. J'ai effectué des tests afin de vérifier la stabilité du système de calibration. Comme les charges physiques injectées sont interprétées par des unités arbitraires en électronique, les convertisseurs analogiques-numériques et les convertisseurs numériques-analogiques, j'ai réalisé un étalonnage électronique nécessaire pour extraire ces facteurs de conversion entre les unités électroniques et physiques. Par exemple, pour un muon traversant une bande de scintillation, une charge déposée de 3 à 6 photoélectrons (p.e) est attendue. Il est donc essentiel de veiller à ce que le seuil de détection soit bien ajusté, ce qui nous permet de maintenir les niveaux de bruit aussi bas que possible et, par conséquent, d'atteindre une efficacité de détection > 98%. Le seuil de détection correspondant pour le TT a été défini comme 1/3 p.e (53fC pour un gain des MaPMT de 10^6). Un seuil bas assure une efficacité très élevée de détection de photoélectrons uniques. De l'autre côté, le seuil doit être suffisemment haut pour éliminer le bruit électronique. Le seuil est commun aux 64 canaux, et il est réglé à l'aide de la puce MAROC3 dans la FEB.

J'ai préparé un système d'injection de charge pour determiner le seuil à être utilisé dans la FEB, avec une charge injectée de 53fC correspondant à 1/3 p.e. Le seuil électronique est défini à 50% d'efficacité de détection pour une charge injectée. J'ai vérifié que le seuil était uniforme et stable sur les 64 voies électronique de la puce. La procédure appelée calibration de charge concerne la détermination du facteur de conversion des charges de sortie (en unités ADC) et des charges physiques (en pC). J'ai également utilisé le système d'injection de charge pour cette calibration sur un canal. Différents valeurs de charges ont été injectées allant de 0pC à 10pC (~ 60 p.e avec 10^6 de gain). Les résultats nous montrent une région linéaire pour des charges jusqu'à 4 pC alors que pour des charges plus élevées une saturation est observée. Dans une première calibration que j'ai réalisé, pour les 6 premières cartes, ces nombres sont autour de 7,5 ADC counts/p.e, tandis que deux cartes montrent une amplification plus élevée (~ 10 ADC counts/p.e). Une seconde calibration que j'ai effectué nous montre une valeur uniforme autour de 10.5 ADC counts/p.e pour toutes les cartes. Ces changements sont dus à la mise à jour du matériel de la FEB, où pour 6 des cartes il était nécessaire des changements de hardware pour améliorer leur fonctionnement. Nous avons également noté une bonne concordance entre mes mesures sur le prototype du Top Tracker et celles du banc de test.

Pour que le photodétecteur soit sensible à un seul p.e, les PMTs fonctionnent à une Haute Tension correspondant à un gain de 10^6. Il est à noter qu'il existe un écart de gain entre les 64 canaux d'un même MaPMT allant jusqu'à un facteur 3. Afin d'égaliser tous les gains, le canal avec le gain le plus élevé est mis à 10^6 en variant la Haute Tension. Pour chacun des autres canaux j'ai ajusté l'amplification à l'entrée de la FEB pour les amener également à un gain équivalent de 10^6. Pour déterminer le gain de chaque canal PMT, le système LED a été utilisé en mode de lumière réduite afin de détecter 1-2 p.e. en moyenne par canal. J'ai ajusté la distribution de charge d'un canal avec une fonction appropriée (fonction de Bellamy). En sélectionnant le canal ayant le gain le plus élevé, j'ai défini un facteur de correction par canal qui permet d'égaliser tous les gains à 10^6. Après application de ces facteurs d'amplification, une distribution plate est obtenue. Après la détermination du canal à gain le plus élevé, j'ai effectué des mesures de LED en faisant varier la haute tension du MA-PMT dans la plage 800-900 V. Les valeurs de gain pour ce canal sont tracées en fonction de la Haute Tension. Une estimation de la Haute Tension qui correspond au gain attendu est ainsi obtenue.

Des tests d'étalonnage ont été appliqués au télescope à muons en utilisant le temps comme paramètre principal. La valeur du temps mort de l'électronique a été déterminée à $10\mu s$. Cette valeur correspond au temps de lecture de la charge de l'ADC Wilkinson 8 bits dans MAROC3. D'autre part, pour obtenir une mesure rapide et précise, il est essentiel que la valeur de retard du signal HOLD soit déterminée de manière relativement précise pour les canaux activés. Cette étude a démontré la dépendance à la charge de la valeur optimale du délai HOLD. Ainsi, un compromis entre les charges élevées et faibles a été trouvé.

Pour mesurer et optimiser l'efficacité de détection du TT j'ai utilisé des muons atmosphériques. Pour cela, il a été nécessaire de faire quelques tests pour déterminer la résolution temporelle intrinsèque du détecteur. Différentes contributions interviennent dans le temps mesuré dont les incertitudes doivent être prises en compte. Une de ces contributions est le temps de marche (t_{walk}). Le temps de marche est dû à la variation des amplitudes des impulsions et du seuil de declanchement. La variation du temps de déclenchement en fonction de la charge injectée, a ainsi été mesurée par moi et prise en compte lors de la reconstruction des traces de muons. Dans un scénario avec un seuil de 1/3 p.e et en considérant les charges, la variation entre les faibles charges, ~ 1 p.e., et les fortes charges, >10 p.e., s'est avérée être supérieure à 6 ns. Ce facteur est également pris en compte dans la détermination du délai du signal HOLD et doit également être pris en compte dans toute étude de synchronisation des détecteurs.

Le développement d'un banc de test était nécessaire pour tester et caractériser la série complète de la version finale de la FEB (1200 cartes) qui sera utilisée dans le Top Tracker. Ce banc de test est automatisé et est équipé d'un système d'injection de charge. Il est également possible d'extraire certains paramètres d'étalonnage à partir des tests de linéarité ou d'efficacité de déclenchement, ainsi que de mesurer le piédestal entre autres tests.

Sur les 1200 cartes FEB testées, 1160 (près de 97%) ont été acceptées et ont déjà été expédiées en Chine pour une installation future dans le TT. Au final, le Top Tracker utilisera 992 de ces cartes, les autres étant utilisées comme cartes de réserve. Les 8 cartes utilisées dans le télescope à muons au cours de cette thèse ont également été testées sur le banc de test.

Pour mesurer le flux de muons atmosphériques, j'ai développé une méthode de sélection afin de classer les candidats muons. La première étape consiste à vérifier les coïncidences XY (avec une fenêtre temporelle de 100 ns) par couche afin de construire des points 3D à partir des canaux MaPMT déclenchés. Une distribution très étroite est obtenue avec écart type de 11 ns prouvant bien que des coïncidences XY sont observées. La distribution temporelle des coïncidences est affectée par le temps de désintégration des fibres, le temps de désintégration de la scintillation, la distance des bandes et le temps de marche.

Le taux de coïncidence XY est mesuré à environ 500 Hz/couche. Le taux de coïncidence par couche est résumé dans le tableau. 3.2. La couche 3 montre un taux plus faible parmi toutes les couches. Ceci est dû en grande partie à la qualité des bandes de scintillateur. Le calcul du taux de muons sera abordé au Chapitre 4.

Le télescope à muons nous permet de mesurer le flux de muons atmosphériques arrivant à Strasbourg. La première étape consiste à vérifier les coïncidences XY par couche. Ensuite, des points 3D peuvent être construits à partir des canaux MA-PMT déclenchés. Ce flux sera utilisé pour étudier différentes méthodes de reconstruction pour le Télescope à Muons dans le chapitre suivant.

CHAPTER 4

Muon Reconstruction

> *"Number is the ruler of forms and ideas, and the cause of gods and demons"*
> Pythagoras.

Contents

In the official JUNO software, a reconstruction method has been implemented for the analysis of the cosmic muons arriving at the Top Tracker, where the cosmic muon flux or cosmogenic background can be estimated. This reconstruction method can be verified in real conditions with the Muon Telescope. As shown in Chapter 3, during the development of this thesis, the electronics implemented in the MT lacks the cards responsible for the L1/L2 triggers. Therefore, the "muon candidates" selection, considering the XY coincidences per layer, needs to be done in the software. Then we require the coincidences in at least 3 layers to build at least 3 3D points from the triggered MA-PMT channels.

This chapter will focus on the description of the methods used for the reconstruction of cosmic muons in the MT. The implementation of the JUNO software for the reconstruction is discussed in Section 4.1. However, a new reconstruction method is required due to some limitations of the JUNO software as will be discussed in Section 4.1. This new method is based on the Hough transform (HT). An introduction to the HT is presented in Section 4.2. The Hough transform is implemented and optimised using the simulation as described in Section 4.3. The chapter concludes with the comparison of the results between JUNO and HT reconstruction methods in Section 4.4.

4.1 Muon Track reconstruction using JUNO official software

To define a muon track in the TT, a minimum of three 3D points are required. The JUNO official software combines the 3D points from triggered MA-PMT channels in the different layers to perform a linear fit.

In a 3D space, the vector form of the equation of a straight line is parameterised by the free parameter λ :

$$\mathbf{r}(\lambda) = \mathbf{r_0} + \lambda \mathbf{v} \tag{4.1}$$

Each point $\mathbf{r} = (x; y; z)$ is mapped by the free parameter using a point passing through the line $\mathbf{r_0} = (x_0; y_0; z_0)$ and the direction vector for the line $\mathbf{v} = (v_x; v_y; v_z)$. In the JUNO official software, a muon track is given by the parameterization of a 3D straight line, as described in Eq. 4.1. The reconstruction algorithm used in JUNO is based on least-squares fitting of a 3D straight line. The best fitting straight line is the one which gives the minimum value of the quantity χ^2 (chi-squared). In 3D, this quantity is defined as :

$$\chi^2 = \sum_{i=1}^{n} \frac{||(\mathbf{r_i} - \mathbf{r_0})) \times \mathbf{v}||^2}{||\mathbf{v}||^2 \sigma_i^2} \tag{4.2}$$

where the number of points used in the fitting is given by n, the uncertainty σ_i is fixed to 13 mm, which corresponds to half width of the TT scintillator strip. The algorithm fits only 4 free parameters (x_0, y_0, v_x, v_y). The other parameters are set $v_z = -1$, to ensure that the tracks are not horizontal, and z_0 is set at the average z centre of the 3D points.

The algorithm reconstructs a possible track with a combinatorial process if the number of 3D points is greater than 3 and less than 80. Therefore, the algorithm is limited by the number of points considered in an event. The algorithm omits events with more than 80 3D points. Such events are likely to be caused by muon showers in the rock. This is done because, if there are too many points, the algorithm takes too long to converge.

If more than 3 points $(n > 3)$ are used in the fitting, the software considers all permutations between the possible points in 3D. Each combination will define a possible reconstructed track. For all tracks with a $\chi^2 < 3$; the algorithm will consider the track as successful and will save the parameters necessary for the calculation of the angular distributions (direction, position, number of points used in the fitting, among others).

However, in the case where the software does not find any successful tracks (i.e. none of the permutations satisfy $\chi^2 < 3$), the algorithm will eliminate one 3D point, i.e. $(n-1)$ points will be used in the fit. Subsequently, permutations will be made between these $(n-1)$ points. The same procedure described above is then applied to these new sets of points.

If despite the above procedure it persists that no track satisfies this χ^2 criteria, the algorithm will again reduce the number of possible points by one and apply the fitting procedure. The reduction of the number of points will be done until there are only three 3D points. In this last case, if the reconstructed track yields a $\chi^2 < 10$, the algorithm will accept these tracks. That is, the algorithm will extend the acceptance of χ^2 to accept tracks that have three 3D points. In case these tracks have a $\chi^2 > 10$, the reconstruction will be considered failed, and the algorithm will stop and move on to the next event.

Fig. 4.1 shows an example of a muon track reconstructed in the TT using the Top Tracker simulation. For this reconstruction, 3 3D points are used and the $\chi^2 = 0.5$. The blue solid line is the muon track reconstructed, and the orange dashed line is the true muon track given by the simulation data.

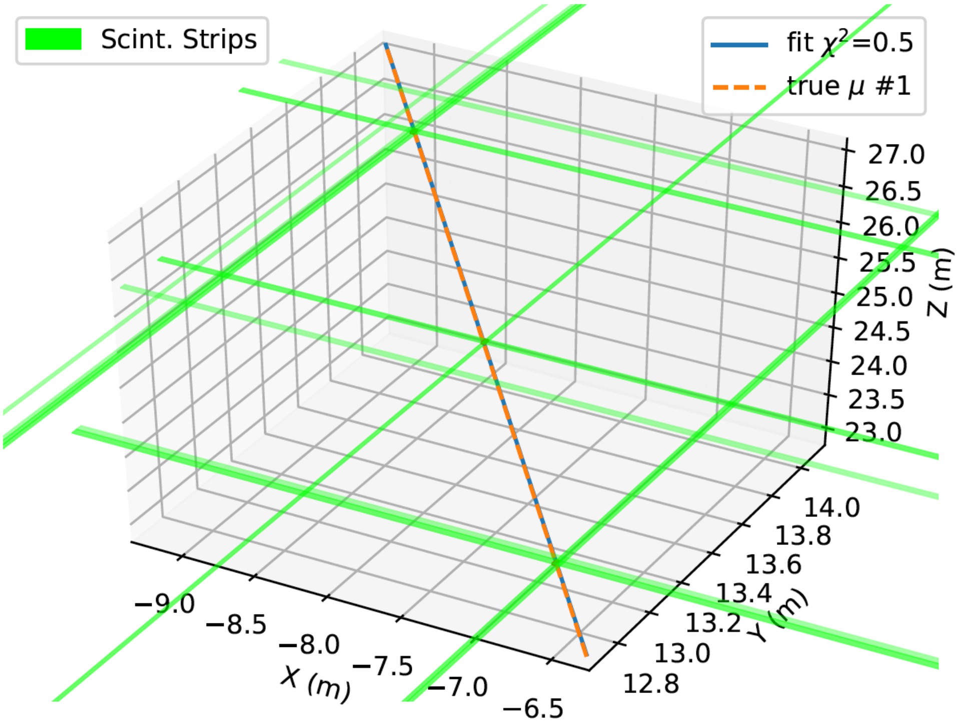

Figure 4.1: An example of the sucessful muon reconstruction in the TT using the JUNO official software [95].

The official JUNO software is also used to reconstruct the cosmic muons from the data recorded by the MT. During the data acquisition, the MT was in a horizontal position as described in Fig. 3.1. This indicates that there is no angle of elevation of the MT with respect to the horizontal.

For the study of the angular distributions originated by cosmic muons, spherical coordinates were used. Fig. 4.2 shows the spherical coordinates (r, θ, ϕ) in a Cartesian space (x, y, z). The spherical coordinates depend on the radial distance r, the zenith angle θ and the azimuthal angle ϕ. The zenith angle varies between 0° and 180°. A zenith angle of 0° is associated for muons arriving from bottom to top; an zenith angle of 90° indicates muons arriving horizontally at the detector; and an angle of 180° indicates muons arriving from top to bottom. The left inset in Fig. 4.2 illustrates the zenith angle in the various scenarios mentioned above. The azimuthal angle varies between 0° and 360°.

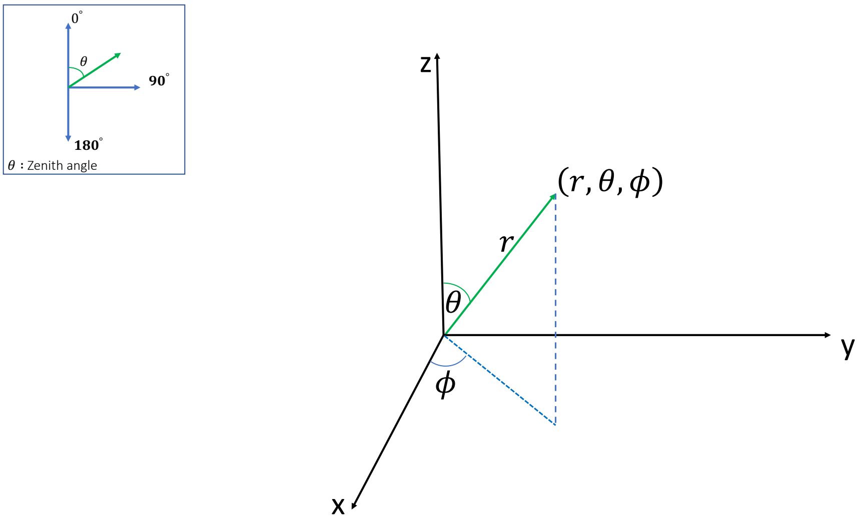

Figure 4.2: Spherical coordinates.

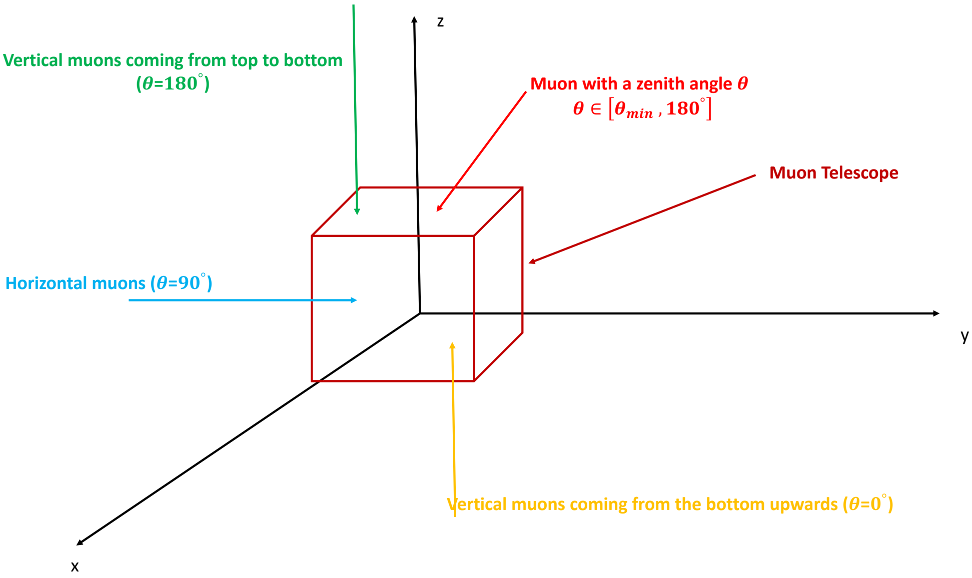

Figure 4.3: Schematic of possible muon directions in the MT. It is not drawn to scale.

In order to visualise some cosmic muons arriving in the MT, the zenith angle θ is considered to describe their direction as shown in Fig. 4.3. The angle θ_{min} describes the acceptance angle in the detector. This angle depends of the geometry of the detector. This angle corresponds to the smallest θ for which a downgoing muon will cross 3 layers of the MT. θ_{min} for the MT is around 110°. This indicates that the reconstructed muons have a zenith angle θ between 110° and 180°. A zenith angle between 0° to 90° will not be measured by the detector, as the imposition of $v_z = -1$ removes the possibility to reconstruct upgoing events.

The angle of acceptance at the TT changes due to the different geometry of the detector. The TT is able to reconstruct muons with zenith angles between 96° and 180°.

The intensity of the muon flux has been observed in great detail experimentally[39]. This flux is a function of the zenith angle θ, following a cosine power law :

$$I(\theta) = I_0 \cos^n \theta \tag{4.3}$$

where I_0 is the vertical muon flux and the exponent n is a real parameter. The intensity of the muon flux depends of the atmospheric conditions, geomagnetic latitude and zenith angle [120]. I_0 is around $70\mathrm{m}^{-2}\mathrm{s}^{-1}\mathrm{sr}^{-1}$ for muons above 1 GeV/c at sea level[39]. The value of the exponent n ~2 has been reported in several experiments, this value depends on muon energy and the atmospheric depth for muons with energies of a few GeV [121, 122].

The muon rate per layer ($R_{\mu_{layer}}$) in the MT is given by :

$$R_{\mu_{layer}} = \int_{\Omega} A I(\theta) d\Omega \tag{4.4}$$

where A is the area of one layer of the MT, which corresponds to 2.85 m^2. I_0 is the intensity of the muon flux described by Eq. 4.3. Ω is the solid angle expressed in a dimensionless unit called a steradian (sr), $d\Omega$ is the differential of the solid angle, which depends of the zenith angle (θ) and azimuth angle (ϕ). In spherical coordinates this differential is given by $d\Omega = \sin\theta d\theta d\phi$. The muon rate per layer is calculated using $n = 2$ in Eq. 4.4 :

$$R_{\mu_{layer}} = \frac{2\pi I_0 A}{3} \tag{4.5}$$

The muon rate per layer ($R_{\mu_{layer}}$) is $\sim$ 419 Hz. The measurement of the muon rate per layer using the cosmic rays in the MT was $\sim$ 500 Hz as shown in Table. 3.2, which implies most coincident triggers are indeed from muons.

Using the JUNO simulation, the dependence of the muon rate on the zenith angle is shown in Fig. 4.4. The zenith distribution provided by the simulation data (green) shows that the value of the exponent n is $\sim$ 4.3. The value of parameter n is larger than 2 due least in part to geometrical effects in the MT. Fig. 4.4 shows also the zenith distribution obtained by the JUNO reconstruction (blue), in this case the value of n agrees with the one obtained by the simulation.

The zenith distribution of the cosmic muons is also measured in the MT during 5 hours. Fig. 4.5 shows the zenith angular distribution, where the zenith angle θ goes from 110° to 180° due to the acceptance angle of the MT. The value of the parameter n is 5 in this case. This number shows a similar departure from $n = 2$ as in the simulation, which is likely due to geometrical effects in this case also.

In the case that a muon passes through at least 3 layers, the total muon rate ($R_{\mu_{total}}$) decreases due to the acceptance angle, geometrical effects in the MT which are encoded in the measured value of n ~5. In this case, the area A is a function of the zenith angle θ. The total muon rate is given by : $R_{\mu_{total}} = \int_{\Omega} A(\theta) I(\theta) d\Omega \sim 100$ Hz, which is to be compared with a total measured rate of $\sim$ 130 Hz for coincidences on 3 layers or more of the MT.

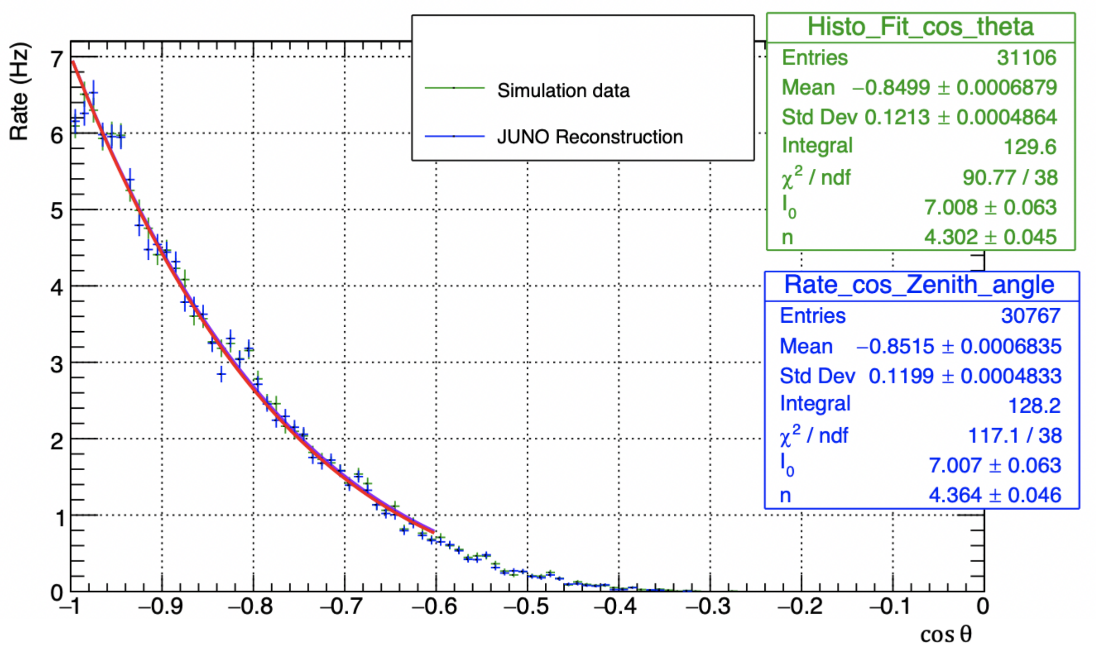

Figure 4.4: Zenith angle distribution reconstructed using the JUNO software (blue) and the Zenith angle distribution by the simulation data of the MT (green).

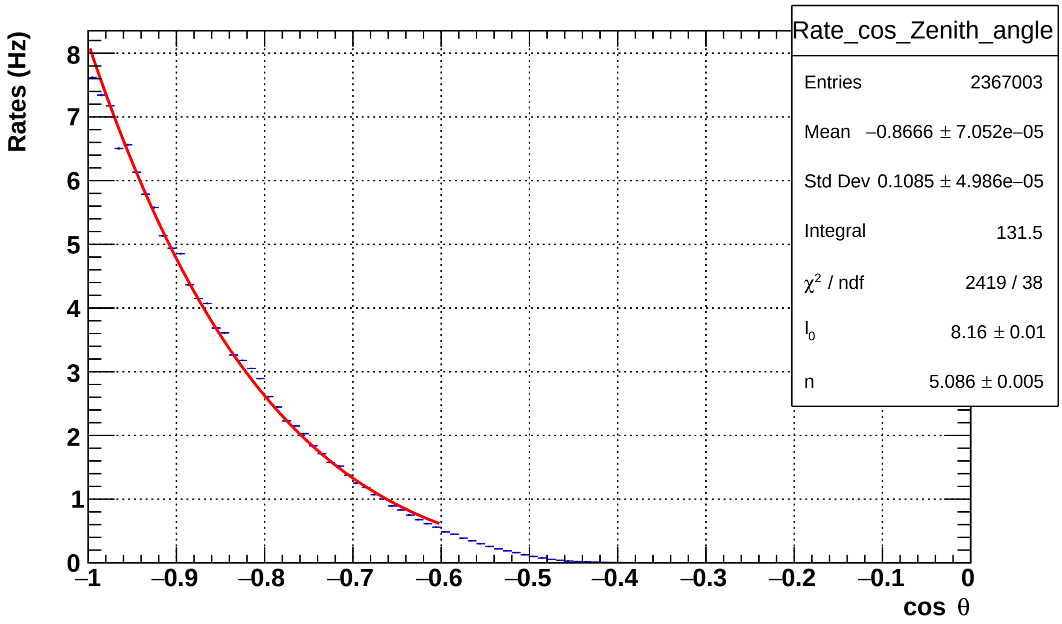

Figure 4.5: Zenith angle distribution reconstructed using the JUNO software for 5 hours of data taking of the MT.

In Fig. 4.6 is presented the azimuthal angular distribution. The azimuth ϕ is often restricted to the interval $(-180°, +180°)$, instead of $(0°, 360°)$. This distribution is expected to be flat. The peaks in the azimuthal distribution at $n * \pi/2$ are due to the geometry of the MT and the fact that each reconstructed hit is placed at the middle of the strips. The peaks are also indicative of a geometrical limitation due to the granularity in the MT.

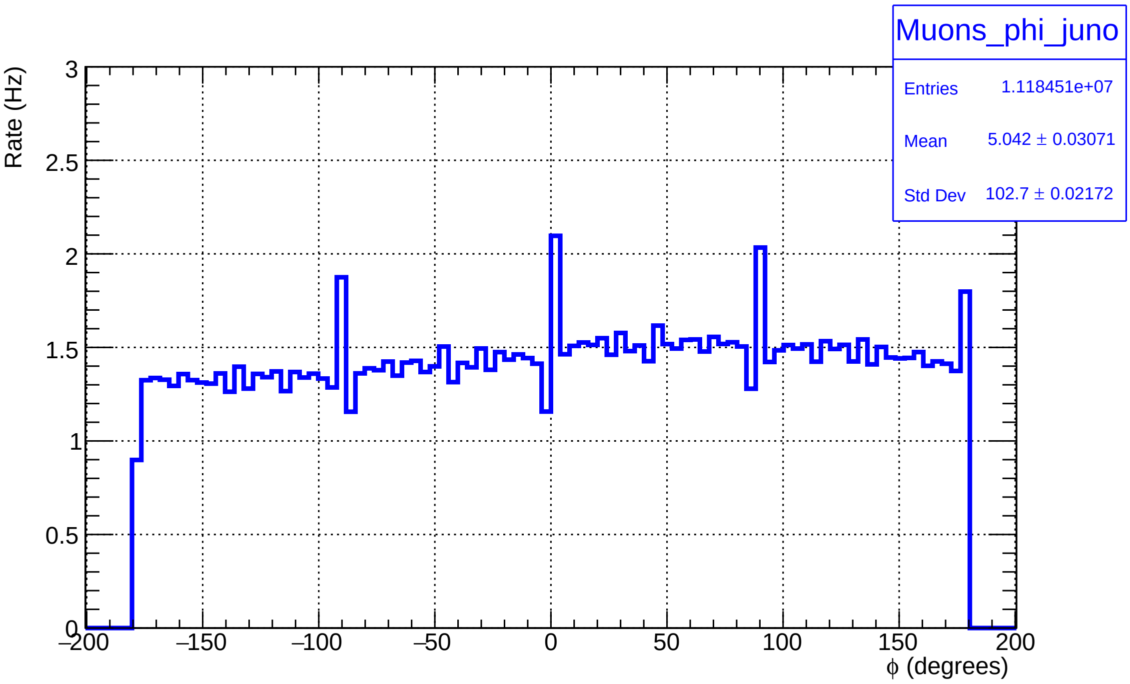

Figure 4.6: Azimuthal angle distribution reconstructed using the JUNO software for 24 hours of data taking of the MT.

The Mollweide projection is a homolographic equal-area projection. The Mollweide projection corresponds to a projection of a sphere into a plane. This projection fills an ellipse whose minor axis (latitude) is twice the major axis (longitude). The longitude is given by the zenith angle - 90°. The latitude is given by the azimuthal angle. The longitude is defined in the interval (-π, +π). The latitude is defined in the interval ($\pi/2$, +$\pi/2$). The muon trajectories were projected using Mollweide coordinates. With the Mollweide projection is possible to make a radiography of the location where is the MT with muons. This projection transforms from latitude and longitude to map coordinates "x" and "y" via the following equations :

$$x = R\frac{2\sqrt{2}}{\pi}(\lambda - \lambda_0)\cos\theta, \tag{4.6}$$

$$y = R\sqrt{2}\sin\xi, \tag{4.7}$$

where ξ is defined by :

$$2\xi + \sin 2\xi = \pi \sin\phi \tag{4.8}$$

and λ is the longitude, λ_0 is the central meridian, ϕ is the azimuthal angle, and R is the radius of the globe to be projected.

The Mollweide projection is useful for observing the distribution of muon directions observed in the MT. Fig. 4.7 shows the Mollweide projection using the JUNO reconstruction software for 24 hours of MT data acquisition. In Fig. 4.7 Longitude lines are shown every 30°, while latitude lines are shown every 22.5°. Reconstructed muons passing through 3 or 4 layers in coincidence of the MT are considered. The field of view of the MT is limited to

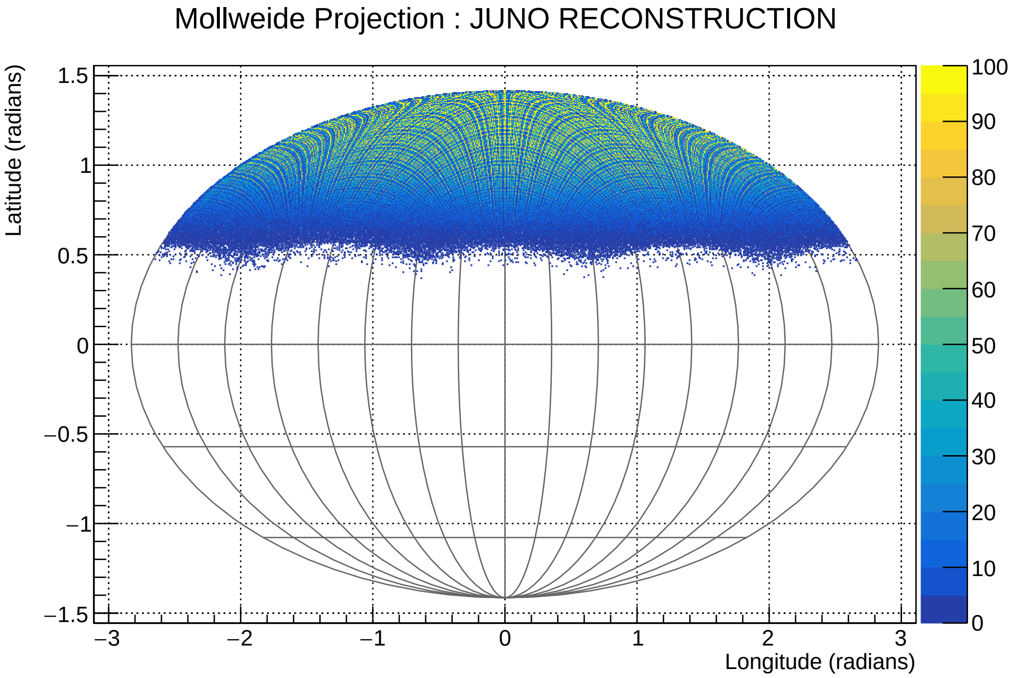

Figure 4.7: Mollweide projection using the JUNO software for 5 hours of data taking in the MT.

about 70° degrees from vertical (according to the angular acceptance in the MT). To expand this value and observe larger part of the sky, the prototype would have to be rotated.

4.2 Hough transform : overview

The official algorithm used by JUNO for muon reconstruction is limited by the number of points. The algorithm spends a long time before converging due to the combinatorial nature of the algorithm. As shown in this section, a new reconstruction method is needed to better cope with the possibility of more noise in the detector.

Experiments interested in the analysis of cosmic muons have developed reconstruction algorithms to filter out background noise. Hough transform(HT) is one of the most cited techniques for detecting straight lines in images. The HT was proposed by Paul V. C. Hough in 1962 [31]. HT has been adapted to many types of shapes, not only to lines, which is an interesting advantage in the development of reconstruction algorithms in some experiments [123, 124, 125, 126]. The purpose of this section is to offer a general introduction to the HT and how it will be implemented as a reconstruction method.

A straight line in 2 dimensions in Cartesian space is represented in the form $y(x) = ax+b$, where a is the slope and b the intercept of the straight line. The classical HT transformation is a linear transform where each point (x_i, y_i) is associated with a line in Hough space of the form $b(a) = -ax_i + y_i$. The Hough space is a 2D plane, where the vertical axis represents the intercept of the line (with the y-axis) and the horizontal axis represents the slope a.

Fig. 4.8 shows the mapping from edge points to the Hough Space for two points. The straight line will be defined by the intersection (a_0, b_0) of the several lines in the Hough space.

In the classical space for vertical lines the slope a is infinite. The crossing would then be in an infinite position. To avoid this situation it would be practical to have bounds in the Hough space. This can be done by representing a straight line in an alternative way as described below.

In two dimensions, a more general representation of a straight line is given by the Hessel normal form :

$$\vec{r} \cdot \hat{n} - \rho = 0 \tag{4.9}$$

where $\vec{r} = x\hat{i} + y\hat{j}$ is the vector of the point in (x, y), $\hat{n} = \hat{i}\cos\theta + \hat{j}\sin\theta$ is the unitary normal vector of the straight line, ρ is the length of the normal line and θ is the angle between the normal line and the x-axis. The straight line in Eq. 4.9 is usually rewritten as :

$$\rho = x\cos\theta + y\sin\theta \tag{4.10}$$

Each point (x, y) in the cartesian space is parametrized by a sinusoidal curve in the Hough space (θ, ρ) using Eq. 4.10. In this space θ is bound in the (x,y) range after this change.

The straight line is defined by the most probable value of (θ_0, ρ_0), which it is obtained from the intersection of the curves in the Hough space. Finding the values (θ_0, ρ_0), the straight line is given by :

$$y = \frac{1}{\sin\theta_0}(\rho_0 - x\cos\theta_0) \tag{4.11}$$

where ρ_0 is the perpendicular distance from line to origin, and θ_0 is the angle the perpendicular makes with the x-axis. If we compare the conventional form of a straight line $(y = ax + b)$ with Eq. 4.11 the y-axis intercept and the slope depend on the parameters θ_0 and ρ :

$$b = \frac{\rho_0}{sin\theta_0}, \qquad a = -\cot\theta_0 \tag{4.12}$$

Fig. 4.9 illustrates a mapping form cartesian space to Hough space using Hessel normal.

The basic idea of this parametrization of the HT is that a point belonging to a straight line in the cartesian space corresponds to a sinusoidal curve in the Hough space. The sinusoidal curves of all feature points on a straight line have a common intersection which is used to detect the line in the Hough space.

The Hough space is defined by a two-dimensional matrix called the accumulator matrix. Each pixel in this matrix depends on the possible values of (ρ, θ). The HT based reconstruction method will largely depend on the bin size of the accumulator matrix. HT has some

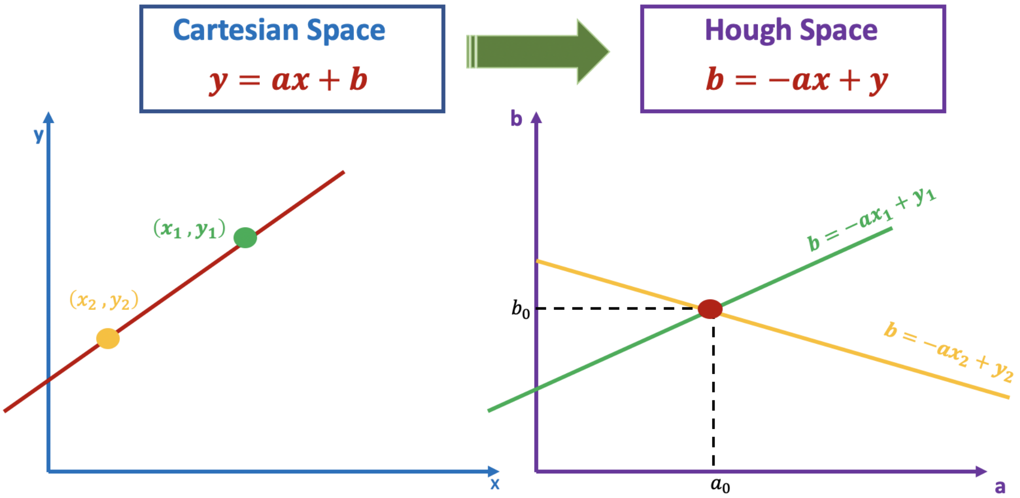

Figure 4.8: Mapping from cartesian points in the Hough space : A line in Cartesian space is shown on the right. On the left is illustrated the slope-intercept parameter space after the Hough transformation.

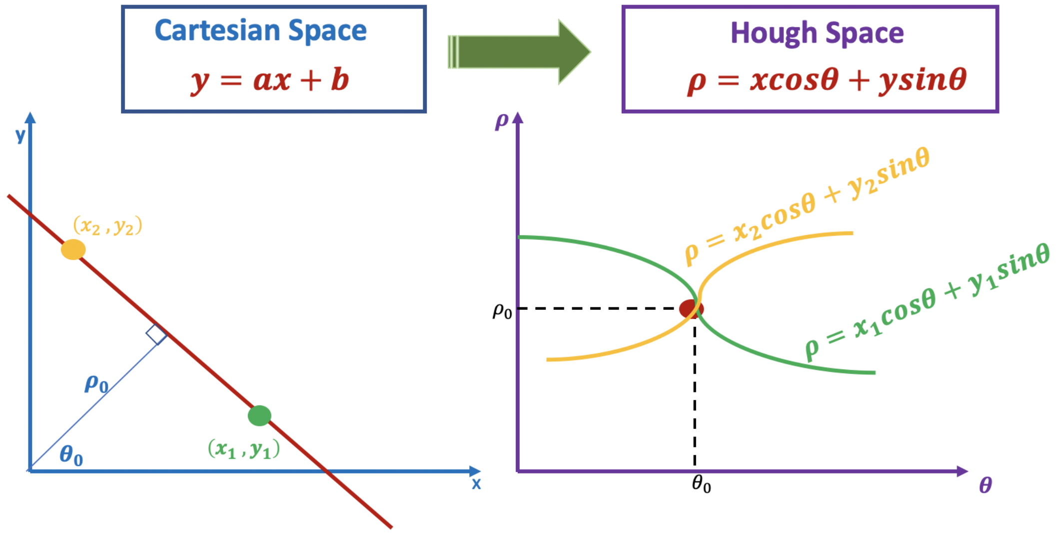

Figure 4.9: Mapping from cartesian to Hough space using Hessel normal form described in Eq.4.10 : On the right is illustrated a line in cartesian space, ρ_0 is the perpendicular distance from line to origin, and θ_0 is the angle the perpendicular makes with the x-axis. The Hough space ($\rho\theta$) is shown on the left.

disadvantages such as the efficiency of the accumulator matrix. If the pixel is too small or too large the visibility of the main pixel will be reduced.

4.3 Muon Track reconstruction using Hough method

The new reconstruction method developed in this thesis for the analysis of cosmic muons in the MT is based on the Hough transform. In this section we will detail how the Cartesian space and the Accumulator matrix are defined for the Hough algorithm. A preliminary evaluation of the performance of the HT algorithm using the JUNO Simulation data is discussed. We will also explain how the best bin size of the Accumulator matrix was chosen.

Unlike the algorithm used in the JUNO software where it works in three dimensions, the HT approaches the reconstruction problem as 2 two-dimensional problems. HT classifies the MA-PMT channels triggered in the modules into XZ and YZ projections. Each projection is analysed separately to then proceed to a 3D track reconstruction.

4.3.1 Hough Space in the MT

The MA-PMT channels activated in the modules are located in the Cartesian space, which are represented by points. This space allows to detect muon hits a spatial granularity of 2.64 cm × 1.06 cm. This granularity is defined from the size of the scintillation strip. For simplicity, we discuss the construction of the Cartesian space for the XZ projection. The YZ projection is implemented in an analogous way.

In the Cartesian space, the vertical axis (z) represents the position of each layer with respect to the centre of the module in cm. The layer 3 is at z=+45 cm, the layer 2 is at z=+25 cm, the layer 1 is at z=-25 cm and the layer 0 is at z=-45 cm. The distance between the top and the bottom layer is 90 cm.

As mentioned in Chapter 3, one module in the MT contains 64 wavelength shifting fibers. Each fiber is at the centre of the scintillation bars. Each fiber is associated with a strip number between (0-63). Each strip is connected to a channel of the MA-PMT. The Cartesian space of the XZ projection also shows the exact location of the 64 strip in the module in cm on the x-axis. Negative values on this axis indicate that a strip number is between $[0,31]$, while positive values are associated with a strip number in the range $[32,63]$.

Fig. 4.10 shows the Cartesian Space for the XZ projection. A muon track (red line) and the parameters of Hough transform were also added.

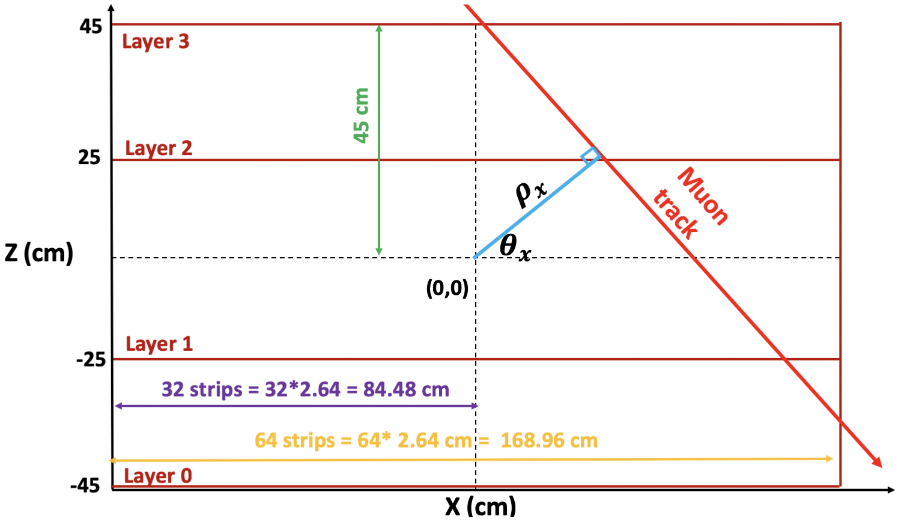

Figure 4.10: Cartesian space definition of the MT for the XZ projection.

A description of the construction of the Hough space for the XZ projection is now addressed. The accumulator matrix depends on the parameters (θ_x, ρ_x). Some criteria are discussed below to define the intervals in which the Hough parameters will be used.

The angle of acceptance calculated for the MT is used to define the values of θ in the HT. From geometrical constraints, the acceptance region is defined in the interval (-70° ,70°). This is imposed by the condition to have hits in at least 3 MT layers.

The maximum value of ρ_{max} is described in Eq. 4.13. This value is also given by the geometry of the detector. The accumulator matrix defined for the horizontal axis (θ_x) an interval between (-70° ,70°), and for the vertical axis (ρ_x) a range of (-100cm , 100cm).

$$\rho_{max} = \sqrt{(32 * 2.64)^2 + (45)^2} \approx 96\text{cm} \tag{4.13}$$

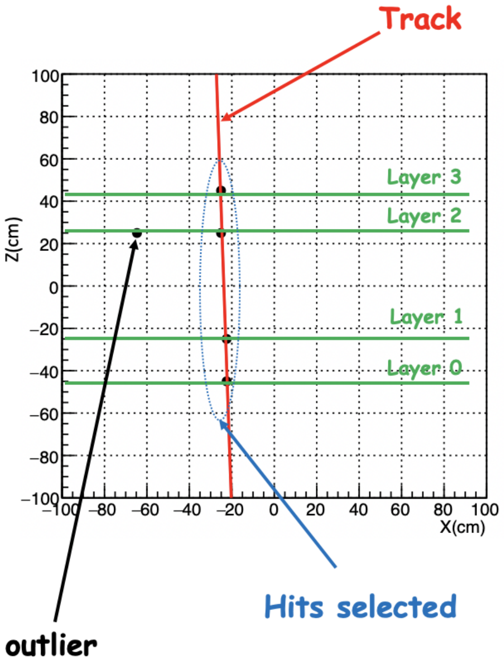

Figure 4.11: Example of triggered channels in XZ projection.

Fig. 4.11 shows the hits in the Cartesian space used for building the accumulator matrix for the XZ projection of one event as shown in Fig. 4.12. In this event, five hits are present. The maximum number of hits in the accumulator matrix is four, i.e four curves are intersected in this cell. In other words, from the accumulator matrix we can conclude that four points are collinear. One outlier is present in layer 2, this outlier is interpreted as a possible background in the event. The cell with the maximum bin content corresponds to (2° , -23.7 cm) as shown in Fig. 4.12. With these values, the reconstructed track is obtained. In Fig. 4.11, the red line shows the track corresponding to the value (2° , -23.7 cm). In this event four hits were selected as expected in the accumulator matrix. The outliers (one in this example) are removed in order to optimise the Hough's algorithm.

The HT is conceptually simple and therefore easy to apply as a reconstruction method.

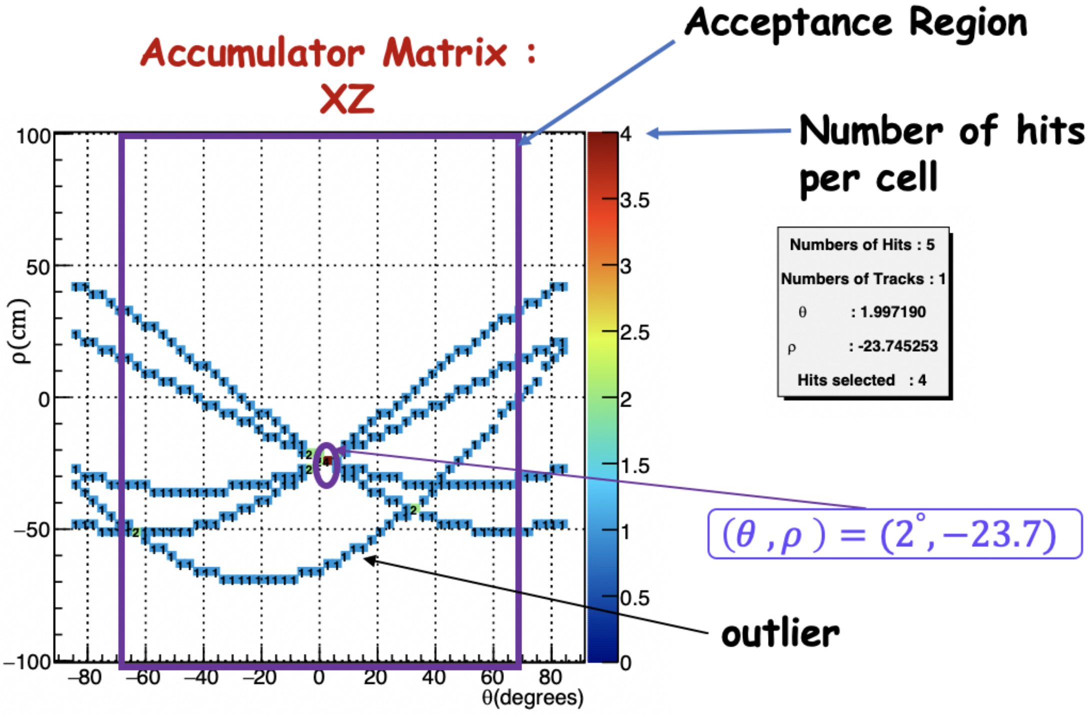

Figure 4.12: Accumulator matrix of the Hough transform using the sample of channels triggered in the XZ projection of Fig.4.11. In the horizontal axis (θ_x) varies between (-90° ,90°), an angular acceptance region is defined in the interval $(-70°, 70°)$. This is imposed by the condition of having hits in at least 3 MT layers. For the vertical axis (ρ_x) varies between (-100cm , 100cm). The value of ρ is given by the geometry of the detector. In this accumulator matrix, five sinusoidal curves are represented. The maximum number of hits per cell varies between 0 and 4. In most cases the sinusoidal curves do not cross. In four cases two sinusoidal curves intersect. The accumulator matrix shows that in the cell (2° , -23.7 cm) four hits are collinear which corresponds to four sinusoidal curves intersecting. An outlier is recorded in layer 2.

HT ensures that the points used in the reconstruction are strictly collinear. The parametrisation of the 3D straight line described by Eq. 4.1 in terms of the Hough parameters $(\theta_x, \rho_x, \theta_y, \rho_y)$ allows to define each component of a point **r** as :

$$x = \frac{\rho_x}{\cos\theta_x} - \lambda\frac{\sin\theta_x}{\cos\theta_x} \tag{4.14}$$

$$y = \frac{\rho_y}{\cos\theta_y} - \lambda\frac{\sin\theta_y}{\cos\theta_y} \tag{4.15}$$

$$z = \lambda \tag{4.16}$$

Using the information for a 3D track and the spherical coordinates, the zenith angle is given by :

$$\cos\theta = \frac{1}{\sqrt{\tan^2\theta_x + \tan^2\theta_y + 1}} \tag{4.17}$$

and the azimuthal angle is defined as:

$$\tan\phi = \frac{\tan\theta_y}{\tan\theta_x} \tag{4.18}$$

4.3.2 Reconstruction algorithm of Hough transform

The total number of tracks is given by the total peaks present in the accumulator matrix. Events with a maximum of 10 "candidate tracks" are considered.

In order to filter the outlier points, the distance between each point and the linear fit by Hough is calculated. If the distance is greater than 5σ (where $\sigma = \frac{2.64}{\sqrt{12.0}}$ cm), these atypical points are eliminated. Removing the outlier points, the track is re-fitted using a linear χ^2 fit with the remaining points. The tracks are classified according to the number of points used for fitting. A single track is defined for events with 3 or 4 points. In case there is a larger number of points (n>4), tracks with a $\chi^2/d.o.f < 15$ are kept as will be discussed. This criterion in χ^2 will be discussed later. It is worth noting that this criterion is different from the one imposed in the JUNO algorithm since the χ^2 treatment there is in 3D, whereas in the Hough method the χ^2 is calculated in 2 dimensions. Note also that the definition of σ is different in each case. In the JUNO software σ corresponds to 1/2 strip size, while in Hough Method the σ was taken as the standard deviation of a uniform distribution of the strip size.

For events with at least 3 points and with the maximum of 2 in the accumulator matrix, the HT selection is not applied. We try to recover the track with a linear fit : $z = ax + b$. Considering the parameters of the line (slope a and z-axis intercept b) we can obtain the values of (θ_x, ρ_x) according to Eq. 4.12.

4.3.3 Angular resolution in the MT

The initial bin size for the accumulator matrix of the Hough transform was defined using the angular resolution. The angular resolution ($\delta\theta$) is defined by the variation of the angular aperture or the precision to measure the zenith angle (θ).

$$\theta(\theta_x, \theta_y) = \arccos\left(\frac{1}{\sqrt{(\tan\theta_x)^2 + \left(\tan\theta_y\right)^2 + 1}}\right) \tag{4.19}$$

with the angular resolution given by :

$$\delta\theta = \sqrt{\left(\frac{\partial\theta}{\partial\theta_x}\delta\theta_x\right)^2 + \left(\frac{\partial\theta}{\partial\theta_y}\delta\theta_y\right)^2} \tag{4.20}$$

where the uncertainty of θ_x, θ_y are calculated using the method of least squares to determine the best fit of a straight line in 2D. The uncertainty of $\delta\theta_x = \gamma\,(\cos\theta_x)^2$ and $\delta\theta_y =$

$\gamma\left(\cos\theta_y\right)^2$. The factor γ is given by :

$$\gamma = \frac{\sigma}{\sqrt{\sum_{i=1}^{n}(z_i)^2 - nz^2}}, \tag{4.21}$$

this factor γ depends of numbers of points (n) on the layers and the distance in z-direction. The position of each hit i in the layers are given by z_i. The error σ is a function of the size of the strip bar ($\sigma = \frac{2.64}{\sqrt{12}}$cm= 0.763cm). Given γ depends only on the position of the layers of the detector, it is constant and it can be determined for the TT and MT assuming there was a single hit per layer. The factor γ is 0.21 for the TT and 0.85 for the MT.

The angular resolution can be rewritten as :

$$\delta\theta = \frac{\gamma}{(\tan\theta_x)^2 + \left(\tan\theta_y\right)^2 + 1} = \gamma\cos^2\theta \tag{4.22}$$

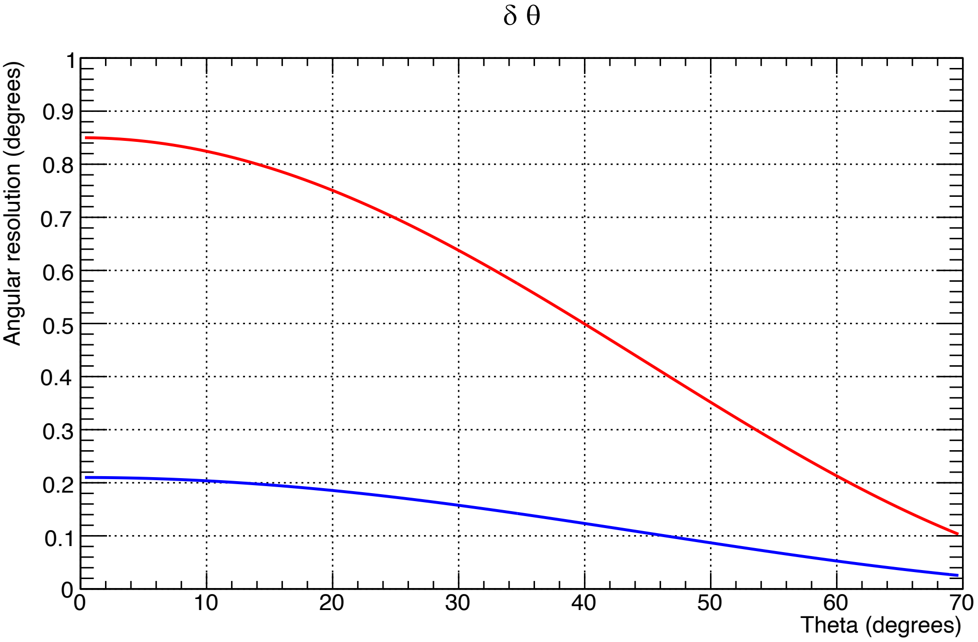

Figure 4.13: Angular resolution for TT (blue line) and MT (red line).

Fig. 4.13 shows the angular resolution for the TT (blue line) and the MT (red line) using Eq. 4.22. Fig. 4.13 shows a better angular resolution for the TT than MT because of the larger distance between layers in the TT. The minimum angular resolution for the TT is 0.02° and the maximum 0.21°. The angular resolution for the MT varies between 0.10° and 0.85°.

The inital bin size for the pixel (ρ,θ) of the accumulator matrix in the HT is defined by (2.64 cm , 0.85°) in the MT. The value of 2.64 cm corresponds to the granularity of the MT (strip size). The value 0.85° is the maximum angular resolution in the MT. As mentioned, in order to remove horizontal tracks, the acceptance angle defined for the MT corresponds to the interval (-70°; 70°). From these values the number of bins for θ is 166 and the number of bins for ρ is 65.

4.3.4 Optimization of Hough transform

To optimize the HT method, cosmic muons are simulated in the MT. This data will be used for the optimization required for finding the best bin size of the accumulator matrix of HT.

The JUNO simulation provides information on the muon directions. As mentioned, applying Hough's method we will obtain the values of $\theta_x, \theta_y, \rho_x, \rho_y$ to define the direction of the muons in 3D. The JUNO simulation is used to compare the reconstruction values obtained by the Hough method. $\Delta\theta_u$ is defined as the difference between the Hough angle ($\theta_{u_{simu}}$) given by the simulation and the Hough angle ($\theta_{u_{reco}}$) given by the reconstruction method in each projection. The component u refers to the reconstruction Hough angle of the projection XZ or YZ ($\theta_u = \theta_x, \theta_y$).

$$\Delta\theta_u = \theta_{u_{simu}} - \theta_u \tag{4.23}$$

Fig. 4.14 shows the distribution associated to $\Delta\theta_x$(blue line) and $\Delta\theta_y$(red line) with a standard deviation of 0.78° and 0.83°, respectively. Both distributions are similar. To produce this results the number of bins on ρ and θ were (40,170). This was choosen using the bin optimization as will be discussed.

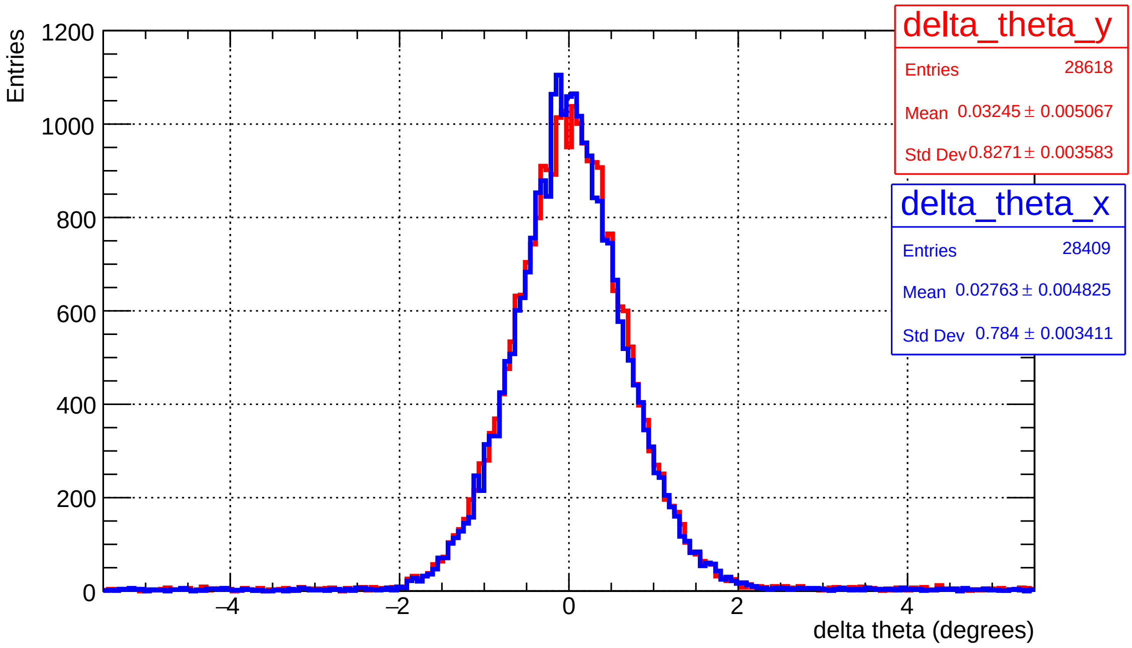

Figure 4.14: Distribution of $\Delta\theta_x$ (blue line) and $\Delta\theta_y$ (red line).

Almost 90% of the tracks were reconstructed with only one track as expected as I simulated 1 muon per event. In case there are more reconstructed they are considered fake tracks. Fig.4.15 shows the number of tracks reconstructed by the HT for XZ projection.

The best track reconstruction is the one which gives the minimum value of the $\chi^2_{Reduced}$. This quantity is defined as $\chi^2_{Reduced} = \chi^2/ndof$, where $ndof$ is the number of degrees of freedom and χ^2 is the chi-squared in 2D for a straight line. The $\chi^2_{Reduced}$ distribution for XZ projection is shown in Fig. 4.16. The $\chi^2_{Reduced}$ in function of the number of tracks for each projection is illustrated in Fig. 4.17 and Fig. 4.18. These figures will be used to impose criteria for the removal of fake reconstructed tracks.

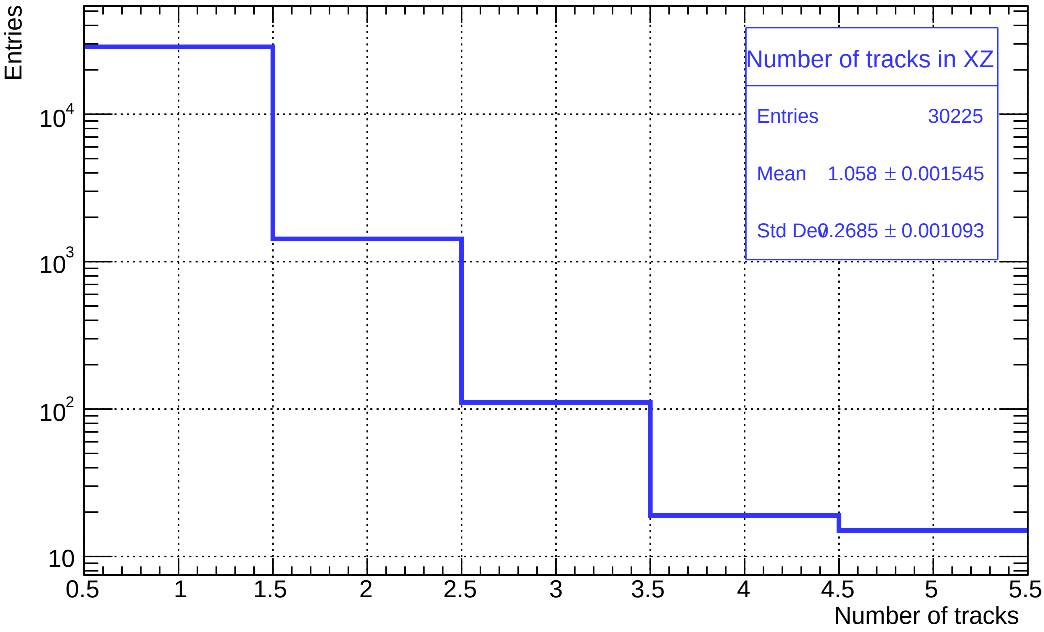

Figure 4.15: Number of tracks reconstructed in XZ projection.

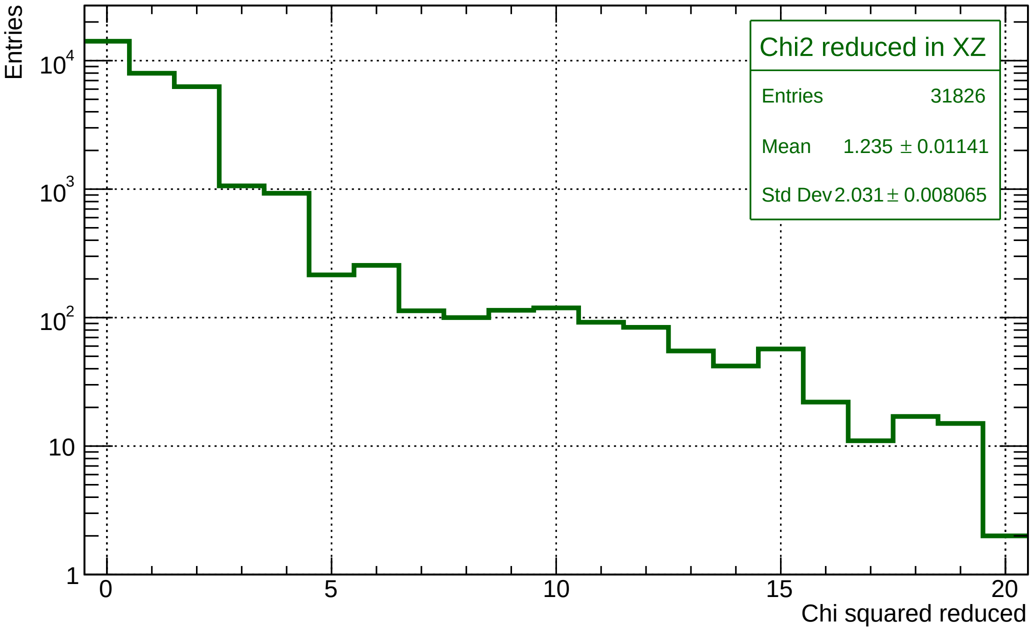

Figure 4.16: $\chi^2_{Reduced}$ distribution for XZ projection.

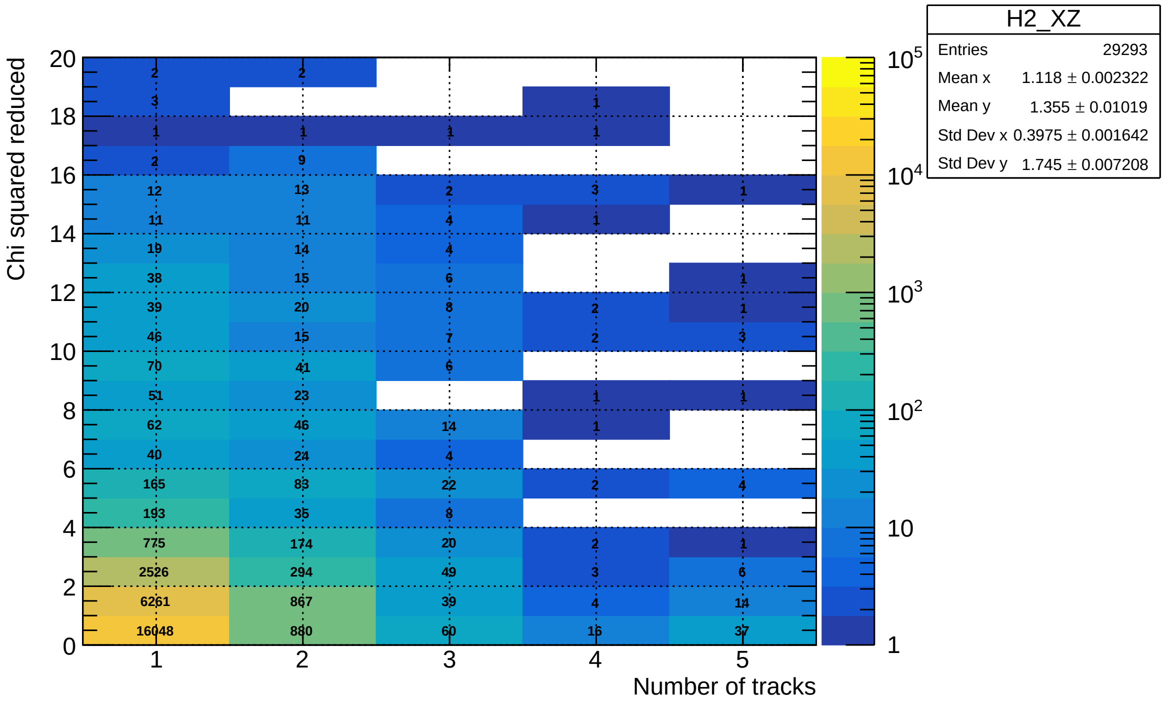

Figure 4.17: Number of tracks saved in the Hough reconstruction for XZ.

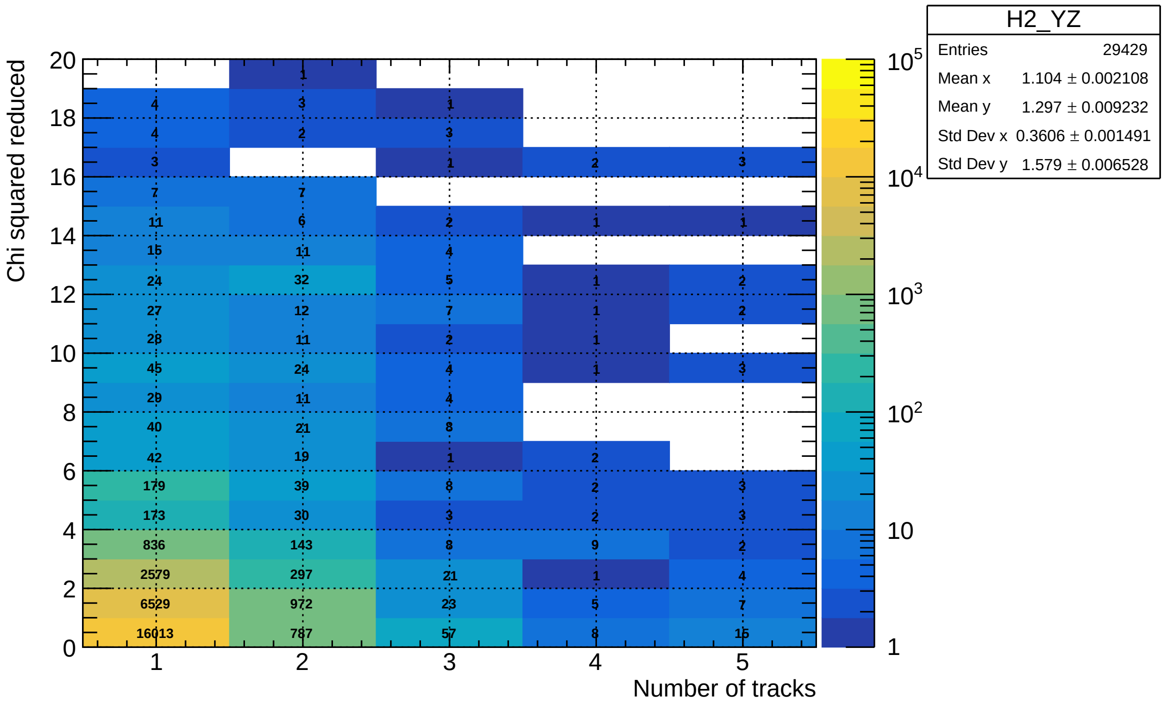

Figure 4.18: Number of tracks saved in the Hough reconstruction for YZ.

Using the simulation data, one example of HT on MT is presented in Fig. 4.19. The simulated track is given by the blue line, the green line corresponds to the JUNO software and the Hough Method is represented by the red line. The reconstruction of the Hough method is in agreement with the simulation and the JUNO reconstruction.

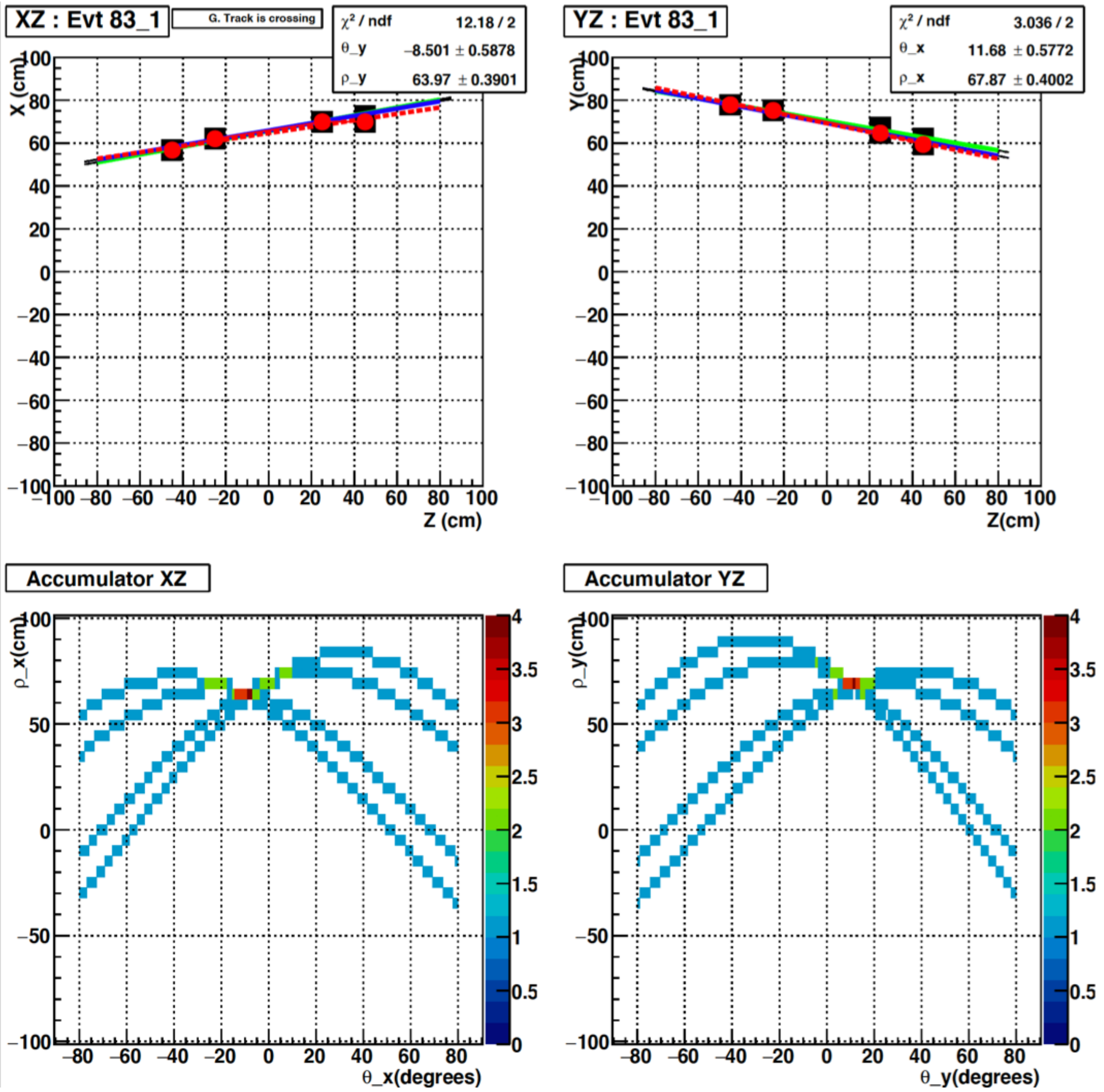

Figure 4.19: Example of Hough Transform on MT using simulation data. The upper part shows the triggered channels for XZ (left side) and YZ (right side) projections. The simulated track is given by the blue line, the green line corresponds to the JUNO software and the Hough Method is represented by the red line. At the bottom is shown the accumulator matrix of the Hough transform using the sample of channels triggered in the XZ projection (left side) and YZ (right side). In the accumulator matrix XZ four sinusoidal curves intersect in the cell (-8.5° , -63.9cm), while the matrix YZ cell is (-11.7° , -67.9cm). For the construction of these accumulator matrices, the optimization results described in Fig.4.20 and Fig.4.21 has been used. The bin size used of each accumulator matrix is (4.9 cm , 0.83°).

As mentioned in the Hough method, the bin size of the accumulator matrix is a fundamental parameter at the time of reconstruction. The best bin size will be defined according to the maximum number of recorded tracks. In other words, a bin optimization procedure will be performed.

The bin optimization is based on the construction of a matrix to be filled by the efficiency of the reconstructed track numbers. In this matrix, the horizontal axis represents the bin numbers for ρ(30,90), the vertical axis corresponds to the bin numbers for θ(90,180), on the right side of the matrix shows the efficiency of the reconstructed track numbers. The bin optimization in XZ and YZ are shown in Fig. 4.20 and Fig. 4.21, respectively.

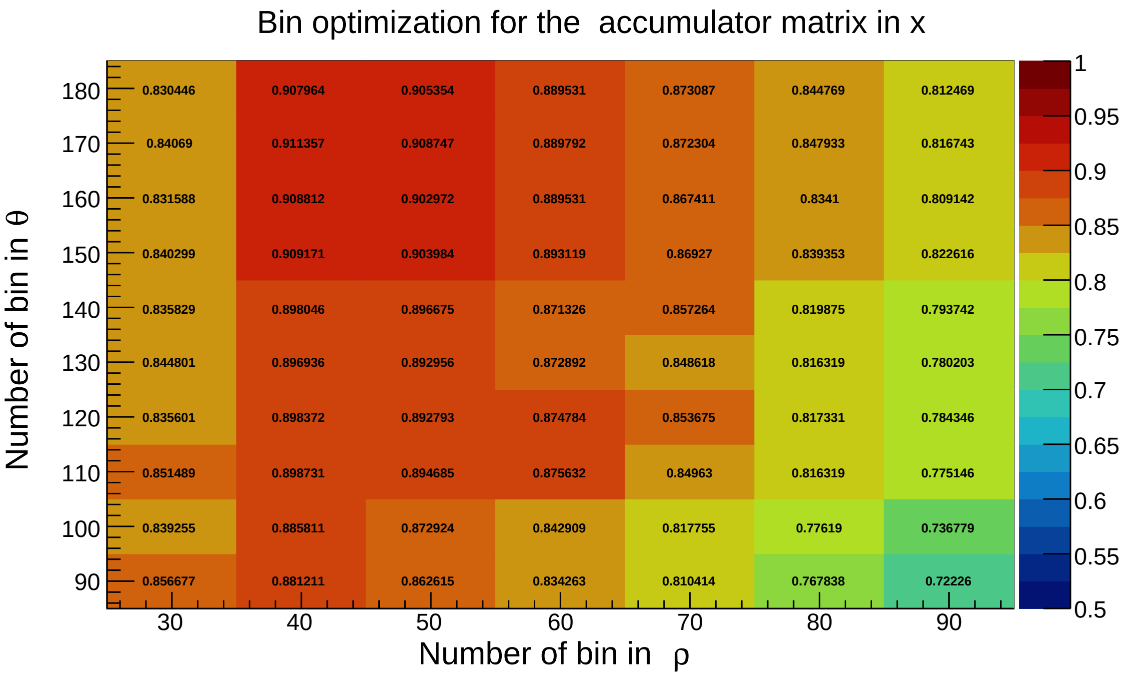

	30	40	50	60	70	80	90
180	0.830446	0.907964	0.905354	0.889531	0.873087	0.844769	0.812469
170	0.84069	0.911357	0.908747	0.889792	0.872304	0.847933	0.816743
160	0.831588	0.908812	0.902972	0.889531	0.867411	0.8341	0.809142
150	0.840299	0.909171	0.903984	0.893119	0.86927	0.839353	0.822616
140	0.835829	0.898046	0.896675	0.871326	0.857264	0.819875	0.793742
130	0.844801	0.896936	0.892956	0.872892	0.848618	0.816319	0.780203
120	0.835601	0.898372	0.892793	0.874784	0.853675	0.817331	0.784346
110	0.851489	0.898731	0.894685	0.875632	0.84963	0.816319	0.775146
100	0.839255	0.885811	0.872924	0.842909	0.817755	0.77619	0.736779
90	0.856677	0.881211	0.862615	0.834263	0.810414	0.767838	0.72226

Figure 4.20: Binning accumulator matrix for XZ projection. Around 91% of the tracks were reconstructed in the pixel (40,170) which corresponds to a bin size of (4.9 cm , 0.83°).

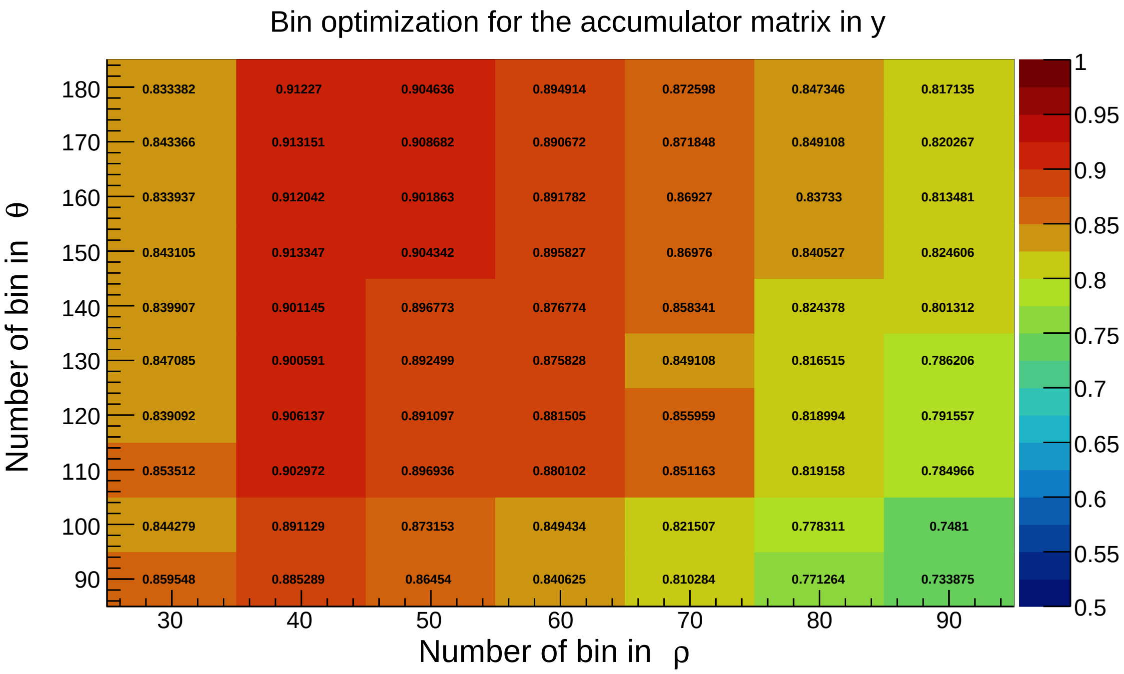

	30	40	50	60	70	80	90
180	0.833382	0.91227	0.904636	0.894914	0.872598	0.847346	0.817135
170	0.843366	0.913151	0.908682	0.890672	0.871848	0.849108	0.820267
160	0.833937	0.912042	0.901863	0.891782	0.86927	0.83733	0.813481
150	0.843105	0.913347	0.904342	0.895827	0.86976	0.840527	0.824606
140	0.839907	0.901145	0.896773	0.876774	0.858341	0.824378	0.801312
130	0.847085	0.900591	0.892499	0.875828	0.849108	0.816515	0.786206
120	0.839092	0.906137	0.891097	0.881505	0.855959	0.818994	0.791557
110	0.853512	0.902972	0.896936	0.880102	0.851163	0.819158	0.784966
100	0.844279	0.891129	0.873153	0.849434	0.821507	0.778311	0.7481
90	0.859548	0.885289	0.86454	0.840625	0.810284	0.771264	0.733875

Figure 4.21: Binning accumulator matrix for YZ projection. The best pixel for YZ is found in (40,150) which corresponds to a bin size of (4.9 cm , 0.93°), where around 91% of the tracks were reconstructed.

The criteria concerning the number of tracks, the reduced χ^2 and $\delta\theta$ angle guarantee a good track selection when reconstructing and guarantees the removal of fake tracks. The bin optimization procedure was constructed considering the following criteria for each projection :

- Number of tracks = 1 or 2
- $-5° \leq \Delta\theta_x \leq 5°$
- $\chi_x^2 \leq 15$. And corresponding criteria for YZ projection.

In Fig. 4.20, the best cell size is found for (40,170) which corresponds to a bin size of (4.9 cm , 0.83°). Around 91% of the tracks were reconstructed. For Fig. 4.21, the best pixel is found in (40,150) which corresponds to a bin size of (4.9 cm , 0.93°), where around 91% of the tracks were reconstructed. It has to be said that a large plateau in reconstructed efficiency is observed between 150 and 170 in θ for XZ and YZ. As XZ and YZ projections are symmetric, we have decided to use the same bin size registered for XZ projection (4.9 cm , 0.83°) also for YZ projection.

4.4 Comparison between JUNO Reconstruction and Hough method

As mentioned, the Muon Telescope provides us the possibility to prepare and test the reconstruction algorithms to be used in the TT. In this section, we will describe the calculation of the detection efficiency of the Muon Telescope using both softwares : JUNO and Hough. The track reconstruction efficiency will be studied using the simulation data and cosmic real data. One comparison between JUNO Reconstruction and Hough Method is focused on the track reconstruction efficiency. The CPU time for both reconstruction methods also will be discussed.

4.4.1 Calculation of the detection efficiency of the MT

The detection efficiency of the strip (ϵ_{MT}) is given by :

$$\epsilon_{MT} = \frac{h_o}{h_e} \tag{4.24}$$

where h_o is the number of hits observed and h_e the number of hits expected. The observed hit corresponds to a trigger recorded in the MT in a given layer. A hit is an expected hit if from the reconstruction the muon is expected to cross this strip. Note that in the TT it will not be possible to calculate the efficiency this way as there are only 3 layers and 3 points are required for reconstruction of muons. In the MT, thanks to it having 4 layers, it is practical to use this method to estimate the detector efficiency as tracks can still be reconstructed when crossing inefficient strips.

To filter out the background noise, the discriminator threshold is set to 1/3 p.e. In addition, to ensure that no possible hits are missed, the possibility that the track passes through the nearest neighbours is also considered.

Using the simulation data, the MT detection efficiencies provided by the JUNO reconstruction (red line), Hough Method (blue line) and the simulation data (green) for C0R is shown in the Fig. 4.22. The MT detection efficiencies for the 3 cases are higher than 95%. The reconstruction methods show that more than 90% of hits are recorded in almost all strips.

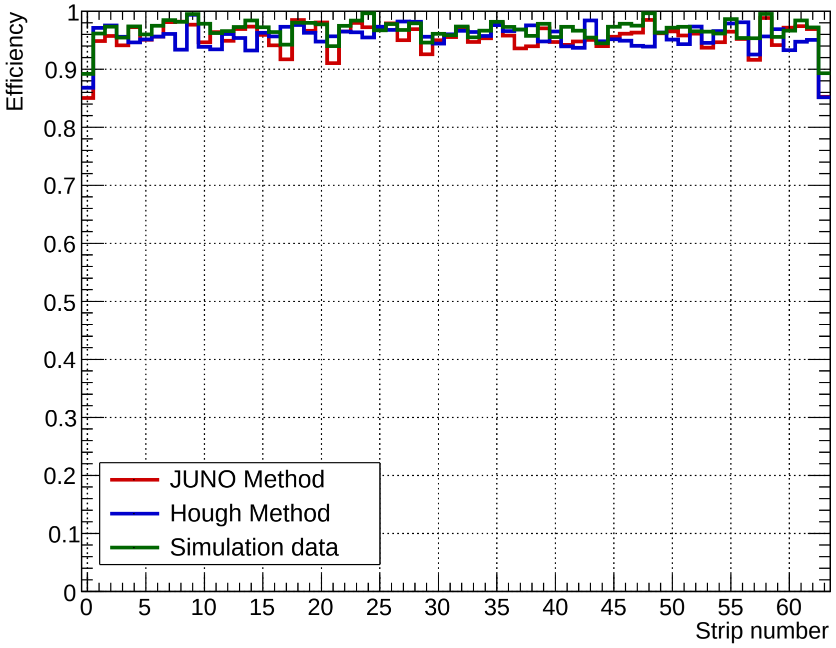

Figure 4.22: The MT detection efficiencies provided by the JUNO and Hough software for C0R.

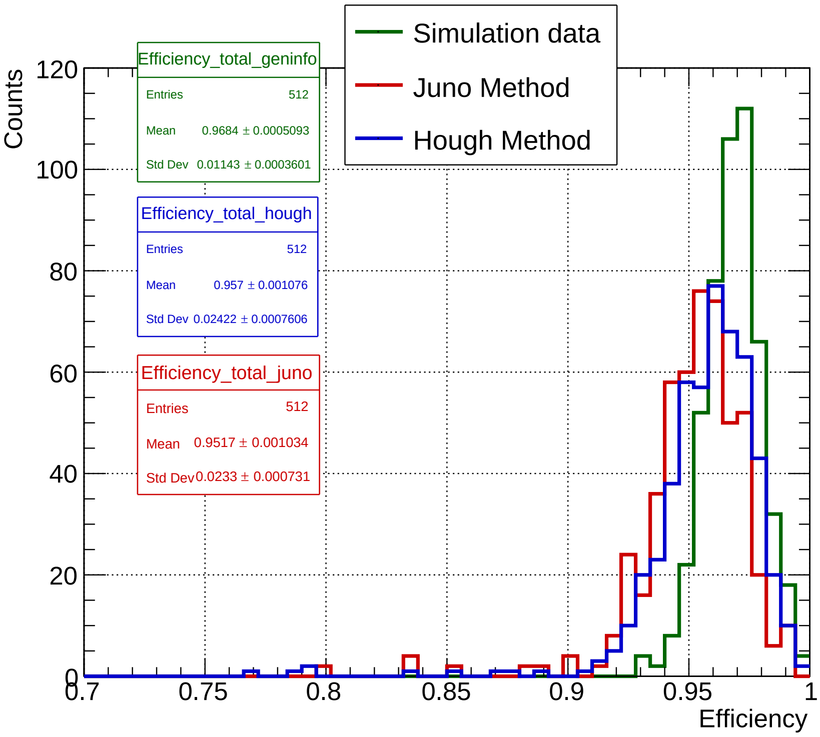

Figure 4.23: The MT detection efficiencies by the JUNO and Hough software using simulation data.

The total efficiency considering the 512 MA-PMT channels of the MT is summarised in Fig. 4.23. The efficiency of Hough's method (blue line) is $\sim$ 96%, which is slightly larger than that of JUNO (red line) at $\sim$ 95%. The efficiency given by the true muon path (green line) is $\sim$ 97%. During the simulation, the module strips are considered uniform. Hough's method shows a slight ($\sim$ 1%) favorable difference at the time of reconstruction compared to JUNO ($\sim$ 2%) with respect to the efficiency provided by the simulation.

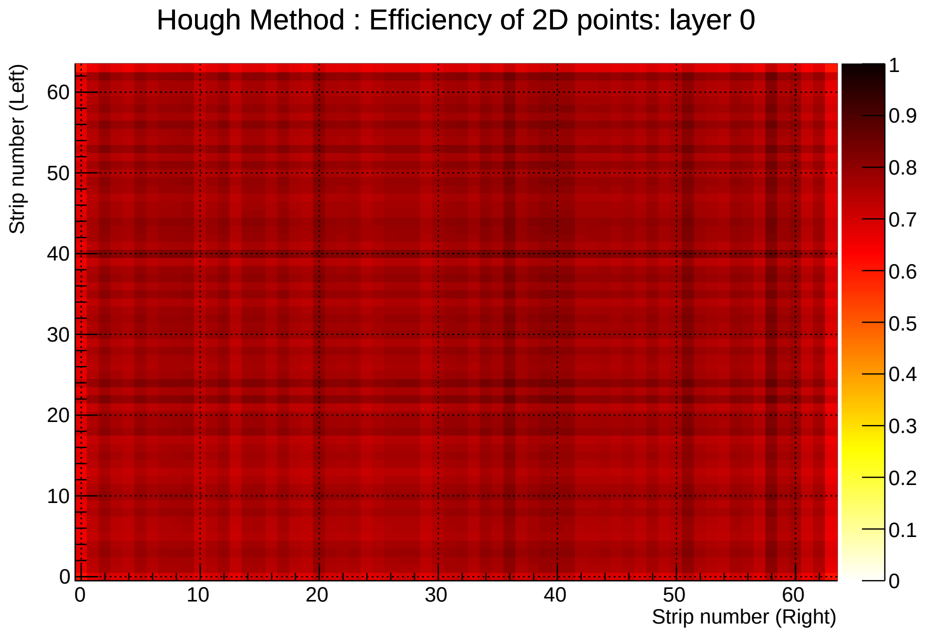

Figure 4.24: The MT detection efficiencies of 2D points provided by the Hough Method for the layer 0 using simulation data.

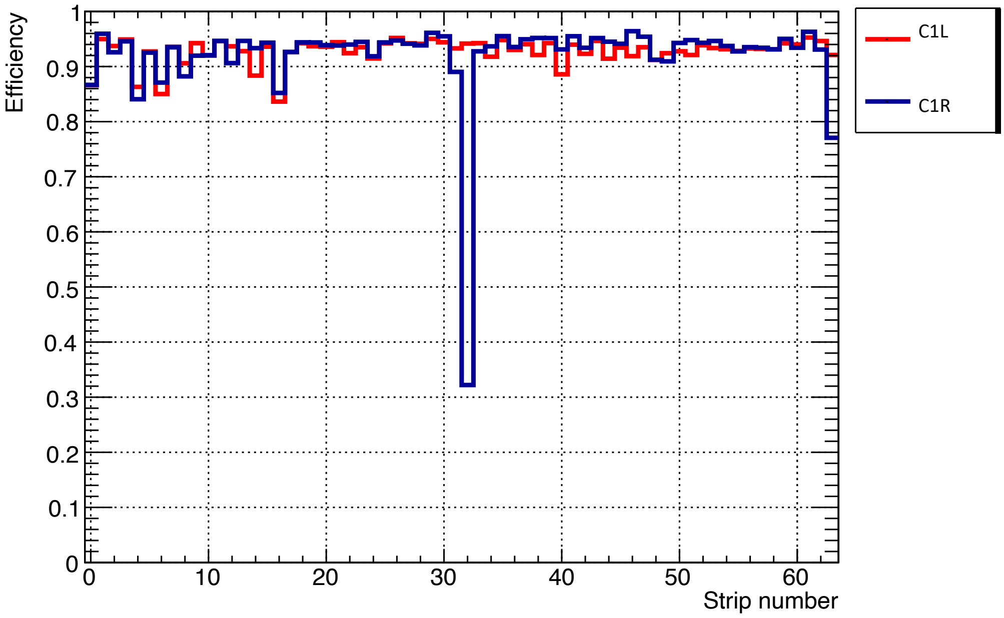

Figure 4.25: Efficiency using real data in the layer 1.

Using the simulation data, Fig. 4.24 shows the MT detection efficiency of 2D points provided by the Hough Method for the layer 0. Each bin size in this histogram is the xy granularity. An efficiency given by the multiplication of the efficiency provided by the strip in the x-direction and the y-direction is associated with each pixel.

Using real data, the efficiency for the cards located in the layer 1 per strip number is shown in Fig. 4.25. The MT detection efficiencies in this layer shows on average of 90% recorded on most strips. However, the channel 32 shows a low efficiency $\sim$ 30%. The low efficiencies reported in some channels in the MT may be the result of the condition of the fibers (damaged or broken), or due to aging of the scintillation bars. As has been mentioned throughout this thesis.

In layer 3, the efficiency ($\sim$ 70%) is lower in comparison to the others layers in the MT, as shown in Fig. 4.26 using the Hough's Method. The MT detection efficiencies of 2D points provided by the Hough Method for the layer 3 are shown in Fig. 4.27. The values obtained for the efficiency in 2D range are between (0.35 ; 0.82) as shown in the layer 3. The low efficiencies reported in some channels in the layer was justified in the previous paragraph.

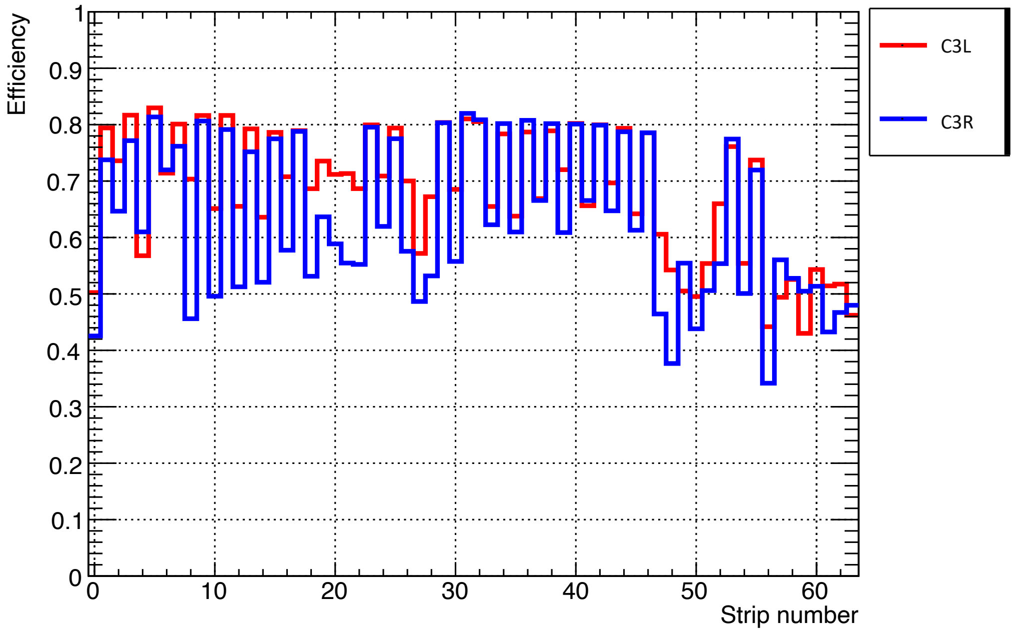

Figure 4.26: Efficiency using real data in the layer 3.

The MT detection efficiencies by the JUNO and Hough software using real data are summarised in Fig. 4.28. Considering the 512 MA-PMT channels, the efficiency of Hough's method is ($\sim$ 98%) is slightly more efficient than JUNO ($\sim$ 95%). The Hough transform shows relatively higher efficiency in comparison to the JUNO Software.

The difference between the values of the efficiencies obtained using the simulation data (Fig. 4.23) and the real data (Fig. 4.28) in the MT is due to the fact that the effects of the quality of the strips must be taken into account in the simulation.

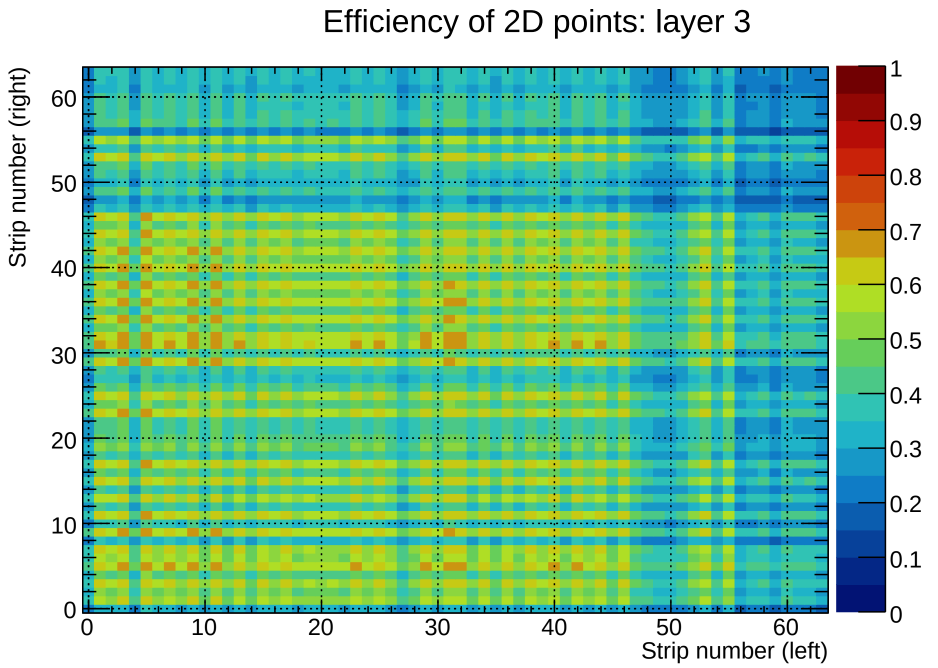

Figure 4.27: The MT detection efficiencies of 2D points provided by the Hough Method for the layer 3, colours indicate the detection efficiency.

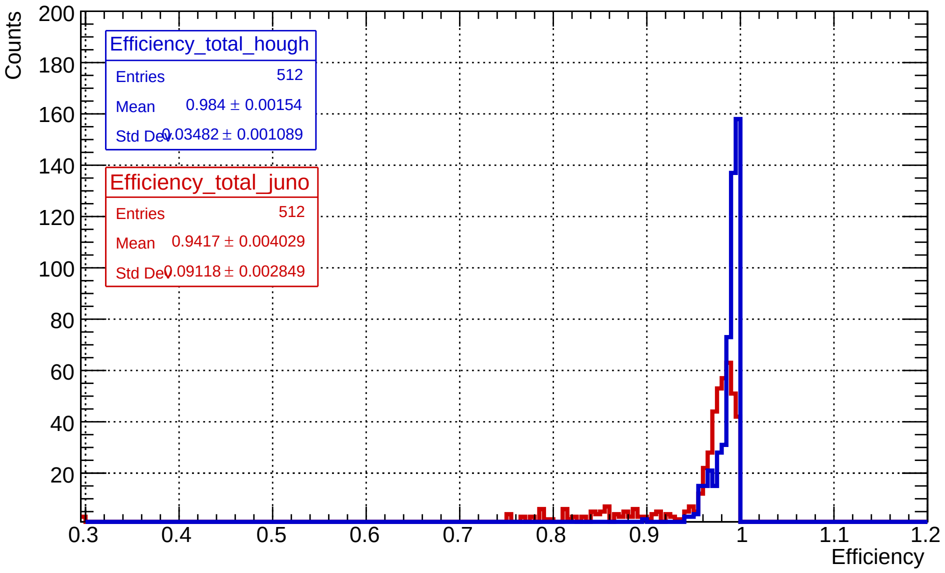

Figure 4.28: The MT detection efficiencies by the JUNO and Hough software using real data.

The trigger rate of the cosmic muons is measured in the MT during 1 hour was calculated using the Hough method and JUNO reconstruction. Fig. 4.29 shows the zenith angular distribution, where the zenith angle θ goes from 110° to 180° due to the acceptance angle of the Muon Telescope. The muon rate observed by Hough and JUNO reconstruction are similar ~ 128 Hz.

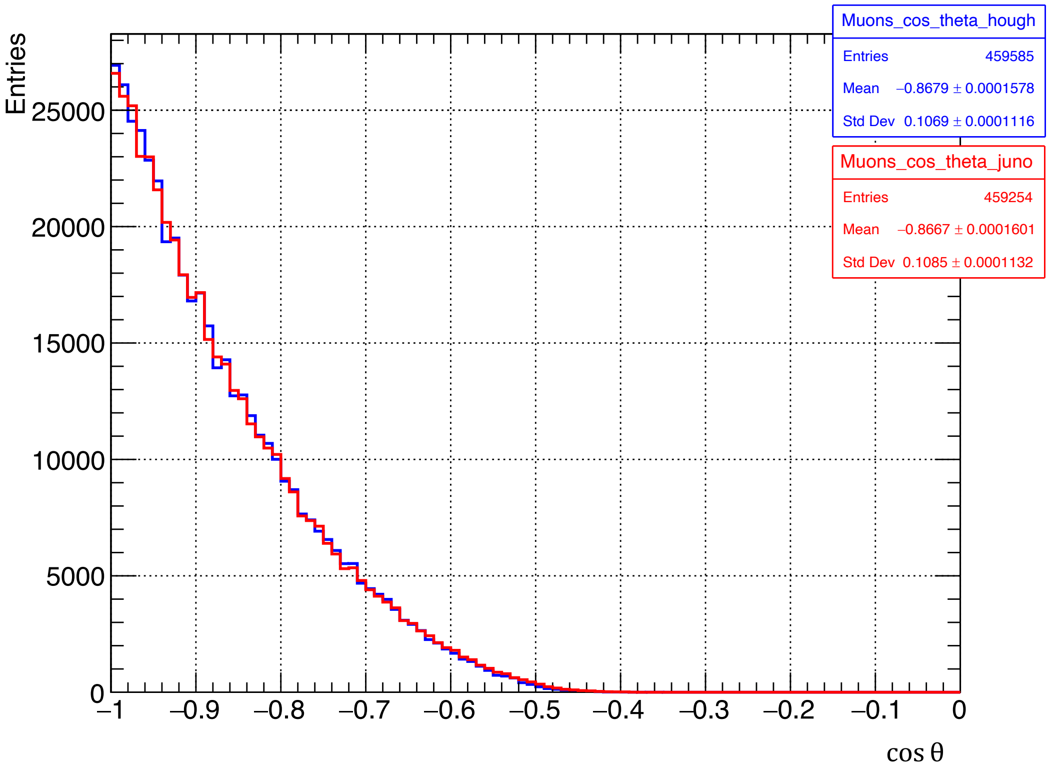

Figure 4.29: Zenith angle distribution using the JUNO software (red line) and Hough Method (blue line) for 1 hour of data taking in the MT.

4.4.2 CPU Time for the reconstruction methods

Other difference between the two methods of reconstruction lies in the CPU time. The CPU time is linear with the amount of data. Table. 4.1 summarises the running time used for JUNO software and the HT method.

Table 4.1: Time running of the reconstruction methods : JUNO and Hough.

Data taking	JUNO	Hough
1 h (51 MB)	1.73 h	0.5h
5h (262 MB)	9.3 h	2.5h
24 h (1324 MB)	42.75h	12h

Fig. 4.30 shows for Hough method (blue line), 50% time used for the data taking is required for the reconstruction analysis. Using the data provided by the simulation and the data measured in the MT, it can be concluded that the Hough reconstruction is a good

method that can be used in the future in the TT. This conclusion is due to the advantages presented against the JUNO algorithm. Hough showed a high efficiency, an excellent execution time and the possibility of including more noise when reconstructing the events.

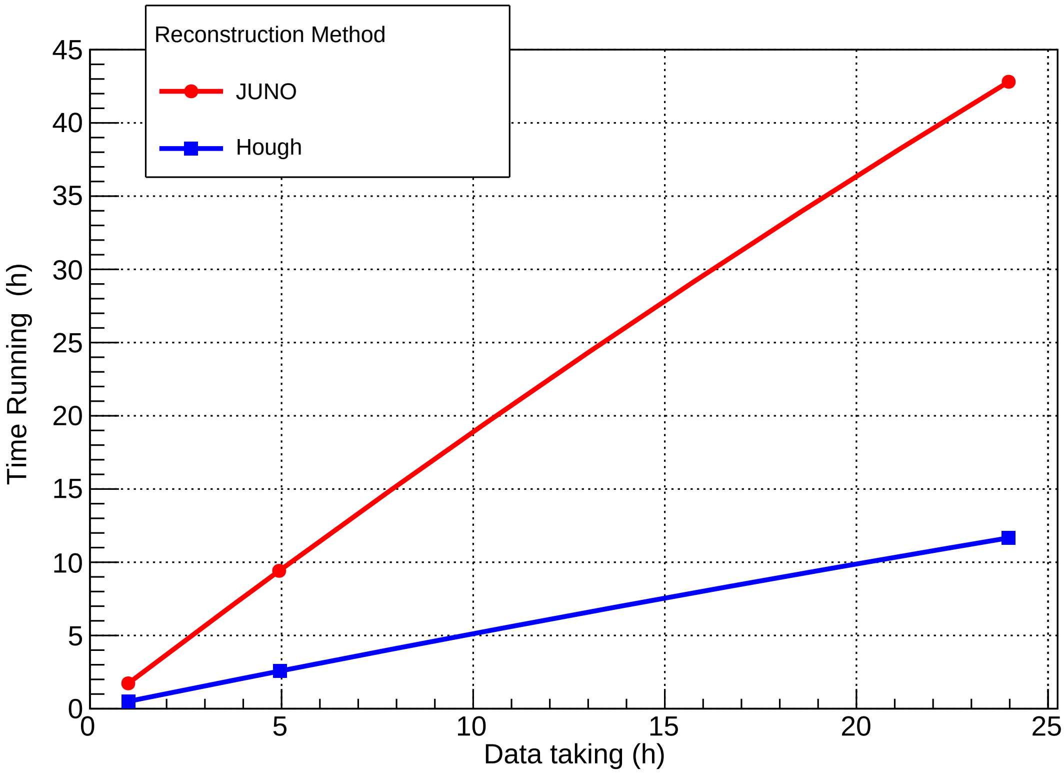

Figure 4.30: CPU time for the reconstruction methods : JUNO (red line) and Hough (blue line).

Reconstruction des muons

> *"Le nombre est le maître des formes et des idées, et la cause des dieux et des démons."*
> Pythagoras.

Dans le logiciel officiel JUNO, une méthode de reconstruction a été mise en œuvre pour l'analyse des muons cosmiques arrivant au TT, où le flux de muons cosmiques ou le bruit de fond cosmogénique peut être estimé. Cette méthode de reconstruction peut être vérifiée en conditions réelles avec le télescope à muons. Comme indiqué dans le chapitre 3, au cours du développement de cette thèse, l'électronique implémentée dans le télescope à muons est dépourvue des cartes responsables des déclenchements L1/L2. Par conséquent, la sélection des "candidats muons", en considérant les coïncidences XY par couche, doit être faite dans le logiciel. Ensuite, nous avons besoin des coïncidences dans au moins 3 couches pour construire au moins 3 points 3D à partir des canaux MA-PMT déclenchés.

Le logiciel officiel de JUNO ajuste une ligne droite 3D à chaque combinaison possible des points 3D détectés dans des couches différentes. L'algorithme de reconstruction utilisé dans JUNO est basé sur l'ajustement aux moindres carrés d'une ligne droite 3D. L'algorithme reconstruit une piste possible avec un processus combinatoire si le nombre de points 3D est supérieur à 3 et inférieur à 80.

Le logiciel officiel JUNO est également utilisé pour reconstruire les muons cosmiques à partir des données enregistrées par le Télescope à Muons. Le télescope était en position horizontale pendant l'acquisition des données. Cela indique qu'il n'y a pas d'angle d'élévation par rapport à l'horizontale.

Avec ces traces de muons reconstruites, la direction de chaque muon est calculée. Utilisant ce logiciel, j'ai calculé un taux de muons de 130 Hz au Télescope à Muons. La distribution de l'angle zenithal va de $110°$ à $180°$. L'intensité du flux de muons a été observée expérimentalement de manière très détaillée. Il a été constaté que ce flux est une fonction de l'angle zénithal, suivant une loi de puissance cosinusoïdale. La valeur théorique calculée pour le flux de muons traversant une couche de télescope à muons est d'environ 419 Hz. Cependant, nous constatons que la valeur expérimentale dans notre télescope correspond à 500 Hz, ce qui implique que la plupart des déclenchements coïncidents proviennent effectivement des muons. Si un muon traverse au moins 3 couches, le taux total de muons diminue en raison de l'angle d'acceptation. Elle est proche des 130 Hz mesurés dans le télescope à muons.

A partir des traces reconstruites, la distribution azimutale a été calculée. Différents pics ont été observés dans cette distribution en raison de la géométrie du télescope à muons et du fait que chaque choc reconstruit est situé au centre des franges. Les pics sont également révélateurs d'une contrainte géométrique due à la granularité du télescope.

Les trajectoires des muons ont été projetées en utilisant les coordonnées de Mollweide, ce qui permet de réaliser une radiographie du bâtiment à l'aide de muons. L'algorithme officiel utilisé par JUNO est limité par le nombre de points, s'il y a trop de points, l'algorithme passe beaucoup de temps avant de converger. Par conséquent, une nouvelle méthode de reconstruction est nécessaire. Afin de résoudre ce problème, j'ai dévéloppé une reconstruction basée sur la transformée de Hough. La transformée de Hough (HT) est un algorithme breveté en 1962. HT est communement utilisé pour extraire des lignes, des cercles et des ellipses.

La mise en œuvre de HT définit un mappage des points (espace cartésien) dans un espace d'accumulation (espace de Hough). Chaque point (x_i, y_i) est paramétré par une fonction sinusoïdale, $\rho = x_i cos\theta + y_i sin\theta$, où ρ est la distance perpendiculaire de la ligne à l'origine et θ est l'angle que fait la perpendiculaire avec l'axe des x. La ligne dans l'espace cartésien est représentée comme le point de croisement (ρ, θ) des courbes sinusoïdales dans l'espace de Hough. Ce chapitre se concentrera sur la description des méthodes utilisées pour la reconstruction des muons cosmiques dans le télescope à muons..

Le méthode de reconstruction basée sur HT dépendra considérablement de la taille de la matrice d'accumulateurs. HT présente inconvénient comme l'efficacité de la matrice d'accumulateurs. Si le pixel est trop petit ou trop grand, la visibilité du pixel principal sera réduite.

Contrairement à l'algorithme utilisé dans le logiciel JUNO où il travaille en trois dimensions, le HT aborde le problème de la reconstruction comme 2 problèmes bidimensionnels.

Le HT classe les canaux MA-PMT déclenchés dans les modules en projections XZ et YZ. Chaque projection est analysée séparément pour ensuite procéder à une reconstruction de la piste en 3D.

Le logiciel officiel JUNO a été adapté pour simuler les muons qui traversent le prototype du TT. Cela m'a permis d'optimiser la matrice de l'accumulateur de HT, de calculer l'efficacité de détection, les distributions angulaires, et surtout de comparer les méthodes de reconstruction JUNO et HT.

A partir de l'optimisation de la matrice de l'accumulateur, j'ai obtenu le nombre de bins nécessaires pour obtenir une efficacité élevée de la méthode de reconstruction. Cette étude a permis de conclure que la taille du bin pour la matrice correspond à (4,9 cm, 0,83°). La valeur de 0,83° est cohérente avec la résolution angulaire calculée pour le télescope à muons.

L'efficacité de détection obtenue avec la HT est 96% utilisant des données simulées, valeur de doit être comparée avec l'efficacité simulée de 97%. La méthode officielle de JUNO cependant donne une efficacité de 95%, légèrement moins performante que pour la HT.

Une autre différence entre les deux méthodes de reconstruction réside dans le temps utilisé pour reconstruire les événements. Le temps CPU est linéaire avec la quantité de données. La méthode de Hough nécessite 50% du temps de la prise de donnée pour l'analyse de la reconstruction.

En utilisant les données fournies par la simulation et les données mesurées dans le MT, on peut conclure que la reconstruction de Hough est une bonne méthode qui peut être utilisée à l'avenir dans le TT. Cette conclusion est due aux avantages présentés par rapport à l'algorithme déjà implémenté dans JUNO.

Conclusion

Several experiments have been performed to study the properties of neutrinos and the parameters of neutrino oscillations. However, many questions remain open, such as the neutrino mass hierarchy, the value of the δ_{cp} phase, the nature of neutrinos, among others. Answers to these questions are essential for a deeper understanding of our universe.

The Jiangmen Underground Neutrino Observatory (JUNO) is a multipurpose underground liquid scintillation detector with a target mass of 20 kt and an energy resolution of 3% at 1 MeV. The main goal of JUNO is to determine the neutrino mass hierarchy at 3σ during 6 years of operation, as well as to provide accurate measurements of neutrino oscillation parameters. For this purpose, JUNO uses antineutrinos from reactors located 53 km from its detector. The excellent energy resolution and the large volume envisaged for the JUNO detector offer exciting possibilities to address many important questions related to neutrinos and astrophysics.

Among its detector parts, JUNO has a muon tracker called Top Tracker. It consists of three layers of plastic scintillator. The Top Tracker plays a key role in JUNO, as it provides accurate tracking of cosmic muons, which is essential for understanding and reducing the cosmogenic background in the detector. This thesis focuses on this part of the JUNO detector.

One of the goals of this thesis was to calibrate part of the electronic chain of the Top Tracker using a prototype Top Tracker called Muon Telescope and to compare some results (such as threshold, linearity) with a test bench. The different data acquisition modes (such as TRT, Pedestal, LED and Normal) were tested. This allowed the development of several calibration tests.

Using the 8 electronic boards of the Muon Telescope, it was possible to extract relevant parameters to be used in the Top Tracker. One of the main parameters is the electronics threshold important for electronic noise reduction during measurements. The threshold was found to be uniform and stable over the 64 electronic channels of the each front end chip.

The conversion factor between physical charge and electronic charge was determined. Linearity tests showed that one photoelectron corresponds to about 10.5 ADC counts. These tests showed a linear region for charges up to 4 pC, corresponding to about 25 p.e. ,while for higher charges a saturation of the system is observed. In order for the photodetector to be sensitive to a single p.e, the MA-PMTs are operated at a High Voltage corresponding to a gain of 10^6. This high voltage was also determined during this thesis.

However, the charge is not the only calibration parameter of the Muon Telescope. Calibration tests were also applied using time as the main parameter. The value of the electronics dead-time was determined to be $10\mu s$, mainly defined by the charge readout time of the 8-bit Wilkinson ADC in MAROC3. In order to have a fast and accurate measurement, it is crucial that the value of the hold delay, is determined relatively accurately for the triggered channels. This study showed a charge dependence with the optimal hold delay value. For this reason a compromise between high and low charges has been found. One other parameter associated with the timing of the detector studied is the time walk (t_{walk}). In a scenario with a threshold of $1/3$ p.e and considering charges, between low charges, ~ 1 p.e., and high charges, >10 p.e., has been found to vary by more than 6 ns. This is also taken into account in the Hold delay determination and has also to be taken into account in any timing studies of the detector.

To measure and optimize the efficiency of the Muon Telescope detection, the cosmic muons arriving in Strasbourg have been measured. In the absence of the concentrator board (card responsible for the XY trigger) a software was used to evaluate it with a selection window defined as large as 100 ns, yielding an XY coincidence rate measured at about 500 Hz/layer.

As a first step, cosmic muons have been reconstructed using the official JUNO software. The Muon Telescope shows a muon rate of 135 Hz. The zenith angle distribution ranges from $113°$ to $180°$ due to the angular acceptance of the Muon Telescope.

The official algorithm used by JUNO is limited by the number of reconstructed points; if there are too many points, the algorithm takes a long time to converge. Therefore, as a second goal of this thesis to solve this problem, a reconstruction based on the Hough transform was developed.

The JUNO simulation software has been adapted to the Muon Telescope. Using the data provided by the simulation, the Hough method was optimized. The binning of the histogram (accumulator) used in the Hough method was optimized by maximizing the number of reconstructed tracks. The optimal bin size of the two considered variables, distance and angle, is (4.9cm, 0.83°). The bin size at Hough's theta angle 0.83° is in accordance with the worse angular resolution of 0.85° observed at $\theta = 180°$.

The advantages of Hough's method over the JUNO reconstruction using the data from the simulation and from the cosmic muons measured at Strasbourg by the Muon Telescope are relevant. The Hough transform shows relatively higher efficiency and significantly shorter runtime in comparison to the existing reconstruction method (JUNO Software).

It can be concluded that these advantages make the Hough transform a good method that can be used in the future in the Top Tracker.

Conclusion

Plusieurs expériences ont été réalisées pour étudier les propriétés des neutrinos et les paramètres des oscillations des neutrinos. Cependant, de nombreuses questions restent ouvertes, comme la hiérarchie des masses des neutrinos, la valeur de la phase δ_{cp}, la nature des neutrinos, entre autres. Les réponses à ces questions sont essentielles pour une meilleure compréhension de notre univers.

L'observatoire souterrain de neutrinos de Jiangmen (JUNO) est un détecteur souterrain polyvalent à scintillation liquide avec une masse cible de 20 kt et une résolution en énergie de 3% à 1 MeV. L'objectif principal de JUNO est de déterminer la hiérarchie des masses de neutrinos à 3σ pendant 6 ans de fonctionnement, ainsi que de fournir des mesures précises des paramètres d'oscillation des neutrinos. Pour ce faire, JUNO utilise des antineutrinos provenant de réacteurs situés à 53 km de son détecteur. L'excellente résolution en énergie et le grand volume envisagé pour le détecteur JUNO offrent des possibilités passionnantes pour aborder de nombreuses questions importantes liées aux neutrinos et à l'astrophysique.

Parmi les éléments du détecteur, JUNO possède un traqueur de muons appelé Top Tracker. Il est constitué de trois couches de scintillateur en plastique. Le Top Tracker joue un rôle clé dans JUNO, car il assure un suivi précis des muons cosmiques, ce qui est essentiel pour comprendre et réduire le bruit de fond cosmogénique dans le détecteur. Cette thèse se concentre sur cette partie du détecteur JUNO.

Un des objectifs de cette thèse était de calibrer une partie de la chaîne électronique du Top Tracker en utilisant un prototype de Top Tracker appelé Télescope à Muons et de comparer certains résultats (tels que le seuil, la linéarité) avec un banc de test. Les différents modes d'acquisition de données (tels que TRT, Pedestal, LED et Normal) ont été testés. Ceci a permis de développer plusieurs tests de calibration.

En utilisant les 8 cartes électroniques du télescope à muons, il a été possible d'extraire les paramètres pertinents à utiliser dans le Top Tracker. L'un des principaux paramètres est le seuil électronique, important pour la réduction du bruit électronique pendant les mesures. Le seuil s'est avéré être uniforme et stable sur les 64 canaux électroniques de chaque puce frontale.

Le facteur de conversion entre la charge physique et la charge électronique a été déterminé. Les tests de linéarité ont montré qu'un photoélectron correspond à environ 10,5 ADC. Ces tests ont montré une région linéaire pour des charges jusqu'à 4 pC, correspondant à environ 25 p.e ,alors que pour des charges plus élevées, une saturation du système est observée. Afin que le photodétecteur soit sensible à un seul p.e, les MA-PMTs sont opérés à une haute tension correspondant à un gain de 10^6. Cette haute tension a également été déterminée au cours de cette thèse.

Cependant, la charge n'est pas le seul paramètre de calibration du Télescope à Muons. Des tests d'étalonnage ont également été appliqués en utilisant le temps comme paramètre principal. La valeur du temps mort de l'électronique a été déterminée comme étant de $10\mu s$, principalement définie par le temps de lecture de la charge de l'ADC de Wilkinson de 8 bits dans MAROC3. Afin d'obtenir une mesure rapide et précise, il est essentiel que la valeur du délai du signal de HOLD soit déterminée de manière relativement précise pour les canaux déclenchés. Cette étude a montré une dépendance de la charge avec la valeur optimale du délai du signal de HOLD. Pour cette raison, un compromis entre des charges élevées et faibles a été trouvé. Un autre paramètre associé au timing du détecteur étudié est le time walk (t_{walk}). Dans un scénario avec un seuil de 1/3 p.e et en considérant les charges, on a constaté que la variation entre les faibles charges, $\sim$ 1 p.e, et les fortes charges, >10 p.e, était supérieure à 6 ns. Ceci est également pris en compte dans la détermination du délai du signal de HOLD et doit également être pris en compte dans toute étude de synchronisation du détecteur.

Pour mesurer et optimiser l'efficacité de la détection du Télescope à muons, les muons cosmiques arrivant à Strasbourg ont été mesurés. En l'absence de la carte concentrateur (carte responsable du déclenchement XY), un logiciel a été utilisé pour l'évaluer avec une fenêtre de sélection définie aussi grande que 100 ns, donnant un taux de coïncidence XY mesuré à environ 500 Hz/couche.

Dans un premier temps, les muons cosmiques ont été reconstruits à l'aide du logiciel officiel JUNO. Le télescope à muons montre un taux de muons de 135 Hz. La distribution de l'angle zénithal varie de 113° à 180° en raison de l'acceptation angulaire du télescope à muons.

L'algorithme officiel de JUNO est limité par le nombre de points reconstruits ; s'il y a trop de points, l'algorithme met beaucoup de temps à converger. Par conséquent, comme deuxième objectif de cette thèse pour résoudre ce problème, une reconstruction basée sur la transformée de Hough a été développée.

Le logiciel de simulation JUNO a été adapté au Télescope à Muons. En utilisant les données fournies par la simulation, la méthode de Hough a été optimisée. Le binning de l'histogramme (accumulateur) utilisé dans la méthode de Hough a été optimisé en maximisant le nombre de pistes reconstruites. La taille optimale du bin des deux variables considérées, la distance et l'angle, est (4.9cm, 0.83°). La taille du bin pour l'angle thêta de Hough de 0,83° est en accord avec la résolution angulaire plus faible de 0,85° observée à $\theta = 180°$(direction verticale).

Les avantages de la méthode de Hough par rapport à la reconstruction JUNO utilisant les données de la simulation et des muons cosmiques mesurés à Strasbourg par le télescope à muons sont significatifs. La transformée de Hough montre une efficacité relativement plus élevée et un temps d'exécution significativement plus court en comparaison avec la méthode de reconstruction existante (logiciel JUNO).

On peut conclure que ces avantages font de la transformée de Hough une bonne méthode qui peut être utilisée à l'avenir dans le Top Tracker.

Glossary

CB Concetrator Board. 56, 78

FAST-OR Global OR of all discriminator outputs of 64 channels of MAROC3. 57

FEB Front-End Board. 56, 78

GTB Global Trigger Board. 56

HT Hough transform. 119

IBD Inverse beta decay. 30

JUNO Jiangmen Underground Neutrino Observatory. 4

MA-PMT Multi-anode PMT. 50

MAROC3 Multi Anode ReadOut Chip. 57, 78

MT Muon Telescope. 77

PMT Photomultiplier tube. 48

ROB Readout Board. 56, 78

TT JUNO Top Tracker. 4, 43

Bibliography

[1] H. Becquerel. On the rays emitted by phosphorescence. *Compt. Rend. Hebd. Seances Acad. Sci.* 122(8):420–421, 1896.

[2] P. Radvanyi et al. The discovery of radioactivity. *Comptes Rendus Physique* 18(9):544–550, 2017. Science in the making: The Comptes rendus de l'Académie des sciences throughout history.

[3] M. Curie et al. *Rayons émis par les composés de l'uranium et du thorium*. Gauthier-Villars, 1898.

[4] E. Rutherford. Viii. uranium radiation and the electrical conduction produced by it. *The London, Edinburgh, and Dublin Philosophical Magazine and Journal of Science* 47(284):109–163, 1899.

[5] J. Chadwick. The intensity distribution in the magnetic spectrum of beta particles from radium (B + C). *Verh. Phys. Gesell.* 16:383–391, 1914.

[6] W. Pauli. Dear radioactive ladies and gentlemen. *Phys. Today* 31N9:27, 1978.

[7] L. M. Brown. The idea of the neutrino. *Phys. Today* 31N9:23–28, 1978.

[8] J. Chadwick. Possible Existence of a Neutron. *Nature* 129:312, 1932.

[9] E. Fermi. An attempt of a theory of beta radiation. 1. *Z. Phys.* 88:161–177, 1934.

[10] F. Reines et al. Detection of the free neutrino. *Phys. Rev.* 92:830–831, 1953.

[11] G. Danby et al. Observation of High-Energy Neutrino Reactions and the Existence of Two Kinds of Neutrinos. *Phys. Rev. Lett.* 9:36–44, 1962.

[12] K. Kodama et al. (DONUT Collaboration). Observation of tau neutrino interactions. *Phys. Lett. B* 504:218–224, 2001, [hep-ex/0012035].

[13] S. Schael et al. (ALEPH, DELPHI, L3, OPAL, SLD, LEP Electroweak Working Group, SLD Electroweak Group, SLD Heavy Flavour Group Collaboration). Precision electroweak measurements on the Z resonance. *Phys. Rept.* 427:257–454, 2006, [hep-ex/0509008].

[14] R. Davis, Jr. et al. Search for neutrinos from the sun. *Phys. Rev. Lett.* 20:1205–1209, 1968.

[15] B. Pontecorvo. Neutrino Experiments and the Problem of Conservation of Leptonic Charge. *Zh. Eksp. Teor. Fiz.* 53:1717–1725, 1967.

[16] S. M. Bilenky et al. Lepton Mixing and Neutrino Oscillations. *Phys. Rept.* 41:225–261, 1978.

[17] Z. Maki et al. Remarks on the unified model of elementary particles. *Prog. Theor. Phys.* 28:870–880, 1962.

[18] B. Pontecorvo. Inverse beta process. *Camb. Monogr. Part. Phys. Nucl. Phys. Cosmol.* 1:25–31, 1991.

[19] Y. Fukuda et al. (Super-Kamiokande Collaboration). Measurement of the flux and zenith angle distribution of upward through going muons by Super-Kamiokande. *Phys. Rev. Lett.* 82:2644–2648, 1999, [hep-ex/9812014].

[20] S. Fukuda et al. (Super-Kamiokande Collaboration). Tau neutrinos favored over sterile neutrinos in atmospheric muon-neutrino oscillations. *Phys. Rev. Lett.* 85:3999–4003, 2000, [hep-ex/0009001].

[21] S. Fukuda et al. (Super-Kamiokande Collaboration). Constraints on neutrino oscillations using 1258 days of Super-Kamiokande solar neutrino data. *Phys. Rev. Lett.* 86:5656–5660, 2001, [hep-ex/0103033].

[22] Q. R. Ahmad et al. (SNO Collaboration). Direct evidence for neutrino flavor transformation from neutral current interactions in the Sudbury Neutrino Observatory. *Phys. Rev. Lett.* 89:011301, 2002, [nucl-ex/0204008].

[23] S. N. Ahmed et al. (SNO Collaboration). Measurement of the total active B-8 solar neutrino flux at the Sudbury Neutrino Observatory with enhanced neutral current sensitivity. *Phys. Rev. Lett.* 92:181301, 2004, [nucl-ex/0309004].

[24] K. Abe et al. (T2K Collaboration). Indication of Electron Neutrino Appearance from an Accelerator-produced Off-axis Muon Neutrino Beam. *Phys. Rev. Lett.* 107:041801, 2011, [1106.2822].

[25] J. K. Ahn et al. (RENO Collaboration). Observation of Reactor Electron Antineutrino Disappearance in the RENO Experiment. *Phys. Rev. Lett.* 108:191802, 2012, [1204.0626].

[26] F. P. An et al. (Daya Bay Collaboration). Observation of electron-antineutrino disappearance at Daya Bay. *Phys. Rev. Lett.* 108:171803, 2012, [1203.1669].

[27] F. An et al. (JUNO Collaboration). Neutrino Physics with JUNO. *J. Phys. G* 43(3):030401, 2016, [1507.05613].

[28] Z. Djurcic et al. (JUNO Collaboration). JUNO Conceptual Design Report. arXiv:1508.07166, 2015.

[29] R. Acquafredda et al. The OPERA experiment in the CERN to Gran Sasso neutrino beam. *JINST* 4:P04018, 2009.

[30] T. Adam et al. The OPERA experiment target tracker. *Nucl. Instrum. Meth. A* 577:523–539, 2007, [physics/0701153].

[31] P. V. Hough. Method and means for recognizing complex patterns, 1962. US Patent 3,069,654.

[32] J. Illingworth et al. A survey of the hough transform. *Computer vision, graphics, and image processing* 44(1):87–116, 1988.

[33] R. O. Duda et al. Use of the Hough transformation to detect lines and curves in pictures. *Commun. ACM* 15(1):11–15, 1972.

[34] A. Pais et al. How Many Charm Quantum Numbers Are There? *Phys. Rev. Lett.* 35:1556, 1975.

[35] S. L. Glashow. Partial Symmetries of Weak Interactions. *Nucl. Phys.* 22:579–588, 1961.

[36] S. Weinberg. A Model of Leptons. *Phys. Rev. Lett.* 19:1264–1266, 1967.

[37] A. Salam. Weak and Electromagnetic Interactions. *Conf. Proc. C* 680519:367–377, 1968.

[38] M. J et al. Standard model of elementary particles. `https://commons.wikimedia.org/w/index.php?curid=4286964`, 2019.

[39] P. A. Zyla et al. (Particle Data Group Collaboration). Review of Particle Physics. *PTEP* 2020(8):083C01, 2020.

[40] G. S. Guralnik et al. Global Conservation Laws and Massless Particles. *Phys. Rev. Lett.* 13:585–587, 1964.

[41] A. Salam. Weak and Electromagnetic Interactions. *Conf. Proc. C* 680519:367–377, 1968.

[42] E. Fabri et al. Quantum field theory and approximate symmetries. *Phys. Rev. Lett.* 16:408–410, 1966.

[43] S. M. Carroll. Lecture notes on general relativity. arXiv:gr-qc/9712019, 1997.

[44] P. Langacker. *The Standard Model and Beyond.* Taylor & Francis, 2017.

[45] R. Bouchendira et al. New determination of the fine structure constant and test of the quantum electrodynamics. *Phys. Rev. Lett.* 106:080801, 2011, [1012.3627].

[46] T. Muta. *Foundations of Quantum Chromodynamics: An Introduction to Perturbative Methods in Gauge Theories, (3rd ed.),* volume 78 of *World scientific Lecture Notes in Physics.* World Scientific, Hackensack, N.J., 3rd edition, 2010.

[47] S. L. Glashow et al. Weak Interactions with Lepton-Hadron Symmetry. *Phys. Rev. D* 2:1285–1292, 1970.

[48] P. W. Higgs. Broken Symmetries and the Masses of Gauge Bosons. *Phys. Rev. Lett.* 13:508–509, 1964.

[49] F. Englert et al. Broken Symmetry and the Mass of Gauge Vector Mesons. *Phys. Rev. Lett.* 13:321–323, 1964.

[50] G. Aad et al. (ATLAS Collaboration). Observation of a new particle in the search for the Standard Model Higgs boson with the ATLAS detector at the LHC. *Phys. Lett. B* 716:1–29, 2012, [1207.7214].

[51] S. Chatrchyan et al. (CMS Collaboration). Observation of a New Boson at a Mass of 125 GeV with the CMS Experiment at the LHC. *Phys. Lett. B* 716:30–61, 2012, [1207.7235].

[52] A. Sen. String theory and Einstein's dream. *Curr. Sci.* 88:2045–2053, 2005, [physics/0609062].

[53] D.-W. Chiou. Loop Quantum Gravity. *Int. J. Mod. Phys. D* 24(01):1530005, 2014, [1412.4362].

[54] N. Poncin et al. The Geometry of Supersymmetry / A concise introduction. arXiv:2207.12974, 2022.

[55] J. de Blas et al. Effective description of general extensions of the Standard Model: the complete tree-level dictionary. *JHEP* 03:109, 2018, [1711.10391].

[56] B. Dasgupta et al. Sterile neutrinos. *Physics Reports* 928:1–63, 2021. Sterile neutrinos.

[57] H. Bethe et al. The 'neutrino'. *Nature* 133:532, 1934.

[58] T. D. Lee et al. Question of Parity Conservation in Weak Interactions. *Phys. Rev.* 104:254–258, 1956.

[59] T. D. Lee et al. Parity Nonconservation and a Two Component Theory of the Neutrino. *Phys. Rev.* 105:1671–1675, 1957.

[60] C. S. Wu et al. Experimental Test of Parity Conservation in β Decay. *Phys. Rev.* 105:1413–1414, 1957.

[61] M. Goldhaber et al. Helicity of Neutrinos. *Phys. Rev.* 109:1015–1017, 1958.

[62] S. M. Bilenky et al. Massive Neutrinos and Neutrino Oscillations. *Rev. Mod. Phys.* 59:671, 1987. [Erratum: Rev.Mod.Phys. 61, 169 (1989), Erratum: Rev.Mod.Phys. 60, 575–575 (1988)].

[63] J. Kersten et al. Right-Handed Neutrinos at CERN LHC and the Mechanism of Neutrino Mass Generation. *Phys. Rev. D* 76:073005, 2007, [0705.3221].

[64] S. M. Bilenky et al. Neutrinoless double-beta decay: A brief review. *Mod. Phys. Lett. A* 27:1230015, 2012, [1203.5250].

[65] K. Alfonso et al. (CUORE Collaboration). Search for Neutrinoless Double-Beta Decay of ^{130}Te with CUORE-0. *Phys. Rev. Lett.* 115(10):102502, 2015, [1504.02454].

[66] M. Auger et al. (EXO-200 Collaboration). Search for Neutrinoless Double-Beta Decay in ^{136}Xe with EXO-200. *Phys. Rev. Lett.* 109:032505, 2012, [1205.5608].

[67] R. Arnold et al. (NEMO-3 Collaboration). Search for neutrinoless double-beta decay of ^{100}Mo with the NEMO-3 detector. *Phys. Rev. D* 89(11):111101, 2014, [1311.5695].

[68] M. J. Dolinski et al. Neutrinoless Double-Beta Decay: Status and Prospects. *Ann. Rev. Nucl. Part. Sci.* 69:219–251, 2019, [1902.04097].

[69] J. N. Bahcall et al. Solar Models, Neutrino Experiments and Helioseismology. *Rev. Mod. Phys.* 60:297–372, 1988.

[70] J. N. Bahcall et al. Solar models and solar neutrino oscillations. *New J. Phys.* 6:63, 2004, [hep-ph/0404061].

[71] B. T. Cleveland et al. Measurement of the solar electron neutrino flux with the Homestake chlorine detector. *Astrophys. J.* 496:505–526, 1998.

[72] B. Pontecorvo. Chalk river laboratory report pd-205 (1946). *Zh. Eksp. Teor. Fiz* 53:1717, 1967.

[73] S. Wanninger et al. Probing neutrino vacuum oscillations with the GALLEX solar neutrino results. *Phys. Rev. Lett.* 83:1088–1091, 1999.

[74] M. Altmann et al. (GNO Collaboration). GNO solar neutrino observations: Results for GNO I. *Phys. Lett. B* 490:16–26, 2000, [hep-ex/0006034].

[75] J. N. Abdurashitov et al. (SAGE Collaboration). Measurement of the solar neutrino capture rate by SAGE and implications for neutrino oscillations in vacuum. *Phys. Rev. Lett.* 83:4686–4689, 1999, [astro-ph/9907131].

[76] J. N. Bahcall. Neutrino solar flux measured by several experiments in comparison with the expected flux from the standard solar model. `http://www.sns.ias.edu/~jnb/SNviewgraphs/snviewgraphs.html`, 2005.

[77] J. N. Bahcall. Solar models and solar neutrinos: Current status. *Phys. Scripta T* 121:46–50, 2004, [hep-ph/0412068].

[78] B. Pontecorvo. Inverse beta processes and non conservation of lepton charge. *Zh. Eksp. Teor. Fiz.* 34:247, 1957.

[79] C. Jarlskog. Commutator of the Quark Mass Matrices in the Standard Electroweak Model and a Measure of Maximal CP Nonconservation. *Phys. Rev. Lett.* 55:1039, 1985.

[80] L. Wolfenstein. Neutrino Oscillations in Matter. *Phys. Rev. D* 17:2369–2374, 1978.

[81] S. P. Mikheev et al. Resonant amplification of neutrino oscillations in matter and solar neutrino spectroscopy. *Nuovo Cim. C* 9:17–26, 1986.

[82] C. Giganti et al. Neutrino oscillations: The rise of the PMNS paradigm. *Prog. Part. Nucl. Phys.* 98:1–54, 2018, [1710.00715].

[83] J. Farine (SNO Collaboration). Measurement of the rate of nu/e + d –> p + p + e- interactions produced by B-8 solar neutrinos at the Sudbury Neutrino Observatory. *Phys. Atom. Nucl.* 65:2147–2155, 2002.

[84] T. Araki et al. (KamLAND Collaboration). Measurement of neutrino oscillation with KamLAND: Evidence of spectral distortion. *Phys. Rev. Lett.* 94:081801, 2005, [hep-ex/0406035].

[85] M. Shiozawa (Super-Kamiokande, Kamiokande Collaboration). Evidence for neutrino oscillations in atmospheric neutrino observations. *Nucl. Instrum. Meth. A* 433:307–313, 1999.

[86] D. Adey et al. (Daya Bay Collaboration). Measurement of the electron antineutrino oscillation with 1958 days of operation at daya bay. *Phys. Rev. Lett.* 121:241805, 2018.

[87] T. R. S. A. of Sciences. For the discovery of neutrino oscillations, which shows that neutrinos have mass. `https://www.nobelprize.org/prizes/physics/2015/summary/`, 2015.

[88] S. F. King. Neutrino Mass and Mixing in the Seesaw Playground. *Nucl. Phys. B* 908:456–466, 2016, [1511.03831].

[89] I. Esteban et al. The fate of hints: updated global analysis of three-flavor neutrino oscillations. *JHEP* 09:178, 2020, [2007.14792].

[90] S. Capelli et al. Absolute neutrino mass scale. *Nucl. Phys. B Proc. Suppl.* 237-238:347–351, 2013.

[91] A. B. Balantekin et al. Addressing the Majorana vs. Dirac Question with Neutrino Decays. *Phys. Lett. B* 789:488–495, 2019, [1808.10518].

[92] G. Altarelli et al. CP violation in neutrino oscillations and new physics. *Nucl. Phys. B* 809:158–182, 2009, [0809.1041].

[93] A. de Gouvea et al. (Intensity Frontier Neutrino Working Group Collaboration). Working Group Report: Neutrinos. In *Community Summer Study 2013: Snowmass on the Mississippi*, 2013.

[94] P. F. De Salas et al. Neutrino Mass Ordering from Oscillations and Beyond: 2018 Status and Future Prospects. *Front. Astron. Space Sci.* 5:36, 2018, [1806.11051].

[95] Q. Huang. *On the way to the determination of the Neutrino Mass Hierarchy with JUNO*. PhD thesis, Ecole Polytechnique, 2019.

[96] A. Abusleme et al. (JUNO Collaboration). JUNO Physics and Detector. arXiv:2104.02565, 2021.

[97] A. Abusleme et al. (JUNO Collaboration). Sub-percent Precision Measurement of Neutrino Oscillation Parameters with JUNO. arXiv:2204.13249, 2022.

[98] A. Abusleme et al. (JUNO Collaboration). TAO Conceptual Design Report: A Precision Measurement of the Reactor Antineutrino Spectrum with Sub-percent Energy Resolution. arXiv:2005.08745, 2020.

[99] L. Zhan et al. Determination of the Neutrino Mass Hierarchy at an Intermediate Baseline. *Phys. Rev. D* 78:111103, 2008, [0807.3203].

[100] V. Kopeikin et al. Reactor as a source of antineutrinos: Thermal fission energy. *Phys. Atom. Nucl.* 67:1892–1899, 2004, [hep-ph/0410100].

[101] C. L. Cowan et al. Large liquid scintillation detectors. *Phys. Rev.* 90:493–494, 1953.

[102] D. Schmidt et al. Characterization of liquid scintillation detectors. *Nucl. Instrum. Meth. A* 476:186–189, 2002.

[103] P. Vogel et al. Angular distribution of neutron inverse beta decay, anti-neutrino(e) + p —> e+ + n. *Phys. Rev. D* 60:053003, 1999, [hep-ph/9903554].

[104] P. Vogel et al. Neutrino Oscillation Studies with Reactors. *Nature Commun.* 6:6935, 2015, [1503.01059].

[105] D. Horrocks. *Applications of liquid scintillation counting*. Elsevier, 2012.

[106] J. B. Birks. *The Theory and practice of scintillation counting*. 1964.

[107] A. Abusleme et al. (JUNO Collaboration). The design and sensitivity of JUNO's scintillator radiopurity pre-detector OSIRIS. *Eur. Phys. J. C* 81(11):973, 2021, [2103.16900].

[108] G. Zhang et al. Addendum: The study of active geomagnetic shielding coils system for JUNO. *JINST* 16(12):A12001, 2021, [2106.09998].

[109] C. H. Lee et al. Characteristics of plastic scintillators fabricated by a polymerization reaction. *Nuclear Engineering and Technology* 49(3):592–597, 2017.

[110] Hamamatsu photonics k.k. and its affiliates. About PMTs. `https://www.hamamatsu.com/eu/en/product/optical-sensors/pmt/about_pmts.html`.

[111] K. Li et al. Gdml based geometry management system for offline software in juno. *Nuclear Instruments and Methods in Physics Research Section A: Accelerators, Spectrometers, Detectors and Associated Equipment* 908:43–48, 2018.

[112] S. Blin et al. MAROC, a generic photomultiplier readout chip. *IEEE Nucl. Sci. Symp. Conf. Rec.* 2010:1690–1693, 2010.

[113] T. Lin et al. (JUNO Collaboration). The Application of SNiPER to the JUNO Simulation. *J. Phys. Conf. Ser.* 898(4):042029, 2017, [1702.05275].

[114] S. Agostinelli et al. (GEANT4 Collaboration). GEANT4–a simulation toolkit. *Nucl. Instrum. Meth. A* 506:250–303, 2003.

[115] X.-Y. Li et al. Simulation of natural radioactivity backgrounds in the JUNO central detector. *Chinese Physics C* 40(2):026001, 2016.

[116] P. Antonioli et al. A Three-dimensional code for muon propagation through the rock: Music. *Astropart. Phys.* 7:357–368, 1997, [hep-ph/9705408].

[117] A. A. Hahn et al. Anti-neutrino Spectra From ^{241}Pu and ^{239}Pu Thermal Neutron Fission Products. *Phys. Lett. B* 218:365–368, 1989.

[118] F. Von Feilitzsch et al. Experimental beta spectra from ^{239}Pu and ^{235}U thermal neutron fission products and their correlated antineutrino spectra. *Phys. Lett. B* 118:162–166, 1982.

[119] A. Abusleme et al. (JUNO Collaboration). Feasibility and physics potential of detecting ^{8}B solar neutrinos at JUNO. *Chin. Phys. C* 45(2):023004, 2021, [2006.11760].

[120] P. K. Grieder. *Cosmic rays at Earth*. Elsevier, 2001.

[121] M. Bahmanabadi. A method for determining the angular distribution of atmospheric muons using a cosmic ray telescope. *Nucl. Instrum. Meth. A* 916:1–7, 2019.

[122] B. Olmos Yáñez et al. A method to measure the integral vertical intensity and angular distribution of atmospheric muons with a stationary plastic scintillator bar detector. *Nuclear Instruments and Methods in Physics Research Section A: Accelerators, Spectrometers, Detectors and Associated Equipment* 987:164870, 2021.

[123] Y. Zhang et al. Track Reconstruction Using the Hough Transform at BESIII. *PoS* ICHEP2018:888, 2019.

[124] L. Calligaris (CMS, Time Multiplex Track Trigger Group Collaboration). Trigger level track reconstruction in CMS with a fully time-multiplexed architecture using a Hough transform implemented in an FPGA. *PoS* ICHEP2016:1000, 2017.

[125] N. Pozzobon et al. A novel approach to Hough Transform for implementation in fast triggers. *Nucl. Instrum. Meth. A* 834:81–97, 2016.

[126] J. Tyler (VERITAS Collaboration). Muon Identification with VERITAS using the Hough Transform. In *33rd International Cosmic Ray Conference*, page 0931, 2013.

Luis F. Piñeres Rico

Track Reconstruction for the Top Tracker of the JUNO Neutrino Experiment

RÉSUMÉ

L'expérience JUNO est un détecteur souterrain polyvalent à scintillation liquide dont la masse cible est de 20 kt et dont la résolution en énergie est de 3% at 1 MeV. L'objectif principal de JUNO est de déterminer la hiérarchie des masses de neutrinos. Le Top Tracker est essentiel pour rejeter le fond cosmogénique dans le détecteur central. Le Top Tracker assure un suivi précis des muons cosmiques en vue d'une détection de bruit pouvant immiter le signal.

Cette thèse se concentre sur la calibration de la chaîne électronique du Top Tracker à l'aide d'un banc de test et d'un télescope à muons. Les méthodes de reconstruction appliquées sur ce télescope à muons sont également détaillées.

La transformée de Hough a été considérée comme une alternative au logiciel officiel de JUNO souffrant de certains inconveniens. La transformée de Hough montre une plus grande efficacité et un temps de éxecution plus court en tant que méthode de reconstruction. Ce qui fait de cette méthode à un candidat sérieux pour la reconstruction des traces dans le Top Tracker.

Mots-clés: JUNO, Top Tracker, télescope à muons, transformée de Hough.

ABSTRACT

The JUNO experiment is a multi-purpose underground liquid scintillation detector with a target mass of 20 kt, and an energy resolution of 3% at 1 MeV. The main objective of JUNO is to determine the neutrino mass hierarchy. Among its parts, JUNO has a muon tracker called Top Tracker. It consists of three plastic scintillator layers. The Top Tracker provides accurate tracking of cosmic muons, which is essential for understanding the cosmogenic background in the detector.

This thesis focuses on the calibration of the Top Tracker electronics chain using a test bench and a prototype detector called Muon Telescope. Reconstruction methods using this prototype are extensively discussed.

The Hough transform is proposed as an alternative reconstruction method to the official one already implemented in the JUNO software. It shows higher efficiency and shorter runtime in comparison to the existing reconstruction method. These advantages make the Hough Transform a good reconstruction method to be used in the Top Tracker.

Keywords: JUNO, Top Tracker, Muon Telescope, Hough transform.